

A420811

Biblioteka Główna i OINT  
Politechniki Wrocławskiej



100100243757

Dz. 3



# Materials Science·Poland

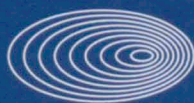
an  
**Interdisciplinary Journal of  
Physics, Chemistry and  
Technology of Materials**

**Vol. 26, No. 2, 2008**

**ISSN 0137-1339  
Index No. 375675**



Wrocław  
University  
of Technology



**CENTRE OF  
ADVANCED MATERIALS AND  
NANOTECHNOLOGY**

Wrocław University of Technology  
Centre of Advanced Materials and Nanotechnology

---

# Materials Science-Poland

1st Polish Conference on Nanotechnology  
NANO 2007

Wrocław, 26–28 April 2007



Vol. 26



No. 2



2008



Oficyna Wydawnicza Politechniki Wrocławskiej

**Materials Science** is an interdisciplinary journal devoted to experimental and theoretical research into the synthesis, structure, properties and applications of materials.

**Among the materials of interest are:**

- glasses and ceramics
- sol-gel materials
- photoactive materials (including materials for nonlinear optics)
- laser materials
- photonic crystals
- semiconductor micro- and nanostructures
- piezo-, pyro- and ferroelectric materials
- high- $T_c$  superconductors
- magnetic materials
- molecular materials (including polymers) for use in electronics and photonics
- novel solid phases
- other novel and unconventional materials

The broad spectrum of the areas of interest reflects the interdisciplinary nature of materials research. Papers covering the modelling of materials, their synthesis and characterisation, physicochemical aspects of their fabrication, properties and applications are welcome. In addition to regular papers, the journal features issues containing conference papers, as well as special issues on key topics in materials science.

Materials Science is published under the auspices of the Centre of Advanced Materials and Nanotechnology of the Wrocław University of Technology, in collaboration with the Institute of Low Temperatures and Structural Research of the Polish Academy of Sciences and the Wrocław University of Economics.

All accepted papers are placed on the Web page of the journal and are available at the address:

<http://MaterialsScience.pwr.wroc.pl>

**Materials Science is abstracted/indexed in: Chemical Abstracts, Materials Science Citation Index, Science Citation Index Expanded.**

### Editor-in-Chief

Juliusz Sworakowski

Institute of Physical and Theoretical Chemistry  
Wrocław University of Technology  
Wybrzeże Wyspiańskiego 27  
50-370 Wrocław, Poland  
[sworakowski@pwr.wroc.pl](mailto:sworakowski@pwr.wroc.pl)

### Associate Editors

Wiesław Stręć

Institute of Low Temperature  
and Structure Research  
Polish Academy of Sciences  
P. O. Box 1410  
50-950 Wrocław 2, Poland  
[strek@int.pan.wroc.pl](mailto:strek@int.pan.wroc.pl)

Jerzy Hanuza

Department of Bioorganic Chemistry  
Faculty of Industry and Economics  
Wrocław University of Economics  
Komandorska 118/120  
53-345 Wrocław, Poland  
[hanuza@credit.ae.wroc.pl](mailto:hanuza@credit.ae.wroc.pl)

### Scientific Secretary

Jan Felba

Faculty of Microsystem Electronics and Photonics  
Wrocław University of Technology  
Wybrzeże Wyspiańskiego 27  
50-370 Wrocław, Poland  
[jan.felba@pwr.wroc.pl](mailto:jan.felba@pwr.wroc.pl)

### Advisory Editorial Board

Ludwig J. Balk, Wuppertal, Germany	Jerzy Lis, Cracow, Poland
Frédéric Bernard, Dijon, France	Tadeusz Luty, Wrocław, Poland
Mikhaylo S. Brodyn, Kyiv, Ukraine	Joop H. van der Maas, Utrecht, The Netherlands
Alexander Bulinski, Ottawa, Canada	Bolesław Mazurek, Wrocław, Poland
Roberto M. Faria, São Carlos, Brazil	Jan Misiewicz, Wrocław, Poland
Reimund Gerhard-Multhaupt, Potsdam, Germany	Jerzy Mroziński, Wrocław, Poland
Paweł Hawrylak, Ottawa, Canada	Robert W. Munn, Manchester, U.K.
Andrzej Kłonkowski, Gdańsk, Poland	Krzysztof Nauka, Palo Alto, CA, U.S.A.
Seiji Kojima, Tsukuba, Japan	Stanislav Nešpůrek, Prague, Czech Republic
Shin-ya Koshihara, Tokyo, Japan	Marek Samoć, Canberra, Australia
Krzysztof J. Kurzydłowski, Warsaw, Poland	Jan Stankowski, Poznań, Poland
Janina Legendziewicz, Wrocław, Poland	Jacek Ulański, Łódź, Poland
Benedykt Licznerski, Wrocław, Poland	Vladislav Zolin, Moscow, Russia

The Journal is supported by the State Committee for Scientific Research

Editorial Office

Jan Wojna

Printed in Poland

© Copyright by Oficyna Wydawnicza Politechniki Wrocławskiej, Wrocław 2008

Drukarnia Oficyny Wydawniczej Politechniki Wrocławskiej  
Zam. nr 335/2008.

# Effects of Ar<sup>+</sup> ion sputtering on morphology and electric conductance of 6H-SiC (0001) surface

P. MAZUR, S. ZUBER, M. GRODZICKI\*, A. CISZEWSKI

Institute of Experimental Physics, University of Wrocław, pl. Maksa Borna 9, 50-204 Wrocław, Poland

The paper reports surface modification of SiC by Ar<sup>+</sup> ion sputtering. Observations were performed with an ultra high vacuum atomic force microscope operating in the contact mode. The surface morphology and topography were investigated with simultaneous measurement of local changes in electric conductance. We show that the Ar<sup>+</sup> ion bombardment of the 6H-SiC wafer surface affects the surface stoichiometry, changing the character of a metal/SiC contact from the Schottky barrier diode type into an ohmic contact type.

Key words: *silicon carbide; metal contact; ion sputtering*

## 1. Introduction

Wide band-gap semiconductor silicon carbide SiC has been recognized as a very promising material for future applications in opto-, high-frequency, high-power, and high-temperature electronics [1–3]. In addition, the material is highly chemically resistant, even to hydrofluoric acid [4]. Preparation of SiC as an output material for a large-scale application in industry is still difficult, mainly due to the presence of numerous defects in single crystals of SiC and troublesome technology of surface-perfection preparation. Another problem occurs with the formation stage of the ohmic contact by deposition of metals and other materials onto this substrate. One of the means of processing the surface for a high cleanness and chemical resistance is ion bombardment. The ion-impact induced processes such as diffusion, segregation and surface diffusion can introduce considerable changes in substrate stoichiometry. Ion sputtering makes the surface disordered, roughened and flattened.

An improper morphology can degrade the quality of thin films grown on the surface and, in consequence, of the electronic components fabricated using the films. The chemical composition, cleanness and structure of the surface play an essential role in

---

\*Corresponding author, e-mail: grodzian@ifd.uni.wroc.pl

the formation process of the metal/semiconductor interface for technology of electronic devices [5]. Surfaces modified by ion sputtering show considerable changes in the conductance type of the contact probe/SiC(0001) surface. From this point of view we undertook this investigation of SiC surface preparation. In the present paper, we report the effect of the  $\text{Ar}^+$  ion bombardment process on the topography and electric conductance of the 6H-SiC(0001) wafer surface.

## 2. Experimental

Samples, around  $3 \times 5 \text{ mm}^2$  in size, were cut out of the nitrogen-doped n-type (resistivity  $0.065 \text{ } \Omega \cdot \text{cm}$ ) 6H-SiC single crystal (0001)-oriented Si-terminated wafers 0.25 mm thick (Cree Research Inc.). Supplier polished samples were degreased in acetone. 1.2 keV  $\text{Ar}^+$  ion bombardment was applied from an ion gun with the  $8 \text{ } \mu\text{A}$  current at the pressure of  $2 \times 10^{-4}$  torr Ar, at room temperature for 2–25 min. Observations were performed at  $\sim 10^{-10}$  torr with the ultra high vacuum AFM (Omicron-made atomic force microscope) operating in the contact mode (nanosensors-made Pt/Ir tip with the force constant of  $0.12 \text{ N/m}$ ). The surface morphology and topography were investigated with simultaneous measurement of the local changes in electric conductance of the probe/6H-SiC(0001) surface system. Next, the effect of  $\text{Ar}^+$  ion bombardment of the sample was investigated by measuring of  $I$ – $V$  characteristics. The area of probed region was  $1 \text{ } \mu\text{m}^2$  covered by 6400 measurement points.

## 3. Results and discussion

AFM topography of the surface of a fresh commercial sample exhibits numerous, randomly oriented scratches of up to 20 nm deep and 200 nm wide, resulting from the polishing process. The ion bombardment process leads to considerable topographic changes of the surface. Figure 1 shows typical AFM images of the topography after 2 and 20 min of sputtering (Figs. 1a, b, respectively) and the corresponding images of the local conductance for the contact system of interest (Figs. 1c, d, respectively). Analysis of the topography showed that the roughness of the surface, as estimated by the RMS ripple parameter within the  $1 \text{ } \mu\text{m}^2$  area frame, decreased with increasing bombardment time (Fig. 2). After a longer bombardment time of 20 min, the formation of grains on the surface was observed which may indicate the appearance of an amorphous layer [6]. The images in Fig. 1d, e, mapping the local conductance in the reverse bias mode show that after 2 min bombardment the surface is weakly and rather uniformly conducting, whereas after a longer exposure to ions the conductance behaviour essentially changes and after 20 min of bombardment the images are electrically non-uniform. The current images are grainy in structure which, however, is not reflected in the topographic image. The long-exposure originated grains reveal a higher conduction in the system of interest. The statistics on the population of these grains

shows their diameters to be steady and the range between 0.4 and 0.6 nm, while the conduction of the system increases with increasing exposure time. For the exposures shorter than 5 min, the current images reveal a uniform and non-grainy structure whereas the surface becomes entirely grainy for longer exposure times. Changes in stoichiometry resulting from  $\text{Ar}^+$  ion bombardment are not well understood so far; quite different results can be found in the literature. Preferential sputtering and the accompanying changes in SiC surfaces are reported. Detailed AES and XPS study on the  $\text{Ar}^+$  sputtered SiC(0001) surface at room temperature revealed that the sputtering restored the surface stoichiometry [7]. Excess silicon [8] and excess carbon [6] surfaces were obtained after  $\text{Ar}^+$  ion sputtering due to the different sputter rates of carbon and silicon.

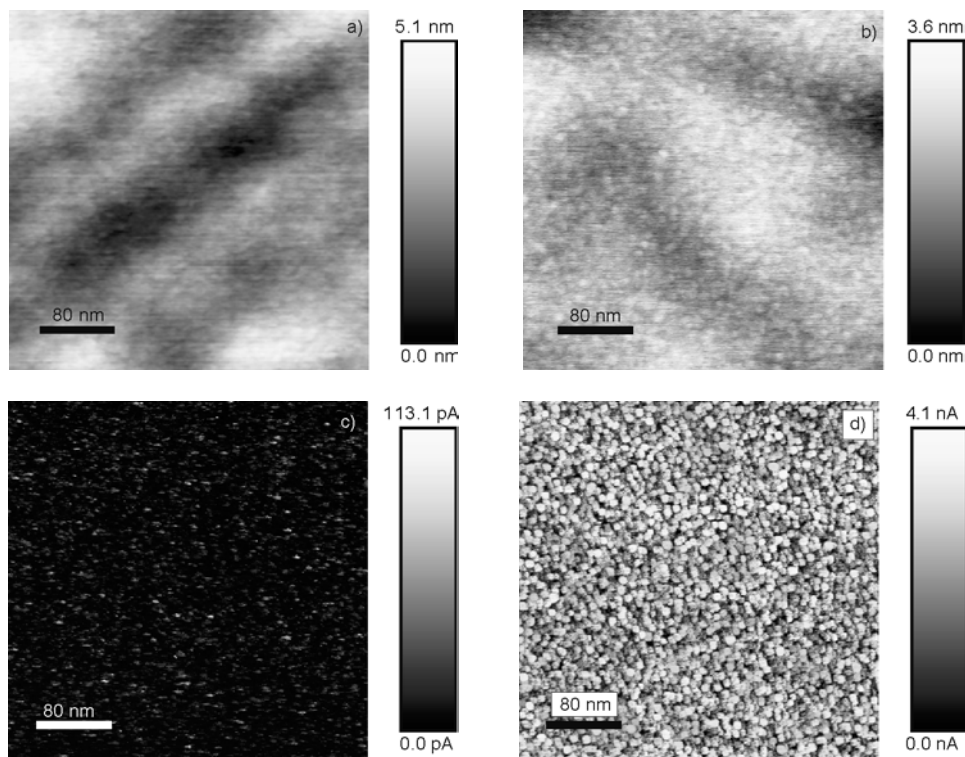


Fig. 1. AFM image of the 6H-SiC(0001) surface topography after 2 min (a), and 20 min (b) of  $\text{Ar}^+$  bombardment (1200 eV, 8 mA), and the corresponding electric conductance images 1.1 V (c) and 0.27 V (d)

Analysis of the  $I$ - $V$  characteristics taken for different bombardment times shows, for the samples which were not subject to  $\text{Ar}^+$  ion sputtering, a considerable difference in characteristics from site to site of the surface. Typical values of averaging are shown in Fig. 3. It is seen from these curves that the conductance character of the contact probe/6H-SiC(0001) surface changes from the diode type to the ohmic type.



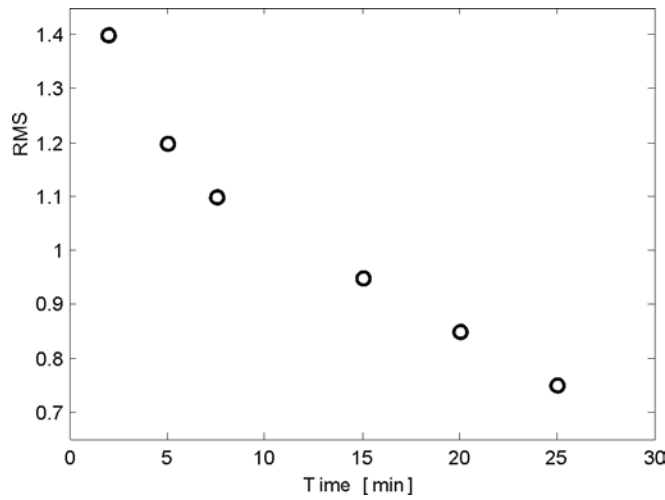


Fig. 2. The roughness of the surface (expressed by the RMS ripple parameter) vs. 1.2 keV  $\text{Ar}^+$  ion bombardment time

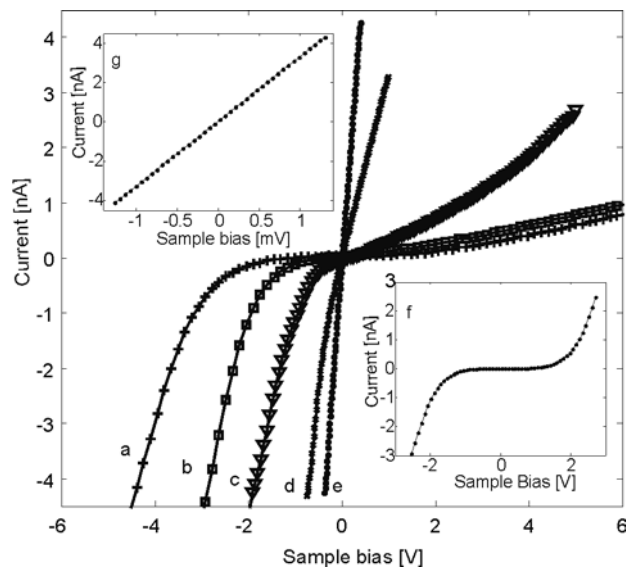


Fig. 3. Evolution of  $I$ - $V$  characteristics for the probe/6H-SiC(0001) surface contact due to  $\text{Ar}^+$  ion bombardment for 2 min (a), 5 min (b), 7.5 min (c), 15 min (d) and 20 min (e);  $I$ - $V$  characteristics for the probe/Si(111) surface contact (f) and for the probe/HOPG surface contact (g)

For bombardment times up to 7.5 min, the contact is rectifying, and the characteristics are nonlinear like the case of measured on silicon (Fig. 3f). A crucial change appears for the times longer than 15 min of ion bombardment, and the obtained contact type becomes almost ohmic. Further bombardment leads to a very good ohmic contact. The linear characteristics, obtained after a longer exposure to  $\text{Ar}^+$  ions, are

typical of graphite (as that shown in Fig. 3g), which may be due to enriching the surface layer of the sample with carbon. Consequently, it is clear that the  $\text{Ar}^+$  ion bombardment process is accompanied by preferential surface sputtering. This fact can be utilized for formation of the ohmic contact of metal/n-type SiC with the formation of the carbon intermediate layer that lowers the Schottky barrier at the interface [9].

#### 4. Summary

It is shown that the roughness of the 6H-SiC(0001) surface is reduced with increasing time of  $\text{Ar}^+$  ion bombardment. The remainders of the crystal polishing process such as the scratches can be efficiently removed. Moreover, the ion bombardment process essentially affects the surface stoichiometry, resulting in the change in conductance of the system of AFM probe/6H-SiC(0001) and, consequently, in the type of the contact from the rectifying one to the ohmic one. Ohmic contacts of metal/semiconductor used to be formed by high temperature annealing whereas the  $\text{Ar}^+$  ion bombardment process can be utilized as another means of room temperature formation of such contacts.

#### References

- [1] JANZÉN E., KORDINA O., *Mater. Sci. Eng.*, B46 (1997), 203.
- [2] SARRO P.M., *Sensors Act.*, 82 (2000), 210.
- [3] MATSUNAMI H., *Microelectr. Eng.*, 83 (2006), 2.
- [4] VERMA A.R., KRISHNA P., *Polymorphism and polytypism in crystals*, Wiley, USA, 1966, p. 99.
- [5] PORTER L.M., DAVIS R.F., *Mater. Sci. Eng.*, B34, (1995), 83.
- [6] PEZOLDT J., STOTTKO B., KUPRIS G., ECKE G., *Mat. Sci. Eng.*, B29 (1995), 94.
- [7] MUEHLHOFF L., CHOYKE W.J., BOZACK M.J., YATES J.T., *J. Appl. Phys.*, 60 (1986), 2842.
- [8] BELLINA J.J., FERRANTE J., ZELLER M.V., *J. Vac. Sci. Techn.*, A4 (1986), 1692.
- [9] SEYLLER TH., EMTSEV K.V., SPECK F., GAO K.Y., LEY L., *Appl. Phys. Lett.*, 88 (2006), 242103.

*Received 28 April 2007*  
*Revised 16 February 2008*

# Fabrication of micro- and nanostructures by scanning probe microscopy. Local anodic oxidation

K. KOLANEK<sup>1\*</sup>, T. GOTSZALK<sup>1</sup>, M. ZIELONY<sup>1</sup>, P. GRABIEC<sup>2</sup>

<sup>1</sup>Wrocław University of Technology, Faculty of Microsystem Electronics and Photonics,  
ul. Janiszewskiego 11/17, 50-372 Wrocław, Poland

<sup>2</sup>Institute of Electron Technology, al. Lotników 32/46, 02-668 Warsaw, Poland

Atomic force microscopy (AFM) is a high resolution imaging technique in which a cantilever with a very sharp tip is scanned over a sample surface. AFM technique can also be used to fabricate micro- and nanostructures on metallic or semiconductor surfaces. Nanolithography by local anodic oxidation or by noncontact atomic force microscopy (NC-AFM) has strong potential to pattern the surface with a well defined feature size at the nanometer regime. In the paper, the growth rate of nanostructures produced by local anodic oxidation process has been investigated. Mechanisms of nanooxidation have been studied and dependences of its rate and resolution on the voltage applied between the tip and a sample surface, tip speed, and ambient humidity.

Key words: *local anodic oxidation; nanolithography; nanotechnology; scanning probe microscopy; atomic force microscope*

## 1. Introduction

Scanning probe microscopy (SPM) is a branch of advanced techniques used to examine properties of surfaces, in which interactions between a near field probe – sharp tip at the end of a cantilever – and the surface are examined [1]. Figure 1 shows experimental setup used in one of the most reliable SPM methods – atomic force microscopy (AFM). In this method, the microtip scans surface and by measuring the interactions with dedicated electronics one may map surface properties.

After developing first scanning probe techniques it became clear that these methods are also capable of changing surface properties with a very high spatial resolution. First experiments showing possibilities of transferring patterns on the surface were conducted in 1990 [2]. It was proven that fabrication of micro- and nanostruc-

---

\*Corresponding author, e-mail: krzysztof.kolanek@pwr.wroc.pl

tures by scanning probe techniques may compete with well known photolithographic methods.

Use of local anodic oxidation technique combined with scanning probe microscopy gives new perspectives to achieve fine resolution below 30 nm with inexpensive equipment needed. One of the main advantages of the technique is the ability to fabricate and examine created micro- and nanostructures at almost the same time.

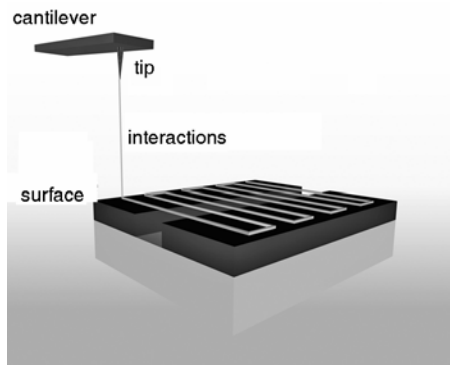


Fig. 1. Idea of the atomic force microscopy

The process of classical anodic oxidation is significantly shrunk when combined with atomic force microscopy. In this method, the conductive tip is approached to the surface to be modified. With the tip radius ca. 10 nm and distance between tip and surface approximately well below a couple of nanometers, very fine patterns may be transferred on the surface. When humidity of the process is controlled in the microscope environmental chamber, the tip of the cantilever is immersed in water acting as an electrolyte covering the whole surface. Oxidation process in this case emerges very locally – only below the conductive tip.

In the paper, experimental investigation has been described conducted at the Faculty of Microsystem Electronics and Photonics of the Wrocław University of Technology. The influence of main parameters on the local anodic oxidation process has been determined. The algorithm responsible for transferring patterns on the surface was explained. In addition, the equipment for the combined surface measurement and nanolithography processes has been shown.

## 2. Experimental

*Local anodic oxidation.* Local anodic oxidation proceeds in an environmental chamber of the noncontact atomic force microscope which ensures, together with a bubbler and a nitrogen source, a constant humidity. The developed system for the anodic oxidation of silicon surfaces is shown in Fig. 2.

Due to the control of humidity, a few monolayers of water are on the surface. The water layer is needed to perform oxidation and acts as an electrolyte. The semiconduc-

tor surface to be oxidized is connected as an anode and together with a conductive tip is immersed in the electrolyte [3].

Strong electric field induced by a sharp conductive tip causes dissociation of water and assures presence of hydroxide groups, reacting with the silicon surface according to the following equations [4, 5]:

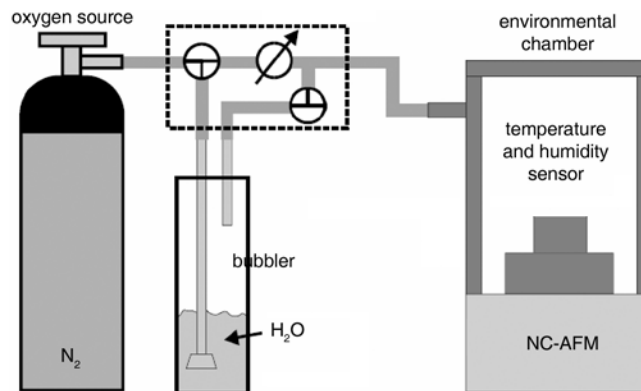


Fig. 2. System maintaining a constant humidity during local anodic oxidation

In order to perform the AFM nanolithography process, the silicon substrate should be preprocessed. It was cleaned with deionized water and dried with pure nitrogen. Then native oxide was removed by 5% dip in HF solution, and the silicon surface was rinsed with deionized water and dried with pure nitrogen. The bath in hydrofluoric acid additionally passivated the surface.

*Algorithm of local anodic oxidation.* Local anodic oxidation algorithm is controlled by a signal processor DSP Adwin-Pro Keithley based system [3]. This approach makes it possible to control executing algorithm with 1  $\mu\text{s}$  time precision. The signal processor executes the program code which enables establishing key factors of local anodic oxidation parameters, such as:

- amplitude of voltage applied between the surface and a conductive tip,
- frequency of voltage modulation,
- rate of movement of the tip over the surface,
- time of approach to anodization point,
- time of anodization on a given point.

The pattern which should be fabricated on the surface is created in especially designed graphic editor. Local anodic oxidation of the silicon surface is performed in a two step procedure [6]. Before oxidation, the line to be transferred on the surface is scanned and topography information is stored in a DSP processor. Then the scanner moves to the beginning of the line and with a feedback loop turned off and based on stored topography information the line is oxidized.

*Measurement set-up.* Experiments were conducted on a surface of n-type Si(100) with a resistivity of  $12 \Omega\cdot\text{cm}$ . An atomic force microscope operated in a noncontact mode was equipped with conductive cantilevers. The average spring constant and resonance frequency were ca.  $1.4 \text{ N/m}$  and  $58 \text{ kHz}$ , respectively. The cantilever was excited at its resonance frequency by a piezoactuator and a function generator Stanford Research Systems DS340. The position of the sample with respect to the tip was derived from measurements of the oscillation amplitude and deflection of the cantilever. The optical signal reflected from the back of the oscillating cantilever illuminated a four-section photodiode. Electrical signal converted by photodiodes was then detected by a lock-in amplifier Stanford Research Systems SR530 and was acquired in a real time by a signal processor. After surface preparation, the sample was closed in an environmental chamber of the atomic force microscope. The environmental chamber was equipped with inlets for dry and  $\text{H}_2\text{O}$  saturated nitrogen. The relative humidity  $\text{RH}_i$  was stabilized at a constant value of 50%. The microscope tip was oscillating at a fixed distance of a few nanometers above the sample surface and a voltage pulse was applied between the tip grounded and the sample. The applied voltage induced the formation of a water bridge between the tip and the sample whenever the voltage strength was above a certain threshold voltage [5]. During the application of the voltage pulse, the electrostatic force induced deflection of the cantilever. It also reduced the oscillation amplitude, however, the tip never got in contact with the surface.

### 3. Results and discussion

In the initial phase of the experiments, the micro- and nanostructure heights as well as the width of the fabricated silicon oxide were examined in function of voltage amplitude

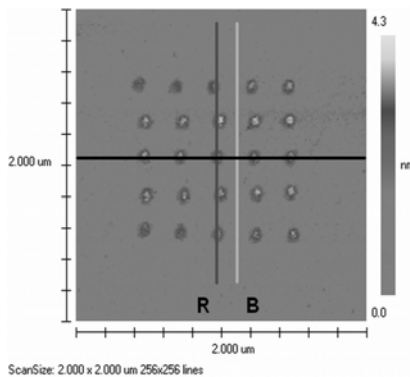


Fig. 3. NC-AFM image of Si(100) surface; 25 dots 80 nm wide and 2 nm high have been written; to each dot, a voltage pulse of 20 V and 10 s is applied between the sample and the tip

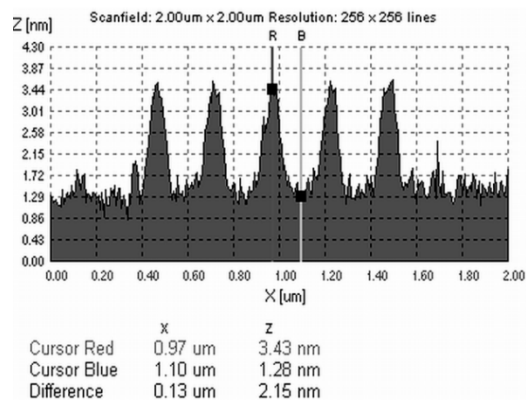


Fig. 4. NC-AFM cross section of fabricated nanostructures produced by static voltage; pulse parameters were 20 V, 10 s

applied between the tip and the surface as well as in function of the duration of the voltage pulse. Figure 3 shows an NC-AFM image of the silicon surface after local anodic oxidation process and Fig. 4 displays the cross-sections of the oxide dots.

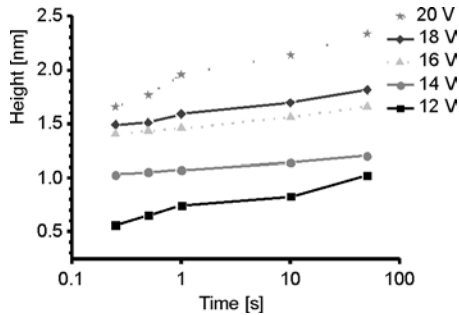


Fig. 5. Dependence of silicon oxides height on pulse duration and static voltage amplitude

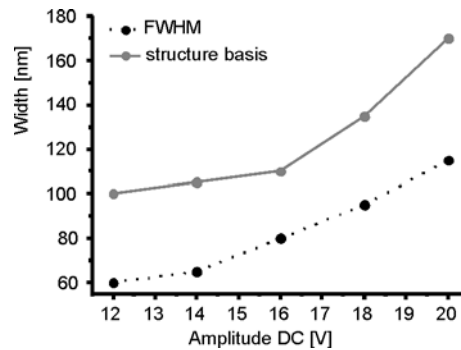


Fig. 6. Dependence of silicon oxide width on static voltage pulse amplitude; pulse duration 250 ms

The results of the whole series of measurements are presented in Figs. 5 and 6. The results shown in Fig. 5 indicate that increasing time of the voltage pulse duration does not significantly influence the height of the produced nanostructures manifesting the logarithmic character. Increase in the static voltage amplitude causes the enlargement not only of the height but also of the width of produced nanostructures as shown in Fig. 6. This is connected with increasing intensity of electric field facilitating formation of water bridges joining the tip and silicon surface [7]. It is possible to fabricate recurrent examples of nanostructures with an appropriate control of static voltage amplitude and pulse duration.

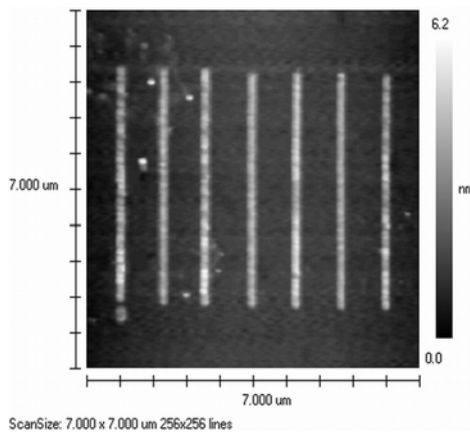


Fig. 7. NC-AFM image of Si(100) surface with fabricated oxide lines; tip speed – 2  $\mu\text{m/s}$ , voltage amplitude – 15  $V_{ac}$ , modulation frequency – 25 Hz and relative humidity 45% RH

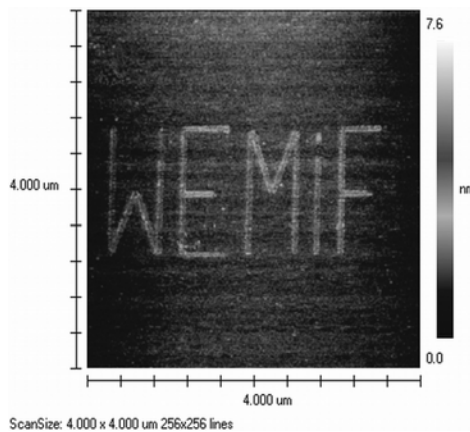


Fig. 8. NC-AFM image of Si(100) surface after local anodic oxidation as an example of more compiled pattern – logo of the Faculty of Microsystem Electronics and Photonics

The next step in the research was to examine possibility to create lines of silicon oxide. In this case, voltage modulation has been used instead of DC voltage. The parameters of the process were tip speed, voltage amplitude and ambient humidity in the microscope environmental chamber. Figures 7 and 8 show NC-AFM exemplary results of the experiments.

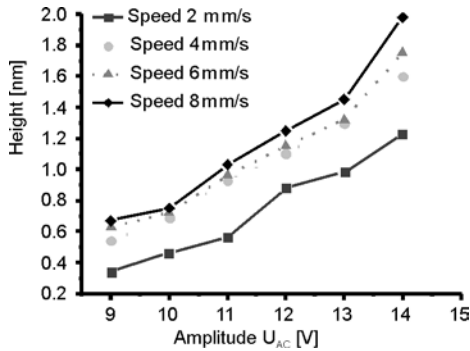


Fig. 9. Dependence of silicon oxide height on voltage amplitude and tip speed; modulation frequency 25 Hz

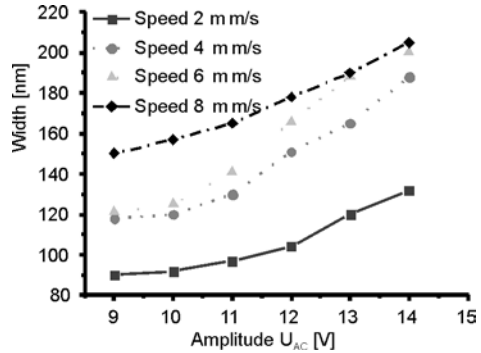


Fig. 10. Dependence of silicon oxide width on voltage amplitude and tip speed; modulation frequency 25 Hz

Figures 9 and 10 show that an increasing voltage modulation amplitude causes approximately linear growth of the width and height of fabricated oxide lines. Reducing the scanning rate also enlarges the height and width of the oxides. Modulation of the voltage applied between the tip and a sample causes removal of space-charge on the oxide surface in initial stage of local anodic oxidation process [8]. As a consequence we observe enhancement of the growth rate and the produced nanostructures are higher.

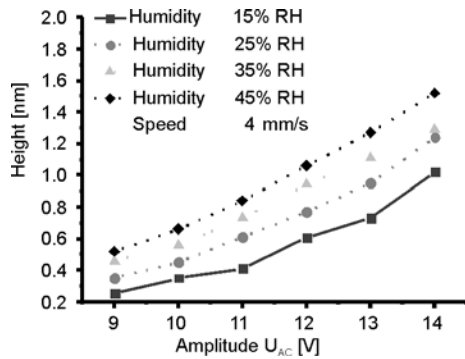


Fig. 11. Dependence of silicon oxide height on voltage amplitude and tip speed; modulation frequency 25 Hz

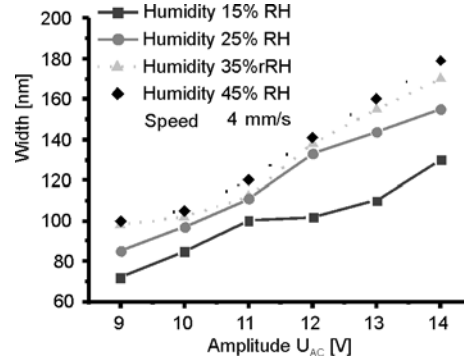


Fig. 12. Dependence of silicon oxide width on voltage amplitude and tip speed; modulation frequency 25 Hz

Humidity in the environmental chamber plays a crucial role in the local anodic oxidation process as shown in Figs. 11 and 12. Decreasing humidity causes the



local anodic process to receive reduced amounts of hydroxide species and thus height and width of the fabricated oxide lines is reduced. A lower humidity also results in difficulty of water bridge formation which also reduces fabricated oxide line volume [9].

## 4. Conclusions

A very precise characterization of the system parameters is required in order to perform reliable nanostructure fabrication on a silicon surface. The most important factors that should be taken into account are: amplitude of the voltage applied between a tip and a sample surface, tip scanning speed and humidity. There are also parameters, verification of which may be problematical, first of all: tip radius, speed of wear of the tip, angle of tip inclination to the surface, the height of tip suspension over the surface, quality of surface as well as moisture in environmental chamber of the atomic force microscope. Additionally, for suitable conditions of local anodic oxidation, the fabricated nanostructures have their height comparable with roughness of the surface, which can result in a misinterpretation of the obtained results.

A well designed and calibrated atomic force microscope is capable of turning local anodic oxidation technique into a method suitable of creation fine structures on a semiconductor surface in the nanometer regime. The spatial resolution can be optimized and the nature of local anodic oxidation phenomenon permits fabrication of features below 100 nm. The method seems considerably superior over many photolithographic techniques. Preliminary tests show that oxide patterns written using the scanning probe microscopy may also serve as a mask for other microelectronics techniques like wet chemical etching. Future optimization of the described technology will be connected with the application of arbitrary voltage shape pulses and application of cantilevers with higher force constants. An advanced system designed for fabrication of micro- and nanostructures by local anodic oxidation has been developed at the Faculty of Microsystem Electronics and Photonics, Wrocław University of Technology.

### Acknowledgements

This work was partially supported by the statutory grant No. 343332 of the Faculty of Microsystem Electronics and Photonics at Wrocław University of Technology

### References

- [1] BINNING G., ROHRER H., GERBER CH., *Phys. Rev. Lett.*, 49 (1982), 57.
- [2] DAGATA J.A., SCHNEIR J., HARARY H.H., EVANS C.J., POSTEK M.T., BENNETT J., *Appl. Phys. Lett.*, 56 (1990), 2001.
- [3] KOLANEK K., SIKORA A., GOTSZALK T., SZELOCH R., *Proc. National Conference of Electronics, KKE 2005, Darłówko Wschodnie*, p. 525.
- [4] DAGATA J.A., PEREZ-MURANO F., ABADAL G., MORIMOTO K., INOUE T., ITOH J., YOKOYAMA H., *Appl. Phys. Lett.*, 76 (2000), 2710.
- [5] GARCIA R., CALLEJA M., ROHRER H., *J. Appl. Phys.*, 86 (1999), 1898.

- [6] KOLANEK K., GOTSZALK T., ZIELONY M., SZELOCH R., Proc. 9th Scientific Conf. Optoelectronic and Electronic Sensors, COE 2006, Kraków–Zakopane, p. 423.
- [7] GARCIA M.A., GARCIA R., Appl. Phys. Lett., 88 (2006), 123115.
- [8] DAGATA J.A., INOUE T., ITOH J., MATSUMOTO K., YOKOYAMA H., J. Appl. Phys., 84, (1998), 6891.
- [9] CALLEJA M., TELLO M., GARCIA R., J. Appl. Phys. 92 (2002), 5539.

*Received 28 April 2007*  
*Revised 16 February 2008*

# Surface nanomodification induced by a neutralized ion beam

Z. W. KOWALSKI\*, J. WILK

Faculty of Microsystem Electronics and Photonics  
Wrocław University of Technology, Wybrzeże Wyspiańskiego 27, 50-370 Wrocław, Poland

The paper presents results of surface nanomodification induced by neutralized ion beam from the glow discharge ion gun with a hollow anode. Processes like surface polishing, surface roughening, generation of various surface/subsurface structure elements (e.g., waves, ripples) resulting from ion bombardment were investigated. All those events are crucial in such areas of science and technology as preparation (ion beam thinning and polishing) of samples for transmission electron microscopes; surface analysis where ion beam sputtering generating unwanted surface structures like e.g., waves is widely used in depth-profile analytical techniques such as secondary ion mass spectroscopy, Auger electron spectroscopy, X-ray photoelectron spectroscopy, Rutherford backscattering spectrometry; formation of patterns in sub-100 nm regime for micro/nanoelectronics where reduction of line etch roughness (LER) must be taken into account (as semiconductor dimensions shrink, LER will be more important because roughness from the resist is transferred to the substrate with further processing steps).

Key words: *surface nanomodification; neutralized ion beam; ion polishing; surface roughening*

## 1. Introduction

Material modification processes like sample thinning, surface polishing, surface roughening, revealing and/or generation of surface/subsurface structure elements can be achieved by the use of ion beam irradiation. The processes in question are very important and must be considered in various areas of science and technology. For example, in surface analysis [1] ion beam sputtering is widely used in depth-profile analytical techniques such as Auger electron spectroscopy (AES), Rutherford backscattering spectrometry (RBS), secondary ion mass spectroscopy (SIMS), X-ray photoelectron spectroscopy (XPS) where a severe problem in analysing concentration profiles is broadening of the profiles by sputter induced roughening (i.e., formation of topographical/structural elements like, for example, waves or ripples presented in

---

\*Corresponding author, e-mail: zbigniew.w.kowalski@pwr.wroc.pl

Fig. 1) leading to a reduced depth resolution. Next, in microelectronics shrinking semiconductor dimensions cause that line resist etch roughness (LER) [2] will be more important because roughness from the resist is transferred to the substrate with further processing steps. Finally, in transmission electron microscopy, ion beam thinning and polishing are widely used processes of sample preparation thanks to well known advantages in comparison to conventional methods.

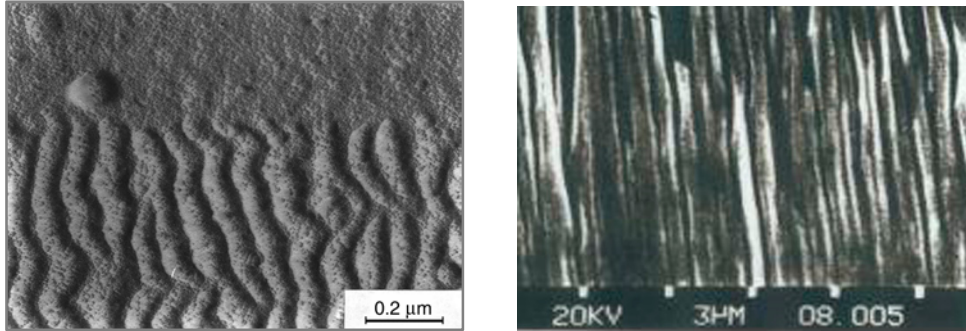


Fig. 1. Unwanted morphological elements induced by neutralized argon ion beam: a) waves on Corning 7059 glass surface [3], b) ripples on 1H18N9T stainless steel surface [4]

The paper presents results of surface nanomodification, i.e. surface polishing, surface roughening, surface etching leading to sample thinning as well as generation of various surface and/or subsurface structure elements reminiscent of waves or ripples in sub-micrometer (nanometer) regime induced by neutralized ion beam from a glow discharge ion gun with a hollow anode. Taking into consideration imposed limitations on the length of the paper, only some selected experimental results have been presented.

## 2. Experimental

*GD ion source.* The ion bombardment induced modifications of solid surfaces were performed in apparatuses equipped with a well known ion beam source – a glow discharge (GD) ion gun with a hollow anode. Simplicity of the gun and d.c. high voltage power supply design, ease of continuous operation, convenience in use and maintenance, and facility of sputtering of non-conductive materials without additional neutralizing systems (the beam is a “mixture” of ions, electrons and neutrals) are only the principal virtues of this source. The gun with earthed cathode and anode at a positive potential (up to 7 kV), yielding ion current of up to 0.1 mA and current density of up to  $5 \mu\text{A}/\text{mm}^2$  has been used to modify surfaces of various materials in micrometer and submicrometer (nanometer) range. The diameter of the neutralized ion beam depends on the cathode orifice diameter  $\Phi_C$  and we used this electrode with optimal value of  $\Phi_C = 1 \text{ mm}$ .

*Surface modification measurements and observations.* To investigate ion beam induced surface polishing or roughening it is convenient to measure changes of roughness parameters. We measured all the main parameters relating to horizontal and vertical features of the surface profile. Here, only results of measurements of the roughness parameter  $R_a$  (arithmetical mean deviation of the surface profile) are presented. The parameter was measured: a) before ion irradiation, b) after each ion bombardment process, using a high quality profilograph (Rank Taylor Hobson's Talysurf) and a calibrated atomic force microscope made at this University [5]. Changes of surface roughness are directly connected with alteration of surface topography. Therefore, the surface topographies were also studied (only selected results are presented here) with scanning electron microscopes (SEMs, e.g. Hitachi S-570, Jeol JSM-5800LV) and a transmission electron microscope (TEM, binary carbon replicas method) in the micrometer range as well as with AFM in the nanometer range. These microscopes were also utilised to observe ion beam revealed and/or generated surface and subsurface defects or structures.

### 3. Results and discussion

#### 3.1. Ion polishing

The neutralized ion beam from GD gun seems to be a good polishing tool not only in the micrometer but also in submicrometer (nanometer) range as is shown in Fig. 2.

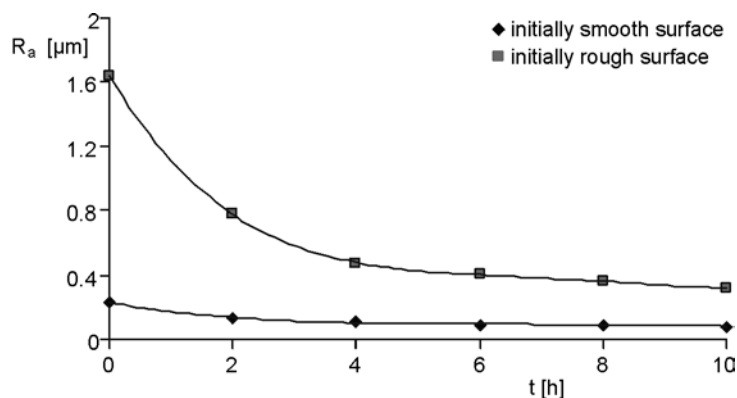


Fig. 2. Micrometer and nanometer changes of the roughness parameter  $R_a$  generated by a very oblique ( $\theta = 87^\circ$ ) neutralized argon ion beam irradiation of initially rough and initially smooth 99.5% polycrystalline titanium surfaces; the curves are the best polynomial fits

Two kinds of titanium surfaces: initially rough and initially smooth were polished with a very oblique neutralized argon ion beam. After 2–4 h of polishing, the intensity of the process decreases and the parameter  $R_a$  diminishes at a rate of several to several

dozen nanometers per hour. The capability of the neutralized ion beam to nanopolishing is especially visible in Fig. 3 where a submicrometer modification of the parameter in question is generated on stainless steel and titanium surfaces by means of a very inclined ( $\theta = 87^\circ$ ) argon ion beam. In the case of steel, the parameter  $R_a$  decreases (on average) less than 4 nm per hour.

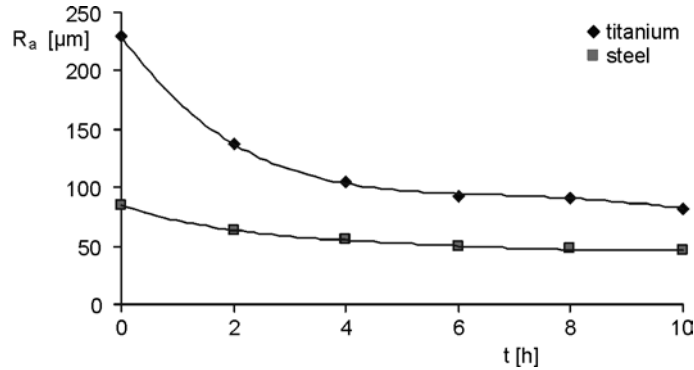


Fig. 3. The influence of neutralized argon ion beam bombardment duration at  $\theta = 87^\circ$  on vertical roughness parameter  $R_a$  of 1H18N9T stainless steel (made in Poland) and 99.5% polycrystalline titanium; the curves are the best polynomial fits

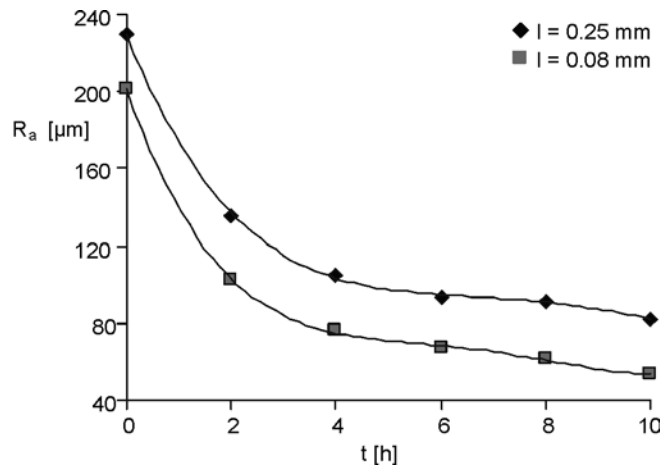


Fig. 4. "Scaling effect" observed on  $R_a(t)$  changes induced on mechanically polished surface of 99.5% polycrystalline titanium by neutralized argon ion beam bombardment at the incidence angle  $\theta = 87^\circ$ ; the curves are the best polynomial fits

In profilometric measurements, all roughness parameters are measured over a range of a conventionally determined elementary segment  $l$ . It is worth noting here that the values of the parameters in question depend on the above-mentioned segment as is shown in Fig. 4. When the length of element  $l$  (scale) was reduced (in our case

from 0.25 mm to 0.08 mm), the surface appeared to be smoother. That “scaling effect” is very important and must be taken into account during roughness measurements.

### 3.2. Ion thinning

It is well known that ion thinning is used in specimen preparation for TEM and that efficiency of the process, i.e. ion thinning rate depends on many factors. Two measuring methods were used to study the parameter in question: profilometric and microscopic (ion sputter-induced step was examined by means of a profilometer and SEM, respectively).

In the case of the GD source with the cathode and anode holes diameters  $\Phi_C = 1$  mm and  $\Phi_A = 4$  mm, respectively, the thinning rate of stainless steel irradiated perpendicularly with a neutralized argon ion beam is about 0.063  $\mu\text{m}/\text{min}$  for the microscopic method and 0.058  $\mu\text{m}/\text{min}$  for profilometric one. After a few dozen hours of gun's work, the cathode orifice diameter  $\Phi_C$  changes (increases to  $\Phi_C = 1.5$  mm) due to ion sputtering process but the rate is the same (as determined by microscopic method) or almost the same (profilometric method) as can be seen in Table 1.

Table 1. Argon ion beam thinning rate of 1H18N9T stainless steel for two selected cathode orifice diameters [6, 7] ( $U_A = 5$  kV,  $I_A = 0.35$  mA,  $t = 2$  h)

Diameter of cathode hole $\Phi_C$ [mm]	Thinning rate [ $\mu\text{m}/\text{min}$ ]	
	Microscopic method	Profilometric method
1.0	0.063	0.058
1.5	0.063	0.062

It seems that the neutralized ion beam from the GD gun is a good and precise thinning tool giving thinning rates in a submicrometer/min range.

### 3.3 Ion roughening

Ion roughening is a process leading to an increase of solid surface roughness due to ion bombardment inducing modification of its surface morphology. The neutralized ion beam from the GD gun applied to roughen surfaces has shown its ability to do that not only in micrometer but also in submicrometer range. That can be seen in Fig. 5 presenting the dependence of  $R_a(t)$  for stainless steel and titanium surfaces irradiated perpendicularly ( $\Theta = 0^\circ$ ) with a krypton neutralized ion beam. The mean value of  $R_a$  increases due to nanoroughening process about 20 nanometers per hour for titanium and about 40 nanometers per hour for steel. Taking into account the results of *ex situ* SEM examinations (not presented here), one can conclude that on increasing of sur-

face roughness, a widening of topographical forms can be observed due to eliminating small dimension features by more extended elements.

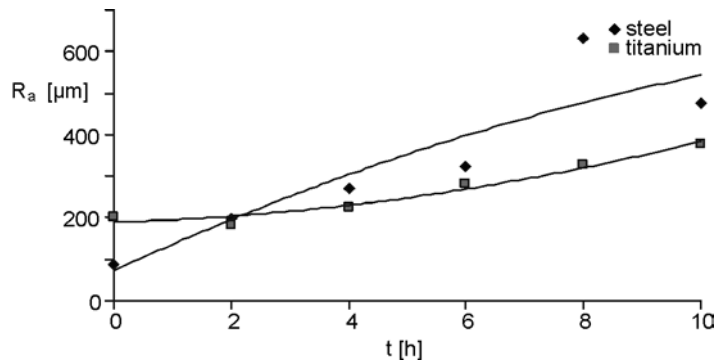


Fig. 5. Time dependences of the roughness parameter  $R_a$  of stainless steel (1H18N9T) and 99.5% polycrystalline titanium surfaces irradiated with a normal neutralized krypton ion beam; the curves are the polynomial fits

Table 2. Vertical roughness parameters  $R_a$  (maximum values) [nm] induced by perpendicular neutralized krypton ion beam irradiation ( $\theta = 0^\circ$ ) and examined by means of atomic force microscope (see [5])

Material	Bombardment duration [h]					
	0	2	4	6	8	10
Polycrystalline 99.5% titanium	95.2	107	153.3	216.4	300.6	372.8
1H18N9T steel	11.1	128	166.1	250	365.5	377.7

Ion roughening of metal targets with the use of a neutralized ion beam in question was also studied by means of a homebuilt contact mode atomic force microscope (see e.g., [5]). All AFM results presented in Table 2 are smaller than  $R_a$  parameters obtained with the use of a profilometer (compare Fig. 5) even though they were measured for the same sample surfaces. The reason of those discrepancies are “scaling effects” mentioned in Section 3.1 – the AFM elementary segment (8  $\mu\text{m}$ ) is much smaller than that of the profilometer (250  $\mu\text{m}$ ) used in our experiments.

### 3.4. Revealing/generating of surface/subsurface structure elements

Neutralized ion beam from the GD gun allows to reveal surface and/or subsurface structures (e.g. grains and grain boundaries) as well as various structure elements like voids, pores, macrodefects, etc. (for further information, see e.g. [6]). On the other hand, there are some unexpected and unwanted results of the beam bombardment, e.g. generation of waves or ripples on irradiated surfaces as was shown on TEM and SEM images presented in Fig. 1. The mean period of waves and ripples is about 75 nm and



700 nm, respectively. Those nanostructures on the surface mean increased roughness – a serious obstacle in surface analysis (see Section 1).

#### 4. Conclusion

Neutralized ion beam from GD gun to surface nanomodification has been used in, e.g., surface polishing, surface roughening, surface etching (leading to sample thinning) as well as generation of various surface and/or subsurface structure elements reminiscent of waves or ripples in sub-micrometer regime. Taking into account results of our experiments (published here and unpublished) it can be stated that the neutralized ion beam in question could be a good modification tool, not only in micrometer but also in nanometer range.

#### References

- [1] LOESING R., GURYANOV G.M., HUNTER J.L., GRIFFIS D.P., *J. Vac. Sci. Techn. B*, 18 (2000), 509.
- [2] REYNOLDS G.W., TAYLOR J.W., *J. Vac. Sci. Techn. B*, 16 (1999), 2723.
- [3] ŁUKASZEWICZ M., KOWALSKI Z.W., *J. Mater. Sci.*, 16 (1981), 302.
- [4] KOWALSKI Z.W., *Morphology of ion sputtered surface – technological and biomedical implications*, Ofic. Wyd. PWr, Wrocław, 2001 (in Polish).
- [5] MARENDZIAK A., GOTSZALK T., WILK J., KOWALSKI Z.W., RANGELOW I.W., *Elektronika*, 6 (2005), 15 (in Polish).
- [6] KAMIŃSKI K., Master Thesis, Department of Microsystem Electronics and Photonics, Wrocław University of Technology, Wrocław, 2005.
- [7] WILK J., KAMIŃSKI K., KOWALSKI Z.W., *Elektronika*, 10 (2007), 58 (In Polish).

*Received 28 April 2007*  
*Revised 16 February 2008*

# XPS study of air exposed copper phthalocyanine ultra-thin films deposited on Si(111) native substrates

M. KRZYWIECKI<sup>1\*</sup>, L. GRZĄDZIEL<sup>1</sup>, L. OTTAVIANO<sup>2</sup>,  
P. PARISSÉ<sup>2</sup>, S. SANTUCCI<sup>2</sup>, J. SZUBER<sup>1</sup>

<sup>1</sup>Department of Electron Technology, Silesian University of Technology, 44-100 Gliwice, Poland

<sup>2</sup>Department of Physics, University of L'Aquila, I-67010 Coppito, Italy

Results are presented of XPS characterization of ultra-thin copper phthalocyanine (CuPc) (16 nm-QCM controlled) films thermally deposited under UHV conditions on p- and n- type Si(111) substrates covered by native oxide. Our attempt has been focused on comparative studies of thin films in terms of the stability and durability of CuPc layers after one year of aging in ambient atmosphere. The impact of the type of the substrate doping was also explored. Our results clearly prove that CuPc layers are chemically stable and durable after one year exposure to air. We also demonstrate the existence of the substrate doping impact on the CuPc ultra-thin film what might be caused by dipole effects.

Key words: *copper phthalocyanine; CuPc; thin films; surface chemistry*

## 1. Introduction

Copper phthalocyanine (CuPc) is an organic semiconductor with a high thermal and chemical stability suitable for thin film technology processing [1–3]. It belongs to metal phthalocyanines (MePc), a class of metal-organic compounds possessing a metal atom surrounded by aromatic rings in the centre of the molecule [4]. It is an important material widely used in optical and electronic devices, among others light emitting diodes, field effect transistors [5], solar cells and, particularly, gas sensors [6]. The sensor mechanism bases on changes in the electrical conductivity of phthalocyanine thin films induced by the presence of small gaseous molecules [7, 8]. It has to be noted as well that the sensing properties of phthalocyanines are determined by the electronic properties of their space charge layer [9]. Following, highly ordered and defined MePc films might be of great importance for sensor device purposes [10]. Such sensors usually work in ambient air and other unfavourable environment. Thus

---

\*Corresponding author, e-mail: maciej.krzywiecki@polsl.pl

stability and durability of MePc layers are in attention due to cost reduction and longevity of designed devices.

Up to now, the studies have been focused on the properties of a CuPc sensing layer under strictly controlled conditions, i.e. a sensing layer on strictly defined atomically clean substrate has been exposed to a given dose of a given gas without the presence of other gases [11, 12]. On the other hand, in the last few years an increasing attention has been paid to study layers deposited on real (covered with native oxide) substrate surfaces because oxidized Si wafers have been used as substrates in the so called organic electronics, in technology of organic field-effect transistors (OFET), where the oxide layer serves as the insulating layer between one electrode and a semi-conducting film [13]. Furthermore, if the oxide layer does not affect the active CuPc film it may turn out that there is a possibility of further cost reduction (in device preparation) by partially abandoning the expensive substrate cleaning process. That is why the examination of the influence of Si substrate covered with native oxide on the surface chemistry, morphology and electronic properties of CuPc thin films is of great importance. There are not too many papers describing the quality (including durability and stability) and properties of organic layers deposited on real substrate surfaces. There is also a necessity to investigate if the electronic properties (i.e., type of conductivity) of such substrate surface, even covered with native oxide, have the influence on the organic ultra-thin film surface chemistry.

In our recent paper [14], a correlation between morphology and electronic properties of CuPc thin films (500 nm) was determined with use of atomic force microscopy (AFM) and photoemission yield spectroscopy (PYS) methods. In this work, the x-ray photoelectron spectroscopy (XPS) investigations of CuPc ultra-thin (16 nm) layers deposited on Si(111) covered with native oxide are reported. Our original attempt includes a comparative examination of thin films due to long term of air exposure (including the chemical quality of the layer) and type of the substrate doping. We suspect that difference in the type of substrate conductivity can affect the chemistry and electronic properties of deposited layers even after long-lasting exposure. That is why the XPS examinations of the chemistry of the CuPc ultra-thin layers after one year of exposure were performed.

The aim of this note is to examine the durability and stability of the CuPc layer in such a period of time. Additionally, the influence of the substrate doping on the ultra-thin CuPc films chemistry has been checked.

## 2. Experimental

Two types of Si(111) substrates covered with native oxide (Bosch, GmbH) were used in this experiment: the n-type (phosphorus-doped with a carrier concentration of  $7 \times 10^{13} \text{ cm}^{-3}$ ) and p-type (boron-doped with a carrier concentration of  $1 \times 10^{15} \text{ cm}^{-3}$ ). The substrates were degreased with acetone in an ultrasonic bath, rinsed with deionized water and then dried with dry air.

CuPc thin films (16 nm) were thermally evaporated in a UHV preparation chamber. For deposition, the CuPc complex sublimed powder was used (delivered by Sensitive Imaging Technologies GmbH, Syntex Division). The pressure during the process (evaporation of CuPc) was better than  $8 \times 10^{-8}$  mbar.

The film thickness was controlled with a quartz crystal microbalance device (deposition rate was about 0.1 Å/s) and verified with XPS by monitoring the attenuation of the intensity of the substrate Si2p peaks due to the organic overlayer [15, 16].

The Si/SiO<sub>2</sub> substrate was examined by XPS and angle-resolved XPS (ARXPS) methods at the Silesian University of Technology, Gliwice. The ARXPS method was used to determine the native oxide layer thickness. Angle resolved XPS measurements (and the XPS measurements done for chemical analysis of the substrate) were performed with a SPECS PHOIBOS 100 hemispherical analyzer equipped with a HSA 3500 power supply unit. The XPS system base pressure was  $2 \cdot 10^{-9}$  mbar. Spectra were taken using AlK<sub>α</sub> source with energy of 1486.6 eV, the analyzer was set to a pass energy of 10 eV. Acquired XPS spectra were calibrated with the silver Ag3d peak at the binding energy of 368.2 eV [17]. The samples were aged in ambient air for one year and then investigated by imaging and photoemission methods.

To obtain high resolution XPS spectra, the CuPc samples were examined at the University of L'Aquila. XPS measurements were performed with a home designed system having a monochromatized AlK<sub>α</sub> source and a PHI hemispherical analyzer. The XPS system base pressure was  $8 \times 10^{-10}$  mbar. XPS spectra were calibrated with respect to gold peak with energy of 84.0 eV [18].

### 3. Results and discussion

The XPS survey spectra of both types of Si substrates are shown in Fig. 1. The upper line corresponds to Si/SiO<sub>2</sub> substrate with a p-type conductivity while the lower one to n-type doped sample. All expected peaks were found. The examination of the spectra reveals the existence of a contamination layer including oxide (O1s) peak and adventitious carbon related species (C1s peak). However, there are not any substantial compositional differences between the substrates. In both cases the ratio between O1s and Si2p peak areas, corrected for atomic sensitivity factors, is close to 2 which entails that the oxide overlayer is composed primarily of a stable SiO<sub>2</sub> layer.

In order to determine the exact substrate bonding configuration between silicon and oxygen, the Si2p peak region was recorded at higher resolution and is shown in Fig. 2 for both types of substrate. The spin-orbit split contributions from Si substrate and oxide layer shifted by about 4 eV are seen. The latter one corresponds to SiO<sub>2</sub> [19] which confirms that it is the main component of the oxide layer; other silicon sub-oxides are not visible.

The native oxide thickness may be determined using XPS measurements under different take off angles. The method is based on changing the relative angle between the sample and the analyzer entrance slit and monitoring the signals emerging from

examined substrate and its overlayer. Under the assumption that an overlayer is uniform, its thickness can be calculated with use of the Beer–Lambert equation [16]:

$$d = \lambda_A \cos \theta \ln \left[ 1 + \frac{R}{R^\infty} \right] \quad (1)$$

where:  $\lambda_A$  is the attenuation length of electrons emitted from a substrate in an overlayer,  $\theta$  is the electron take-off angle,  $R$  is the ratio of overlayer ( $\text{SiO}_2$  component) to substrate (Si) peak areas,  $R^\infty$  is the ratio of overlayer to substrate sensitivity factors.

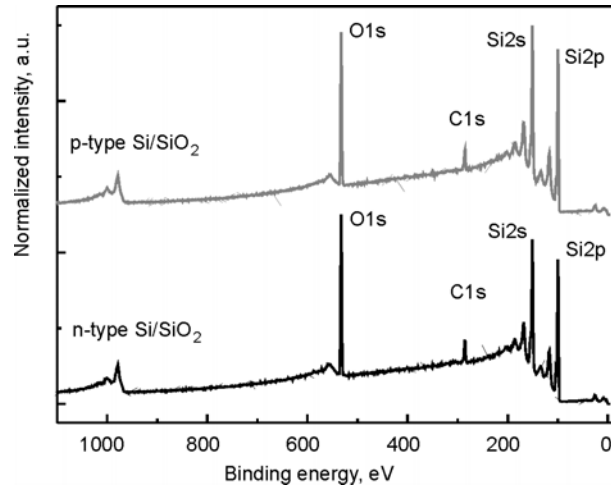


Fig. 1. Survey spectra of p-type doped  $\text{Si}/\text{SiO}_2$  and n-type doped  $\text{Si}/\text{SiO}_2$ ; all main spectral lines have been identified

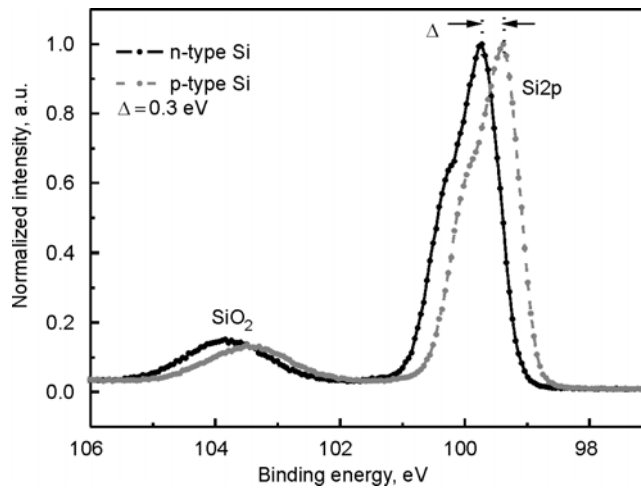


Fig. 2.  $\text{Si}2p$  peaks of n- and p-type substrates. An evident energy shift caused by doping is visible; shape of the spectral line clearly shows that the oxide layer contains only silicon dioxide

It follows from Eq. (1) that the dependence of  $\ln(R + R^\infty)$  on  $1/\cos\theta$  should yield a straight line. The slope of the line is then the thickness divided by the attenuation length. Figure 3 presents the transformed ARXPS data for the p-type substrate. For calculations, the value of  $\lambda_A = \lambda_{\text{SiO}_2} = 3.5$  nm was taken [16]. The oxide thickness for the p-type substrate is 0.77 nm; a similar analysis for the n-type one gives 0.80 nm. Auxiliary AFM investigations were done in order to check the surface structure of the used substrates. In both cases, the surface roughness was determined as 0.15 nm (data to be published elsewhere). Besides the energy shift of about 0.3 eV, there are no other qualitative and quantitative differences between the spectra. The origin of the energy shift can be related to various substrate dopings which manifests itself in various Fermi level positions.

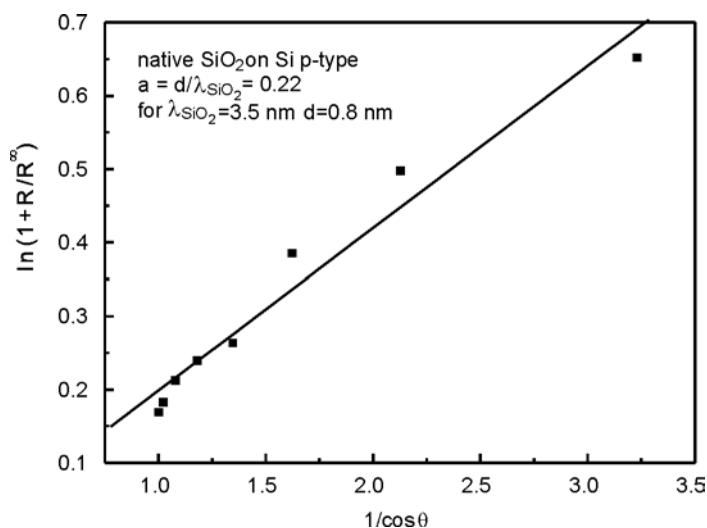


Fig. 3. Compositional depth profiling for p-type Si sample via angle dependent core level XPS

In Figure 4, the XPS survey spectra of examined 16 nm CuPc layers deposited on n-type (upper line) and p-type (lower line) substrate are shown. The samples were aged for one year in the ambient atmosphere before the examination. The spectra are characteristic of CuPc films; N1s and Cu2p peaks appeared and the C1s peak intensity drastically increased due to C=C and C–N contributions inherent in CuPc. Simultaneously, the substrate peaks diminished indicating that all the substrate is covered with CuPc film and the layers did not erode during the exposure period. The O1s peak can be treated as the contamination caused by coexistence of molecular oxygen and water vapours from the atmosphere; no other contaminants were detected.

The observed difference in intensities of O1s peaks can be related to a stronger (in the case of a p-type substrate) interaction between deposited layer (affected by substrate) and oxidizing ambience (oxygen and water vapours). This could be the reason why the O1s peak exhibits a higher intensity in the case of the p-type sample. No other

explanations are likely, as the two Si substrates have almost the same oxide thickness and composition (only SiO<sub>2</sub>) and they have been prepared under identical conditions (substrate temperature and evaporation rate).

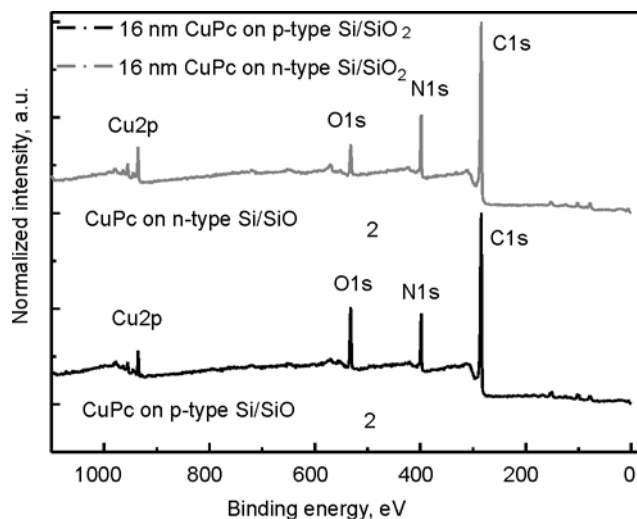


Fig. 4. Survey spectra of 16 nm CuPc films obtained from n-type and p-type samples

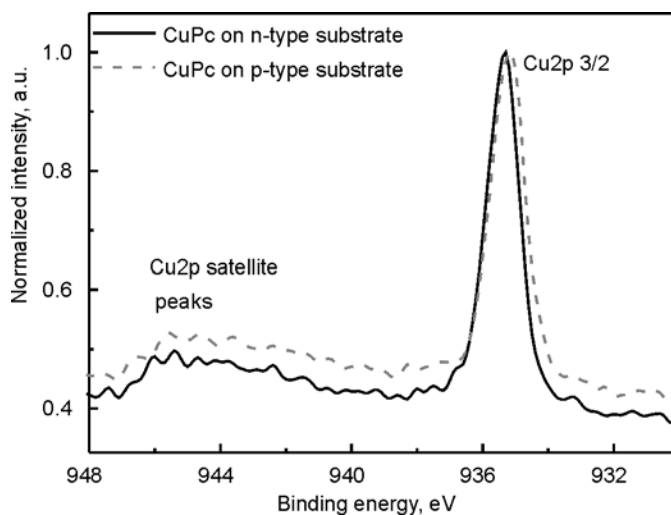


Fig. 5. Cu<sub>2p</sub> 3/2 XPS peak obtained for 16 nm CuPc film evaporated on n- and p-type Si/SiO<sub>2</sub> substrate

Auxillary XRD investigations showed that CuPc thin films were in the  $\alpha$ -phase on both types of substrates and the number of CuPc monolayers was also the same (data

not shown for brevity). The exact morphological information is currently under an analysis and will be published elsewhere.

For better characterization of the CuPc layer, the Cu2p<sub>3/2</sub>, N1s, and C1s spectral windows were taken at higher resolutions. In order to determine chemical stability of the CuPc layer after long term exposure in atmosphere, we verified the shape of Cu2p<sub>3/2</sub> XPS peak (due to its highest surface sensitivity). Figure 5 presents Cu2p spectra taken from both types of samples. One can observe a characteristic shape of Cu2p peak as well as satellite peaks very typical of stable CuPc layer [20, 21]. This confirmed our expectations that CuPc ultra-thin films are extremely robust even after long term aging. A more precise analysis of the Cu2p<sub>3/2</sub> XPS peaks energy positions points that the energy shift between n- and p-type samples is about 0.15 eV (for the n-type samples the energies are greater than for the p-type ones).

A similar effect was observed for N1s XPS peaks (not shown for brevity). It seems that the substrate doping causes the energy shift (the 0.3 eV shift originating from substrate is reduced by the phthalocyanine layer, however it still exists). We can assume that for thicker layers the effect will diminish but the assumption has to be verified by additional investigations.

## 4. Conclusions

Based on the XPS examination of both the Si/native oxide substrate and CuPc thin film (16 nm) one can conclude that CuPc layer is stable and durable after long term (one year) air exposure. It was proved by the unchanged characteristic chemical bonds which are clearly seen in the XPS spectra. Furthermore, the shapes of Cu2p<sub>3/2</sub> and N1s peaks characteristic of phthalocyanine have not been corrupted by any additional component resulting from undesired surface reactions. The only influence of the conductivity type of the substrate is clearly visible in the energy shift of the main XPS components of CuPc spectra. This is probably caused by dipole effects (we suspect that copper phthalocyanine creates surface dipole with oxygen and water vapours on p-type substrate) but the origin of such phenomena remains unrecognized and further investigations are currently in progress.

### Acknowledgements

The work was partially sponsored by the Ministry of Scientific Research and Information Technology within the research project No. N515 054 31/1986.

## References

- [1] GUTMAN F., LYONS L.E., *Organic Semiconductors*, Wiley, New York, 1967.
- [2] SIMON J., ANDRÉ J.J., *Molecular Semiconductors*, Springer, Berlin, 1985.
- [3] SNOW A.W., BARGER W.R., [in:] *Phthalocyanines: Properties and Applications*, C.C. Leznoff, A.B.P. Lever (Eds.), VCH Publishers, New York, 1989, Chapt. 5.



- [4] ZHIVKOV I., SPASSOVA E., DANEV G., ANDREEV S., IVANOV Tz., *Vacuum*, 51 (1998), 189.
- [5] HIGUCHI T., MURAYAMA T., ITOH E., MIYAIRI K., *Thin Solid Films*, 499 (2006), 374.
- [6] COLLINS R.A., MOHAMMED K.A., *J. Phys. D*, 21 (1988), 154.
- [7] WRIGHT J.D., *Prog. Surf. Sci.*, 31 (1989), 1.
- [8] NONAKA T., NAKAGAWA Y., MORI Y., HIRAI M., MATSUNOBE T., NAKAMURA M., TAKAHAGI T., ISHITANI A., LIN H., KOUMOTO K., *Thin Solid Films*, 256 (1995), 262.
- [9] SZUBER J., GRZADZIEL L., *Thin Solid Films*, 376 (2000), 214.
- [10] Ji Z.G., WONG K.W., TSE P.K., KWOK R.W.M., LAU W.M., *Thin Solid Films*, 402 (2002), 79.
- [11] GUILLAUD G., SIMON J., GERMAIN J.P., *Coord. Chem. Rev.*, 178–180 (1998), 1433.
- [12] QIU W., HU W., LIU Y., ZHOU S., XU Y., ZHU D., *Sens. Act. B*, 75 (2001), 62.
- [13] OSSO J.O., SCHREIBER F., ALONSO M.I., GARRIGA M., BARRENA E., DOSCH H., *Org. Electr.*, 5 (2004), 135.
- [14] GRZADZIEL L., ŽAK J., SZUBER J., *Thin Solid Films*, 436 (2003), 70.
- [15] PEISERT H., SCHWIEGER T., KNUPFER M., GOLDEN M. S., FINK J., *J. Appl. Phys.*, 88, (2000), 1535.
- [16] WATTS J.F., WOLSTENHOLME J., *Surface Analysis by XPS and AES*, Wiley, Chichester, 2003.
- [17] ANTHONY M.T., SEAH M.P., *Surf. Interface Anal.*, 6 (1984), 95.
- [18] LINDAU I., PIANETTA P., YU K.Y., SPICER W.E., *Phys. Rev. B*, 16 (1976), 492.
- [19] YAMASHITA Y., ASANO A., NISHIOKA Y., KOBAYASHI H., *Phys. Rev. B*, 59 (1999), 15872.
- [20] PEISERT H., KNUPFER M., SCHWIEGER T., AUERHAMMER J.M., GOLDEN M.S., FINK J., *J. Appl. Phys.*, 91 (2002), 4872.
- [21] OTTAVIANO L., LOZZI L., RISPOLI F., SANTUCCI S., *Surf. Sci.*, 402–404 (1998), 518.

*Received 28 April 2007*

*Revised 16 February 2008*

## Magnetic properties of ultrathin Co(0001) films on vicinal Si(111) substrate

A. STUPAKIEWICZ<sup>1,2\*</sup>, A. FLEURENCE<sup>2</sup>, R. GIENIUSZ<sup>1</sup>, A. MAZIEWSKI<sup>1</sup>,  
T. MAROUTIAN<sup>2</sup>, P. GOGOL<sup>2</sup>, B. BARTENLIAN<sup>2</sup>, R. MÉGY<sup>2</sup>, P. BEAUVILLAIN<sup>2</sup>

<sup>1</sup>Institute of Experimental Physics, University of Białystok, ul. Lipowa 41, 15-424 Białystok, Poland

<sup>2</sup>Institut d'Electronique Fondamentale, Université Paris XI, CNRS, UMR 8622, F-91405 Orsay, France

In the present work we report on magnetization reversal process, anisotropy and domain structures in ultrathin Au/Co(0001)/Au films deposited on vicinal Si(111) substrates. The measurements were performed using a magneto-optical Kerr effect based magnetometer, a polarizing optical microscope and a ferromagnetic resonance spectrometer. Co thickness induced spin-reorientation from out-of-plane into in-plane magnetization was studied. Changes of in-plane magnetic anisotropy symmetry were deduced from shapes of magneto-optical hysteresis loops and from analysis of angular dependences of the resonance field. The experimental data have been discussed taking into account both uniaxial out-of-plane anisotropy and step-induced uniaxial in-plane anisotropy. A preferential orientation of domain walls in 3ML thick Co films was observed. The finding is explained by the step-induced magnetic anisotropy.

Key words: *magnetic anisotropy; ultrathin films; cobalt; domain structure*

### 1. Introduction

Ultrathin Au/Co/Au structures have been intensively studied due to their strong perpendicular anisotropy [1] making them ideal candidates for application in magnetic memory devices. For magnetic ultrathin films, parameters such as growth mode [2], interface roughness [3], substrate nature and orientation play a key role in their structural and magnetic properties such as crystal phase, magnetic anisotropy energy, Curie temperature, spin-reorientation transition (SRT), etc. Magnetic films grown on vicinal surfaces, where density of monoatomic height steps and their orientation are tunable with the miscut angle and miscut direction, exhibit a strong influence on their magnetic properties [4]. Steps on a vicinal Pt surface strongly influence both magnetic anisotropy and the magnetic moment of Co atoms rows [5]. In addition to the magnetocryst-

---

\*Corresponding author: and@uwb.edu.pl

talline anisotropy, a uniaxial in-plane anisotropy is induced by a stepped surface. For systems such as Fe/Ag(001) and Co/Cu(001), the induced easy axis is aligned with the step edges [6] whereas in the case of Fe grown on stepped W(001) and stepped Pd(001) it is perpendicular to the step edges [7].

In our work, we focused on the magnetic properties of a Au/Co/Au structure grown on a vicinal Si(111) surface.

## 2. Sample preparation

A vicinal Si(111) substrate  $2^\circ$  misoriented with respect to the  $[\bar{1}\bar{1}2]$  direction was prepared under UHV conditions by flashing with direct current heating up to  $1250^\circ\text{C}$  during a few seconds. The temperature was checked by a thermocouple up to  $550^\circ\text{C}$  and by an infrared pyrometer for higher temperatures. After substrate processing, the silicon surface is constituted of single- and triple-layers high steps (Fig. 1). Such a Si(111) surface with  $7\times 7$  reconstructed terraces was examined [8]. A schematic representation of the vicinal surface and basic crystallographic orientations are shown in Fig. 1.

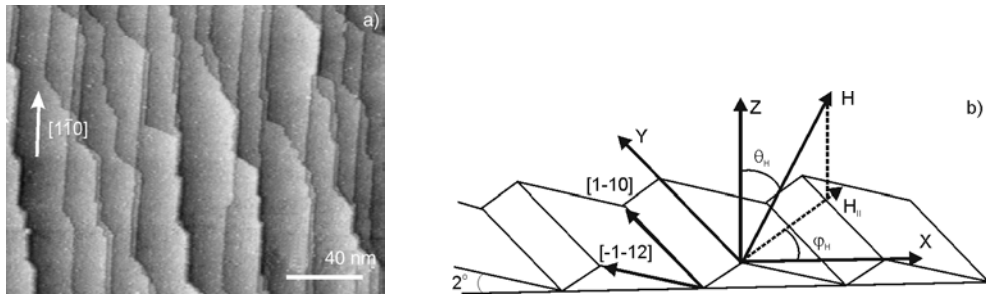


Fig. 1. In-situ STM image (a) and schematic representation of vicinal Si(111) surface (b)

The following structures were deposited by the molecular beam epitaxy on the vicinal Si(111) substrate: a Cu buffer layer 4 monolayers (ML) thick, deposited at  $100^\circ\text{C}$  (i); other layers were deposited at room temperature: 30 ML thick Au(111) underlayer (ii),  $d = 3, 5, 7$  and 15 ML thick Co layers (iii) and 30 ML thick Au cover layer (iv). Cobalt deposited on the Au(111) surface is expected to form the *hcp* Co(0001) crystallographic phase [1].

## 3. Results and discussion

Magnetic properties of the samples at room temperature were studied using magneto-optical Kerr effect (MOKE) using a magnetometer with the laser light of  $\lambda = 640\text{ nm}$ . Magnetization reversal processes enabled one to determine the Kerr rotation and ellipticity in both polar (P-MOKE) and longitudinal (L-MOKE) configura-

tions with perpendicular  $H_{\perp}$  and in-plane  $H_{\parallel}$  magnetic field applied. The magnetic anisotropy was studied using a ferromagnetic resonance (FMR) X-band spectrometer. The external magnetic field was applied to the sample along directions defined by polar  $\theta_H$  and azimuthal  $\varphi_H$  angles measured, respectively, from the film normal and substrates miscut directions in the sample plane (Fig. 1). The measured resonance field ( $H_r$ ) is related to the magnetic anisotropy constants and enables determination of the easy magnetization axes (minima in  $H_r(\theta_H, \varphi_H)$ ).

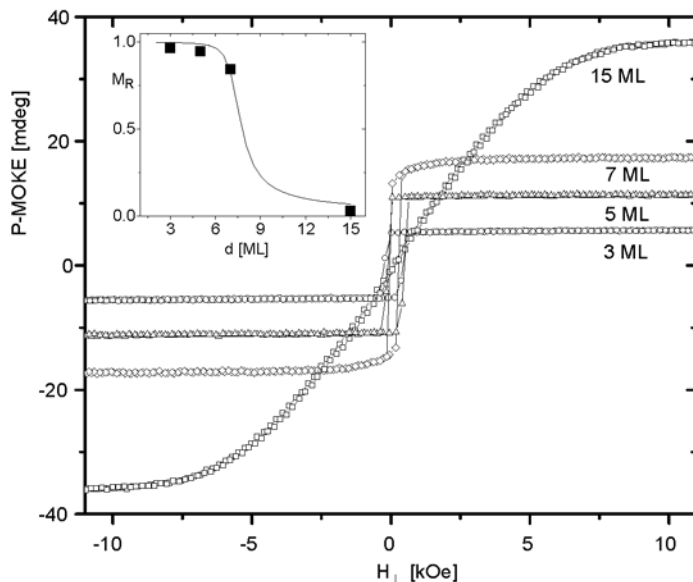


Fig. 2. Hysteresis loops measured by P-MOKE for 3, 5, 7, 15 ML Co film thickness.

Inset: dependence of normalized remnant magnetization on the Co thickness; experimental data (dots) and solid line calculated assuming anisotropy constants (Eq. (1)) defined from the resonance field  $H_r$ .

Figure 2 shows P-MOKE hysteresis loops and normalized remnant magnetization  $M_R = M_{(H=0)}/M_s$  (inset) for various Co film thicknesses. A canted magnetization state could be deduced from the magnetization curve recorded for 7 ML Co films. In general, the reorientation could be tuned by overlayer and/or underlayer structures [2, 9]. The SRT undergoes for about 9 ML thick Co film, in gold envelope, deposited on a flat substrate. Thus the morphology of our vicinal substrate influences decrease of the SRT thickness.

Figure 3 shows L-MOKE hysteresis loops for the 15 ML Co thick film with the magnetization mainly in the sample plane. The influence of the step-edges of the vicinal surface on the magnetic anisotropy was deduced from azimuthal dependence of the normalized in-plane ellipticity remanence ( $M_{in}$ ) (Fig. 3, inset a)). The  $[1\bar{1}0]$  direction appears clearly as an easy axis with a square L-MOKE hysteresis loop when the field is applied in this direction and the loop with a negligible hysteresis for the field applied in the perpendicular direction. The azimuthal dependence of the coercive field

$H_c(\varphi_H)$  in the sample plane was studied by L-MOKE for a 15 ML thick Co film (Fig. 3, inset b)). The plot gives additional evidence for the hard axis orientation along the direction perpendicular to the step edges ( $0^\circ$  and  $180^\circ$ ).

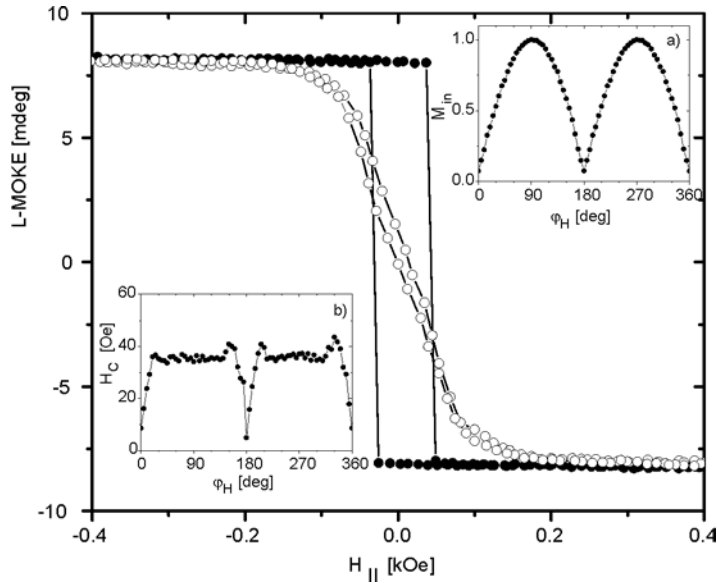


Fig. 3. Hysteresis loops measured by L-MOKE for 15 ML Co film thickness and the angles  $\varphi_H = 0$  (open circles) and  $90^\circ$  (full circles). Insets show angular dependences measured by L-MOKE of: a) normalized in-plane ellipticity remanence, b) coercivity field

The angular dependences of the resonance field  $H_r(\theta_H, \varphi_H)$  for 15 ML thick Co film are plotted in Fig. 4. The magnetic anisotropy symmetry can be deduced from these dependences. Figure 4 shows that the easy magnetization axis is close to the  $[1\bar{1}0]$  direction.

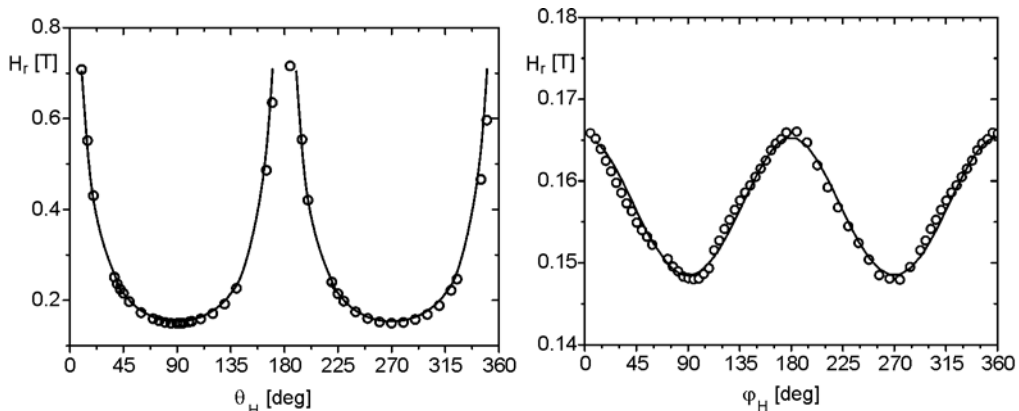


Fig. 4. FMR dependence  $H_r(\theta_H, \varphi_H)$  for 15 ML thick Co sample. Solid lines fitted using the anisotropy constants as follows:  $K_{ul} = 0.81 \text{ MJ/m}^3$ ,  $K_{vic} = -0.009 \text{ MJ/m}^3$

The following expression of the magnetic anisotropy was used for the FMR curves fitting

$$E_A(\theta, \varphi, d) = \left( K_v + \frac{2K_s}{d} \right) \left( 1 - (\mathbf{m} \times \mathbf{v}_{\text{mis}})^2 \right) - \frac{1}{2} \mu_0 M_s^2 \sin^2 \theta + K_{\text{vic}} \sin^2 \theta \sin^2 \varphi \quad (1)$$

where  $K_v$  and  $K_s$  are the volume and surface anisotropy constants, respectively,  $M_s$  is the saturation magnetization;  $\mathbf{m}$  is the normalized magnetization vector and  $\mathbf{v}_{\text{mis}}$  is the normalized vector of the vicinity direction [10],  $K_{\text{vic}}$  is the step-induced uniaxial anisotropy constant. The fitted  $H_r(\theta_H, \varphi_H)$  curves (with magnetic anisotropy constants  $K_{u1} = (K_v + 2K_s/d) = 0.81 \text{ MJ/m}^3$ ,  $K_{\text{vic}} = -0.009 \text{ MJ/m}^3$ ) are shown in Fig. 4 as solid lines. The solid line in Fig. 2 was calculated using  $K_v = 0.45 \text{ MJ/m}^3$  and  $K_s = 0.54 \text{ mJ/m}^2$  anisotropy constants. The uniaxial out-of-plane anisotropy constant is in agreement with that expected of the *hcp* Co phase [2, 11]. Analysis of the magnetization curve recorded for  $H_{\parallel}$  applied along the hard axis (Fig. 3) gives a similar uniaxial in-plane anisotropy field  $H_{\text{vic}} = 2K_{\text{vic}}/M_s = 0.013 \text{ T}$ .

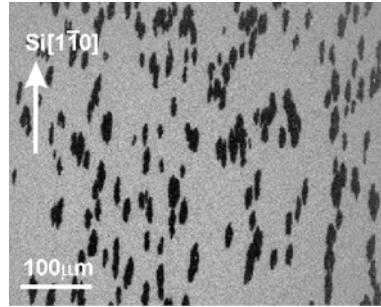


Fig. 5. Remnant domain structure for 3 ML thick Co sample

P-MOKE microscopy is a powerful tool to study magnetization reversal processes in magnetic film with a perpendicular anisotropy [12]. Figure 5 shows the remanent domain structure image recorded for a 3 ML thick Co film. The preference of domain wall orientation along the  $[1\bar{1}0]$  direction is well visible. The preference could be explained by a step-induced in-plane magnetic anisotropy determined from both FMR and L-MOKE measurements. A similar preference of domain wall orientation structure was also observed in ultrathin Co film deposited on a vicinal sapphire substrate [13].

## 4. Conclusion

Au/Co/Au structures were grown on a vicinal Si(111) surface with various thicknesses of Co layers. The symmetry of the magnetic anisotropy observed by both MOKE and FMR is connected with growth of *hcp* Co(0001) film. The out-of-plane and step-induced uniaxial in-plane magnetic anisotropies were studied in a 15 ML

thick Co film. The anisotropies were found to strongly influence the domain wall propagation along the step edges of the vicinal surface.

#### Acknowledgements

This work was supported by the Marie Curie Fellowships for “Transfer of Knowledge” (“NANO-MAG-LAB” N 2004-003177) and the ACI Nanoscience of the French government.

#### References

- [1] CHAPPERT C., LE DUANG K., BEAUVILLAIN P., HURDEQUINT H., RENARD D., *Phys. Rev. B*, 34 (1986), 3192.
- [2] KISIELEWSKI M., MAZIEWSKI A., TEKIELAK M., WAWRO A., BACZEWSKI L.T., *Phys. Rev. Lett.*, 89 (2002), 087203.
- [3] VAZ C.A.F., STEINMULLER S.J., BLAND J.A.C., *Phys. Rev. B*, 75 (2007), 132402.
- [4] LEE S., PARK S., FALCO C.M., *J. Magn. Magn. Mater.*, 240 (2002), 457.
- [5] GAMBARDILLA P., DALLMEYER A., MAITI K., MALAGOLI M.C., EBERHARDT W., KERN K., CARBONE C., *Nature*, 416 (2002), 301.
- [6] KAWAKAMI R.K., ESCORCIA-APARICIO E.J., QIU Z.Q., *Phys. Rev. Lett.*, 77 (1996), 2570.
- [7] CHOI H.J., KAWAKAMI R.K., ESCORCIA-APARICIO E.J., QIU Z.Q., PEARSON J., JIANG J.S., LI D., OSGOOD R.M. III, BADER S.D., *J. Appl. Phys.*, 85 (1999), 4958.
- [8] WEI J., WANG X.-S., GOLDBERG J.L., BARTELT N.C., WILLIAMS E.D., *Phys. Rev. Lett.*, 68 (1992), 3885.
- [9] LANGER J., HUNTER DUNN J., HAHLIN A., KARIS O., SELLMANN R., ARVANITIS D., MALETTA H., *Phys. Rev. B*, 66 (2002), 172401.
- [10] STUPAKIEWICZ A., GIENIUSZ R., MAZIEWSKI A., POSTAVA K., WAWRO A., BACZEWSKI L.T., *Phys. Stat. Sol. (b)*, 243 (2006), 202.
- [11] JEONGA J.-R., BLAND J., LEE J.-W., PARK Y.-S., SHIN S.-C., *Appl. Phys. Lett.*, 90 (2007), 022509.
- [12] POMMIER J., MEYER P., PÉNISSARD G., FERRÉ J., BRUNO P., RENARD D., *Phys. Rev. Lett.*, 65 (1990), 2054.
- [13] STUPAKIEWICZ A., TEKIELAK M., MAZIEWSKI A., ZABLOTSKII V., BACZEWSKI L.T., WAWRO A., *J. Magn. Magn. Mater.*, 316 (2007), e136.

*Received 28 April 2007*  
*Revised 16 February 2008*

## Urea–urethane nanocomposites obtained from modified methylalumoxane oligomers

A. BOCZKOWSKA<sup>1\*</sup>, M. MARCZEWSKI<sup>2</sup>, E. CIECIERSKA<sup>1</sup>,  
B. SIENKIEWICZ<sup>2</sup>, A. PIETRZYKOWSKI<sup>2</sup>

<sup>1</sup>Warsaw University of Technology, Faculty of Materials Science and Engineering,  
ul. Wołoska 141, 02-507 Warsaw, Poland

<sup>2</sup>Warsaw University of Technology, Faculty of Chemistry,  
ul. Noakowskiego 3, 00-664 Warsaw, Poland

Urea–urethane elastomers were synthesized in a polyaddition reaction of ethylene oligoadipate (OAE) of an average molecular weight 2000 u with bis(4-isocyanatephenyl)methane (MDI). Dicyandiamide was used as a chain extender. In order to obtain hybrid nanocomposites, OAE was modified by the reaction with methylalumoxanes (MAO) prior to use. The excess of active methyl groups of MAO was deactivated by reactions with alcohols or alkylphosphates. This method allowed one to introduce nano-sized aluminum-oxide based moieties into the polyurethane. The amount of nanoparticles was equal to 3 wt. %. The aim of the study was a homogeneous molecular dispersion of aluminum-oxide units in order to obtain urea–urethane nanocomposites with a higher fire resistance and improved mechanical properties. Microstructure of the nanocomposites was studied with the high resolution scanning electron microscopy (HRSEM). Mechanical properties were examined by standard testing procedures. Flammability tests were also performed using a cone calorimeter under heat flux equal to 50 kW/m<sup>2</sup>. The results of the microstructure studies show even distribution of the nano-sized aluminum-oxide units in the polyurethane bulk. We observed an increase of such properties as Young's modulus and hardness, accompanied by a significant decrease in the heat release rate.

Key words: *urea–urethane elastomer; nanocomposite; methylalumoxanes*

### 1. Introduction

Polymer matrix–ceramic composites are nowadays commonly researched and developed for variety of applications. For example, particles of SiO<sub>2</sub>, SiC, TiC, Al<sub>2</sub>O<sub>3</sub> are added to polymer matrices to increase their hardness, stiffness and wear resistance [1].

---

\*Corresponding author, e-mail: abocz@meil.pw.edu.pl



Polymer nanocomposites are formed through the union of two very different materials with organic and mineral pedigrees. They are distinguished by high tensile strength, elastic modulus and heat distortion temperature without a loss in impact resistance. They also have a lower water sensitivity, permeability to gases and thermal coefficient of expansion. Due to those features, such nanocomposites found many industrial applications, especially in food packaging and automobile industries [2].

Segmented urea–urethane elastomers have their macromolecules built of soft (S) and hard segments (H). The soft segments are formed in an addition reaction of oligodiols with diisocyanate. The hard segments are obtained in a polyaddition reaction of the isocyanate groups ( $-NCO$ ) with the chain extender such as low-molecular-weight compound terminating with hydroxyl ( $-OH$ ) or amino groups ( $-NH_2$ ) [3]. The molar ratio of hard and soft segments can be changed according to the molar ratio of substrates. Urea–urethane elastomers are characterized by such advantageous properties like high tear strength and tensile modulus. Therefore they have found many applications for a wide range of products like for instance sieves for mining industry.

We have developed a new method of fabrication of hybrid urea–urethane nanocomposites obtained from oligodiols modified with methylalumoxanes [4]. Oligodiols were reacted with methylalumoxanes (MAO) prior to their use. This method allowed to introduce nano-sized aluminium oxide based moieties into the polyurethane [5].

In this work, we present results of our studies on introduction of modified methylalumoxanes as fillers of urea–urethane elastomers. This allowed us to obtain hybrid urea–urethanes with nano-sized  $(AlO)_n$  moieties evenly distributed in the elastomer. The aim of the study was to obtain urea–urethane nanocomposites with higher fire-resistance and improved mechanical properties.

## 2. Experimental

Urea–urethane elastomers were synthesized in a polyaddition reaction of ethylene oligoadipate (OAE) of an average molecular weight 2000 a.u. with bis(4-isocyanatophenyl)methane (MDI). Dicyandiamide (DCDA) was used as a chain extender. DCDA contains two amino groups and one highly polar cyanimine group bonded to the same carbon atom. The polar urea groups are formed as a result of the reaction of amino and isocyanate groups. The presence of a strong polar urea group and a strong polar nitylimide side-group in every short hard segment influences the urea–urethane properties. Such polyurethanes are distinguished by low water absorption, high resistance to hydrolysis and high resistance for abrasive wear, especially at the moisture conditions. They are also characterized by such advantageous properties like high tear strength and tensile modulus.

The urea–urethane polymer and its composites were synthesized in a one-pot reaction of MDI with OAE and DCDA at a molar ratio of MDI/(OAE+DCDA) equal to 2.0. All reactions were carried out in a vacuum reaction vessel at 2–5 hPa with a me-

chanical stirring. In order to obtain hybrid nanocomposites, methylalumoxanes (MAO) were modified by the reaction with OAE, alcohols and/or alkylphosphates prior to use. The modification process is described in Sect. 3. The amount of MAO based fillers introduced into polyuretanes was equal to 3 % by weight. The mixture of substrates was cast into special moulds and then curing process was carried out at elevated temperature.

Microstructure of the nanocomposites was studied using the HRSEM LEO 1530 (Zeiss). Mechanical properties were examined by standard testing procedures developed for elastomers. The parameters measured were: tensile strength, elastic modulus, tear strength, elongation at break, hardness and abrasive wear.

Flammability tests were made using a cone calorimeter under the heat flux equal to  $50 \text{ kW/m}^2$ . The following parameters were measured: maximum heat release rate, average specific extinction area, average CO and  $\text{CO}_2$  yields and time to sustained ignition.

### 3. Results and discussion

Alumoxanes are compounds containing Al–O–Al groups. Their properties have been intensively studied as they play a key role in the Ziegler-type polymerization [6]. Despite many detailed studies, the structure of methylalumoxane (MAO) still remains a “black box”. It cannot be elucidated directly, because of multiple equilibria present in MAO solutions. The structure of MAO can be described as oligomers of  $[\text{CH}_3\text{AlO}]$  moieties containing some associated  $(\text{CH}_3)_3\text{Al}$  molecules. The formula of commercially available MAO is best represented as  $[-(\text{CH}_3)_{1.4-1.5}\text{AlO}_{0.75-0.80}]_n$  [7, 8]. Molecular weights of MAO range from 1000 to 2700 [7, 9, 10]. In the present studies, we have used methylalumoxane purchased from Crompton GmbH as 10% solution in hexane (MAO2), and the only structurally characterised methylalumoxane, synthesised in our group [11] (MAO1). The structure of the latter alumoxane is presented in Fig. 1.

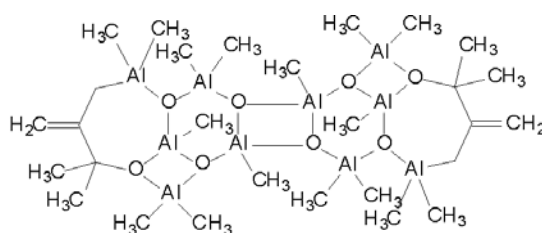
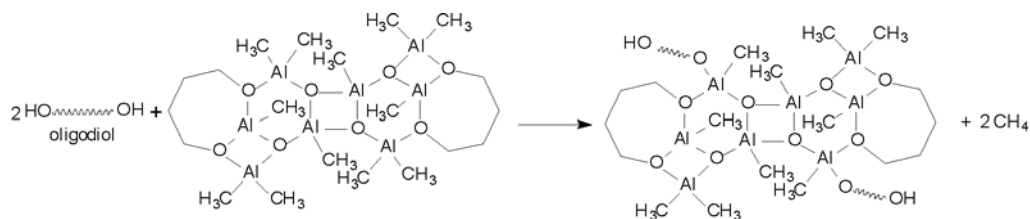


Fig. 1. The structurally characterised methylalumoxane (MAO1)

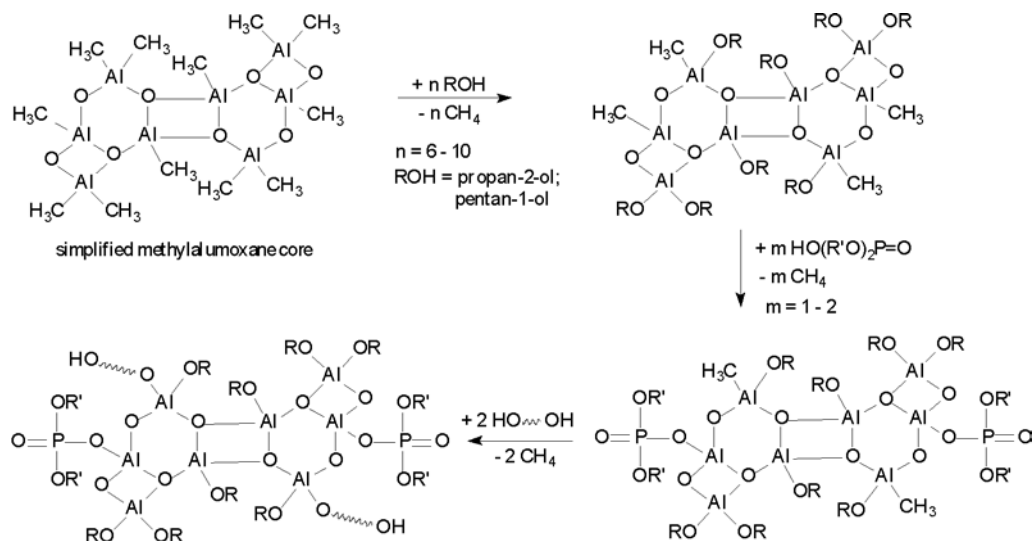
Methylalumoxane molecules have several methyl groups bonded to aluminum. These reactive groups have been used for a modification. The idea of the modification was to react a molecule of methylalumoxane with two molecules of ethylene oligo-

adipate (OAE) used in the synthesis of polyurethane. This should lead to the formation of the following compound (Scheme 1):



Scheme 1

The remaining methyl groups had to be blocked to prevent their further reactions. It was achieved by the reactions with alcohols (propan-2-ol or pentan-1-ol) and/or with alkylphosphates. The final products retained the character of a diol and were used for synthesis of polyurethanes with evenly distributed nano-sized  $[-Al-O-]_n$  moieties. A simplified scheme of the synthetic procedure of modified methylalumoxanes is presented in Scheme 2.



Scheme 2

The diameter of the molecule of the structurally characterised methylalumoxane is about 1.5 nm, while the size of inorganic particles incorporated into polyurethane structure is within the range of 20–100 nm (Figs. 2 and 3). This indicates that further association of alumoxane molecules occurs during modification and the actual structure of alumoxane moieties remains unknown. Nevertheless, this schematic picture illustrates the idea of an incorporation of alumoxane moieties into the polyurethane chains.

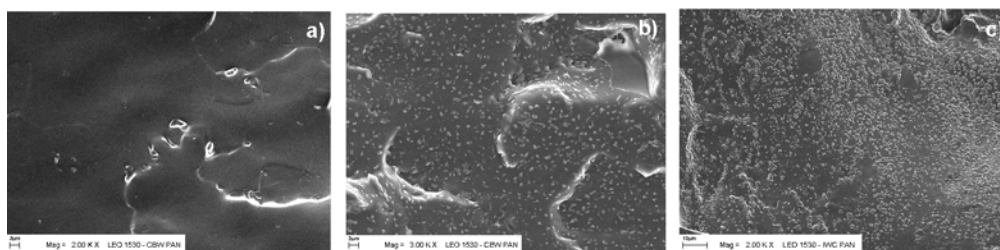


Fig. 2. SEM images of brittle fractures of PU without nanofillers (a) and with: b) PU + M1, c) PU + MP4

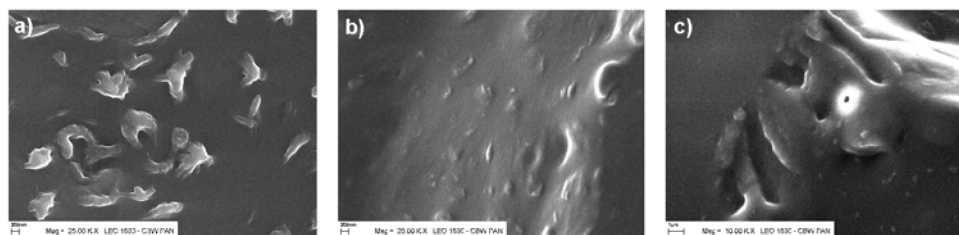


Fig. 3. SEM images of brittle fractures of PU nanocomposites obtained from: a) MAO1 with propan-2-ol, b) MAO1 with pentan-1-ol, c) MAO2 with pentan-1-ol

The reagents used for the fabrication of the samples are listed in Table 1.

Table 1. Reagents used for the fabrication of samples

Sample	Metyloalumoxane	Alcohol	Ester <sup>a</sup>
PU + M1	MAO1	propan-2-ol	–
PU + M2	MAO1	pentan-1-ol	–
PU + M3	MAO2	pentan-1-ol	–
PU + MP7	MAO1	pentan-1-ol	ester 1
PU + MP1	MAO2	–	ester 2
PU + MP3	MAO2	pentan-1-ol	ester 2
PU + MP4	MAO2	pentan-1-ol	ester 1
PU + M4	MAO2	pentan-1-ol	–
PU + MP5	MAO2	pentan-1-ol	ester 2
PU + MP6	MAO2	pentan-1-ol	ester 2
PU + MP11	–	–	ester 1

<sup>a</sup>Ester 1 –  $\text{CH}_3\text{P}(\text{O})(\text{OCH}_3)_2$ , ester 2 –  $[\text{CH}_3(\text{CH}_2)_3\text{CH}(\text{CH}_2\text{CH}_3)\text{CH}_2\text{O}]_2\text{P}(\text{O})\text{OH}$

As is shown in Fig. 2, the use of oligoadipate chemically bonded to methylalumoxane leads to even distribution of the nano-sized aluminum-oxide units in the polyurethane matrix.

The aluminum-oxide units may differ in shape and size according to the kind of MAO (MAO1 or MAO2) and the way of its modification. The modification of both

MAO1 and MAO2 with pentan-1-ol leads to the formation of more elongated (needle-like) particles (Figs. 3b, c). Modification of MAO2 with ester 2 gives spherical nanoparticles (Figs. 4a, b) in comparison to modification with ester 1 (Fig. 4c). Such differences in nanocomposite structures can influence their mechanical properties.

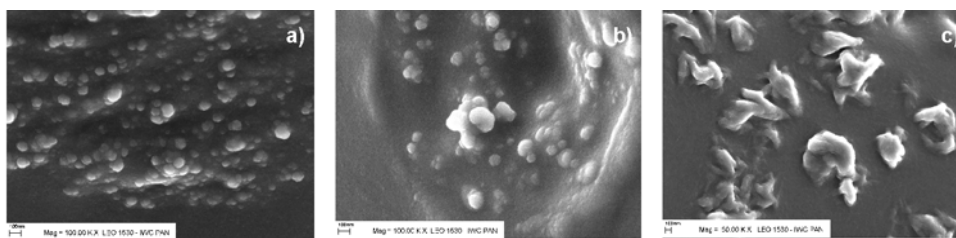


Fig. 4. SEM images of brittle fractures of nanocomposites obtained from:  
a) MAO2 with ester 2, b) MAO2 with pentan-1-ol and ester 2, c) MAO2 with ester 1

It was found that the highest increase in Young's modulus is observed after modification of MAO2 with pentan-1-ol and additionally with ester 2 (Fig. 5). Modification of PU matrix with nanoparticles gives a significant increase of Young's modulus and slight increase of the hardness (Fig. 6).

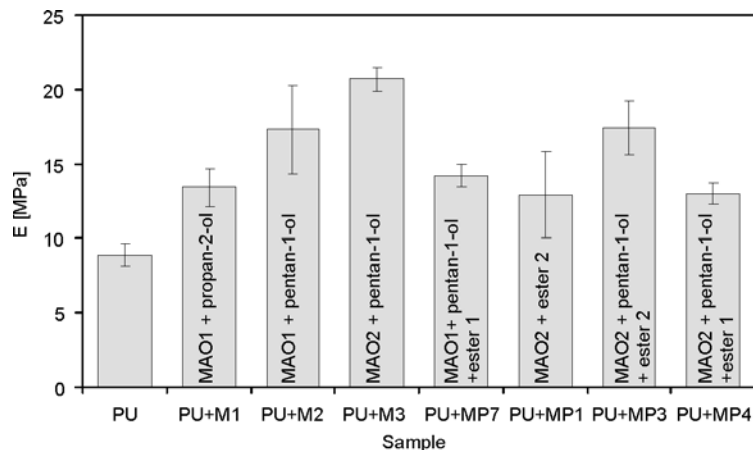


Fig. 5. Young's modulus of poly(urea-urethane) nanocomposites

One of the most important properties of polyurethanes studied was their abrasive wear. As is shown in Fig. 6, the incorporation of methylalumoxanes after the modification only with alcohol did not change the abrasive wear. A significant increase in the abrasive wear was observed in nanocomposites obtained from MAO modified with esters.

Flammability test results are shown in Table 2. The addition of MAO modified with phosphoric acid esters to PU matrix led to a significant reduction of  $HRR_{max}$ . Unfortunately, the reduction of SEA, which is responsible for smoke emission, was

not achieved. The benefit of usage of MAO modified with phosphoric acid ester was a visible shortening of the sustained ignition time. The sample PU + MP11 was modified only with phosphoric acid ester. It was found that such modification without application of MAO did not give satisfactory flammability results.

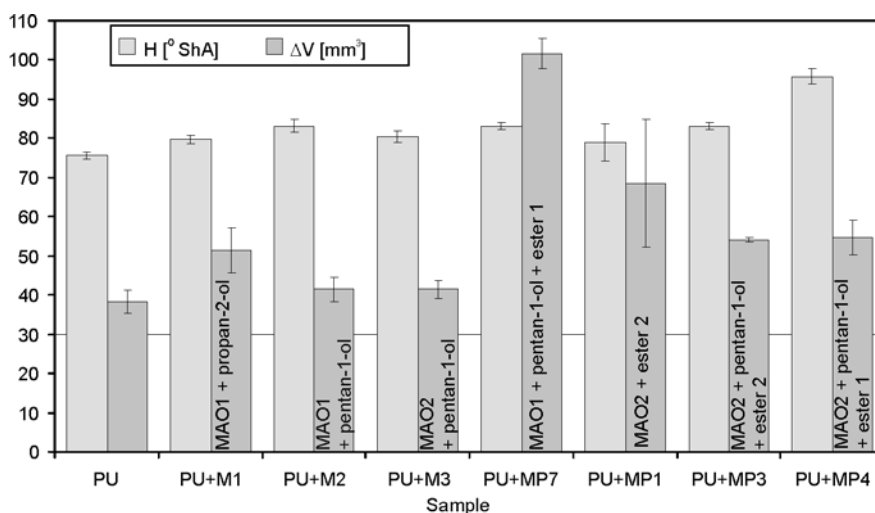


Fig. 6. Hardness and abrasive wear of poly(urea-urethane) nanocomposites

Table 2. Results of the flammability test

Symbol	Parameter	PU	PU + M4	PU + MP4	PU + MP5	PU + MP6	PU + MP11
HRR <sub>max</sub>	maximum heat release rate [kW/m <sup>2</sup> ]	1178	1704	703	621	694	1166
		±92	±176	±34	±40	±38	±91
SEA	specific extinction area [m <sup>2</sup> /kg]	218	203	299	287	323	381
		±24	±9	±82	±61	±22	±25
t <sub>ig</sub>	time to sustained ignition [s]	26.39	22.78	25.20	20.08	23.34	22.81
		±0.13	±0.73	±0.35	±0.02	±0.35	±0.37
CO	average CO yield [kg/kg]	0.07769	0.06530	0.01673	0.01546	0.01632	0.14231
		±0.04815	±0.02492	±0.00091	±0.00113	±0.00197	±0.01425
CO <sub>2</sub>	average CO <sub>2</sub> yield [kg/kg]	1.95632	2.07708	1.86797	2.00365	1.96577	1.76922
		±0.03287	±0.09619	±0.00769	±0.05704	±1.01983	±0.05274

## 4. Conclusions

It was found that methylalumoxanes with methyl groups substituted by alcohols (propan-2-ol or pentan-1-ol) and/or alkylphosphates and ethylene oligoadipate can be successfully applied in synthesis of urea-urethane hybrid polymers. The results of the studies of microstructure show even distribution of the nano-sized aluminum-oxide units in the polyurethane bulk. Young's modulus, hardness and tensile strength at

100% elongation increased; on the other hand, a significant decrease was observed in the heat release rate.

#### Acknowledgements

This work was supported by the Polish State Committee for Scientific Research (KBN), grant No. PBZ-KBN-095/T08/2003.

#### References

- [1] CHUNG D.D.L., *Composite Materials: Science and Applications*, Springer, London, 2003.
- [2] PINNAVAIA T.J., BEALL G.W., *Polymer-Clay Nanocomposites*, Wiley, New York, 2001.
- [3] GRUIN I., *Advances in Urethane Science and Technology*, Vol. 11, Technomic Publishing Co. Inc., Lancaster, 1992.
- [4] BOCZKOWSKA A., PIETRZYKOWSKI A., MARCZEWSKI M., SIENKIEWICZ B., CIECIERSKA E., KUNICKI A.R., OLSZYNA A., PL patent application No. P. 381280, 2006.
- [5] BOCZKOWSKA A., MARCZEWSKI M., SIENKIEWICZ B., PIETRZYKOWSKI A., KUNICKI A.R., ZIEMKOWSKA W., ZAWADA A., OLSZYNA A., *Inż. Mater.*, 6 (2006), 1323.
- [6] PASYNKIEWICZ S., *Polyhedron*, 9 (1990), 429.
- [7] SINN H., *Macrom. Symp.*, 97 (1995), 27.
- [8] IMHOFF D.W., SIMERAL L.S., SANGOKOYA S.A., PEEL J.H., *Organomet.*, 17 (1998), 1941.
- [9] BABUSHKIN D.E., SEMIKOLENOVA N.V., PANCHENKO V.N., SOBOLEV A.P., ZAKHAROV V.A., TALSI E.P., *Macromol. Chem. Phys.*, 198 (1997), 3845.
- [10] TRITTO I., MELARES C., SACCHI M.C., LOCATELLI P., *Macromol. Chem. Phys.*, 198 (1997), 3963.
- [11] PIETRZYKOWSKI A., unpublished results.

*Received 28 April 2007*  
*Revised 16 February 2008*

## Aerosol-assisted synthesis of SiC-based nanopowders from organosilicon precursor systems

C. CZOSNEK<sup>1\*</sup>, S. KLUSKA<sup>2</sup>, J. F. JANIK<sup>1</sup>

<sup>1</sup>Faculty of Fuels and Energy, AGH University of Science and Technology,  
al. Mickiewicza 30, 30-059 Cracow, Poland

<sup>2</sup>Faculty of Materials Science and Ceramics, AGH University of Science and Technology,  
al. Mickiewicza 30, 30-059 Cracow, Poland

Thermally-driven decomposition of various organosilicon derivatives under a neutral gas atmosphere constitutes a reliable way for the preparation of carbon/silicon carbide C/SiC composites (modified carbon materials) in the nanosized range. The two-stage aerosol-assisted synthesis method appears to be especially well suited to fabricate such materials while offering spherical particle morphology with tailored particle size capability. In this method, in the first stage an aerosol mist is generated from a liquid precursor system and transported in a neutral gas stream to a pre-heated ceramic tube reactor where complex physical and chemical changes take place resulting in the formation of solid particles collected on an exit filter. The raw product is usually pyrolyzed in the second stage at appropriately high temperatures to complete the anticipated removal of residual oxygen if excess C is present *via* carbothermal reduction. In this study, preliminary results on the target C/SiC composites prepared with the aerosol method from selected organosilicon precursors are presented. The precursors included hexamethyldisiloxane, tetramethoxysilane, and silicone oil (poly(dimethylsiloxane)) and its ethanol solutions. In the first stage, the aerosols were subject to decomposition at 1200 °C under an Ar flow and raw products containing SiO<sub>x</sub>C<sub>y</sub>/SiO<sub>2</sub> and free C of varied proportions were produced. In the second stage, the raw powders were pyrolyzed at 1650 °C for 1 h under an Ar flow. The presence of a sufficient excess of free C in the raw product should lead in principle to efficient carbothermal reduction processes and conversion of SiO<sub>x</sub>C<sub>y</sub>/SiO<sub>2</sub> to SiC in a composite system with the remaining free carbon, if any; otherwise, SiC/SiO<sub>2</sub> or even SiC/SiO<sub>2</sub>/Si composites can be produced.

Key words: *silicon carbide; C/SiC; composite; aerosol; nanocrystalline material*

### 1. Introduction

Due to many advantageous properties, silicon carbide SiC has found numerous applications in ceramics and electronics. In recent years, many expectations have

---

\*Corresponding author, e-mail: czosnek@agh.edu.pl



rested with specific properties of nanocrystalline forms of SiC. For example, a plausible combination of quantum size effect and donor sites has resulted in nano-SiC emitting in the blue range which may have great potentials in optoelectronics [1]. Also, an attractive optical behaviour has been detected in nano-SiC dispersed in photopolymer matrices [2, 3]. Pure and doped SiC powders have been probed as dielectrics at microwave frequencies of 4–18 GHz to appraise their insulating properties and absorption of electromagnetic waves [4]. On the application side in ceramics, high thermal and mechanical resistance of SiC resulted in its utilization as a valuable component in various composite systems. In the case of carbons, SiC is frequently considered as the component of choice by advantageously modifying high temperature properties of carbon materials (C/SiC composites) [5, 6].

Classical approaches to the synthesis of SiC usually include reactions of elemental silicon with carbon or carbothermal reduction of SiO<sub>2</sub> with carbon (elemental C or C source derived from *in situ* decomposition of various hydrocarbons). In both cases, due to required high processing temperatures, microcrystalline SiC is produced. The prerequisite mechanical grounding/milling/mixing of solid precursors in such syntheses may be additionally a source of serious contamination of the product. As far as nanocrystalline SiC is concerned, it is commonly prepared via sol-gel processes from resulting organosilicon-derived colloids [7].

In our previous studies on the C/SiC system, we applied homogenized mixtures of a coal tar pitch and silicon precursors such as poly(carbosilane), elemental silicon [8], and poly(dimethylsiloxane) [9]. The final pyrolysis at 1650 °C was necessary in these systems to produce a prevailing regular polytype of SiC ( $\beta$ -SiC) with 14–24 nm average crystallite sizes mixed with a poorly crystallized turbostratic carbon. In this regard, the utilization of poly(carbosilanes) as single source precursors containing Si–C bonds enabled Yajima et al. preparation of SiC fibres on the commercial scale (Nicalon fibres) [10, 11].

Yet another way to approach the preparation of nanocrystalline powders of SiC or C/SiC composites is the application of the aerosol-assisted synthesis method utilizing neat organosilicon derivatives or their suitable solutions. In this method, upon generation the aerosolized precursor mist is transported in a stream of neutral gas through a pre-heated ceramic tube reactor. In the high temperature zone and under appropriate conditions, complex physical and decomposition reactions take place producing solid particles of spherical morphology that are collected on an exit filter. This raw product is usually subject to a second-step pyrolysis under special conditions (temperature, time, gas atmosphere) to complete the anticipated changes and yield the final product. It is instructive to point out that one of the outstanding features of the aerosol-assisted process is that all reactions take place within very small liquid/solid particles suspended in a gas stream. In favourable cases, this creates more advantageous conditions for processing toward nanosized particles compared to typical one-stage bulk pyrolysis methods.

One has to be aware of the fact that thermal decomposition of some organosilicon precursors, especially those containing oxygen, may result in the formation of transient glassy  $\text{SiO}_x\text{C}_y$  phases of variable composition depending on the type of precursor. Furthermore, some by-product carbon clusters are known to be entrapped in such phases. It has been reported that the silicon oxycarbide glasses can be stable up to 1200 °C [12, 13] while higher temperatures of the order of 1400–1600 °C result in phase separation and/or progressing carbothermal reduction to yield mostly  $\beta$ -SiC or C/SiC if enough carbon is present while  $\beta$ -SiC/SiO<sub>2</sub> (nanocrystalline or amorphous) [14] or  $\beta$ -SiC/Si are formed in the systems deficient in carbon and rich in silicon [15]. A similar behaviour was noticed in the case of silsesquioxanes where the decomposition of the transient silicon oxycarbides in the 1200–1400 °C range resulted in the formation of mostly amorphous mixtures of SiC and SiO<sub>2</sub> in addition to small quantities of crystalline SiC and turbostratic graphitic carbon [16].

In this report, preliminary results of the study on the nanocrystalline composite C/SiC powders prepared *via* the two-stage aerosol-assisted method utilizing selected oxygen-bearing organosilicon precursor systems have been discussed. The progress of decomposition and evolution of final products is described, based on the characterization with powder XRD spectroscopy, FT-IR spectroscopy, SEM examination, and carbon content determinations.

## 2. Experimental

The raw powders were made by the aerosol-assisted synthesis method. The experimental set-up consisted of an ultrasound aerosol generator with the output connected to a ceramic tube reactor, ID = 76 mm, length = 1500 mm, while a fine nylon filter was attached at the air-cooled reactor exit. The reactor was placed in an electric tube furnace routinely preheated to 1200 °C. The aerosol mist was transported through the reactor in an argon gas stream, 4 dm<sup>3</sup>/min, and the solid product was collected on the filter. Neat hexamethyldisiloxane  $[(\text{CH}_3)_3\text{Si}]_2\text{O}$  (Aldrich), neat tetramethoxysilane  $\text{Si}(\text{OCH}_3)_4$  (Aldrich), and a 50:50 (by volume) ethanol solution of poly(dimethylsiloxane)  $[-\text{O}-\text{Si}(\text{CH}_3)_2-]_n$  (Silikony Polskie, Nowa Sarzyna, Poland) were used as precursors. The raw products were dark brown to black free flowing powders. They were pyrolyzed in the second stage at 1650 °C for 1 h under an Ar flow. Instrumental characterization methods included the powder XRD determinations (PANalytical, Model X'Pert Pro, Holland,  $\text{CuK}\alpha$ ,  $\lambda = 1.54060 \text{ \AA}$ ), FT-IR spectroscopy (Nicolet 380, Thermo Electron Corporation, KBr pellets), and SEM (Hitachi, Model S-4700). In order to evaluate the free carbon contents, mild oxidation of powder samples in air, 700 °C, 90 min, was carried out and the resulting changes of sample weights were used in calculations assuming  $\text{C} + \text{O}_2 = \text{CO}_2 \uparrow$  and no significant reactions of the SiC component under applied conditions. In addition, the total carbon contents were evalu-

ated by combustion of powder samples in oxygen at 1300 °C with detection of CO<sub>2</sub> by an IR analyzer (ACS-40/1350 IR-analyzer, PIE Warsaw, Poland).

### 3. Results and discussion

A typical morphology of raw powders examined with SEM is displayed in Fig. 1. The powders obtained from hexamethyldisiloxane (a) and ethanol solution of poly(dimethylsiloxane) (b) show a characteristic spherical particle morphology of quite uniform sizes while, occasionally, individual particles tend to be partially fused and agglomerated. Similar spheroidal appearance is shown by the powder from tetramethoxysilane (c) alas with seemingly more deformed particles.

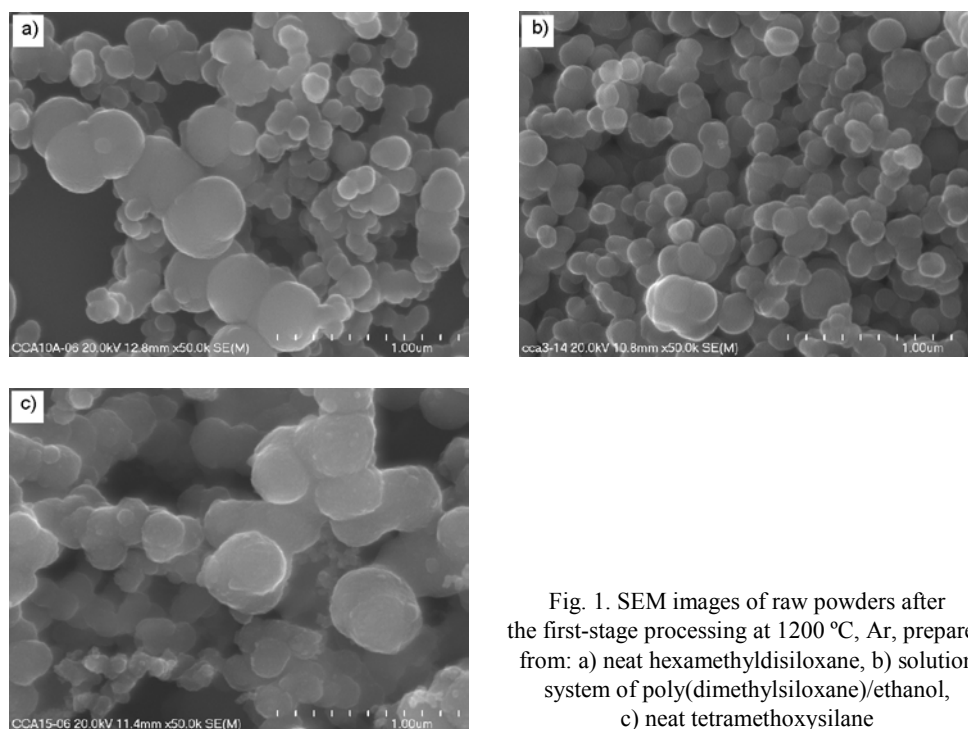


Fig. 1. SEM images of raw powders after the first-stage processing at 1200 °C, Ar, prepared from: a) neat hexamethyldisiloxane, b) solution system of poly(dimethylsiloxane)/ethanol, c) neat tetramethoxysilane

The prevailing spherical shape of the particles stems from both the characteristics of the aerosol generation step and dynamics of the following decomposition/polymerization processes. In this regard, in the initial stage spherical droplets in the mist are introduced into the preheated reactor to undergo thermochemically induced changes. If a precursor solution is used, the evaporation of the solvent and precipitation of the precursor that may possibly collapse into a smaller-diameter sphere first take place. In the case of all our precursors, the progressing decomposition of the neat precursor is associated with continuing polymerization processes occurring main-

ly from the outer layers toward the core of the spheres and resulting in time-dependent increasing viscosities while preserving the overall shape of stiffened particles. Some incidental impacts and possible bursting events, the latter due to developed hindrances in volatiles evolution from the core, may cause particle deformation at this stage, too. At a certain point, the polymerization and accompanying carbothermal reduction processes eventually result in solidification of individual particles or particle agglomerates.

The particle morphology “imprinted” in the first stage is found to be, generally, preserved after the subsequent second-stage pyrolysis at 1650 °C under an Ar flow. The molecular-scale or micro-scale carbothermal reduction, phase separation, and crystallization phenomena taking place during the pyrolysis do not appear to influence the overall macrosized particle shape and diameter (typically, up to several micrometers). It is worth pointing out that relatively large SiC crystallites with well developed facets were occasionally observed among the prevailing spheres, the former indicative of recrystallization/growth phenomena taking place locally under advantageous conditions. Also, in the final product from tetramethoxysilane some severely fused agglomerates were detected that were absent in the raw powder and this supported a partial melting and fusing of the particles during the final pyrolysis. Small quantities of whiskers were additionally observed in this product, possibly resulting from the gas phase reaction of the type:

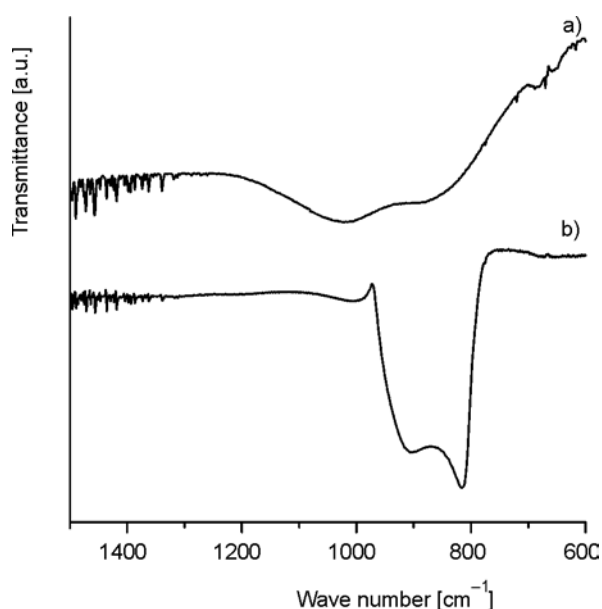
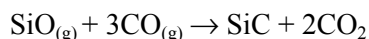


Fig. 2. FT-IR spectra for products prepared from neat hexamethyldisiloxane (KBr pellets): a) raw powder after first-stage processing at 1200 °C, Ar, b) final powder after second-stage pyrolysis at 1650 °C, Ar

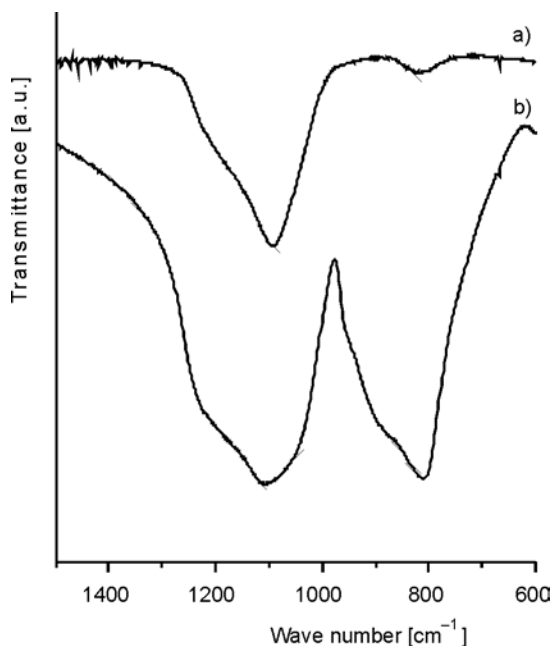


Fig. 3. FT-IR spectra of products prepared from neat tetramethoxysilane (KBr pellets): a) raw powder after first-stage processing at 1200 °C, Ar, b) final powder after second-stage pyrolysis at 1650 °C, Ar

Figures 2 and 3 present FT-IR spectra of the products prepared from hexamethyldisiloxane and tetramethoxysilane, respectively. In each case, the spectrum a) was collected for the raw product and spectrum b) for the final product in the system. Both spectra for the raw products appear to be similar to each other in the characteristic spectral ranges, i.e., they contain absorption bands associated with Si–O bonds (stretching mode at ca. 1060  $\text{cm}^{-1}$ ) and Si–C bonds (stretching mode at ca. 850  $\text{cm}^{-1}$ ). On the other hand, the respective IR spectra of the final products after the pyrolysis at 1650 °C point out to their different chemical make-up. In the case of the powder from hexamethyldisiloxane (Fig. 2b), there are exclusively absorptions related to Si–C bonds while for the powder from tetramethoxysilane (Fig. 3b) Si–O bonds seem to persist and can be linked to some silica  $\text{SiO}_2$ . The latter is further corroborated by the powder XRD determinations (*vide infra*). The presence of silica indicates a deficiency of carbon in the raw product of which definite excess is inevitable for carbothermal reduction to occur in the second stage. The excess C affects the extent of oxygen removal from  $\text{SiO}_x\text{C}_y/\text{SiO}_2$  in the form of volatile carbon oxides (carbon as oxygen scavenger) and, therefore, creates right conditions for the formation of the target SiC or C/SiC products.

The XRD patterns of the powders prepared from hexamethyldisiloxane are shown in Fig. 4, the diffractogram a) is recorded for the raw powder and diffractogram b) for the final product. The diffractogram a) is typical of the prevalingly amorphous material. The very broad halo at  $2\theta \approx 25^\circ$  can be interpreted as related to small quantities

of disordered graphitic carbon structures and that at  $2\theta \approx 35^\circ$  can likely be linked to emerging nanocrystalline  $\beta$ -SiC. On the other hand, the most intense peaks in the pattern b) are assigned to the major regular phase of  $\beta$ -SiC (average crystallite size of 32 nm as determined from the Scherrer equation) and the remaining small intensity peaks are associated with the minor hexagonal  $\alpha$ -SiC polytype. No broad features typical of turbostratic carbon are seen here (within the detection limits of the powder XRD method) that, to be recalled, was detected in the raw powder in this system. This observation is consistent with the most of the free carbon being consumed in the carbothermal reduction of  $\text{SiO}_x\text{C}_y/\text{SiO}_2$  during the second-stage pyrolysis. In this regard, low temperature oxidation of the final powder showed some 7.7 wt. % of free C to be compared with 9.5 wt. % of free C in the raw powder. The presence in the product of such a small proportion of turbostratic carbon, possibly, resulted in broadening of the low intensity diffraction peaks due to C beyond detection limits of the XRD method.

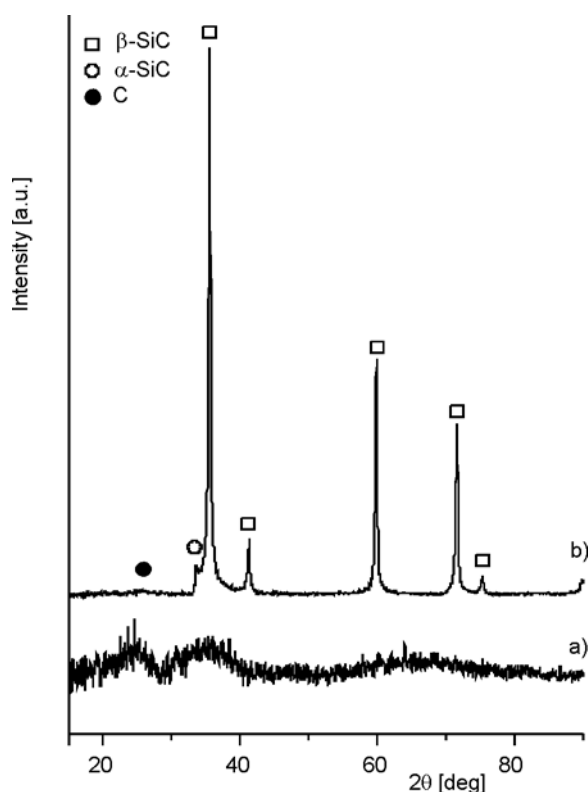


Fig. 4. Powder XRD patterns for products prepared from neat hexamethyldisiloxane: a) raw powder after first-stage processing at 1200 °C, Ar, b) final powder after second-stage pyrolysis at 1650 °C, Ar

Figure 5 contains the XRD patterns for the raw product (a) and final product (b) in the poly(dimethylsiloxane)/ethanol system. The diffractogram a) shows only three broad halos at  $2\theta$  equal approximately to 25, 43, and 80° characteristic of the turbo-

stratic graphitic domains. This corresponds well with significant quantities of free C available in the raw product from the thermal cracking of ethanol; the excess carbon was analyzed in the product at 85.5 wt. % and the total carbon at 94.9 wt. %.

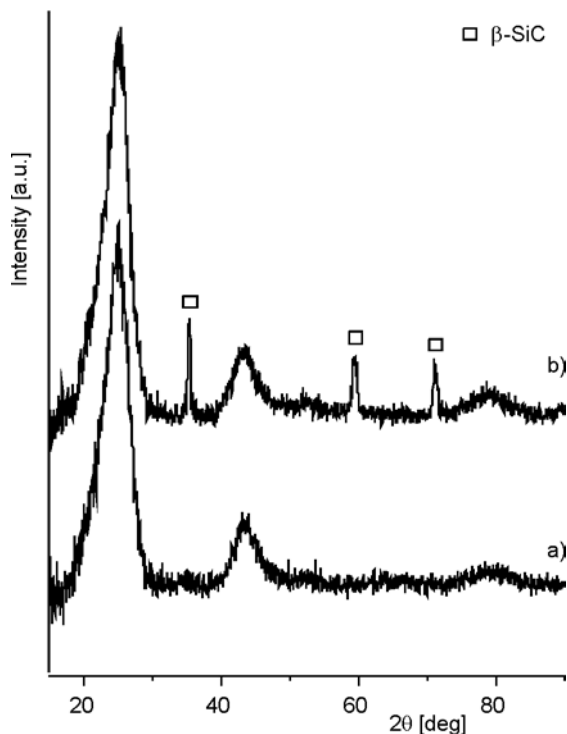


Fig. 5. Powder XRD patterns for products prepared from the solution system of poly(dimethylsiloxane)/ethanol: a) raw powder after first-stage processing at 1200 °C, Ar, b) final powder after second-stage pyrolysis at 1650 °C, Ar

The diffractogram b) for the pyrolyzed powder also shows the peaks for turbostratic carbon and the widths of the peaks appear to be very similar to those in the diffractogram a). This kind of behaviour suggests that the additional pyrolysis at 1650 °C does not result in a detectable increase of crystalline ordering of carbon in this powder. In addition to the carbon phase, the peaks due to the minor phase of  $\beta$ -SiC (average crystallite size of 9 nm) are also seen. Free carbon in the final powder was found at 73.5 wt. % and the total carbon at 94.5 wt. % supporting only small nonetheless detectable extent of carbothermal reduction during the second-stage pyrolysis in this system with a large excess of free carbon.

The XRD patterns for the raw and final products prepared from tetramethoxysilane are shown in Fig. 6. The broad feature in Fig. 6a at  $2\theta$  ranging approximately from 20° to 22° can be assigned to highly amorphous  $\text{SiO}_2$  apparently already formed in the first stage at 1200 °C. The final product is composed of the major  $\beta$ -SiC and

minor  $\alpha$ -SiC phases as well as of some cristobalite  $\text{SiO}_2$  as supported by Fig. 6b. Moreover, a small quantity of re-solidified tiny spheres likely to be elemental Si (m.p. 1410 °C) was found in the crucible bottom after product discharge.

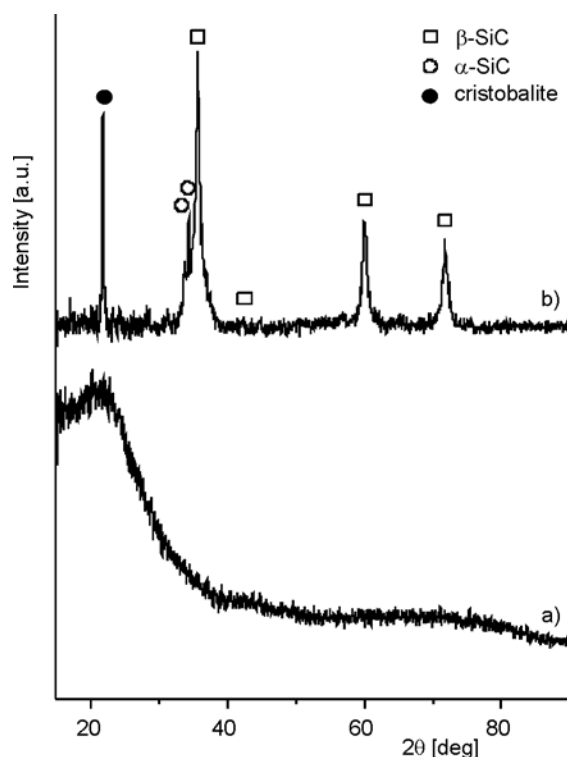


Fig. 6. Powder XRD patterns for products prepared from neat tetramethoxysilane: a) raw powder after first-stage processing at 1200 °C, Ar, b) final powder after second-stage pyrolysis at 1650 °C, Ar

All this has to be confronted with the low temperature determination of free carbon, <1 wt. %, and the total carbon content of mere 7.2 wt. %. Based on that, one can deduce that there is a severe deficiency of carbon in this system, the latter needed for the efficient carbothermal reduction of  $\text{SiO}_2$  (and/or  $\text{SiO}_x\text{C}_y$ ) to SiC according to the overall reaction  $\text{SiO}_2 + 2\text{C} \rightarrow \text{SiC} + \text{CO}_2\uparrow$ . With the deficiency of carbon, some unreacted  $\text{SiO}_2$  may persist and/or even elemental Si may be formed from incomplete reduction/carbidization according to  $\text{SiO}_2 + \text{C} \rightarrow \text{Si} + \text{CO}_2\uparrow$  as demonstrated in this system.

#### 4. Conclusions

The average crystallite sizes of the SiC-based powder nanocomposites prepared with the aerosol-assisted method from the pool of readily available organosilicon pre-



cursors can be reasonably controlled. The method provides the powders with spherical/spheroidal particle morphology of quite uniform sizes and with varying degrees of primary agglomeration, *i.e.*, loose or partially fused spheres.

The utilization of neat hexamethyldisiloxane under applied conditions yields the powder composed of the major  $\beta$ -SiC and minor  $\alpha$ -SiC phases and very small quantities of free carbon. It is worth pointing out that this product upon a mild oxidation treatment could be a source of pure nanocrystalline SiC powders.

The use of the solution precursor system of poly(dimethylsiloxane)/ethanol is advantageous for the prevailing formation of  $\beta$ -SiC in the composite system with excess free carbon. There is ample room in this system for adjusting the C/SiC composition by setting up the solvent to precursor ratios within the miscibility range.

Finally, the utilization of neat tetramethoxysilane with, apparently, insufficient available carbon to complete the carbothermal reduction processes yields mixtures of SiC with SiO<sub>2</sub> and elemental Si. From the viewpoint of the target composite C/SiC, in order to remedy the problem of carbon deficiency in this system, one can preferably apply a suitable organic solvent (source of carbon *via* solvent cracking) in the aerosol generation stage or ensure an additional source of carbon during the second-stage pyrolysis. Such options are planned to be explored in the near future.

#### Acknowledgements

The authors acknowledge a financial support of the Polish Ministry of Science and Higher Education, Grant No. 3 T08D 035 30.

#### References

- [1] MATSUMOTO T., TAKAHASHI J., TAMAKI T., FUTAGI T., MIMURA H., KANEMITSU Y., Appl. Phys. Lett. 64 (1994), 226.
- [2] KASSIBA A., TABELLOUT M., CHARPENTIER S., HERLIN N., EMERY J.R., Solid State Commun. 115 (2000), 389.
- [3] KITYK I.V., MAKOWSKA-JANUSIK M., KASSIBA A., PLUCINSKI K.J., Opt. Mater. 13 (2000), 449.
- [4] SUN J., LI J., SUN G., ZHANG B., ZHANG S., ZHAI H., Ceram. Int. 28 (2002), 741.
- [5] YIN X., CHENG L., ZHANG L., XU Y., Carbon 40 (2002), 905.
- [6] CHENG L., XU Y., ZHANG L., LUAN X., Carbon 40 (2002), 2229.
- [7] MARTIN H.-P., ECKE R., MULLER E., J. Eur. Ceram. Soc. 18 (1998), 1737.
- [8] CZOSNEK C., RATUSZEK W., JANIK J.F., OLEJNICZAK Z., Fuel Proc. Techn. 79 (2002), 199.
- [9] CZOSNEK C., WOLSZCZAK J., DRYGAŚ M., GÓRA M., JANIK J.F., J. Phys. Chem. Solids 65 (2004), 647.
- [10] YAJIMA S., Am. Ceram. Soc. Bull. 62 (1983), 893.
- [11] YAJIMA S., HASEGAWA Y., HAYASHI J., IIMURA M., J. Mater. Sci. 13 (1978), 2569.
- [12] PARMENTIER J., SORARÙ G.D., BABONNEAU F., J. Eur. Ceram. Soc. 21 (2001), 817.
- [13] SORARÙ G.D., SUTTOR D., J. Sol-Gel Sci. Technol. 14 (1999), 69.
- [14] BREQUEL H., PARMENTIER J., SORARÙ G.D., SCHIFFINI L., ENZO S., Nanostruct. Mater., 11 (1999), 721.
- [15] GREGORI G., KLEEBE H.-J., READEY D.W., SORARÙ G.D., J. Am. Ceram. Soc., 89 (2006), 1699.
- [16] HURWITZ F.I., HEIMANN P., FARMER S.C., J. Mater. Sci. 28 (1993), 6622.

Received 28 April 2007  
Revised 16 February 2008



# Synthesis of ceria-based nanopowders suitable for manufacturing solid oxide electrolytes

M. DUDEK\*, M. MRÓZ, Ł. ZYCH, E. DROŹDŹ-CIEŚLA

AGH-University of Science and Technology,  
Faculty of Materials Science and Ceramics, 30-059 Cracow, Poland

Co-precipitation method and hydrothermal synthesis were used to fabricate nanopowders of pure  $\text{CeO}_2$  and singly or co-doped ceria materials in the  $\text{CeO}_2\text{-Sm}_2\text{O}_3\text{-Y}_2\text{O}_3$  or  $\text{CeO}_2\text{-Gd}_2\text{O}_3\text{-Sm}_2\text{O}_3$  systems. All sintered powders and samples were found to be pure  $\text{CeO}_2$  and ceria-based solid solution of fluorite-type structure. The surface areas of  $\text{CeO}_2$ -based nanopowders were measured by the one-point BET method. The morphologies of powders were observed by means of transmission electron microscopy. Particle sizes of ceria powders synthesised by the hydrothermal method ranged from 9 to 15 nm, the particle sizes of powders calcined at 800 °C ranged from 13 to 26 nm. The TEM observations indicated that all  $\text{CeO}_2$ -based powders consisted of isometric in shape and agglomerated particles. Scanning electron microscope was used to observe the microstructure of the sintered samples. Electrical conductivity was studied by the a.c. impedance spectroscopy in the temperature range 200–700 °C. The oxygen transference number was determined from EMF measurements of oxide galvanic cells. It was found that co-doped ceria materials such as  $\text{Ce}_{0.8}\text{Sm}_{0.1}\text{Y}_{0.1}\text{O}_2$  or  $\text{Ce}_{0.85}\text{Gd}_{0.1}\text{Sm}_{0.05}\text{O}_2$  seem to be more suitable solid electrolytes than singly-doped ceria  $\text{Ce}_{1-x}\text{M}_x\text{O}_2$  (M – Sm, Gd, Y,  $x = 0.15$  or  $0.20$ ) for electrochemical devices working in the temperature range 600–700 °C.

Key words: *nanopowder; ceria-based electrolyte; solid oxide fuel cell; electrochemical gas sensor*

## 1. Introduction

Until now, yttria-stabilized zirconia (8YSZ) is the most often used solid oxide electrolyte in electrochemical devices such as solid oxide fuel cells (SOFC), gas sensors, oxygen pumps and probes for controlling metal processing. This is due to its low electronic and high ionic conductivities, chemical stability under reducing and oxidising atmospheres at high temperatures (800–1000 °C), moderate mechanical properties and relatively low production costs [1–4]. Lowering of the operation temperature of a SOFC down to around 700–600 °C would result in an increase in the cell stability

---

\*Corresponding author, e-mail: potoczek@uci.agh.edu.pl

(lower degradation of components) and allow one to use cheaper materials such as ferritic stainless steels for interconnectors [5, 6]. Ceria based solid solutions  $\text{Ce}_{1-x}\text{M}_x\text{O}_2$  (Me – Sm, Gd, Y) and  $x = 0.15\text{--}0.20$  have been regarded as promising oxide electrolytes for SOFCs and electrochemical sensors for exhaust gases due to higher ionic conductivities than that of fully stabilized zirconia (8YSZ) in the temperature range 600–800 °C [7, 8]. The main drawback of ceria-based electrolytes, complicating their commercial application, is an increased electronic conduction under low oxygen partial pressure accompanied by reduction of  $\text{Ce}^{4+}$  to  $\text{Ce}^{3+}$  [9, 10]. It has been reported that reduction of ceria can be neglected at lower temperatures around 600–700 °C. However, such low temperatures are not suitable for singly doped ceria as electrolyte in SOFC or other devices, due to high electrical resistance [11]. Structural modification of ceria-based solid solutions by co-doping is one of possible ways to improve their electrical conductivity at this temperature range. Some ternary system involving  $\text{CeO}_2\text{--Sm}_2\text{O}_3$  solid solutions have been studied from viewpoint of structure and electrical properties, the third component being: CaO [12, 13],  $\text{Y}_2\text{O}_3$  [14],  $\text{Pr}_6\text{O}_{11}$  [15]. Ceria-based materials with the formula depending on chemical composition and phase composition have generally improved electrical conductivity, although in some cases deterioration of the ionic conductivity and increase of electronic conduction is observed. The microstructures of sintered samples, affected by chemical composition, properties of powders and sintering conditions, strongly affect the electrolyte performance [16].

The paper focuses on the preparation of sinterable nanopowders of singly and co-doped ceria materials in the  $\text{CeO}_2\text{--Sm}_2\text{O}_3\text{--Y}_2\text{O}_3$  or  $\text{CeO}_2\text{--Gd}_2\text{O}_3\text{--Sm}_2\text{O}_3$  systems as well as on investigation of the properties crucial to application of ceria-based materials as oxide electrolytes in electrochemical devices. The practical aim of this research was to obtain a co-doped ceria based material which could be applied as a component of electrochemical devices working at the temperature range 600–700 °C.

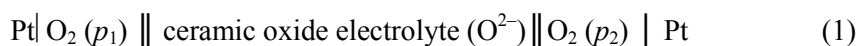
## 2. Experimental

The starting materials used in this study were  $\text{Ce}(\text{NO}_3)_3 \times 6\text{H}_2\text{O}$ ,  $\text{Sm}(\text{NO}_3)_3 \times 6\text{H}_2\text{O}$ ,  $\text{Gd}(\text{NO}_3)_3 \times 6\text{H}_2\text{O}$  and  $\text{Y}(\text{NO}_3)_3 \times 6\text{H}_2\text{O}$  (all 99.99% purity, supplied by Aldrich). Aqueous  $\text{NH}_3$  solution was used as a precipitating agent. The reagents were mixed in distilled water in order to prepare pure  $\text{CeO}_2$ , singly doped ceria –  $\text{Ce}_{1-x}\text{M}_x\text{O}_2$  (M = Sm, Y, Gd),  $0.10 < x < 0.25$  or co-doped ceria-based materials with the formulas  $\text{Ce}_{0.8}\text{Y}_{0.2-x}\text{Sm}_x\text{O}_2$  or  $\text{Ce}_{0.85}\text{Gd}_{0.15-x}\text{Sm}_x\text{O}_2$ ,  $x = 0.02, 0.05, 0.1, 0.15$ . A solution containing respective cations was slowly added to continuously stirred  $\text{NH}_3$  solution and final pH was adjusted to 10. The co-precipitated products were washed with distilled water. For all compositions, the gels obtained were divided into two parts and used to synthesise ceria-based materials in two different routes. In the co-precipitation-calcination route, (method A), the dried gels were calcined at 800 °C for 1 h and then rotary-vibratory milled with zirconia grinding media in ethyl alcohol. In

the hydrothermal crystallization route (method B), the gels were hydrothermally treated at 240 °C for 6 h in water solution under autogeneous water pressure, washed with distilled water and dried at room temperature.

Studies of thermal decomposition processes in the range of 25–1000 °C, each step 10 °C /min in air, were conducted using the thermogravimetric analysis (TG), differential thermal analysis (DTA) and evolved gas analysis (EGA) of volatile products with a quadrupole mass spectrometer. The phase compositions of powders and sintered samples were identified using the XRD analysis. X-ray line broadening enabled determination of the sizes of crystallites. Specific surface areas of powders were measured by the one-point BET method. The samples were outgassed in vacuum. The results were used to calculate equivalent particle sizes,  $d_{\text{BET}}$ . The morphologies of powders were observed under transmission electron microscopy. Densification behaviour of pellets was monitored in air via dilatometry using a constant heating rate 5°/min at the 25–1200 °C temperature range. Scanning electron microscopy observations of the polished and thermally etched surfaces provided quantitative characteristic of the sample microstructures. Apparent density of the sintered bodies was measured by the Archimedeian method. To verify stability of materials prepared under reduction conditions, the CeO<sub>2</sub>-based samples were isothermally heated at 800 °C for 24 h in (5 vol. % H<sub>2</sub> in Ar) gas mixture. The fracture toughness  $K_{Ic}$  of CeO<sub>2</sub>-based samples of polished surfaces was determined by Vickers' indentation. A loading force of 9.81 N imposed for 10 s was applied. The Palmqvist crack model was used [17] to calculate  $K_{Ic}$ .

Electrical conductivities were measured by a.c. impedance spectroscopy in the temperature range 200–800 °C. To estimate the oxygen ion transference number of the ceria-based samples, the EMF of the oxide galvanic cell (1) at the temperature range 500–750 °C was measured:



The electromotive force (EMF) of the cell (1) was measured as a function of temperature (550–700 °C) and oxygen partial pressure (from 10<sup>-6</sup> atm to 1 atm). The ionic transference number ( $t_{\text{ion}}$ ) in the sample was calculated based on the electromotive force (EMF) values ( $E_m$ ) measured for the cell (1) and on the EMF values ( $E_i$ ) obtained for the cell (1) with a pure oxygen ion conductor. The procedure was similar to that described in Ref. [12].

### 3. Results and discussion

Typical DTA and TG curves recorded for samaria-doped ceria Ce<sub>0.85</sub>Sm<sub>0.15</sub>O<sub>2</sub> (15SDC) precursor, obtained by the method A are shown in Fig 1. First feature seen on the DTA curve at ~100 °C is an endothermic peak connected with dehydration and a significant loss in weight. Following the dehydration, the continuous heating causes decomposition of NH<sub>4</sub>NO<sub>3</sub> and other nitrate precursors leading also to a large weight

loss at temperature range 100–500 °C. An exothermic peak at ~ 270 °C probably originated from crystallisation of ceria solid solution. The observations were confirmed by the EGA measurements. They also revealed that both decomposition of nitrates and crystallisation of ceria solid solution proceeded with formation of NO, NO<sub>2</sub>, N<sub>2</sub>O, O<sub>2</sub> and H<sub>2</sub>O. Above 500 °C, the sample weight remained unchanged, indicating that a stable crystalline CeO<sub>2</sub> structure formed.

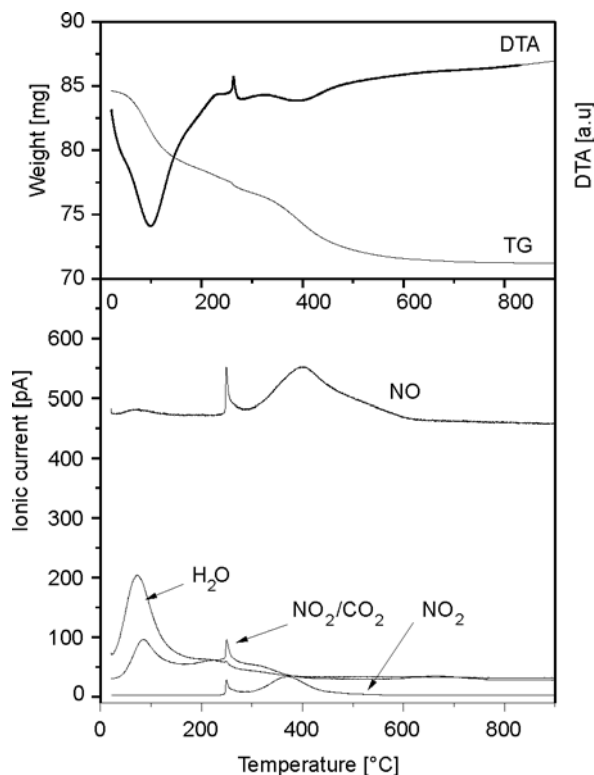


Fig. 1. DTA, TG and EGA curves of the Ce<sub>0.85</sub>Sm<sub>0.15</sub>O<sub>2</sub> (15SDC) dried precursor obtained by the co-precipitation-calcination method

Figure 2 shows XRD patterns of the Ce<sub>0.85</sub>Sm<sub>0.15</sub>O<sub>2</sub> (15SDC) dried (a) precursor and its calcination product at 290 °C (b), 500 °C (c) and 800 °C (d). The XRD pattern of Ce<sub>0.85</sub>Sm<sub>0.15</sub>O<sub>2</sub> sintered sample (e) is also given. The XRD pattern recorded for 15SDC dry sample reflects CeO<sub>2</sub> structure but the peaks are wide and their intensities low. It appears from Fig. 2 that with increasing temperature the half-widths of peaks become lower and their intensities stronger. Fully crystalline patterns of Ce<sub>0.85</sub>Sm<sub>0.15</sub>O<sub>2</sub> solid solutions were observed at temperatures above 600 °C. Similar DTA, TG curves and XRD patterns were recorded for other chemical compositions of singly or co-doped ceria samples.

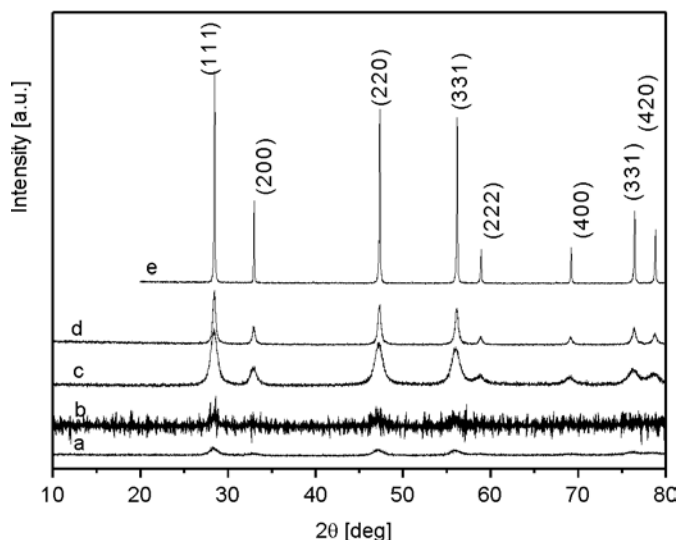


Fig. 2. Evolution of the XRD diffraction patterns recorded for the 15SDC dried precursor (a) and after calcination at 290 °C (b), 700 °C (c) and for sample sintered at 1500 °C for 2 h (d)

Only  $\text{CeO}_2$  phase was identified by the XRD analysis in all powders obtained by the methods A and B and also in the sintered samples. No phases other than cubic  $\text{CeO}_2$  were found in the XRD diffraction patterns of the samples exposed in an ( $\text{H}_2$ –Ar) gas mixture. Basic characteristics of the starting powders obtained by both methods are collected in Table 1. The data show that crystallite sizes of hydrothermally synthesised  $\text{CeO}_2$ -based powders ranged from 7 nm to 16 nm. The  $\text{CeO}_2$ -based powders with the same chemical composition but calcined at 800 °C, consisted of larger particles (17–29 nm in size).

Table 1. Basic data on pure  $\text{CeO}_2$ , and co-doped ceria based powders obtained by co-precipitation calcination (A) method and hydrothermal (B) synthesis

Parameter	$\text{CeO}_2$	$\text{Ce}_{0.8}\text{Sm}_{0.2}\text{O}_2$ (20SDC)	$\text{Ce}_{0.8}\text{Y}_{0.1}\text{Sm}_{0.1}\text{O}_2$ (10S10YDC)	$\text{Ce}_{0.85}\text{Gd}_{0.15}\text{O}_2$ (15GDC)	$\text{Ce}_{0.85}\text{Gd}_{0.1}\text{Sm}_{0.05}\text{O}_2$ (10G5SDC)
Crystallite size, $d_{(hkl)}$ [nm]	17.4 (A)	24.8 (A)	23.2 (A)	24.8 (A)	25.7 (A)
	6.2 (B)	14.6 (B)	14.1 (B)	12.8 (B)	14.6 (B)
Particle size, $d_{(\text{BET})}$ [nm]	29.4 (A)	36.5 (A)	34.4 (A)	32.1 (A)	40.2 (A)
	11.2 (B)	21.4 (B)	24.4 (B)	19.4 (B)	22.2 (B)

The consistency of particle sizes determined by the X-ray analysis and BET surface measurements suggest that the powders are mostly composed of isometric and rather weakly agglomerated particles. A small increase of particle size (Fig. 3) was observed with samarium  $\text{Ce}_{1-x}\text{M}_x\text{O}_2$ ,  $\text{Ce}_{0.8}\text{Y}_{0.2-x}\text{Sm}_x\text{O}_2$  or  $\text{Ce}_{0.85}\text{Gd}_{0.15-x}\text{Sm}_x\text{O}_2$  solid solutions compared to pure  $\text{CeO}_2$ . The TEM observations of 15SDC powder calcined at 800 °C for 1h (Fig. 4a) or crystallized in water solution under autogeneous water

pressure (240 °C, 6 h) (Fig. 4b) revealed presence of agglomerated particles of 15SDC powders and confirmed conclusions derived from X-ray and BET examinations.

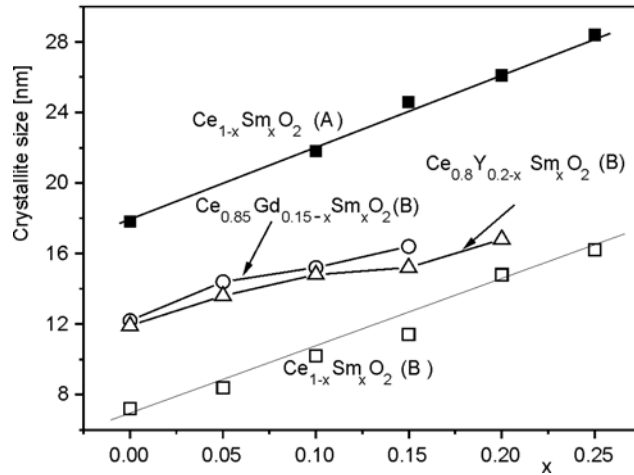


Fig. 3. Dependence of crystallite size on samarium content  $x$  in singly doped ceria  $Ce_{1-x}Sm_xO_2$  and co-doped ceria  $Ce_{0.8}Y_{0.2-x}Sm_xO_2$  or  $Ce_{0.85}Gd_{0.15-x}Sm_xO_2$  powders obtained by the co-precipitation calcination method (A) and hydrothermal synthesis (B)

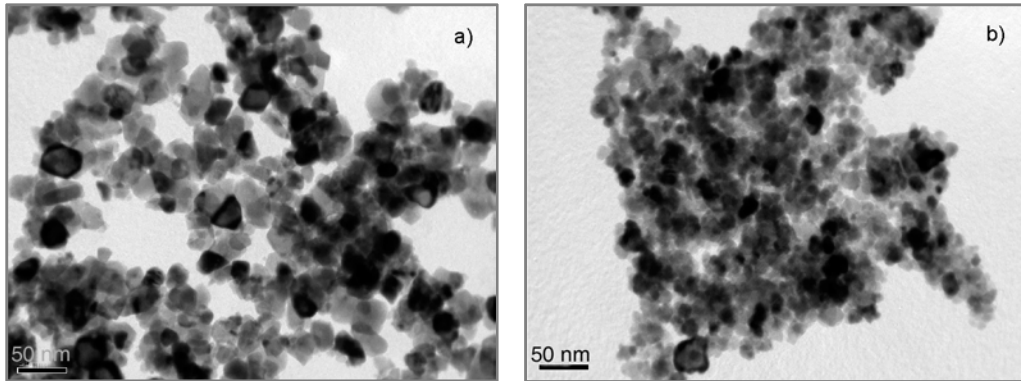


Fig. 4. TEM micrographs of 15SDC powders obtained from: a) co-precipitation calcination method, b) hydrothermal treatment of co-precipitated gel

Further observations of all powders allow us to state that there are no distinct differences in their morphologies, irrespective of the rate of their fabrication. Figure 5 shows the densification of selected pellets obtained from the investigated powders. For all pellets the shrinkage began at 200 °C and on further heating an intensive densification started at ca. 450–500 °C or 800–1000 °C for samples obtained from powders synthesized by hydrothermal (B) or co-precipitation calcination (A) method, respectively.

Hydrothermally synthesised ceria-based materials sintered at 1300–1350 °C for 2 h exhibited relative densities higher than 98%. On the other hand,  $CeO_2$ -based solid



solutions with formula  $Ce_{1-x}Sm_xO_2$ , Me – Sm, Gd, Y,  $0 < x < 0.25$  or co-doped ceria materials  $Ce_{0.8}Y_{0.2-x}Sm_xO_2$ , had to be sintered at 1500–1550 °C for 2 h to obtain more than 96% of theoretical densities. Figure 6 shows the microstructure of  $Ce_{0.8}Sm_{0.1}Y_{0.1}O_2$  samples sintered at 1500 °C or 1350 °C for 2 h. Both samples were characterized by isometric grains of 0.3–0.6 μm (method B) or 3–5 μm (method A) in size. No additional cracks and pores were observed for co-doped ceria samples after additional hydrogen treatments. The obtained results indicate that the investigated methods are suitable for preparation of fine sinterable powders for manufacturing gas tight samples which could be applied as solid electrolytes in electrochemical devices.

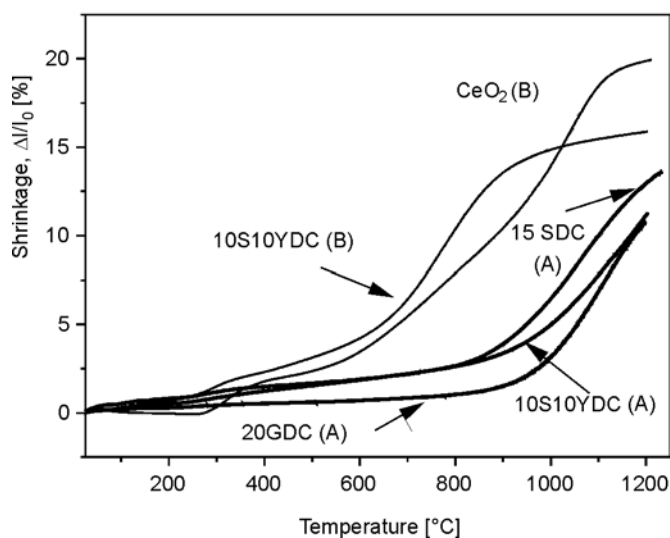


Fig. 5. Dilatometric curves recorded for selected  $CeO_2$ -based pellets obtained from powders prepared by co-precipitation-calcination method (A) and hydrothermal synthesis (B)

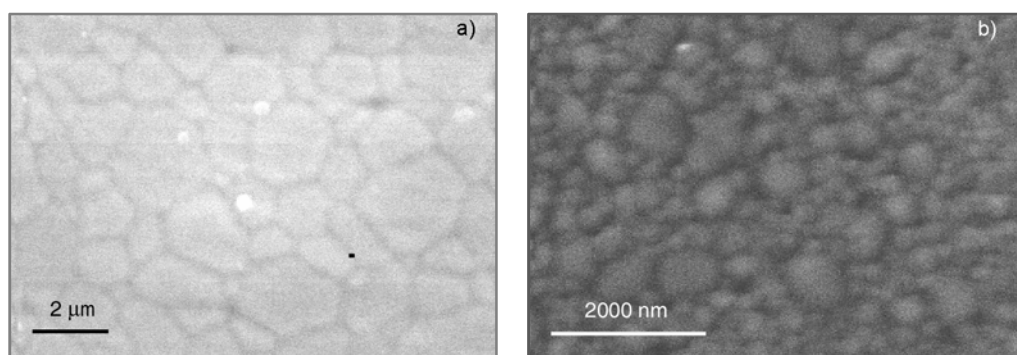


Fig. 6. Microstructures of  $Ce_{0.8}Sm_{0.1}Y_{0.1}O_2$  ceramics obtained from powders synthesised by the method A, sintered at: 1500 °C for 2 h (a), and by the method B, sintered at 1350 °C for 2 h (b)

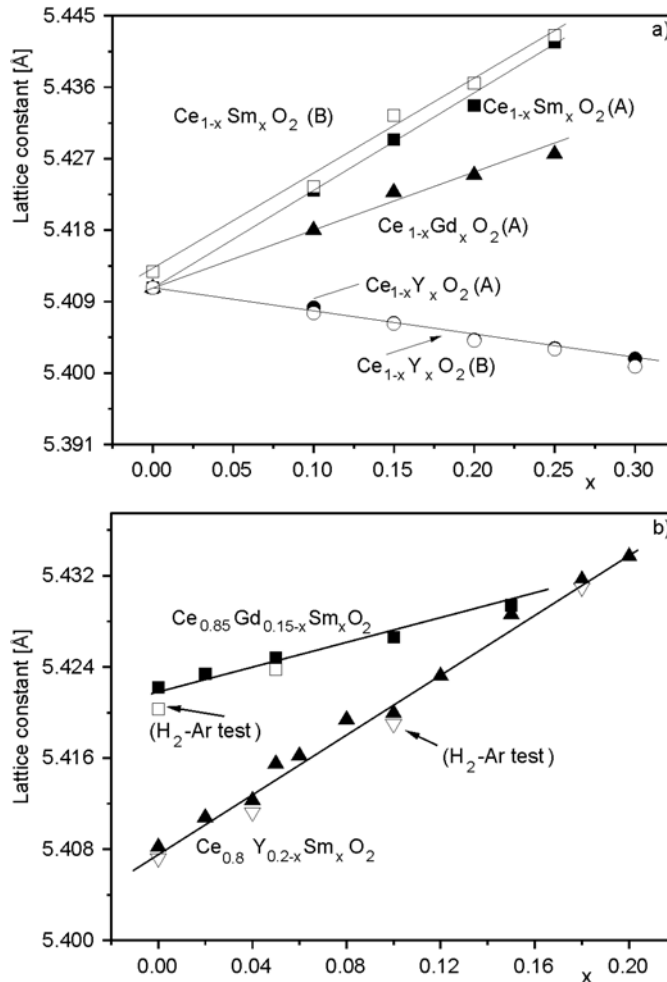


Fig. 7. The lattice constant of singly doped ceria  $Ce_{1-x}Me_xO_2$  ( $Me = Sm, Gd, Y$ ) (a) and  $Ce_{0.8}Y_{0.2-x}Sm_xO_2$  or  $Ce_{0.85}Gd_{0.15-x}Sm_xO_2$  (b) obtained from powders synthesised by co-precipitation calcination method (A) and hydrothermal synthesis (B); samples sintered at 1500 °C or 1350 °C for 2 h

The lattice parameters of  $Ce_{1-x}M_xO_2$ ,  $M = Sm, Gd$ ,  $0 < x < 0.25$  and co-doped ceria-based materials  $Ce_{0.85}Gd_{0.85-x}Sm_xO_2$ , or  $Ce_{0.8}Y_{0.2-x}Sm_xO_2$  (Fig. 7) linearly increased with  $x$  but the slope was lower for ceria samples doubly doped with gadolinium and samarium than for those doped with yttrium and samarium. The decrease of the lattice parameter is observed for ceria–yttria solid solution. These observations are in good agreement with effective ionic radius considerations [18]. An additional heat treatment in 10 vol. % H<sub>2</sub>–Ar gas mixtures caused a small decrease of cell parameters of all investigated samples.

Good mechanical properties of CeO<sub>2</sub>-based ceramics are also necessary for applications as solid electrolytes in SOFCs, sensors for exhaust gases in automotive indus-

try. The fracture toughness  $K_{Ic}$  (Table 2) measurements for selected samples revealed a small increase in the fracture toughness with increasing samarium, gadolinium or yttrium content in  $Ce_{1-x}M_xO_2$  compared to pure  $CeO_2$ . On the other hand, in the case of co-doped ceria materials with the formula  $Ce_{0.8}Sm_{0.2-x}Y_xO_2$  or  $Ce_{0.85}Gd_{0.15-x}Sm_xO_2$ ,  $0 < x < 0.15$ , the fracture toughness remains unchanged within an experimental error. The values of  $K_{Ic}$  for 8YSZ samples are also presented in Table 2. The results given in the table indicate that ceria based materials have slightly worse mechanical properties than the 8YSZ electrolyte.

Table 2. Fracture toughness  $K_{Ic}$  determined for  $CeO_2$ -based materials

Material	$D$ , average grain size [ $\mu\text{m}$ ]	$K_{Ic}$ $\text{MPa}\times\text{m}^{0.5}$
$CeO_2$	11.51 (A)	$1.3\pm 0.2$
$Ce_{0.85}Sm_{0.15}O_2$	3.89 (A)	$2.1\pm 0.2$
	0.58 (B)	$2.4\pm 0.1$
$Ce_{0.8}Sm_{0.2}O_2$	3.41 (A)	$2.2\pm 0.2$
	0.48 (B)	$2.3\pm 0.1$
$Ce_{0.85}Gd_{0.15}O_2$	3.16 (A)	$1.9\pm 0.1$
	0.54 (B)	$2.1\pm 0.2$
$Ce_{0.8}Y_{0.2}O_2$	2.80 (A)	$1.7\pm 0.3$
	0.62 (B)	$1.9\pm 0.2$
$Ce_{0.8}Sm_{0.1}Y_{0.1}O_2$	2.68 (A)	$2.2\pm 0.3$
	0.67 (B)	$2.4\pm 0.2$
$Ce_{0.85}Gd_{0.1}Sm_{0.05}O_2$	3.12 (A)	$2.1\pm 0.3$
	0.56 (B)	$1.9\pm 0.2$
8YSZ	2.68 (A)	$2.8\pm 0.2$
	0.55 (B)	$3.2\pm 0.2$

Table 3. Electrical conductivities  $\sigma$  at 600 °C of the  $CeO_2$ -based samples obtained from powders prepared the co-precipitation calcination (A) or hydrothermal method (B)

Composition	$\sigma$ [S/cm]		$E_a$ [eV]	
	Bulk	Grain boundary	Bulk	Grain boundary
$CeO_2$	$6.16\times 10^{-5}$	$1.21\times 10^{-6}$	1.51	1.81
$Ce_{0.85}Sm_{0.15}O_2$	$5.72\times 10^{-3}$ (A)	$4.23\times 10^{-3}$ (A)	0.84	1.01
	$1.56\times 10^{-2}$ (B)	$1.34\times 10^{-2}$ (B)	0.82	0.89
$Ce_{0.8}Sm_{0.2}O_2$	$6.61\times 10^{-3}$ (A)	$5.18\times 10^{-3}$ (A)	0.87	0.98
	$1.11\times 10^{-2}$ (B)	$1.89\times 10^{-2}$ (B)	0.80	0.88
$Ce_{0.8}Y_{0.2}O_2$	$4.68\times 10^{-3}$ (A)	$1.18\times 10^{-3}$ (A)	0.98	1.06
	$9.47\times 10^{-3}$ (B)	$5.53\times 10^{-3}$ (B)	0.93	0.97
$Ce_{0.8}Sm_{0.1}Y_{0.1}O_2$	$8.16\times 10^{-3}$ (A)	$7.62\times 10^{-3}$ (A)	0.82	0.93
	$2.06\times 10^{-2}$ (B)	$2.56\times 10^{-2}$ (B)	0.78	0.84
$Ce_{0.85}Gd_{0.15}O_2$	$6.87\times 10^{-3}$ (A)	$5.17\times 10^{-3}$ (A)	0.93	1.04
	$1.16\times 10^{-2}$ (B)	$1.14\times 10^{-2}$ (B)	0.89	0.96
$Ce_{0.85}Gd_{0.1}Sm_{0.05}O_2$	$8.15\times 10^{-3}$ (A)	$7.86\times 10^{-3}$ (A)	0.92	1.01
	$2.67\times 10^{-2}$ (B)	$1.62\times 10^{-2}$ (B)	0.85	0.92

Impedance spectroscopy measurements enabled one to determine the bulk ( $\sigma_b$ ) and grain boundary ( $\sigma_{gb}$ ) conductivities of CeO<sub>2</sub>-based samples. Respective values of the conductivities at 600 °C are given in Table 3. The values of activation energy calculated for the temperature range 200–800 °C are also given. It can be seen from Table 3 that the bulk and grain boundary conductivities of Ce<sub>1-x</sub>M<sub>x</sub>O<sub>2</sub>, M – Sm, Y, Gd increased up to  $x = (0.15-0.20)$  and decreased for higher substitution levels. The activation energy shows an opposite trend. As previously reported [19], ionic conductivities are significantly enhanced in Ce<sub>1-x</sub>Sm<sub>x</sub>O<sub>2</sub> solid solutions by increasing the concentration of oxygen vacancies ( $V_O^{\bullet\bullet}$ ), ascribed to defect associations of the type  $Sm'_{Ce}V_O^{\bullet\bullet}$  at higher concentrations of  $x$ . The introduction of yttria into ceria–samaria solid solutions caused a small increase of ionic conductivity. The total electrical conductivity (calculated as a sum of grain boundary and bulk conductivities) reached a maximum value of  $1.60 \times 10^{-2}$  or  $4.58 \times 10^{-2}$  (S/cm) at 600 °C for Ce<sub>0.8</sub>Sm<sub>0.1</sub>Y<sub>0.1</sub>O<sub>2</sub> sintered samples obtained by the methods A or B, respectively. A partial substitution of gadolonia by samaria in Ce<sub>0.85</sub>Gd<sub>0.15-x</sub>Sm<sub>x</sub>O<sub>2</sub> up to  $x = 0.05$  also improves the total electrical conductivity compared to only ceria-doped gadolonia Ce<sub>0.85</sub>Gd<sub>0.15</sub>O<sub>2</sub>.

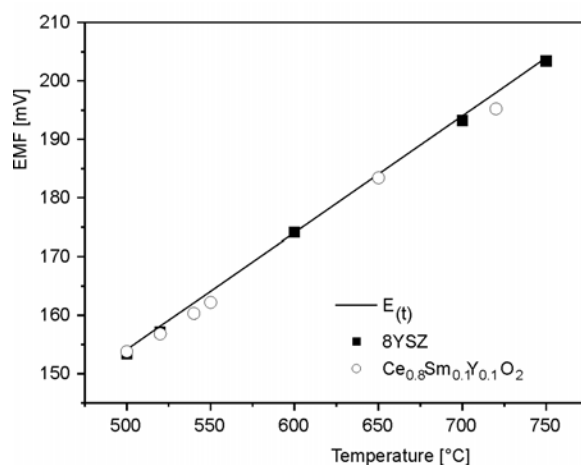


Fig. 8. Temperature dependence of the EMF of cell (1); working electrode – Pt | (Ar–O<sub>2</sub>)  $p_2 = 2 \times 10^{-5}$  atm, reference electrode – Pt | air

The EMF values of the cell (1) measured in the temperature range 500–750 °C (Fig. 8) were compared with the EMF ( $E_t$ ) values obtained for the cell containing 8YSZ. The calculated values of the transference oxygen numbers ( $t_{ion}$ ) for Ce<sub>0.8</sub>Me<sub>0.2</sub>O<sub>2</sub> or Ce<sub>0.85</sub>Me<sub>0.15</sub>O<sub>2</sub>, Me – Sm, Gd, Y, and for co-doped ceria based samples Ce<sub>0.8</sub>Y<sub>0.1</sub>Sm<sub>0.1</sub>O<sub>2</sub> or Ce<sub>0.85</sub>Gd<sub>0.1</sub>Sm<sub>0.05</sub>O<sub>2</sub> were close to 1, which indicates practically pure oxygen ionic conductivity in the investigated samples. A comparison of the changes of electrical conductivities of ceria-based solid solutions indicates that the reason of the conductivity enhancement with respect to singly-doped ceria is an increase in concentration of oxygen vacancies.

## 4. Conclusions

Singly-doped ceria or co-doped ceria materials  $\text{CeO}_2\text{-Sm}_2\text{O}_3\text{-Y}_2\text{O}_3$  or  $\text{CeO}_2\text{-Gd}_2\text{O}_3\text{-Sm}_2\text{O}_3$  were successfully prepared both from powders obtained by the co-precipitation calcination (A) method and hydrothermal (B) synthesis. The application of ceria-based powders prepared by the hydrothermal synthesis allowed one to reduce the sintering temperature of ceria based electrolytes from 1500 °C to ca. 1300–1350 °C. Higher sintering temperatures lead to high manufacturing costs for SOFC systems because ceria based electrolytes and other components such as cathode and anode cannot be cofired at higher temperatures (e.g. higher than 1300 °C). Contrary to mechanical properties, the electrical conductivity of ceria-based electrolytes can be improved by controlling the grain sizes. The obtained values of electrical conductivities and activation energies for  $\text{Ce}_{0.8}\text{Sm}_{0.1}\text{Y}_{0.1}\text{O}_2$  or  $\text{Ce}_{0.85}\text{Sm}_{0.1}\text{Gd}_{0.05}\text{O}_2$  with average grain size of 0.5–0.7  $\mu\text{m}$  show that the prepared materials seem to be promising materials for SOFCs and other electrochemical devices operating at 600–700 °C.

### Acknowledgement

This work was carried out under contracts no 3T08 D01926 (2004–2007) with the Polish Scientific Research Committee.

### References

- [1] FERGUS J.W., *J. Power Sources*, 162 (2006), 30.
- [2] MINH N.Q., TAKAHASHI T., *Science and Technology of Ceramic Fuel Cells*, Elsevier, Amsterdam 1995.
- [3] GIBBSON R.W., KUMAR R.V., FRAY D.J., *Solid State Ionics*, 121(1999), 43.
- [4] BESRA L., COMPSON CH., LIU M., *J. Am. Ceram. Soc.*, 89 (2006), 3003.
- [5] TIETZ F., BUCHKREMER H., STÖVER., *Solid State Ionics*, 152–153 (2002), 373.
- [6] BRYLEWSKI T., NANKO M., MARUYAMA T., PRZYBYLSKI K., *Solid State Ionics*, 143 (2001), 131.
- [7] INABA H., TAGAWA H., *Solid State Ionics*, 83 (1996), 1.
- [8] KHARTON V., FIGUEIREDO F., NAVARRO L., NAUMOVICH E., KOVALEVSKY A., YAREMCHENKO A., VISKUP A., CARNEIRO A., MARGUES M., FRADE J., *J. Mater. Sci.*, 36 (2001), 1105.
- [9] XIONG Y., YAMAJI K., HORITA T., SAKAI N., YOKOKAWA H., *J. Electrochem. Soc.*, 149 (2002), 450.
- [10] SAMESHIMA S., HIRATA Y., EHIRA Y., *J. All. Comp.*, 408–412(2006), 628.
- [11] HONG J., MEHTA K., *J. Electrochem. Soc.*, 145 (1998), 638.
- [12] MORI T., IKEGAMI T., YAMAMURA H., *J. Electrochem. Soc.*, 146 (1999), 4380.
- [13] DUDEK M., ZIEWIEC K., *Adv. Mater. Sci.*, 6 (2006), 53.
- [14] SHA X., LÜ Z., HUANG X., MIAO Z., JIA L., XIN X., SU W., *J. All. Comp.*, 424 (2006), 315.
- [15] JI Y., LIU J., HE T., WANG J., SU W., *J. All. Comp.*, 389 (2005), 317.
- [16] DRENNAN J., AUCHTERLONIE G., *Solid State Ionics*, 134 (2000), 75.
- [17] NIIHARA K., *J. Mater. Sci. Lett.*, 2 (1983), 221.
- [18] SHANNON R., PREWITT T., *Acta Cryst. B*, 25 (1969), 925.
- [19] HUNG W., SHUK P., GREENBLATT M., *Solid State Ionics*, 113–115 (1998), 305.

*Received 28 April 2007*  
*Revised 16 February 2008*



# Nanometric $Y_2O_3$ – $TiO_2$ – $ZrO_2$ solid solution powders and their utilization in the synthesis of composite powders with $TiB_2$ and $TiC$ inclusions

N. MOSKAŁA<sup>1\*</sup>, J. MORGIEL<sup>2</sup>, W. PYDA<sup>1</sup>

<sup>1</sup>AGH University of Science and Technology, Faculty of Materials Science and Ceramics,  
Department of Advanced Ceramics, al. Mickiewicza 30, 30-059 Cracow, Poland

<sup>2</sup>Institute of Metallurgy and Materials Science, Polish Academy of Sciences,  
ul. Reymonta 25, 30-059 Cracow, Poland

Carbothermal reduction of  $TiO_2$  dissolved in  $ZrO_2$  and  $B_2O_3$  is a method of fabrication of fine composite powders in the  $ZrO_2$ – $TiB_2$ – $TiC$  system. The method requires nanopowders of the zirconia–titania solid solution with a high  $TiO_2$  concentration. A technique of fabrication of zirconia nanopowders doped with 18 mol % titania and 2–3 mol % yttria is described in the paper. The nanopowders were obtained in a co-precipitation process followed by hydrothermal crystallization at 240 °C. The phase composition (XRD) and EDS measurements proved formation of a solid solution as the only phase. DTA and TG analyses showed that there are no amorphous phases. A nanometric morphology was proved by the TEM observations and the specific surface area measurements (BET). Dynamic light scattering was used to measure the agglomerate size distribution. A usefulness of the zirconia–titania–yttria nanopowders to the *in-situ* syntheses of composite powders in the  $ZrO_2$ – $TiB_2$ – $TiC$  system was described. The composite powders were fabricated in the reaction of titanium oxide dissolved in the  $TiO_2$ – $Y_2O_3$ – $ZrO_2$  solid solution with boron oxide and carbon. A mixture of zirconia solid solution nanopowder containing 2–3 mol % of  $Y_2O_3$ , 18 mol % of  $TiO_2$  and 79–80 mol % of  $ZrO_2$ , boric acid and 20 wt. % alcohol solution of phenol-formaldehyde resin was used for the synthesis. The phase compositions of the composite powders were characterized by X-ray diffractometry.

## 1. Introduction

Titanium oxide incorporated in the zirconium oxide solid solution can be used in an *in-situ* process leading to obtain fine inclusions of hard phases such as titanium carbide [1–4] and titanium boride [5] in zirconia based powders. The method is based on the carbothermal reduction of  $TiO_2$  and  $B_2O_3$ . The so far presented technologies

---

\*Corresponding author, e-mail: nmos1@agh.edu.pl

[1–5] involved  $\text{Y}_2\text{O}_3\text{--TiO}_2\text{--ZrO}_2$  nanopowders crystallized in the solid state at temperatures around 650 °C.  $\text{Y}_2\text{O}_3$  is introduced to the system to stabilize tetragonal  $\text{ZrO}_2$  in sintered polycrystals. Such crystallization conditions do not enable one to maximize the surface area of the powder and an accessibility of  $\text{TiO}_2$  for carbides and borides fabrication is not optimum. From that point of view, a hydrothermal process seems to be more suitable. It involves co-precipitation and hydrothermal crystallization of gels containing zirconium, titanium and yttrium cations. Because of low crystallization temperature (ca. 250 °C), such a method enables production of nanopowders with a large surface area. Additionally, water environment favours a decreased agglomerate strength. This is very useful for homogeneous distribution of the boron and carbide precursors within the  $\text{Y}_2\text{O}_3\text{--TiO}_2\text{--ZrO}_2$  solid solution nanopowders and thus simplifies preparation of mixtures for the synthesis of carbides and borides.

The amount of  $\text{TiO}_2$  dissolved in a zirconia solid solution limits the content of *in-situ* synthesized hard phases in an obvious way. Therefore, it is required to elucidate if the hydrothermal synthesis is an effective method of fabrication of  $\text{Y}_2\text{O}_3\text{--TiO}_2\text{--ZrO}_2$  solid solution nanopowders with a high titanium oxide concentration.

## 2. Experimental

A co-precipitation method followed by hydrothermal crystallization was used to prepare the  $\text{Y}_2\text{O}_3\text{--TiO}_2\text{--ZrO}_2$  solid solution nanopowders, containing from 2 to 3 mol % yttria, 18 mol % titania and from 79 to 80 mol % zirconia. Homogeneous yttria–titania–zirconia hydrogels were co-precipitated from aqueous solutions of appropriate chlorides with  $\text{NH}_3\cdot\text{aq}$  at  $\text{pH} \geq 9$ . The following chemical reagents were used:  $\text{ZrOCl}_2\cdot 8\text{H}_2\text{O}$  – zirconia content > 99.7% (Si – 0.03%, Fe – 0.02%, Al – 0.015%), Beijing Chemicals Import and Export Corporation, China;  $\text{TiCl}_4$  – purity > 98 %, Fluka, Switzerland;  $\text{Y}_2\text{O}_3$  – purity 99.99 %,  $\text{NH}_3\cdot\text{aq}$  – analytically pure, Polish Chemical Works, Poland. The hydrogels were hydrothermally treated for 4 h at 240 °C under the pressure of saturated water vapour (ca. 3.8 MPa) at pH between 7.5 and 7.6. After the crystallization, the powders were dried at 65 °C.

The composite powders containing TiC and  $\text{TiB}_2$  were prepared by an *in-situ* route. It involved a reaction between titanium oxide dissolved in the  $\text{TiO}_2\text{--Y}_2\text{O}_3\text{--ZrO}_2$  solid solution, boron oxide and carbon. The uniform mixtures of a hydrothermally crystallized zirconia solid solution nanopowder, boric acid (a. p.) and 20 wt. % alcohol solution of phenol–formaldehyde resin were used. Each mixture was first dried in an argon flow to decompose  $\text{H}_3\text{BO}_3$  and then the resin. Finally it was heat treated for 1.5 h at 1500 °C in vacuum under the pressure not exceeding  $2 \times 10^{-3}$  mbar to synthesize the composite powder.

Phase compositions of the powders were determined by the X-ray diffraction analysis (radiation  $\text{CuK}_{\alpha 1}$ ,  $2\theta$  range 20–90°, step 0.008°). The Rietveld refinements of the diffraction data were carried out by means of the X'Pert Plus v1.0 program (Philips) to determine phase fractions. Scherrer's equation [6] was applied to calculate the



crystallite sizes of  $Y_2O_3$ - $TiO_2$ - $ZrO_2$  solid solution powders. DTA and TG curves were obtained in air at temperatures ranging from 30 °C to 1000 °C at the heating rates of 10 °C/min. Specific surface areas were measured by the multipoint nitrogen adsorption at -196 °C. The BET adsorption model was involved in calculations. TEM, combined with EDS, was used to characterize a morphology and chemical compositions of the  $Y_2O_3$ - $TiO_2$ - $ZrO_2$  solid solution powders. The agglomerate size distributions were determined by the dynamic light scattering technique in the range up to 6  $\mu$ m. These measurements were carried out in water dispersions at pH ranging from 9 to 11.

### 3. Results and discussion

#### 3.1. Powders of $Y_2O_3$ - $TiO_2$ - $ZrO_2$ solid solution

The XRD measurements showed that the powders in the  $Y_2O_3$ - $TiO_2$ - $ZrO_2$  system, crystallized at the hydrothermal conditions described above, consisted of tetragonal and monoclinic zirconia polymorphs (Fig. 1). The X-ray diffraction patterns did not contain peaks from either titanium or yttrium rich phases. This is a strong argument for the formation of zirconia solid solutions of the designed  $TiO_2$  and  $Y_2O_3$  concentration. The monoclinic  $ZrO_2$  polymorph content was moderate, up to 12.6 vol. % (Table 1). It is ca. 45% lower than that measured for the powders with similar chemical composition but crystallized by using the calcination process at 650 °C [2–4].

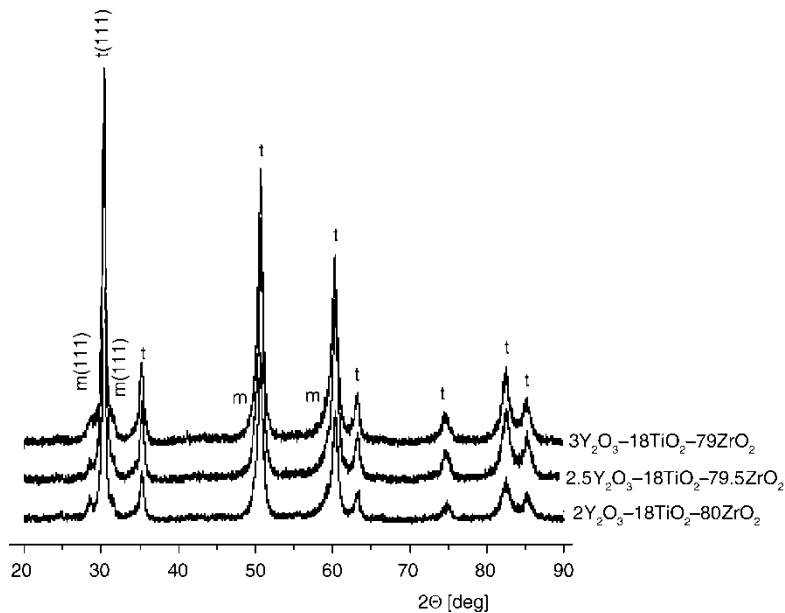


Fig. 1. XRD patterns of the powders; t – tetragonal  $ZrO_2$ , m – monoclinic  $ZrO_2$

Table 1. Phase composition of the  $Y_2O_3$ - $TiO_2$ - $ZrO_2$  powders

Powder	Tetragonal $ZrO_2$ [vol. %]	Monoclinic $ZrO_2$ [vol. %]
$2.0Y_2O_3-18TiO_2-80ZrO_2$	$87.4 \pm 0.4$	$12.6 \pm 0.3$
$2.5Y_2O_3-18TiO_2-79.5ZrO_2$	$92.2 \pm 0.4$	$8.0 \pm 0.3$
$3.0Y_2O_3-18TiO_2-79ZrO_2$	$89.7 \pm 0.4$	$10.3 \pm 0.3$

Table 2. Specific surface area of the  $Y_2O_3$ - $TiO_2$ - $ZrO_2$  hydrothermal powders and mean crystallite sizes of tetragonal  $ZrO_2$  in the direction perpendicular to the (011) lattice plane for various chemical compositions

Powder	$S_{BET}$ [ $m^2/g$ ]	$d_{(111)}$ [nm]
$2.0Y_2O_3-18TiO_2-80ZrO_2$	$83.0 \pm 0,2$	18.6
$2.5Y_2O_3-18TiO_2-79.5ZrO_2$	$86.3 \pm 0,3$	17.8
$3.0Y_2O_3-18TiO_2-79ZrO_2$	$90.3 \pm 0,8$	16.5

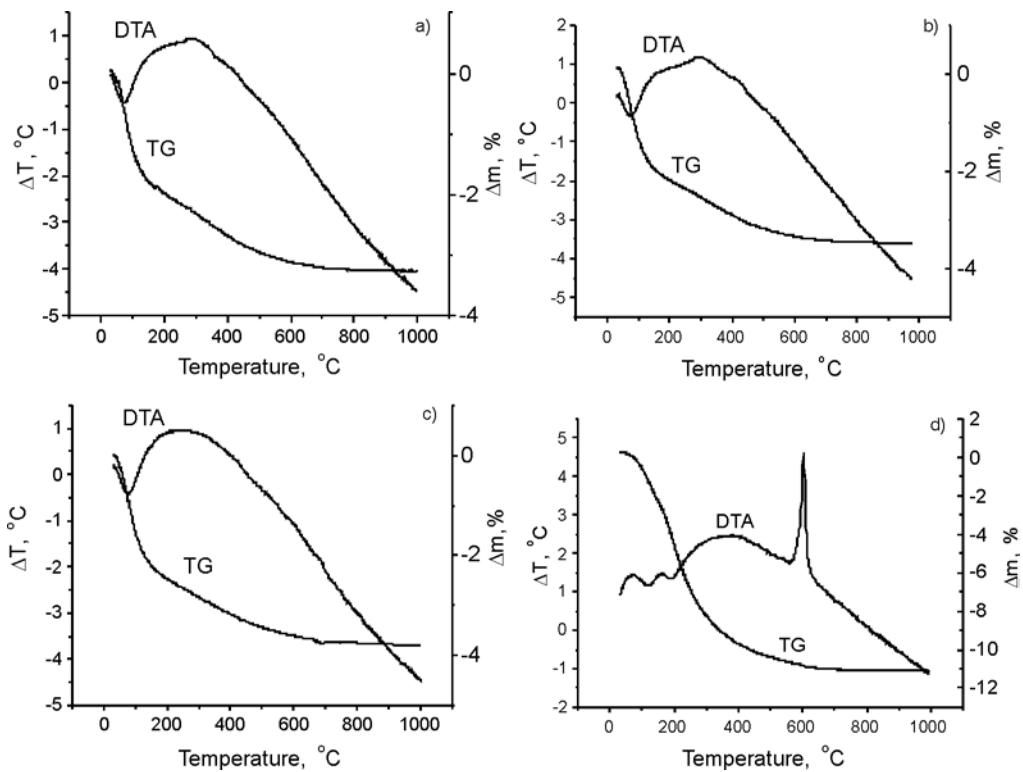


Fig. 2. DTA and TG curves: a)  $2Y_2O_3-18TiO_2-80ZrO_2$  hydrothermal powder, b)  $2.5Y_2O_3-18TiO_2-79.5ZrO_2$  hydrothermal powder, c)  $3Y_2O_3-18TiO_2-79ZrO_2$  hydrothermal powder, d) hydrogel corresponding to  $2.5Y_2O_3-18TiO_2-79.5ZrO_2$

The DTA and TG analyses of hydrothermally treated powders revealed no thermal effects at 625 °C (Fig. 2) as distinct from the amorphous zirconia hydrogel (Fig. 2d).

The comparison proves that the originally amorphous yttria–titania–zirconia hydrogels crystallized totally under applied hydrothermal conditions.

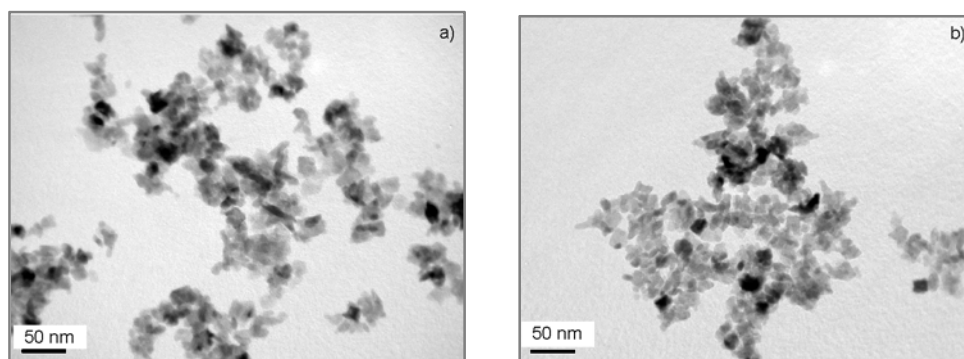


Fig. 3. TEM micrographs of the hydrothermal zirconia powders:  
a)  $2Y_2O_3$ - $18TiO_2$ - $80ZrO_2$ , b)  $2.5Y_2O_3$ - $18TiO_2$ - $79.5ZrO_2$

The TEM observations (Fig. 3) together with specific surface area and crystallite size measurements (Table 2) proved the nanometric size of the powder particles. The mean crystallite size was between 15 and 20 nm. The specific surface area was close to  $90 \text{ m}^2/\text{g}$ . The value is over 30 higher than that of the zirconia powders of similar chemical composition, crystallized by calcination at  $700 \text{ }^\circ\text{C}$  [3, 4]. On the other hand, the presented  $Y_2O_3$ - $TiO_2$ - $ZrO_2$  nanopowders consist of slightly bigger grains than those hydrothermally treated without titanium oxide dissolved in the solid state whose mean grain size was of ca. 10 nm [7]. This suggests that  $TiO_2$  affects significantly crystallite growth during the hydrothermal crystallization process.

As shown in Fig. 3, the zirconia nanopowders contained crystallites not only isometric in shape but also a small content of needle-shaped ones. This observation, together with the data collected in Table 1, suggests that these crystallites belong to monoclinic zirconia.

Figure 4 shows the results of EDS chemical composition measurements for the  $3Y_2O_3$ - $18TiO_2$ - $79ZrO_2$  nanopowder. The analysis, made along the line marked, proved that the crystallites consist of yttrium, titanium, zirconium and oxygen. Local signal maxima for particular elements align together very well. This observation is the second evidence, together with the XRD measurements, for the lack of titanium and/or yttrium segregation into separate phases, additionally proving that titanium and yttrium oxides are totally dissolved in the zirconia solid phase. Unfortunately, the EDS scan is insufficiently sensitive for evaluation of the titanium and yttrium segregation inside a single nanocrystallite.

Agglomerate size distributions of the zirconia nanopowder depend on the preparation history as is shown in Fig. 5. The powder which was not dried after hydrothermal treatment consisted of the agglomerates of practically monomodal size distribution

(Fig. 5a) with a modal size close to 50 nm. Such an agglomerate consists of a few crystallites.

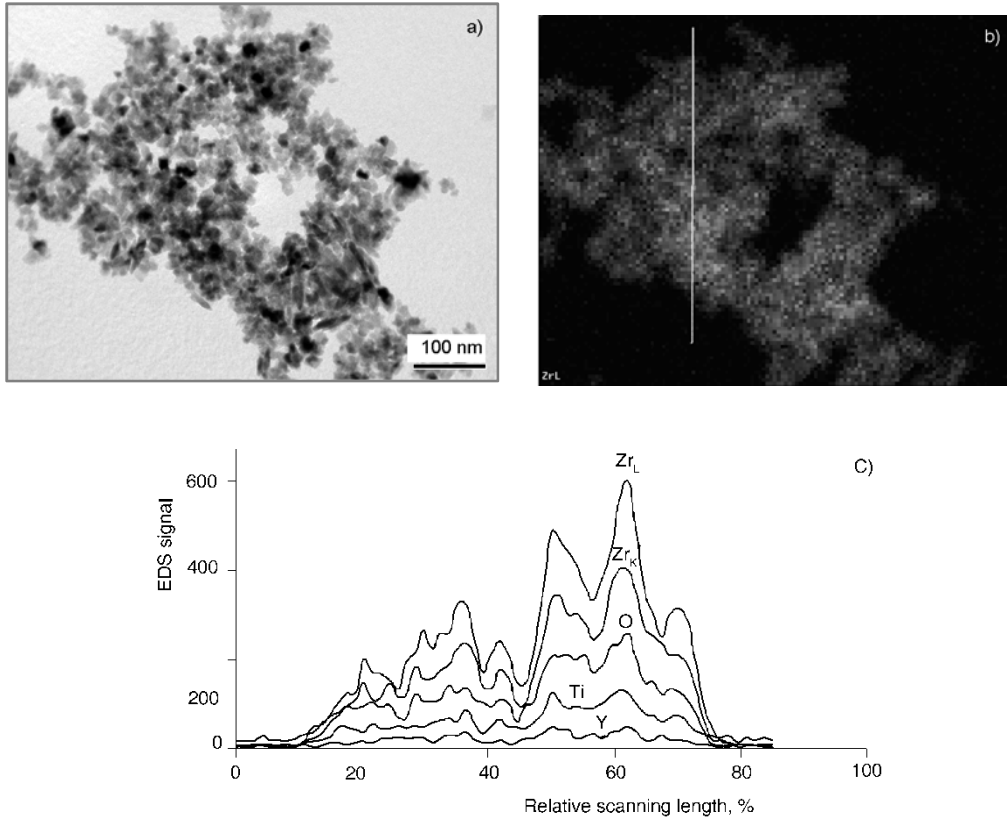


Fig. 4. Results of chemical analysis of  $3Y_2O_3-18TiO_2-79ZrO_2$  nanopowder: a) TEM micrograph, b) map of zirconium distribution c) EDS analysis along the line marked in Fig. 4b

During final drying stages, because of capillary and dispersion attractive forces among crystallites, the nanopowder becomes more and more agglomerated. The resultant agglomerate size distribution turns into trimodal (Fig. 5b), and the majority of agglomerates becomes larger than  $1\ \mu\text{m}$ . However, the agglomerates are still relatively mechanically weak. Their sizes can be easily reduced by external forces, for example by ultrasonic treatment. After 5 min of ca. 100 W sonification, the modal size of agglomerates reverts to 50 nm (Fig. 5c). This confirms usability of the hydrothermal crystallisation for fabrication of zirconia nanopowders composed of soft agglomerates. This feature seems to be advantageous for a synthesis of  $ZrO_2/TiC/TiB_2$  composite powders using the *in-situ* method [5].

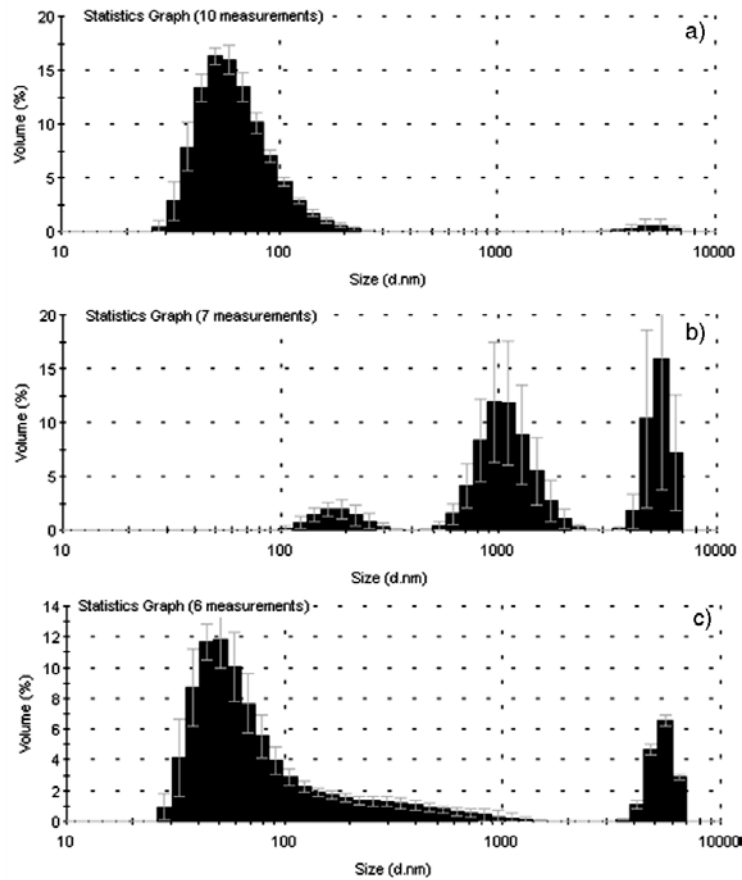
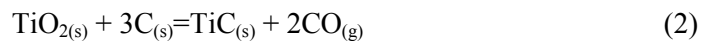
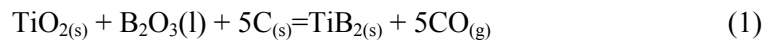


Fig. 5. Agglomerate size distributions of the  $2.5Y_2O_3$ - $18TiO_2$ - $79.5ZrO_2$  nanopowders: a) without drying after hydrothermal crystallization, 5 min of ultrasonic treatment, b) dried, without ultrasonic treatment; c) dried, 5 min of ultrasonic treatment

### 3.2. Composite powders in the $Y_2O_3$ - $ZrO_2$ / $TiC$ / $TiB_2$ system

Figure 6 and Table 3 show phase compositions of zirconia composite powders synthesized by using the *in-situ* reactions in a qualitative and quantitative way, respectively. The powders consisted of tetragonal and monoclinic zirconia polymorphs blended with  $TiC$ ,  $TiB_2$  and  $ZrB$ . This confirms that  $TiO_2$  dissolved in zirconia was involved in production of the  $TiB_2$  and  $TiC$  inclusions, most probably according to the following reactions:



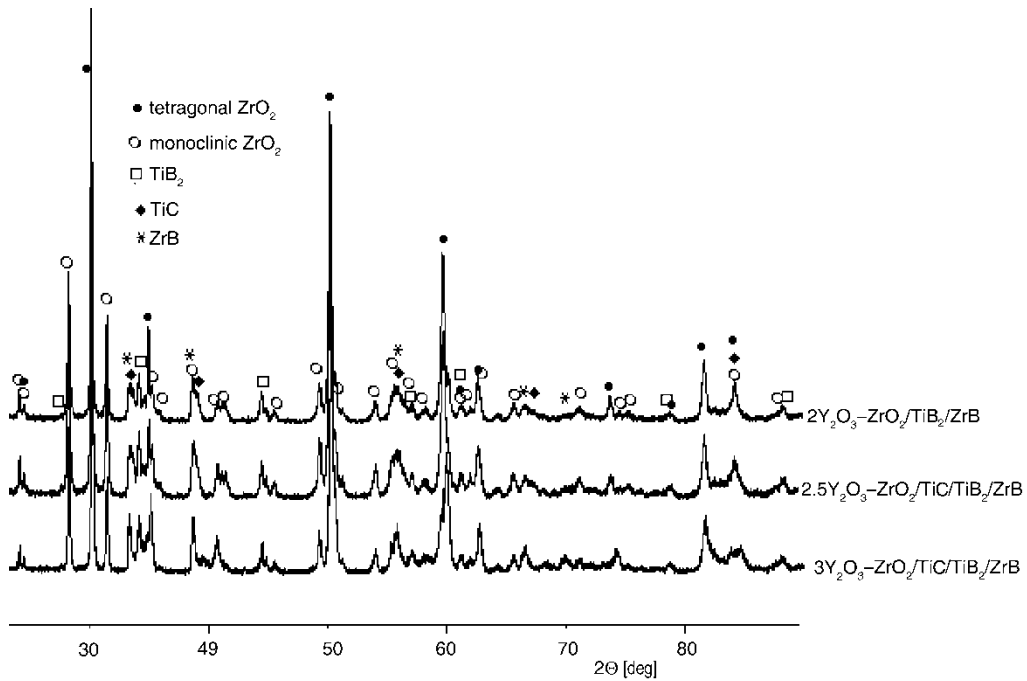


Fig 6. XRD patterns of the composite powders of the original zirconia nanopowders

Table 3. Phase compositions [wt. %] of the composite powders

Original powder	Tetragonal ZrO <sub>2</sub>	Monoclinic ZrO <sub>2</sub>	TiB <sub>2</sub>	TiC	ZrB
2Y <sub>2</sub> O <sub>3</sub> -18TiO <sub>2</sub> -ZrO <sub>2</sub>	48.9 ± 0.3	34.8 ± 0.3	7.7 ± 0.3	–	8.6 ± 0.1
2.5Y <sub>2</sub> O <sub>3</sub> -18TiO <sub>2</sub> -ZrO <sub>2</sub>	37.1 ± 0.2	41.2 ± 0.2	5.1 ± 0.2	12.3 ± 0.3	4.4 ± 0.1
3Y <sub>2</sub> O <sub>3</sub> -18TiO <sub>2</sub> -ZrO <sub>2</sub>	43.2 ± 0.2	35.4 ± 0.2	5.4 ± 0.2	11.7 ± 0.1	4.5 ± 0.3

At 1500 °C under the CO partial pressure of  $2 \times 10^{-3}$  mbar, changes of the Gibbs free energy for reactions (1) and (2) were calculated to be  $-1107.5$  kJ/mol and  $-458.2$  kJ/mol, respectively. Thus the former reaction is more favourable than the latter one. The content of TiB<sub>2</sub> will be higher than that of TiC in the equilibrium state. However, the data collected in Table 3 show that the system was not in equilibrium. In the case of the 2.5Y<sub>2</sub>O<sub>3</sub>-18TiO<sub>2</sub>-ZrO<sub>2</sub> and 3Y<sub>2</sub>O<sub>3</sub>-18TiO<sub>2</sub>-ZrO<sub>2</sub> nanopowders, TiC dominates over TiB<sub>2</sub>, while it is absent in the composite powder originated from the 2Y<sub>2</sub>O<sub>3</sub>-18TiO<sub>2</sub>-ZrO<sub>2</sub> nanopowder. It clearly points that the reaction kinetics controls the final composition of the composite powder. The presence of zirconium boride indicates that ZrO<sub>2</sub> reacted with B<sub>2</sub>O<sub>3</sub> and C according to Eq. (1). ZrB seems to be a secondary inclusion phase but not in the case of the powder based on the 2Y<sub>2</sub>O<sub>3</sub>-18TiO<sub>2</sub>-ZrO<sub>2</sub> nanopowder. This may suggest that Y<sub>2</sub>O<sub>3</sub> affected the kinetics of TiB<sub>2</sub>, TiC, ZrB formation. Nevertheless, ZrB seems to be stable only at low CO pressures. It disappeared during sintering of the analogical composite powder in argon of technical purity at 1500 °C [5].

## 4. Conclusions

Co-precipitation followed by hydrothermal crystallization is an effective way for production of zirconia solid solution nanopowders with 18 mol % titania and 2–3 mol % yttria. Mean crystallite sizes of the nanopowders are 15–20 nm, while specific surface area is close to 90 m<sup>2</sup>/g. Titanium oxide dissolved in the nanosized crystallites can react with B<sub>2</sub>O<sub>3</sub> and carbon resulting in the formation of TiC and TiB<sub>2</sub>. The same process of carbothermal reduction gives ZrB as a secondary phase in the composite powders.

### Acknowledgements

This work was supported by the Polish government under the grant No. N507 017 31/0527.

### References

- [1] PYDA W., Proc. 2nd Int. Conf. Composite Science and Technology, A. Adali, E. V. Morozov, V.E. Verijenko (Eds.), Dep. Mech. Eng., University of Natal, Durban (Rep. South Africa), 1988, pp. 195–200.
- [2] HABERKO K., PYDA W., PEŁDZICH Z., BUĆKO M.M., J. Eur. Ceram. Soc., 20 (2000), 2649.
- [3] PYDA W., Mater. Ceram., 4 (2002), 151.
- [4] PYDA W., Ceramics International 30 (2004), 333.
- [5] MOSKALA N., PYDA W., Kompozyty (Composites) 5 (2005), 56.
- [6] SCHERRER P., *Göttinger Nachrichten* (1918); cf. also R. Zsigmondy, *Kolloidchemie* (3rd Ed.) Spamer, Leipzig, 1920, p. 394.
- [7] PYDA W., HABERKO K., BUĆKO M., J. Am. Ceram. Soc., 74 (1991), 2622.

*Received 28 April 2007*  
*Revised 16 February 2008*

## Titanium-ceramic nanocomposites fabricated by the mechanical alloying process

K. NIESPODZIANA<sup>1\*</sup>, K. JURCZYK<sup>2</sup>, M. JURCZYK<sup>1</sup>

<sup>1</sup>Poznań University of Technology, Institute of Materials Science and Engineering,  
pl. Skłodowskiej-Curie 5, 60-965 Poznań, Poland

<sup>2</sup>Poznań University of Medical Sciences, Department of Conservative Dentistry and Periodontology,  
ul. Bukowska 70, 60-812 Poznań, Poland

Wide use of titanium and its alloys as biomaterials stems from their low elastic moduli, good fatigue strength and better corrosion resistance compared to other metals and alloys used in medicine. However, they have poor tribological properties and a release of titanium alloy elements into surrounding tissues can cause eventual inflammation, failure and removal of an implant. For this reason, there is a great need for creating composite materials using ceramic particles to reinforce titanium which would give the possibility of optimizing mechanical and biological properties. In the present work Ti hydroxyapatite (HA, 3, 10 vol. %) and Ti-SiO<sub>2</sub> (3, 10 vol. %) nanocomposites were fabricated by a combination of mechanical alloying (MA) and sintering processes. Mechanical properties and corrosion resistance of these composites were investigated by the Vicker hardness measurement and *in vitro* studies. The experimental results show that Ti-10 vol. % HA and Ti-10 vol. % SiO<sub>2</sub> nanocomposites have good corrosion resistance ( $I_c = 1.1 \times 10^{-6}$ ,  $E_c = -0.48$ ;  $I_c = 9.23 \times 10^{-7}$ ,  $E_c = -0.45$ , respectively) in comparison with microcrystalline titanium ( $I_c = 2.7 \times 10^{-5}$ ,  $E_c = -0.47$ ). Vickers' microhardness of the prepared nanocomposites is a few times higher than that of microcrystalline titanium. In conclusion, titanium ceramic nanocomposite is a suitable material for hard tissue replacement from the point of view of both mechanical and corrosion properties.

Key words: *titanium; bioceramics; nanocomposite; mechanical alloying*

### 1. Introduction

Titanium and titanium alloys are employed widely in biomedical and dental applications because of relatively low moduli of elasticity, low densities, high strength, good biocompatibility and corrosion resistance. Titanium and titanium alloys are generally regarded to have good biocompatibility and high corrosion resistance *in vitro* [1] although accumulation of titanium in tissues adjacent to the implant has been re-

---

\*Corresponding author, e-mail: katarzyna.niespodziana@put.poznan.pl



ported signifying metal release and corrosion *in vivo* [2, 3]. Besides, titanium and titanium alloys have relatively poor tribological properties because of their low hardness [4]. In addition, metal implants may loose and even separate from surrounding tissues during implantation because of their low bonding strength [5–7]. Much better biomaterials for hard tissue replacement implants may be acquired by the preparation of titanium composites. The most commonly used materials are ceramics such as hydroxyapatites, silicas or bioglasses.

Hydroxyapatite (HA,  $\text{Ca}_{10}(\text{PO}_4)_6(\text{OH})_2$ ), the basic mineral in natural bones, shows excellent biocompatibility with the bone. Besides, HA is bioactive and able to form strong chemical bonds with natural bone [8, 9]. Silica ( $\text{SiO}_2$ ) is also a bioactive material with high corrosion resistance. Unfortunately, neither hydroxyapatite nor silica can be used for hard tissue replacement implants due to their poor mechanical properties [10].

Therefore, the connection of excellent biocompatibility and bioactivity of ceramics with good mechanical properties of titanium is considered to be a promising approach for fabrication of more perfect hard tissue replacement implants. There are two creative ways to meet this idea: use of ceramics as a coating or as a reinforcing phase in metallic-ceramic composites [11]. In general, the coating techniques became a common method, although they have some drawbacks: the toughness of ceramic is low; during the coating stage interfacial cracks can occur; the metal/ceramic adherence is low and can diminish in time [12]. For this reason, composite materials containing both ceramic and titanium are expected to have broad practical applications due to the fact that each material can compensate for the shortcomings of the other. To date, however, there are only few reports dealing with the microcomposite of ceramics and titanium manufactured by powder metallurgy [13–15].

The aim of this study was to develop new materials composed of Ti and hydroxyapatite or silica for biomedical applications. The Ti–HA (3, 10 vol. %) and Ti– $\text{SiO}_2$  (3, 10 vol. %) composites were prepared by a combination of mechanical alloying and powder metallurgical process. The structure and mechanical and corrosion properties of the composites were investigated.

## 2. Experimental

The starting materials used were titanium ( $< 45 \mu\text{m}$ ), hydroxyapatite and silica ( $< 68 \mu\text{m}$ ) powders. The raw powders with various Ti/HA and Ti/ $\text{SiO}_2$  mixing ratios were first blended by mechanical alloying processes under argon atmosphere using an SPEX 8000 Mixer Mill. The vial was loaded and unloaded in a Labmaster 130 glove box in high purity argon atmosphere. The mixture of Ti–HA (3, 10 vol. %) and Ti– $\text{SiO}_2$  (3, 10 vol. %) powders were ball milled for 44 and 20 h, respectively. Then the milled powders were compacted at 1300 MPa and heat treated at 1150 °C in a gas atmosphere composed of 95% Ar and 5%  $\text{H}_2$  under the pressure of 0.15 MPa holding for 2 h.

X-ray diffraction (XRD) was employed to study the effect of mechanical alloying and of any subsequent heat treatment on the phases present in the samples. Typical crystallite sizes were estimated from the half-width of lines using the Scherrer equation. A scanning electron microscope (SEM) with energy dispersive spectrometry (EDS) was used to study the microstructure and chemical composition of the produced samples. The effect of various amounts of HA or SiO<sub>2</sub> on mechanical properties of titanium composites was assessed by density measurements (Archimedes method) and Vickers' microhardness tester on polished surface under the load of 200 g.

The corrosion resistance in 0.1 M H<sub>2</sub>SO<sub>4</sub> aqueous solution was measured using *in vitro* potentiodynamic corrosion tests. Saturate calomel electrode was used as the reference electrode and graphite as the counter electrode. The polarization curves were obtained for each specimen and corrosion potentials and corrosion current densities were determined by the Tafel extrapolation methods.

### 3. Results and discussion

MA process on Ti–HA (3, 10 vol. %) and Ti–SiO<sub>2</sub> (3, 10 vol. %) composites has been studied by X-ray diffraction. For example, Fig. 1a shows the XRD pattern of the starting titanium and hydroxyapatite powders. During MA process, the originally sharp diffraction lines of starting materials gradually become broader and their intensities decreased with the milling time. The amorphous phase forms directly from the starting mixture of the compounds (Ti, HA) without formation of other phases (Fig. 1b). Formation of the nanocomposites was achieved by annealing of the amorphous material in high purity gas atmosphere composed of 95% Ar and 5% H<sub>2</sub> at 1150 °C for 2 h.

XRD analysis of Ti–3 vol. % HA showed the presence of  $\alpha$ -Ti (hexagonal-type structure with cell parameters  $a = 2.768 \text{ \AA}$ ,  $c = 4.497 \text{ \AA}$ ) and HA phases (Fig. 1c). When hydroxyapatite is added to titanium, the lattice constants of Ti decrease, as manifested by a shift of the diffraction peaks of the (100), (002) and (101) crystal planes of titanium towards larger angles in comparison with pure titanium.

XRD analysis of Ti–3 vol. % SiO<sub>2</sub> showed the presence of  $\alpha$ -Ti (hexagonal-type structure with the cell parameters  $a = 2.972 \text{ \AA}$ ,  $c = 4.774 \text{ \AA}$ ). The formation of crystalline SiO<sub>2</sub> phase was not observed (Fig. 1d).

Table 1 shows the average crystallite size of titanium-silica and titanium-hydroxyapatite composites estimated from XRD experiment.

The results of the EDS analysis and a scanning electron micrograph of the surface of Ti–3 vol. % HA and Ti–3 vol. % SiO<sub>2</sub> nanocomposites mechanically alloyed and heat treated at 1150 °C for 2 h are shown in Fig. 2. EDS analysis shows that the Ti–3 vol. % SiO<sub>2</sub> nanocomposite consists of titanium matrix with silica or silicon particles (Fig. 2a). A similar microstructure can be observed in Ti–10 vol. % SiO<sub>2</sub> nanocomposite.

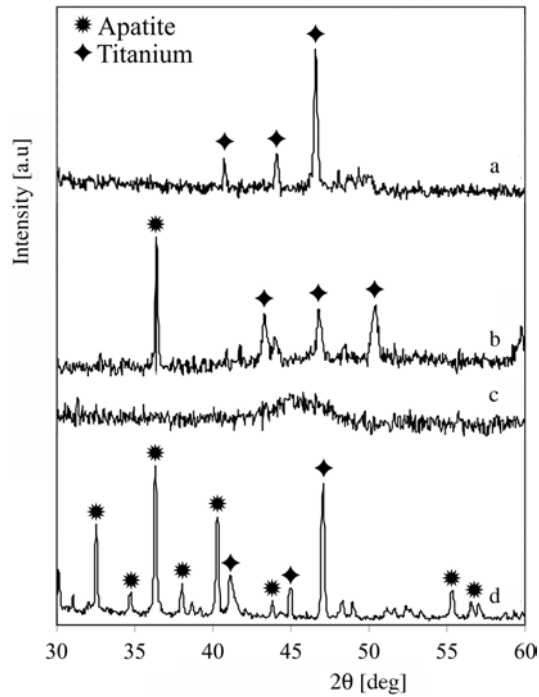


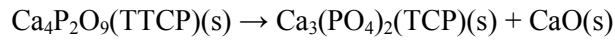
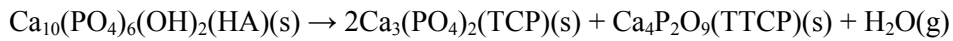
Fig. 1. XDR spectra of Ti-3 vol. % HA and Ti-3 vol. % SiO<sub>2</sub> nanocomposites: a) Ti, HA powders – 0 h MA, b) Ti-3 vol. % HA – 44 h MA, c) Ti-3 vol. % HA after annealing, d) Ti-3 vol. % SiO<sub>2</sub> after MA and annealing

Table 1. Characteristics of Ti-HA and Ti-SiO<sub>2</sub> nanocomposites and titanium

Nanocomposite	$d$ [nm]	$HV_{0.2}$	$\rho$ [g/cm <sup>3</sup> ]
Ti-3 vol. % HA	25	480	3.51
Ti-10 vol % HA	40	1500	4.03
Ti-3 vol. % SiO <sub>2</sub>	40	550	4.26
Ti-10 vol. % SiO <sub>2</sub>	50	670	4.48
Ti	–	250	4.51

The EDS results indicate that a predominant phase in Ti-HA composites is titanium with some amount of apatites with various Ca/P ratios. The Ti-3 vol. % HA nanocomposite consisted of titanium matrix with apatites (Fig. 2b) with the Ca/P ratios 1.6 and 0.51 which were close to the values characteristic of hydroxyapatite and Ca(PO<sub>3</sub>)<sub>2</sub>, respectively. Ti-10 vol. % HA nanocomposite consisted of titanium matrix with calcium and titanium matrix with apatite, in which Ca/P ratio was 1.07, the value similar to the Ca/P ratio in Ca<sub>2</sub>P<sub>2</sub>O<sub>7</sub> (not shown). The existence of a second phase is a common feature of HA-based composites because the presence of titanium can degrade the structural stability of HA crystal and promote dehydration and decomposi-

tion of HA phase [15–17]. Besides, extreme heating conditions can produce secondary HA phases such as tricalcium phosphate (TCP), tetracalcium phosphate (TTCP) and calcium oxide (CaO). This is the result of cooling from a high temperature which can be postulated in the following reactions [18]:



These secondary HA phases can influence the final properties of Ti–HA nanocomposites as well. The presence of some amount of iron atoms in the nanocomposite Ti–HA could be explained by Fe impurities trapped in the MA powders from erosion of the milling media [19].

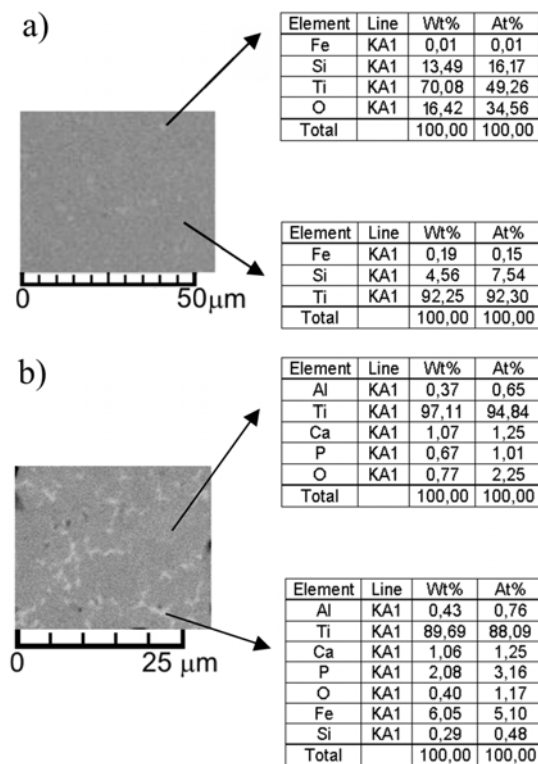


Fig. 2. EDS spectra of surfaces: a) Ti–3 vol. %  $\text{SiO}_2$ , b) Ti–3 vol. % HA nanocomposites produced by mechanical alloying followed by annealing

Properties of fabricated nanocomposites depend on the processing parameters. A detailed description of the influence of mechanical alloying and annealing times on mechanical properties of Ti–10 vol. % HA nanocomposite was given elsewhere [20, 21]. Differences in the phase contents of titanium-ceramic nanocomposites also

lead to changes of their properties. As shown in Fig. 3, Vickers' microhardness of bulk samples prepared by mechanical alloying depends on the composite constitution. Vickers' hardness of bulk samples prepared by mechanical alloying is higher than that of a pure microcrystalline Ti metal ( $250 HV_{0.2}$ ) and strongly increases for Ti-10 vol. % HA nanocomposite ( $1500 HV_{0.2}$ ) being three times higher than that of Ti-3 vol. % HA material ( $480 HV_{0.2}$ ). Vickers' hardnesses of Ti-3 vol. %  $SiO_2$  and Ti-10 vol. %  $SiO_2$  composites are  $550 HV_{0.2}$  and  $670 HV_{0.2}$ , respectively.

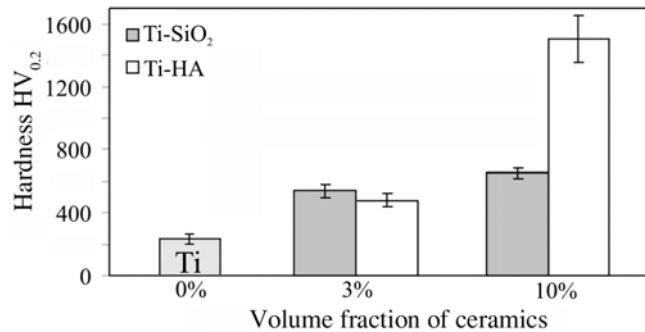


Fig. 3. The influence of volume fraction of HA or  $SiO_2$  on Vickers' hardness in titanium-ceramic nanocomposites

Relative densities of the Ti-HA composites are higher than 85% of the theoretical density of Ti and are lower than that of Ti- $SiO_2$  composites (90% of theoretical density) (Table 1). The composites with lower volume fractions of ceramics have low densities, which indicates that they are more porous.

Table 2. Mean values of corrosion current densities and corrosion potentials of Ti-HA and Ti- $SiO_2$  nanocomposites and titanium

Composite	$I_c$ [ $A/cm^2$ ]	$E_c$ [V]
Ti-3 vol. % HA	$7.2 \times 10^{-5}$	-0.36
Ti-10 vol % HA	$1.1 \times 10^{-6}$	-0.48
Ti-3 vol. % $SiO_2$	$3.59 \times 10^{-5}$	-0.42
Ti-10 vol. % $SiO_2$	$9.23 \times 10^{-7}$	-0.45
Ti	$1.49 \times 10^{-5}$	-0.47

The corrosion current densities and corrosion potentials of various specimens were determined from the potentiodynamic polarization curves by the Tafel extrapolation method and summarized in Table 2. For example, the potentiodynamic polarization curves of the nanocrystalline Ti-10 vol. % HA and Ti-10 vol. %  $SiO_2$  composites in 0.1 M  $H_2SO_4$  water solution are shown in Fig. 4. For the sake of comparison, the results obtained for microcrystalline titanium are also shown. The polarization curves

(Fig. 4b, c) of Ti–10 vol. % HA and Ti–10 vol. % SiO<sub>2</sub> composites were wider in the passive range in comparison with microcrystalline titanium (curve a).

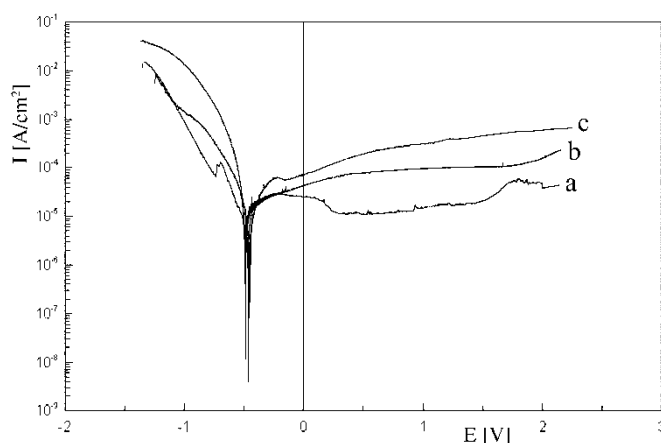


Fig. 4. Potentiodynamic polarization curves of: a) Ti, b) Ti–10 vol. % HA composites, c) Ti–10 vol. % SiO<sub>2</sub> in 0.1 M H<sub>2</sub>SO<sub>4</sub> distilled water solution

According to Table 2, the corrosion resistance increases with the rise of ceramics contents. The corrosion resistance of the Ti–10 vol. % SiO<sub>2</sub> composite ( $I_c = 9,23 \times 10^{-7}$  A/cm<sup>2</sup>,  $E_c = -0.45$  V) was better than Ti–3 vol. % SiO<sub>2</sub> composite ( $I_c = 3,59 \times 10^{-5}$  A/cm<sup>2</sup>,  $E_c = -0.42$  V). The Ti–10 vol. % HA nanocomposite possesses higher corrosion resistance and thus higher corrosion current densities ( $I_c = 1.1 \times 10^{-6}$  A/cm<sup>2</sup>) than microcrystalline titanium ( $I_c = 1.49 \times 10^{-5}$  A/cm<sup>2</sup>) unlike Ti–3 vol. % HA composite ( $I_c = 7.2 \times 10^{-5}$  A/cm<sup>2</sup>). The Ti–3 vol. % HA nanocomposite executed worse corrosion properties in comparison with other composites and titanium because of its different chemical composition and low density, which indicates that it has a highly porous structure and could easier corrode in a corrosive environment. It is also seen that titanium composites with silica have better corrosion resistances than those with hydroxyapatite. Therefore, an addition of ceramics caused significant changes of corrosion behaviour of titanium.

#### 4. Conclusions

It can be concluded that the titanium-ceramic nanocomposites were successfully fabricated from Ti, HA and SiO<sub>2</sub> powders by mechanical alloying and powder metallurgical process. As the EDS analysis has shown, the Ti–HA and Ti–SiO<sub>2</sub> nanocomposites consist mainly of titanium rich matrix with various apatites and calcium or silica and silicon particles, respectively. The results show an improvement of the properties due to the nanoscale structures in consolidated materials. Vickers' hardness changed upon density changes increasing with the increase of ceramic content, especially in

Ti-10 vol. % HA composite. Besides, titanium-hydroxyapatite composite with 10 vol. % of HA possesses higher corrosion resistance than microcrystalline titanium. The corrosion resistance of the Ti-10 vol. % SiO<sub>2</sub> nanocomposite is also better than that of pure titanium. The results of electrochemical studies show that titanium-ceramic composite with 3 vol. % of ceramic has lower corrosion resistance than microcrystalline titanium. As discussed above, Ti-10 vol. % HA or SiO<sub>2</sub> nanocomposite is suitable for heavy load-bearing hard tissue replacement from the point of view of both mechanical and corrosion properties.

#### Acknowledgements

The financial support of the Polish National Committee for Scientific Research is gratefully acknowledged (contract no N507 071 32/2092).

#### References

- [1] GONZALEZ J.E.G., MIRZA-ROSCA J.C., *J. Electroanal. Chem.*, 471 (1999), 109.
- [2] MU Y., KOBAYASHI T., SUMITA M., YAMAMOTO A., HANAWA T., *J. Biomem. Mater. Res.*, 49 (2000), 283.
- [3] BROWNE M., GREGSON P.J., *Biomater.*, 21 (2000), 385.
- [4] LIU X., CHU P.K., DING C.H., *Mater. Sci. Eng. R*, 47 (2004), 49.
- [5] TAKESHITA F., AYUKAWA Y., IYAMA S., MURAI K., SUETSUGU T., *J. Biomed. Mater. Res.*, 37 (1997), 235.
- [6] LONG M., RACK H.J., *Biomater.*, 19 (1998), 1621.
- [7] KHAN M.A., WILLIAMS R.L., WILLIAMS D.F., *Biomater.*, 20 (1999), 765.
- [8] HENCH L.L., *J. Am. Ceram. Soc.*, 74 (1991), 1487.
- [9] AOKI H., *Science and Medical Applications of hydroxyapatite*, JAAS, Tokyo, 1991.
- [10] THIAN E.S., LOH N.H., KHOR K.A., TOR S.B., *Biomater.*, 23 (2002), 2927.
- [11] HENCH L.L., *Bioceramics*, 81(1998), 1705.
- [12] TRENTZ O.A., PLATZ A., HELMY N., TRENTZ O., *Swiss Surg.*, 4 (1998), 203.
- [13] POPA C., SIMON V., VIDA-SIMITI I., BATIN G., CANDEA V., SIMON S., *J. Mater. Sci. Mater. Med.*, 16 (2005), 1165.
- [14] CHENGLIN C., JINGCHUAN Z., ZHONGDA Y., SHIDONG W., *Mater. Sci. Eng. A*, 271 (1999), 95.
- [15] NING C.Q., ZHOU Y., *Biomaterials*, 23 (2002), 2909.
- [16] CHU C., LIN P., DONG X., XUE X., ZHU J., YIN Z., *J. Mater. Sci.: Mater. Med.*, 13 (2002), 985.
- [17] GROSS K.A., BERNDT C.C., STEPHENS P., DINNEBIER R., *J. Mater. Sci.*, 33 (1998), 3985.
- [18] TAS A.C., KORKUSUZ F., TIMUCIN M., AKKAS N., *J. Mater. Sci.: Mater. Med.*, 8 (1997), 91.
- [19] JURCZYK M., SMARDZ K., RAJEWSKI W., SMARDZ L., *Mater. Sci. Eng., A*, 303 (2001), 70.
- [20] NIESPODZIANA K., JURCZYK K., JURCZYK M., *Inż. Mater.*, 151 (2006), 636.
- [21] NIESPODZIANA K., JURCZYK K., JURCZYK M., *Nanopages*, 1, (2006), 219.

*Received 28 April 2007*  
*Revised 16 February 2008*

## The influence of iron nanocrystallite size on a nitriding process rate

R. PELKA<sup>\*</sup>, P. GLINKA, W. ARABCYK

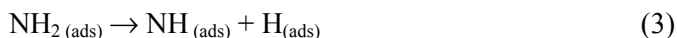
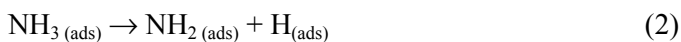
Institute of Chemical and Environment Engineering,  
Szczecin University of Technology, ul. Pułaskiego 10, 70-322 Szczecin

In the course of nitriding process of nanocrystalline iron promoted with aluminum and calcium oxides, nitrides such as Fe<sub>4</sub>N and Fe<sub>3-2</sub>N were fabricated. The process rate was studied making use of a flow differential tubular reactor with thermogravimetric measurement of mass changes. Nanocrystalline iron was reduced under hydrogen atmosphere at 500 °C and 800 °C. Average crystallite sizes determined by the XRD method after reduction performed at 500 °C as well as at 800 °C and after passivation were 18 and 42 nm, respectively. The nitriding process rate as well as catalytic ammonia decomposition rate were limited by the ammonia dissociative adsorption rate on the surface of iron and were dependent on the ratio of the crystallite surface area to crystallite volume. Obtained results were explained based on the adsorption range model.

Key words: *nanocrystalline iron; nitriding process; ammonia decomposition; thermogravimetry; XRD*

### 1. Introduction

Ammonia and nanocrystalline iron react in two parallel reactions. Apart from nanocrystalline iron nitriding, catalytic ammonia decomposition occurs. Grabke [1, 2] assumed that the rate limiting step during the initial stage of iron nitriding is chemical reaction on the interface between solid and gaseous phases. Chemical reaction resulting in obtaining atomic nitrogen, interstitially dissolved in iron lattice is considered a sequence of the following reactions:



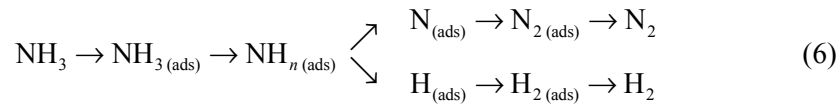
---

<sup>\*</sup>Corresponding author, e-mail: rpelka@ps.pl





In the case of nanomaterials, diffusion in solid state can be regarded as negligible on the account of relatively short distances of mass transport. Thus, the diffusion through the product layer can be neglected [1]. When the equilibrium state between solid and gaseous phases is reached, only catalytic ammonia decomposition reaction occurs:



Thus the content of nitrogen in the nitrides is dependent on temperature and ammonia concentration in the reacting gas mixture [3, 4]. At temperatures higher than 400 °C, the catalytic reaction of ammonia decomposition on the nanocrystalline iron and created nitrides was observed [3, 4].

When the process is limited by the surface reaction of ammonia decomposition to atomic nitrogen, the phase transition of iron to  $\gamma\text{-Fe}_4\text{N}$  phase occurs according to the adsorption range model [6]. It was assumed that mass transport between nanocrystallites was negligible. Thus the nanocrystallites react forming the product in a sequence of their sizes, viz. from the smallest to the largest crystallites.

## 2. Experimental

The kinetics of nitriding of nanocrystalline iron with ammonia was investigated making use of a set-up equipped with a flow tubular differential reactor enabling one to conduct thermogravimetric measurements (Fig. 1). Changes of the gas phase composition in the reaction volume of the reactor were analysed. Samples of the gas phase were collected from two sampling points placed over and under a platinum basket carrying solid sample. Hydrogen concentration in the reacting gas mixture was determined directly. Applied gases, i.e. hydrogen, ammonia and nitrogen were let to the reactor from a gas cylinder through reduction valves. Flow rates of gas reactants were determined by means of mass flow controllers. Mass and temperature of analysed solid samples as well as data concerning gas concentrations in the gas mixture were recorded digitally. In a platinum basket hanging on a balance arm, ca. 1 g of an analysed substance was placed in the form of a single layer of grains. The resolution of the measurements of mass changes was 0.1 mg.

In order to enhance the specific surface area of iron, aluminum and calcium oxides were used. Analysed nanocrystalline iron was obtained by fusion of magnetite with structured promoters of nanocrystalline iron. The obtained alloy was crushed and fraction of grains of the size in the range of 1.0–1.2 mm was separated. Prereduction process

of the material so obtained was performed at 500 °C and at pure hydrogen load (99.999 %) under atmospheric pressure. When the prereduction process was done, nanocrystalline iron was passivated at low temperature (< 100 °C) and at low oxygen pressure.

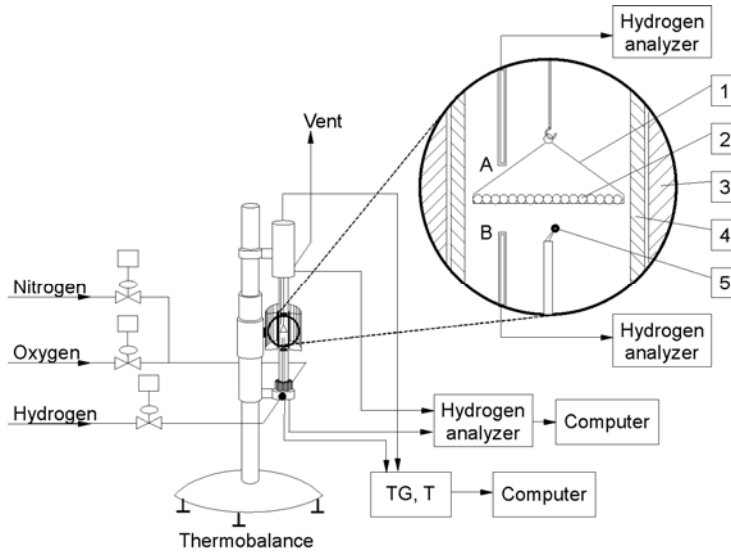


Fig. 1. Experimental setup: 1 – sample holder, 2 – single layer of grains, 3 – reactor furnace, 4 – reactor wall, 5 – thermocouple

The content of aluminum and calcium oxides stabilising the structure of enhanced surface of nanocrystalline iron was 3.3 wt. % and 2.8 wt. %, respectively, in relation to the prerduced form of the analysed material. The analysed material was divided into two parts. One part of material was reduced in a tubular furnace for 3 h under hydrogen atmosphere at 800 °C in order to perform recrystallisation of nanocrystalline iron. Mean sizes of iron nanocrystallites before and after recrystallisation process were determined by means of the XRD method.

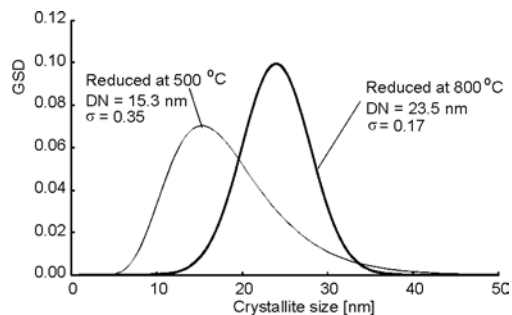


Fig. 2. Crystallite size distributions for nanocrystalline iron reduced at 500 °C and 800 °C

The recrystallisation resulted not only in increasing the mean size of iron crystallites, but also in changing their size distribution (Fig. 2). Analysed samples of

nanocrystalline iron had the same chemical composition but different crystallite sizes resulting from the recrystallisation process performed at different temperatures. The specific surface area was determined by means of temperature-programmed desorption of nitrogen.

Reduction process of the obtained alloy, followed by nanocrystalline iron nitriding, was performed at 500 °C and at pure hydrogen (99.999 %) load of  $500 \text{ cm}^3 \cdot \text{min}^{-1} \cdot \text{g}^{-1}$  under atmospheric pressure. The nitriding process was conducted under ammonia atmosphere (1 bar) at isothermal conditions, at temperatures ranging from 300 °C to 450 °C and ammonia load of  $200\text{--}500 \text{ cm}^3 \cdot \text{min}^{-1} \cdot \text{g}^{-1}$  until analysed sample mass was stable, what could be seen on TG curves as a horizontal line.

### 3. Results and discussion

Steady values of the conversion degree of ammonia during its catalytic decomposition with applied grain diameters (Fig. 3) show that the process was conducted in the kinetic reaction region, and internal diffusion effects could be neglected. Thus the reaction rate does not depend on the gas flow rate as well, i.e., the reactor used in our experiments could be regarded as a differential one. In such a case, diffusion effects do not influence neither the catalytic ammonia decomposition nor the nitriding reaction.

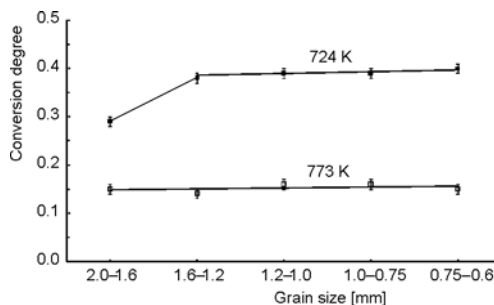


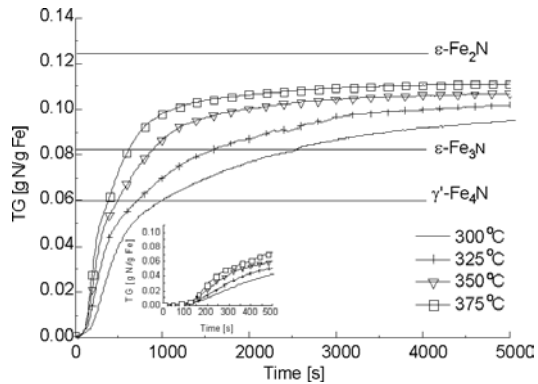
Fig. 3. Dependence of the ammonia conversion degree on the grain size

Results of gas phase composition measurements performed over and under the solid bed during nitriding prove that in the reactor, and hence also in the nanocrystalline iron bed, the mixing of components of reacting gas mixture occurs because of intensive convection. Platinum, of which the sample holder is made, did not affect the analysed process under process conditions. The mean size of crystallites of samples prereduced and then passivated was 18 nm, whilst the mean size of crystallites recrystallised and then passivated was 42 nm. The specific surface area of nanocrystalline iron reduced at 800 °C was  $3.5 \text{ m}^2/\text{g}$ , whereas that of nanocrystalline iron reduced at 500 °C was  $11 \text{ m}^2/\text{g}$ .

In the course of nanocrystalline iron nitriding, the mass of analysed samples increased. Exemplary TG curves obtained for nanocrystalline iron reduced at 500 °C and then nitrided under the ammonia load of  $200 \text{ cm}^3 \cdot \text{min}^{-1} \cdot \text{g}^{-1}$  are presented in Fig. 4.

Stoichiometric compositions of  $\gamma'$ -Fe<sub>4</sub>N and  $\epsilon$ -Fe<sub>3-2</sub>N nitrides are marked in the figure. The composition of  $\epsilon$ -Fe<sub>3-2</sub>N is unstable.

Fig. 4. TG curves for nitriding process of nanocrystalline iron reduced at 500 °C (ammonia load: 200 cm<sup>3</sup>·min<sup>-1</sup>·g<sup>-1</sup>)



Initially, a small increase of the sample mass (0.002–0.004 g N/g Fe during the first 100 s of the process) is observed. This is an effect of adsorption of ammonia upon nanocrystalline iron. Mass gain relevant to nitriding reaction did not occur, because concentration of ammonia mixed with hydrogen that left inside the reactor after reduction was too low. Then significant increase of the nitriding process rate is observed, because of formation of the  $\gamma'$ -Fe<sub>4</sub>N phase.

In Figure 5, TG curves for nitriding process of nanocrystalline iron reduced at 800 °C (a) and 500 °C (b) under the ammonia load of 500 cm<sup>3</sup>·min<sup>-1</sup>·g<sup>-1</sup> are presented.

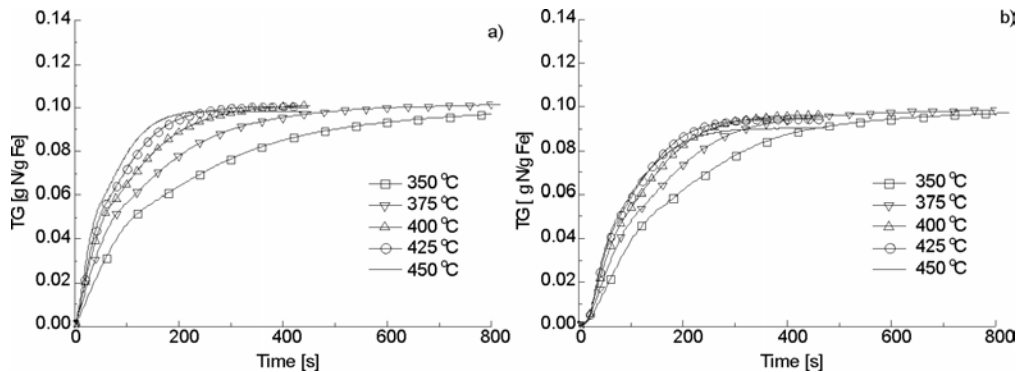


Fig. 5. TG curves for nitriding process of nanocrystalline iron reduced at: a) 800 °C, b) 500 °C (ammonia load 500 cm<sup>3</sup>·min<sup>-1</sup>·g<sup>-1</sup>)

The nitriding reaction rate increases with temperature. The conversion degree of the reaction reached the highest value and remained unchanged at each temperature through twice longer time than it is shown in Figs. 4 and 5, despite a prolonged exposure to the nitriding atmosphere. The process has many stages. Some inflection points

on the TG curves in the vicinity of phase transitions can be seen. The sections of the curves observed between inflection points can be considered approximately linear.

Nanocrystalline iron nitriding process caused the changes of gas phase composition, recorded against a background of physical mixing process and gas exchange process taking place in the reactor. From the experimental data concerning hydrogen contents in the gas phase, hydrogen concentration in the reaction volume resulting from ammonia load feeding the reactor as well as from nitriding and catalytic ammonia decomposition has been determined. Taking into account the mass balance of a stirred tubular reactor, it was possible to determine the ammonia and nitrogen concentrations in the gas mixture. Changes of ammonia concentration for selected experiments concerning nitriding process of nanocrystalline iron reduced at 800 °C and 500 °C are presented in Figs 6a, b, respectively. In a stationary state, only catalytic ammonia decomposition occurred and ammonia concentrations were the lower the higher process temperature was maintained.

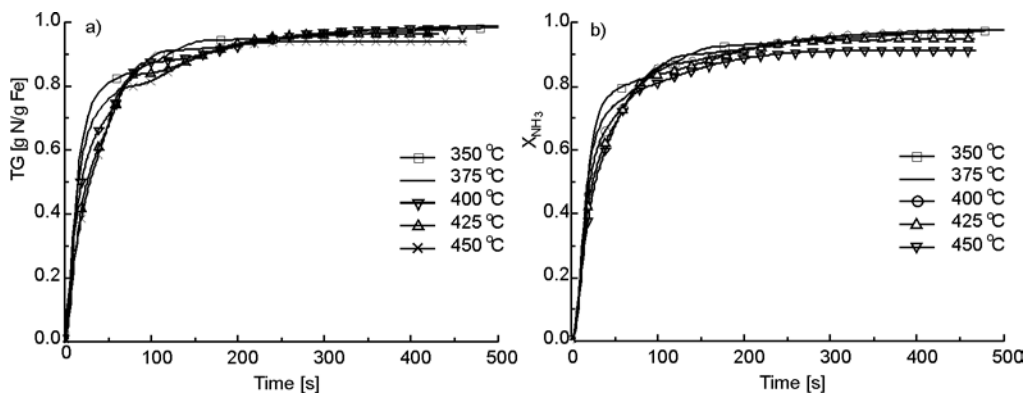


Fig. 6. Time dependence of ammonia concentration in the nitriding process (ammonia load  $500 \text{ cm}^3 \cdot \text{min}^{-1} \cdot \text{g}^{-1}$ ) of nanocrystalline iron reduced at a) 800 °C, b) 500 °C

In Figure 7a, the TG curves for nitriding process (ammonia load  $500 \text{ cm}^3 \cdot \text{min}^{-1} \cdot \text{g}^{-1}$ ) of nanocrystalline iron reduced at 800 °C and at 500 °C are shown. In Figure 7b, the comparison of obtained results concerning the gas phase composition is presented. Results for temperatures of 350 °C and 450 °C were selected. Based on TG curves from Fig. 7a, one can conclude that in the case of nitriding performed at relatively low temperature (350 °C), the same equilibrium composition of the solid is reached. In the stage of creation of  $\gamma'$ -Fe<sub>4</sub>N nitride, the TG curves are parallel to each other, thus the crystallite size does not considerably influence the nitriding process. The rate of creation of  $\epsilon$ -Fe<sub>3-2</sub>N phase at 350 °C is higher upon nanocrystalline iron reduced at 500 °C than that upon iron reduced at 800 °C.

The nitriding process performed at higher temperature (450 °C) proceeds faster, thus  $\gamma'$ -Fe<sub>4</sub>N and  $\epsilon$ -Fe<sub>3-2</sub>N phases occur below 350 °C. In the entire process of nitrides creation at higher temperatures, differences between nitriding reaction rates are ob-

served for nanocrystalline iron reduced at 500 °C and at 800 °C because participation of decomposition of catalytic ammonia reaction in the entire nitriding process increases with temperature (Fig. 7b).

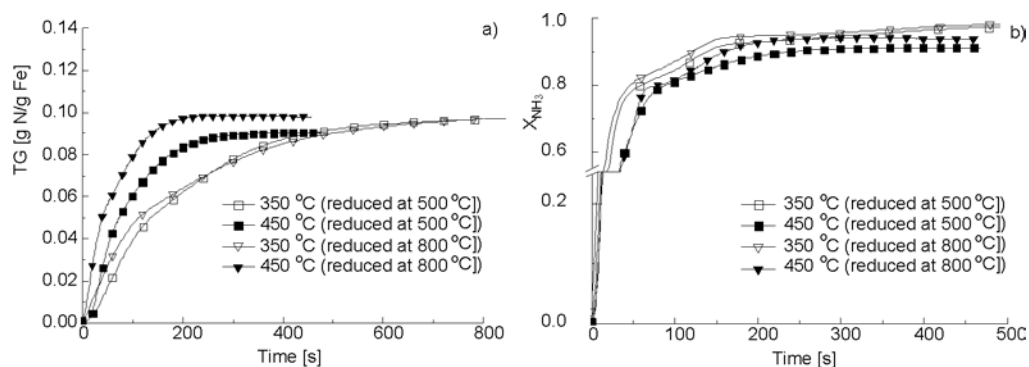


Fig. 7. TG curves (a) and time dependences of ammonia concentration (b) in the nitriding of nanocrystalline iron reduced at 800 °C and 500 °C under ammonia load  $500 \text{ cm}^3 \cdot \text{min}^{-1} \cdot \text{g}^{-1}$

The activation energy of decomposition of catalytic ammonia is higher than the activation energy of reaction of nitriding [6], thus increasing the temperature results in increasing rate of the catalytic ammonia decomposition resulting in a decrease of ammonia concentration in the gas mixture and diminishing the nitriding reaction rate. Catalytic decomposition of ammonia can proceed slower upon nanocrystalline iron reduced at 800 °C than upon nanocrystalline iron reduced at 500 °C (Fig. 7b) due to smaller specific surface area of the first material. Then, a higher nitriding potential occurs in the analysed system and nitriding reaction rate is higher.

## 4. Conclusions

The nitriding reaction rate depends mostly on the compositions of the solid and gas phases. Mean size of crystallites, and thus the specific surface area, influence the rate of reaction of catalytic ammonia decomposition being lower over nanocrystalline iron of the mean crystallite diameter of 42 nm than over nanocrystalline iron of the mean crystallite diameter of 18 nm. The higher temperature, the more important catalytic ammonia decomposition reaction is. This means that the value of mean crystallite size does not affect significantly the rate of nitriding process performed at lower temperatures. The obtained results were discussed on based on the adsorption range model.

## References

- [1] GRABKE H. J., Ber. Bunsenges. Phys. Chem., 4 (1968), 533.
- [2] GRABKE H. J., Archiv. Eisenhüttenwesen, 44 (1973), 603.

- [3] ARABCZYK W., ZAMLYNNY J., *Catal. Lett.*, 60 (1999), 167.
- [4] WRÓBEL R., ARABCZYK W., *J. Phys. Chem. A*, 110 (2006), 9219.
- [5] ARABCZYK W., WRÓBEL R., *Solid State Phen.*, 94 (2003), 185.
- [6] ZAMLYNNY J., *Examination of kinetics of nitriding of ferrous catalyst* (in Polish) PhD Thesis, Szczecin University of Technology, 2001.

*Received 28 April 2007*  
*Revised 16 February 2008*

# Preparation of carbon encapsulated cobalt nanoparticles by catalytic ethane decomposition

M. PODSIADŁY<sup>1\*</sup>, U. NARKIEWICZ<sup>1</sup>, W. ARABCZYK<sup>1</sup>,  
M. J. WOŹNIAK<sup>2</sup>, K. J. KURZYDŁOWSKI<sup>2</sup>

<sup>1</sup>Institute of Chemical and Environment Engineering, Szczecin University of Technology,  
ul. Pułaskiego 10, 70-322 Szczecin

<sup>2</sup>Faculty of Materials Science and Engineering, Warsaw University of Technology,  
ul. Wołoska 141, 02-507 Warsaw, Poland

Decomposition of ethane over cobalt nanoparticles was studied in isothermal conditions in the temperature range 375–500 °C. The obtained products were examined using XRD and HR-TEM techniques. Carbon deposit was reduced by a flow of hydrogen in the temperature range 500–575 °C. The kinetics of hydrocarbon decomposition and carbon deposit hydrogenation were investigated using the thermogravimetry method. The values of apparent activation energies of these processes have been determined.

Key words: *cobalt; encapsulates; nanotubes; thermogravimetry; TEM; XRD*

## 1. Introduction

Nanocrystalline ferromagnetic metals have found a wide range of application, including high-density magnetic data storage, magnetic toners in xerography, fillers in polymers or ferrofluids [1]. Because nanometals have a very high surface area to volume ratio and high reactivity, they have many considerable disadvantages and are prone to environmental degradation. This feature restricts a potential industrial application of nanocrystalline metals. One of the ways to protect metal nanoparticles is to encapsulate the particles in resistant graphitic shells. Carbon coating protects the particles against oxidation and ensures their stability in air and corrosive liquids. Carbon encapsulated magnetic metals are interesting candidates for many bio-engineering applications including drug delivery, biosensors, magnetic hyperthermia and magnetic contrast agents for magnetic resonance imaging [2–6]. Many methods have been used to prepare carbon-encapsulated magnetic nanoparticles such as arc discharge technique [7–10], laser technique [11] or catalytic method [12–24]. A catalytic method

---

\*Corresponding author, e-mail: mpodsiadly@ps.pl



generally involves decomposition of carbon-containing molecules such as hydrocarbons or CO on metal particles. In this work, a study of preparation of carbon-coated cobalt nanocapsules by decomposition of ethane over cobalt nanoparticles has been presented.

## 2. Experimental

The preparation of cobalt nanoparticles and carbon coated cobalt nanoparticles has been described in our previous papers [25, 26]. To synthesize Co(C) nanoparticles cobalt(II) nitrate, calcium nitrate and aluminum nitrate were used. The salts were dissolved in water. A solution of 25%  $\text{NH}_{3(\text{aq})}$  was added to obtain pH equal to 8. Metal hydroxides were precipitated from the solutions; the obtained deposit was washed with water, filtered and dried at 70 °C. The next preparation step was calcination at 500 °C for one hour to obtain the precursor of nanocrystalline cobalt – cobalt oxide (with small amounts of structural promoters – CaO and  $\text{Al}_2\text{O}_3$ ). The role of structural promoters was to stabilise the nanocrystalline cobalt structure at elevated temperatures. The chemical composition of the samples was determined using inductively coupled plasma atomic emission spectroscopy (ICP-AES, JY 238 Ultrace, Jobin Yvon). The samples of cobalt precursor containing 0.2% CaO, 1.5%  $\text{Al}_2\text{O}_3$  were obtained. Cobalt oxide powder was pressed, crushed and sieved to obtain a grain size fraction in the range of 1.2–1.5 mm. Reduction of cobalt oxide, cobalt carburisation and carbon deposit hydrogenation were carried out in a differential reactor with thermogravimetric mass measurement. A sample of cobalt oxide of 0.5 g was placed as a single layer of grains in a platinum basket. The reduction process was carried out in the temperature range of 25–500 °C, with the heating rate of 10 °C/min, under pure hydrogen (99.999%) flow (20  $\text{dm}^3/\text{h}$ ). The carburisation process was performed under pure ethane (99.95%) flow (20  $\text{dm}^3/\text{h}$ ) in the temperature range of 375–500 °C. After carburisation, the samples were cooled in helium (99.9996%) flow or reduced under hydrogen flow (20  $\text{dm}^3/\text{h}$ ) in the temperature range of 500–575 °C. The phase compositions of the samples were determined using the XRD technique (Philips X'Pert Pro,  $\text{CuK}_\alpha$  radiation). The cobalt surface area was determined using the BET technique (Micrometrics ASAP 2010). The morphology of the samples after carburisation was characterized using HRTEM method (Jeol JEM 3010).

## 3. Results and discussion

The average crystallite size of cobalt particles, estimated using Sherrer's equation and was equal to 90 nm. The surface area measured by the BET method was equal to 14.6  $\text{m}^2/\text{g}$ . Based on the BET data, the particle size was also calculated, assuming that the particles are spherical, from the equation:

$$d = \frac{6}{S\rho} \quad (1)$$

were  $d$  [m] is the average size of a spherical crystallite,  $S$  [m<sup>2</sup>/g] is the specific surface area, and  $\rho$  – the density of cobalt ( $8.9 \times 10^6$  g/m<sup>3</sup>). The calculated grain size was equal to 46 nm being twice smaller than the measured value. The difference is due to the grain size distribution of cobalt crystallites.

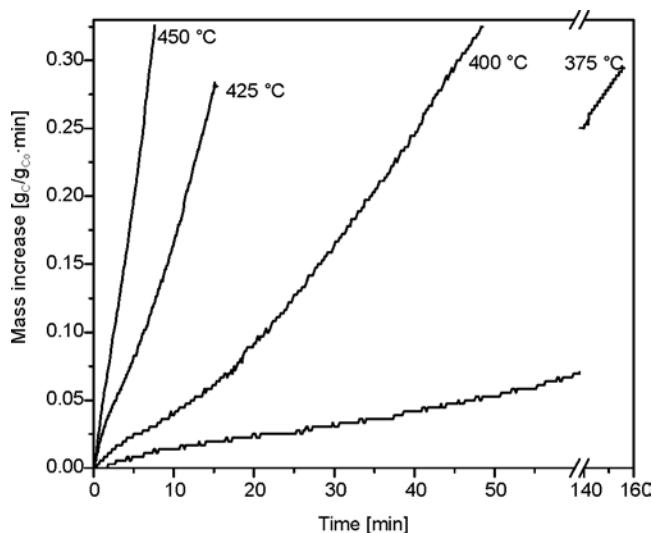


Fig. 1. TG curves of cobalt carburisation under ethane atmosphere at various temperatures

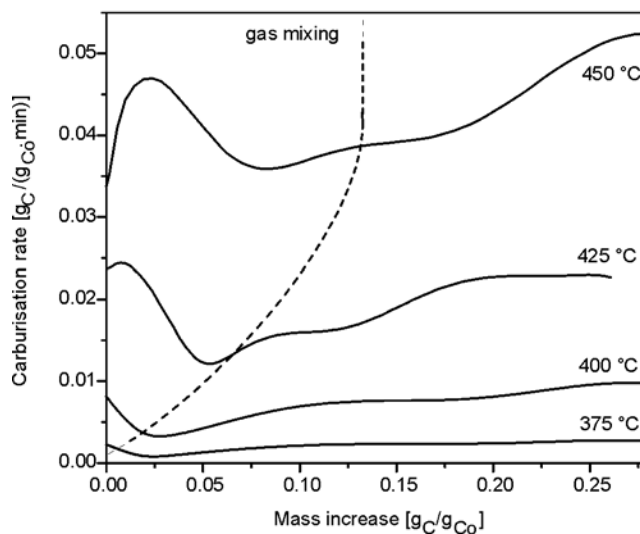


Fig. 2. DTG curves of cobalt carburisation under ethane at various temperatures

Directly after reduction, the samples were carburised in the same reactor under pure ethane flow. The process of ethane decomposition over cobalt was investigated in the temperature range of 425–500 °C. Figure 1 shows the TG lines illustrating sample mass increase during the carburisation process. Figure 2 presents the changes of the reaction rate during the carburisation process (DTG curves). The shape of TG and DTG curves are similar at all temperatures. The shapes of these lines are also similar to those recorded during methane decomposition over cobalt [27]. This may suggest that the mechanism of decomposition of both gases on nanocrystalline cobalt is probably the same. At the beginning of carburisation process, the reaction rate increases because the hydrocarbon content in the gas flow increases as a result of replacing hydrogen with ethane. The time necessary to fully fill the reactor volume with hydrocarbon is equal to 3.5 min. After this time (marked in Fig. 2 as a dotted line) only ethane is present in the reactor volume. Ethane decomposition leads to a formation of carbon layers which cover the metal surface. As a result, the reaction rate decreases and reaches a minimum. At the next stage of the process, the rate of carburisation increases. One of the ways to explain the fact of increase of the carburisation rate after blocking the cobalt surface by carbon is the ability of hydrocarbon to decompose over the carbon deposit [28]. Another possible explanation is a growth of carbon nanotubes on a free metal particle, detached from the metal surface (end growth) or from a free part of the particle still connected with the bulk (base growth). The rate of ethane decomposition over cobalt is expressed by the equation:

$$r = kp_{\text{C}_2\text{H}_6} \quad (2)$$

where  $k$  is the rate constant of ethane decomposition,  $r$  is the carburisation rate and  $p_{\text{C}_2\text{H}_6}$  is ethane partial pressure in the reaction mixture. However, carburisation is performed under pure ethane so hydrocarbon pressure is equal to 1 and Eq. (2) can be rewritten as:

$$r = k \quad (3)$$

The values of reaction constant rates were taken from a section of DTG curves (Fig. 2) where carburisation degree is equal to 0.17 gC/gCo. Close to this carburisation degree, the DTG lines are almost horizontal – the reaction rate is constant. Using these values, the Arrhenius dependence for ethane decomposition was plotted (Fig. 3). The value of apparent activation energy was calculated from this dependence as equal to 150 kJ/mol.

The XRD pattern of sample after carburisation at 500 °C is presented in Fig. 4. The cobalt oxide phase was reduced during reduction process and peaks characteristic of metallic cobalt were found. Cobalt exists in two forms: hexagonal close packed (*hcp*) and face centred cubic (*fcc*). The XRD pattern shows a relatively sharp peak of carbon around  $2\theta = 26.01^\circ$ . That peak is shifted in comparison with carbon pattern ( $2\theta = 26.43^\circ$ ). The interlayer spacing value of (002) diffraction peaks calculated from this

profile was 0.342 nm. Nanoparticles of cobalt are very prone to oxidation in air. Due to carbon coating, the metal surface is protected against oxidation and the peaks attributed to cobalt oxide have very low intensity.

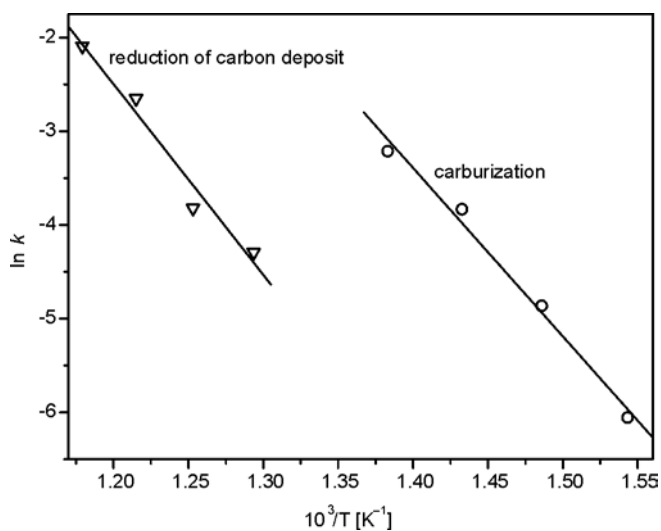


Fig. 3. Arrhenius plots of carburisation and reduction of carbon deposit processes

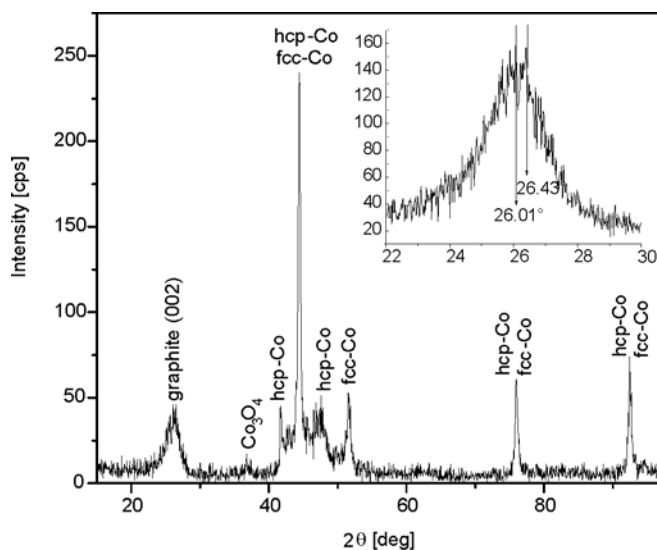


Fig. 4. The XRD patterns of a sample after carburisation at 500 °C, and a magnified image of the (002) diffraction profiles of carbon (inset)

The process of carbon deposit hydrogenation is one of the ways of purification of carbon products [29, 30]. During reduction with hydrogen, at an appropriate tempera-

ture, amorphous carbon can be removed from the sample. Before hydrogenation, each sample was carburised under ethane at 500 °C to obtain carbon content of ca. 0.35 gC/gC<sub>0</sub>. Then the carburised samples were reduced under hydrogen in isothermal conditions at temperatures from 500 °C to 575 °C. The hydrogenation was carried out until constant mass of the sample was obtained. The thermogravimetric data (not shown here) were used to plot time dependences of the conversion degree (Fig. 5). The experimental results were then fitted with the equation:

$$\alpha = A(1 - \exp(-kt)^n) \quad (4)$$

where  $\alpha$  is the conversion degree,  $A$  is the maximum conversion degree,  $k$  is reaction rate constant,  $t$  is time and  $n$  is a time-independent parameter.

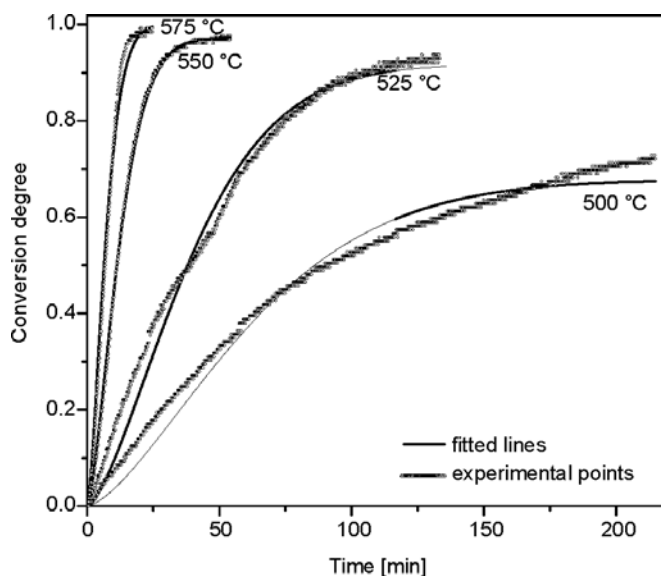


Fig. 5. Time dependence of the conversion degree of the process of hydrogenation of carbon deposit

The value of  $A$  depends on temperature. At lower temperatures, the conversion degree reaches lower values and more carbon still remains in a sample. When hydrogenation temperature is higher, more carbon is reduced and the conversion degree reaches the highest value equal to 1; carbon is totally removed from the sample. The values of  $A$ ,  $k$ , and  $n$  have been calculated from Eq. (4). The results are given in Table 1.

The values of reaction constant rates calculated from Eq. (3) were used to plot the Arrhenius dependence (Fig. 3). The apparent activation energy of hydrogenation process was determined from the Arrhenius dependence as equal to 170 kJ/mol.

A high resolution TEM image of a sample after carburisation at 500 °C is presented in Fig. 6. The TEM micrograph shows that the carbon nanotubes, carbon fib-

bres and carbon encapsulated cobalt nanoparticles are products of the synthesis. TEM observation also showed that cobalt particles are trapped at the ends of nanotubes.

Table 1. Parameters of the hydrogenation process

$T$ [°C]	$k$	$R^2$	$n$	$A$	$E_a$ [kJ/mol]
500	0.01367	0.988	1.4	0.69	170
525	0.02188	0.993		0.99	
550	0.07066	0.996		0.99	
575	0.12341	0.987		1.00	

Only small cobalt particles (with diameters of 20–30 nm) are encapsulated into the nanotubes or fibres; thus these structures can grow only from particles with the size smaller than 30 nm. The width of these nanotubes depends on cobalt particle sizes. When a cobalt particles were larger than 30 nm, carbon-coated cobalt particles were obtained. TEM image of these nanoparticles shows a metallic core and a graphite shell. The interplanar distance between two adjacent graphene planes was about 0.340 nm, the value being in good agreement with the value of interlayer spacing calculated from carbon diffraction profile (Fig. 4, inset). Both of these interplanar distances are close to the (002) lattice distance in graphite (0.335 nm). The observed higher lattice spacing was attributed to the defects in the graphite structure. The thickness of the coating shell of nanocapsules is about 15–20 nm which gives 45–60 graphene layers.

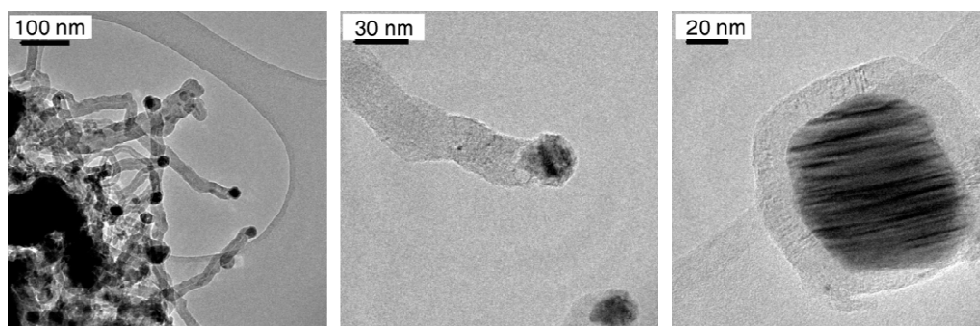


Fig. 6. The HRTEM micrographs of a sample carburised at 500 °C

#### 4. Conclusions

Ethane decomposes on nanocrystalline cobalt at temperatures above 375 °C. The apparent activation energy of the cobalt carburisation process is about 150 kJ/mol. The obtained product contains multiwall carbon nanotubes of the diameter of approximately 20–30 nm, ended with cobalt nanoparticles of the same diameter. Cobalt nanoparticles having diameters greater than 30 nm are encapsulated by carbon coating composed of 40–60 graphene layers. The products of cobalt carburisation can be hydrogenated in

order to remove amorphous carbon (at lower temperatures, ca. 500 °C) or to completely remove carbon and obtain pure dispersed nano-cobalt (hydrogenation process in this case should be conducted above 550 °C).

### References

- [1] LIU B.H., DING J., ZHONG Z.Y., DONG Z.L., WHITE T., LIN J.Y., Chem. Phys. Lett., 358 (2002), 96.
- [2] PAUSER S., RESZKA R., WAGNER S., Anti-Cancer Drug Des., 112 (1997), 125.
- [3] RUDGE S.R., KURTZ T.L., VESSELY C.R., CATTERALL L.G., WILLIAMSON D.L., Biomater., 21 (2000), 1411.
- [4] GOODWIN S., PETERSON C., HOH C., BITTNER C., J. Magn. Magn. Mater., 194 (1999), 132.
- [5] RUDGE S., PETERSON C., VESSELY C., KODA J., STEVENS S., CATTERALL L., J. Control. Rel., 74 (2000), 335.
- [6] JAIN T.K., MORALES M.A., SAHOO S.K., LESLIE-PELECKY D.L., LABHASETWAR V., Mol. Pharm., 2 (2005), 194.
- [7] BONARD J.M., SERAPHIN S., WEGROWE J.E., JIAO J., CHATELAIN A., Chem. Phys. Lett., 343 (2001), 251.
- [8] SESHADRI R., SEN R., SUBBANNA G.N., KANNAN K.R., RAO C.N., Chem. Phys. Lett., 231 (1994), 308.
- [9] SUN X., GUTIERREZ A., YACAMAN M.J., DONG X., JIN S., Mater. Sci. Eng. A, 286 (2000), 157.
- [10] JIAO J., SERAPHIN S., J. Phys. Chem. Solids, 61 (2000), 1055.
- [11] KWOK K., CHIU W.K., Diamond & Related Mat. 15 (2006), 1438-1446.
- [12] LIU B.H., DING J., ZHONG Z.Y., DONG Z.L., WHITE T., LIN J.Y., Chem. Phys. Lett., 358 (2002), 96.
- [13] ZHONG Z., LIU B., SUN L., DING J., LIN J., TAN K.L., Chem. Phys. Lett., 362 (2002), 135.
- [14] MA X., CAI Y., LI X., WEN S., Mater. Sci. Eng. A, 357 (2003), 308.
- [15] LIM S., SHIMIZU A., YOON S.H., KORAI Y., MOCHIDA I., Carbon 42 (2004), 1273.
- [16] HERNADI K., FONSECA A., NAGY J.B., SISKA A., KIRIESI I., Appl. Catal. A-Gen. 199 (2000), 245.
- [17] QIAN W., LIU T., WEI F., WANG Z., LI Y., Appl. Catal. A, 258 (2004), 121.
- [18] WANG Z.H., CHOI C.J., KIM B.K., KIM J.C., ZHANG Z.D., Carbon, 41 (2003), 1751.
- [19] LIU S., BOESHORE S., FERNANDEZ A., SAYAGUES M.J., FISHER J.E., GEDANKEN A., J.Phys. Chem. B, 105 (2001), 7606.
- [20] ZHANG Y., SMITH K.J., Catal. Today, 77 (2002), 257.
- [21] WANG H.Y., RUCKENSTEIN E., Carbon, 40 (2002), 1911.
- [22] AVDEEVA L.B., KOCHUBEY D.I., SHAIKHUTDINOV SH.K., Appl. Catal. A, 117 (1999), 43.
- [23] ZHONG Z., CHEN H., TANG S., DING J., LIN J., TAN K.L., Chem. Phys. Lett. 330 (2000), 41.
- [24] RANA R.K., XU X.N., YESHURUN Y., GEDANKEN A., J. Phys. Chem. B, 106 (2002), 4079.
- [25] LENDZION-BIELUŃ Z., PODSIADLY M., NARKIEWICZ U., ARABCZYK W., Rev. Adv. Mater. Sci., 12 (2006), 145.
- [26] NARKIEWICZ U., PODSIADLY M., PELECH I., ARABCZYK W., WOŹNIAK M.J., KURZYDŁOWSKI K.J., Solid State Phenom. 128 (2007), 249.
- [27] NARKIEWICZ U., PODSIADLY M., ARABCZYK W., WOŹNIAK M.J., KURZYDŁOWSKI K.J., Mater. Sci Eng. C, in press.
- [28] BAI Z., CHEN H., LI B., LI W., J. Anal. Appl. Pyrol., 73 (2005), 335.
- [29] IVANOV V., FONSECA A., NAGY J.B., LUCAS A., LAMBIN P., BERNARTS D., ZHANG X.B., Carbon, 33 (1995), 1727.
- [30] HERNADI K., FONSECA A., NAGY J.B., BERNAERTS D., RIGA J., LUCAS A., Synt. Metals, 77 (1996), 31.

*Received 28 April 2007*

*Revised 16 February 2008*

# **Structure and properties of polyurethane nanocomposites modified by dibutyl phosphate boehmite**

J. RYSZKOWSKA\*, M. JURCZYK

Warsaw University of Technology, Faculty of Materials Science and Engineering,  
ul. Wołoska 141, 02-507 Warsaw, Poland

The paper reports on the application of the quantitative analysis of images to describe morphological properties of nanocomposites composed of polymers and organically modified boehmite. Images of boehmite, as well as the fracture and cut surfaces of composites, were obtained using high resolution electron microscopy technique and atomic force microscopy. Quantitative analysis of the images of fracture structure obtained by the SEM technique allowed one to explain the mechanism of changes of the mechanical properties of polyurethane nanocomposites. Parameters of stereological analysis were used to evaluate the diameter of the agglomerates of nanofillers and the analysis of relationships between the nanocomposite structure and properties.

*Key words: image analysis; nanocomposite; boehmite; polyurethane; dibutyl phosphate; thermal analysis*

## **1. Introduction**

Polymer composites are manufactured for many applications such as automobiles, aerospace functions, etc. One of the dimensions of the fillers of new materials is of the order of a nanometres. The combination of mechanical, thermal and electrical properties of a material and low concentration of the filler necessary to produce changes in the polymer matrix, has generated much interest in the field of nanocomposites. The nanocomposites can be fabricated and processed in ways similar to those employed for conventional polymer composites. The transition from microparticles to nanoparticles causes difficulties, and only nanoscale can dramatically change physical properties [1–3]. Physical properties of nanocomposites are greatly influenced by the size scale of their components and the degree of mixing between the two phases. Depending on the method of preparation, the nature of the polymer matrix and of the nanofillers, composites significantly differing in properties can be obtained [3]. Properties of polymer-

---

\*Corresponding author, e-mail: jrysz@meil.pw.edu.pl



clay nanocomposites depend on the interaction mechanism between the polymer and clay. The differences in interaction between these phases result from the polarity, molecular weight, hydrophobicity, reactive groups, etc. of the polymer, the type of solvent, and the clay mineral type.

Various techniques of characterisation have been used in polymer research [2]. The commonly used techniques are scanning electron microscopy (SEM), transmission electron microscopy (TEM), atomic force microscopy (AFM), wide-angle X-ray diffraction (WAXD), and small-angle X-ray diffraction (SAXS) [3]. AFM and SEM are also required to characterize nanoparticle dispersion or distribution.

Imaging has already become a universal tool in many areas of science and engineering. Usually only the results of the qualitative analysis of microscopic observations are published, a quantitative image analysis of nanocomposite structure being rarely performed.

The paper presents the application of quantitative image analysis to describe morphological properties of boehmite and its nanocomposites. Nanosized ceramics, highly dispersed into polymer matrix materials, are widely investigated in terms of modification of polymer properties. The addition of ceramics with primary particle sizes of several nanometres allows specific tailoring of relevant thermal properties, e.g. lowering of the peak heat release rates (PHRR). The aim of our activities is to produce improvements in the fire performance of polyurethane. The nanocomposites were composed of polymers and organically modified boehmite. Boehmite is laminar aluminum oxyhydroxide with generalized formula  $\text{AlO}(\text{OH})$  and is used as a flame retardant. It was modified with dibutyl phosphate. Modification with dibutyl phosphate causes changes of size and shapes of the boehmite grain. The combination of phosphate and clays in polyurethanes for higher flame retardant effects was studied.

In this paper, the influence of the quantity of boehmite and the size of agglomerate on the thermal and mechanical properties is presented.

## 2. Experimental

*Materials.* Dibutyl phosphate was supplied by Aldrich. Boehmite was modified by reaction with dibutyl phosphate for 1 h by the reported procedure [4]. Components used for PU synthesis were: poly(ethylene adipate) (PEA) mol. wt. 2000 Alfaster T620 (Alfa Systems), 4,4'-diphenylmethane diisocyanate (MDI), Isonate M 125 (Dow Chemical), glycol (G1) and glycerine (G2) – G1, G2 (POCH).

*Preparation of polyurethane/boehmite composite.* Polyurethane nanocomposite matrices with the PEA:MDI:G1:G2 molar ratio of 6:9:2:1 were synthesized. Boehmite was added to the PU matrix in 0.5, 1.5, and 3.5 wt. % (Table 1). All samples were synthesized by a one-step method in *in situ* polymerization. Samples were formed by casting. The curing reaction was performed at 120 °C for 16 h. Samples were aged at

room temperature for 14 days. Determination of the density of polyurethane and nanocomposites was performed according to ISO 2781.

*SEM observations.* The microstructure of nanocomposites was investigated on microsection and fracture surfaces. The fracture surface was obtained by breaking at liquid nitrogen temperature ( $-196\text{ }^{\circ}\text{C}$ ). Then the samples were coated with a thin film of carbon. The morphology of boehmites and nanocomposites was characterized by high resolution scanning electron microscopy (HRSEM) LEO 1530.

*Image analyses.* Surface images were subject to graphic treatment by manual detection of particle contours. The obtained contour was transferred to the MicroMeter program, a quantitative analysis was performed and the equivalent diameter ( $d_2$ ) of the agglomerate was calculated [5]. Measurements were performed for at least 200 agglomerates.

*AFM observations.* AFM topographic images were obtained using a Multimode Nanoscope IIIa (Digital Instrument INC., USA) working in a tapping mode. Nanocomposite samples were microtomed at  $-10\text{ }^{\circ}\text{C}$  using a glass knife with microtome Leica RM 2165 with system LN 21.

*Thermal analyses.* The properties of the fire reaction were investigated using a cone calorimeter according to the standard method prescribed in ISO 5660 at the heat flux equal to  $50\text{ kW/m}^2$ . The nanocomposite samples  $100\times 100\text{ mm}^2$  in size and 4 mm thick were held in retaining frames protecting the specimen edges during testing. Each experiment was repeated three times. Peak heat release rate (PHRR), total heat release (THR), average specific extinction area (SEA), and time-to-ignition ( $t_{ig}$ ) have been measured.

*Mechanical properties.* A tensile test was performed using an Instron 1115 tensile tester. The samples were elongated at the rate of 500 mm/min according to ISO 527. Hardness was measured using an indentation hardness tester according to ASTM D2240-75, abrasive wear was measured according to ISO 4649.

### 3. Results and discussion

Particles of modified boehmite form agglomerates. Modification with tributyl phosphate causes changes of size and shapes of boehmite grains (Fig. 1). The boehmite structure changes after the modification, and the particles form oval and fibre grains (Fig. 1). The modification caused the reduction of specific area of powders from  $209.7\text{ m}^2/\text{g}$  for unmodified boehmite to  $39.9\text{ m}^2/\text{g}$  for modified tributyl phosphate boehmite.

The microstructure of nanocomposites was investigated on the fracture surface; exemplary SEM images are presented in Fig. 2. Figure 3 presents binary images on the fracture surface of boehmite agglomerates in the polyurethane matrix.

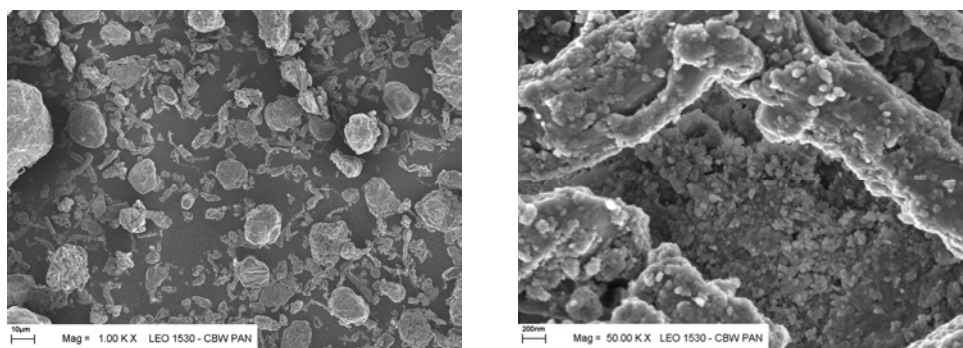


Fig. 1. SEM images of modified boehmite: agglomerate (left), structure of agglomerate (right)

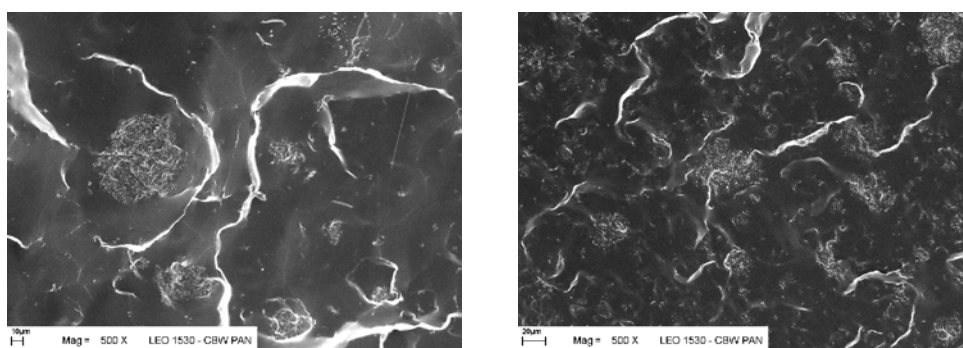


Fig. 2. SEM images of the fracture surfaces of nanocomposites with modified boehmite: 1.5 wt. % (left) and 3.5 wt.% (right)

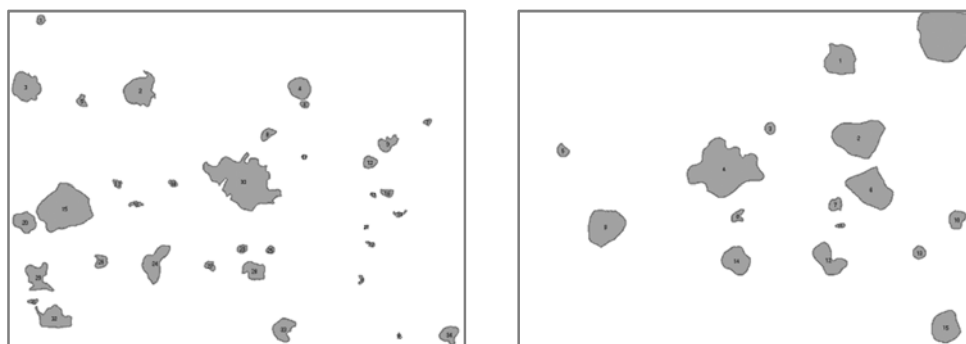


Fig. 3. Binary images of agglomerates of modified boehmite in the polyurethane matrix: 1.5 wt. % (left) and 3.5 wt.% (right) of boehmite

The results of the analysis of the sizes of boehmite agglomerates in the polyurethane matrix are given in Table 1.

Table 1. Sample identification and composition

Identification	Composition	Size of agglomerate, $d_2$ [ $\mu\text{m}$ ]
PU/B1	polyurethane + modified boehmite 0.5 wt. %	$16.7 \pm 9.2$
PU/B2	polyurethane + modified boehmite 1.5 wt. %	$23.2 \pm 12.7$
PU/B3	polyurethane + modified boehmite 3.5 wt. %	$26.1 \pm 14.4$
PU/BN	polyurethane + unmodified boehmite 3.5 wt. %	$38.5 \pm 13.6$

Figure 4 shows time dependences of the heat release rate (HRR) for polyurethane and a nanocomposite with 3.5 wt. % of modified boehmite. In the case of the nanocomposite, lower peak heat release rates (PHRR) were always combined with a reduction of the time to ignition (from 48 s for PU to 29 s for nanocomposites). Average smoke density did not change.

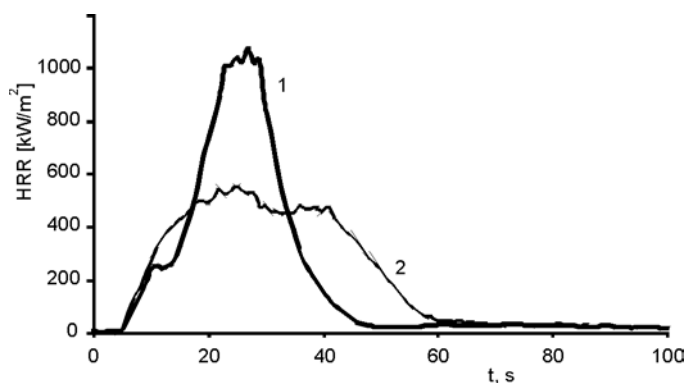


Fig. 4. Heat release rate curves for samples of polyurethane (1) and polyurethane with 3.5% of modified boehmite (2)

Table 2. Selected physico-mechanical properties of the samples

Sample	Density [ $\text{g}/\text{cm}^3$ ]	Tensile strength [MPa]	Elongation at break [%]	Tension set [%]	Abrasive wear [ $\text{cm}^3$ ]
PU	1,2274	39,4	500	2,1	24,4
PU/B1	1,2341	17,6	605	4,6	32,9
PU/B2	1,2385	22,1	660	6,8	32,9
PU/B3	1,2433	25,8	580	7,5	31,4
PU/BN	1,2456	42,6	580	4,4	64,3

The tensile strength of nanocomposites with modified boehmite is lower than that of neat polyurethane (Table 2). Addition of unmodified boehmite causes a double increase of the abrasive wear, and addition of modified boehmite causes an increase of the abrasive wear of about 10% (Table 2).

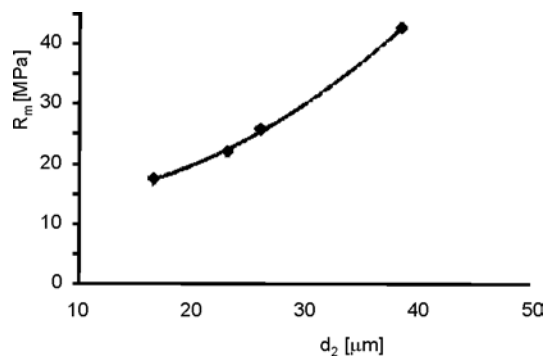


Fig. 5. Dependence of the tensile strength on the diameter of the agglomerate

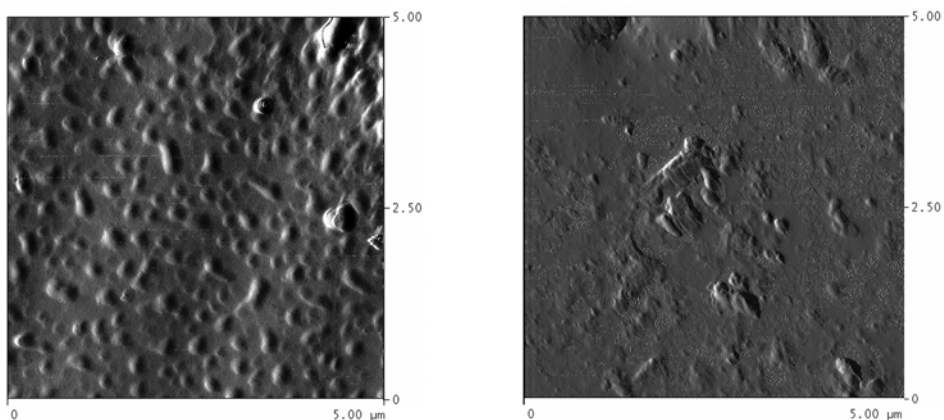


Fig. 6. AFM images of the surface of the cross sections of nanocomposites with 0.5 wt. % (left) and 1.5 wt. % of modified boehmite

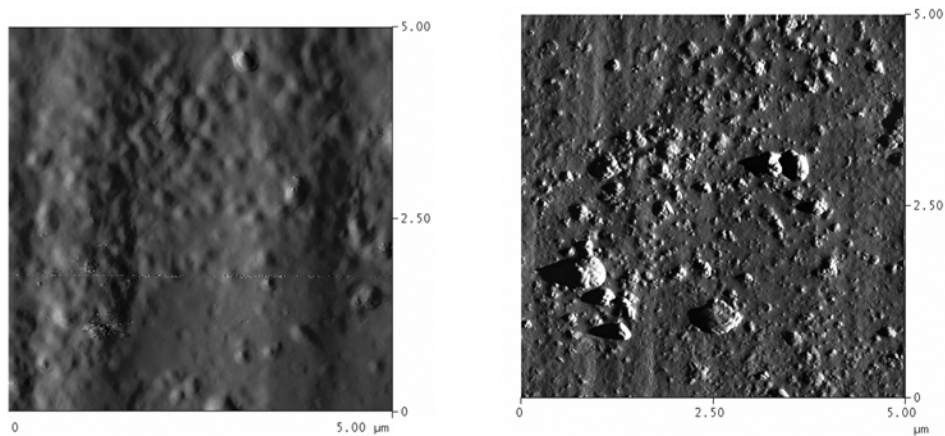


Fig. 7. AFM images of the surfaces of the cross sections of nanocomposites with 3.5 wt. % of modified boehmite (left) and unmodified boehmite (right)

It can be expected that the nanoparticle homogeneous dispersion will not change the value of the nanocomposite abrasive wear. To explain the reason for the lower tensile strength of nanocomposites with boehmite, the dependence of the tensile strength on the diameter of an agglomerate was analysed, and the results are shown in Fig. 5. It was found that the tensile strength increases with the increasing diameter of the agglomerate of boehmite.

Physical properties of nanocomposites depend on properties of polymer matrices. The change of the elongation at break and tension set could suggest that during synthesis the domain structure of polyurethane matrix changes. This observation was confirmed by the AFM image analysis (the surface was scanned between agglomerates of boehmite) (Fig. 6, 7) and the density measurements (Table 2). Phosphate compounds influence the reaction kinetics of polyurethane substrates, and this may cause formation of the polyurethane domain structure.

#### 4. Conclusion

Boehmite modified with tributyl phosphate reduced the peak heat release rates of polyurethane nanocomposites but also reduced the time to ignition. A better dispersion in the polymer matrix is necessary for optimizing this potentially new class of fire retardant additives. The results show that boehmite based nanocomposites may be used for the preparation of halogen-free and environmentally friendly flame retardant polyurethane materials. The change in polymerization of polyurethane matrix needs to be explained by further research.

#### Acknowledgement

The authors acknowledge Prof. Z. Florjańczyk and Mrs. A. Wolak for supplying the modified boehmite. This scientific work was funded from the finances for education in the years 2005–2008 as research project No. 3T08E/04527.

#### References

- [1] SCHULZ M.J., KELKAR A.D., SUNDARESAN M.J., *Nanoengineering of Structural, Functional and Smart Materials*, CRC Taylor and Francis, New York, 2006.
- [2] GOGOTSI Y., *Nanomaterials Handbook*, CRC Taylor and Francis, New York, 2006.
- [3] MAI Y. -W., YU Z. -Z., *Polymer Nanocomposites*, CRC Press, Boca Raton, 2006.
- [4] FLORJAŃCZYK Z., ROGALSKA-JOŃSKA E., NAWROCKA K., MOLEND A., AFFEK M., *Polimery*, 47 (2002), 611.
- [5] RUSS J.C., DEHOFF R.T., *Practical Stereology*, Plenum Press, New York, 1999.

Received 28 April 2007  
Revised 16 February 2008

# Structural and textural evolution of zirconia nanocrystals induced by thermal treatment

A. ADAMSKI<sup>1\*</sup>, P. JAKUBUS<sup>2</sup>, Z. SOJKA<sup>1,3</sup>

<sup>1</sup>Jagiellonian University, Faculty of Chemistry, ul. Ingardena 3, 30-060 Cracow, Poland

<sup>2</sup>Szczecin University of Technology, Institute of Chemistry and Environment Protection, al. Piastów 42, 71-065 Szczecin, Poland

<sup>3</sup>Regional Laboratory of Physicochemical Analyses and Structural Research, ul. Ingardena 3, 30-060 Cracow, Poland

Nanometric tetragonal and monoclinic zirconia was synthesized from zirconyl chloride by the modified forced hydrolysis method. Phase transitions and morphological changes accompanying zirconia calcination in the temperature range 600–1000 °C were studied by XRD, HR-TEM techniques and N<sub>2</sub>-porosimetry. Ageing of the amorphous hydrous zirconia at 100 °C for 48 h in the mother solution and its subsequent calcination at 600 °C for 6 h strongly favoured formation of single-phase tetragonal ZrO<sub>2</sub> of the thermal stability enhanced by 250 °C. Influence of the calcination temperature on phase composition, grain size, grain boundaries and pore structure of the resultant ZrO<sub>2</sub> material was analyzed.

Key words: *nanostructured ZrO<sub>2</sub>; polymorphism; thermal evolution; grain size*

## 1. Introduction

Growing importance of nanosized zirconium dioxide in various practical applications is strongly related to its unique structural and physicochemical properties which remain decisive also for designing smart materials, tailored specifically to satisfy particular industrial needs. The most spectacular applications of ZrO<sub>2</sub> and related systems include ceramics, piezoelectrics, refractories, pigments, solid electrolytes and oxygen sensors [1, 2]. After morphological, textural and chemical valorization such materials can also be used in catalysis as active phases or supports [3, 4]. Many zirconia applications require high surface area development which should remain stable under process conditions. In the case of ZrO<sub>2</sub>, structural and textural properties are strongly related to

---

\*Corresponding author, e-mail: adamski@chemia.uj.edu.pl

its specific polymorphism. The crystalline structures of three  $\text{ZrO}_2$  polymorphs such as low-temperature monoclinic ( $P2_1/c$ ), high-temperature tetragonal ( $P4_2/nmc$ ) and cubic ( $Fm\bar{3}m$ ) ones have been extensively studied [5, 6], however the extension of temperature windows of the occurrence of the two high-temperature phases is still a subject of research. These polymorphs cannot simply be quenched to room temperature, because they spontaneously undergo a martensitic transition to the monoclinic form. They can, however, be effectively metastabilized by an appropriate bulk doping [4] or by controlling the size of particles [7]. Metastable phases are considered to be much more useful in many practical applications. Their principal advantages are related to a higher surface area and better developed pore structure. Therefore, an optimization of preparation procedure, leading to a desired form of zirconium oxide remains very often a vital necessity. A common route for preparation of zirconia consists in precipitation of a hydrous gel from aqueous solutions of a precursor salt and subsequent calcination of the amorphous precipitate. Short range ordering of oligomeric species formed in the parent solution containing fresh zirconia gel determines the spatial structure of the molecular framework, playing the role of a matrix for the topotactic crystallization of zirconia in a particular polymorph [8, 9]. Very important in this context is the role of ageing. Phase-oriented  $\text{ZrO}_2$  synthesis should, however, include not only the control of parameters influencing zirconia proto-structures in aqueous solutions, but also of those which remain important during subsequent solid state changes accompanying thermal treatment.

The processes occurring during zirconia precipitation have already been discussed elsewhere [10]. In the present paper, influence of thermal treatment on the phase composition, crystal growth, and the textural properties of the resultant zirconium oxide will be analyzed based on the XRD and HR-TEM results, completed with  $\text{N}_2$ -porosimetry.

## 2. Experimental

Hydrous zirconia samples were obtained by the forced hydrolysis method from 0.6 M aqueous solutions of  $\text{ZrOCl}_2 \cdot 8\text{H}_2\text{O}$  (Aldrich 99.99 %) with 25% ammonia at temperatures ranging from ambient temperature to 100 °C. Wet precipitate was washed with dilute  $\text{NH}_4\text{NO}_3$  solution until negative test for  $\text{Cl}^-$  ions, and then divided into two parts. The first part was aged in the mother liquor (at  $\text{pH} \approx 9$ ) at 100 °C for 48 h under reflux and at the periodical supplementation of  $\text{NH}_3(\text{aq})$ , then dried at 100 °C for 24 h, and calcined in air at 600 °C for 6 h. The other part was not subject to ageing, separated from the parent solution, dried and subsequently calcined in the same conditions.

X-ray diffraction patterns of the dried and calcined samples were recorded with the DRON-3 diffractometer (Bourestnik, Russia) equipped with an iron filter, using



CuK $_{\alpha}$  and CoK $_{\alpha}$  radiations. The phase composition of the samples was calculated from the following equations:

$$X_t = \frac{I_t(111)}{I_t(111) + I_m(111) + I_m(11\bar{1})} \quad \text{and} \quad X_m = 1 - X_t \quad (1)$$

where  $X_t$  and  $X_m$  stand for the fractions of the tetragonal and the monoclinic forms, respectively, whereas  $I_t$  and  $I_m$  are the intensities of their diagnostic peaks [4]. The grain size was evaluated based on the Scherrer equation [11]

$$D_{hkl} = \frac{K\lambda}{B_{hkl} \cos \theta} \quad (2)$$

where  $\lambda$  stands for wavelength of the incident X-ray,  $B$  for the full width at the half maximum,  $\theta$  is the corresponding Bragg angle and  $K$  is a constant

$$K = 2(\ln(2/\pi))^{1/2} = 0.93$$

For variable-temperature XRD experiments (VT-XRD), the samples were not pre-calcined but only dried and then heated stepwise to 1200 °C. At each 100 °C step an XRD pattern was recorded.

High resolution transmission electron microscopy (HR-TEM) was carried out using a JEM-100CX II UHR instrument (JEOL) operating at 100 kV. The specimens were prepared by deposition of the samples, ultrasonically dispersed in ethanol, on a holey carbon film supported on a copper grid.

### 3. Results and discussion

A distinct difference exists in structural response to increase of temperature between ZrO $_2$  samples prepared by conventional precipitation from aqueous solutions, i.e., without ageing, and those subject to ageing in the mother liquid at 100 °C for 48 h. As revealed by the results of VT-XRD experiments, crystallization of the amorphous non-aged hydrous zirconia occurs between 300 °C and 400 °C. In the XRD pattern recorded at 400 °C, a strong single line attributed to the (111) reflection of the tetragonal phase appeared in the diagnostic  $2\theta$  region between 25° and 33° for CuK $_{\alpha}$  radiation (or 31° and 38° for CoK $_{\alpha}$  radiation) [4] (Fig.1). Low-temperature tetragonal polymorph is a metastable phase, appearing in variable concentration in zirconia prepared by precipitation. In our case, it was the only phase existing in the temperature range of 400–600 °C. The next phase transition, related to the transformation of the metastable tetragonal ZrO $_2$  to the thermodynamically stable monoclinic one, occurred between 600 °C and 700 °C. In the XRD pattern recorded at 700 °C, a distinct line due to the (11 $\bar{1}$ ) reflection and a broadening of the (111) reflection appeared, being diag-

nostic of the monoclinic phase. Both polymorphs coexisted in the temperature range of 700–800 °C but the contribution of  $t$ -ZrO<sub>2</sub>, equal to  $X_t \approx 71.5\%$  at 700 °C decreased upon temperature increase, reaching zero after annealing of the samples at 900 °C. For the aged samples, temperatures of both phase transitions are shifted up by at least 100 °C, as can be seen in Fig. 1. Aged ZrO<sub>2</sub>· $x$ H<sub>2</sub>O crystallized between 400 °C and 500 °C in the tetragonal form and weak Bragg maxima from  $m$ -ZrO<sub>2</sub> appeared at first at 1000 °C. Disappearance of  $t$ -ZrO<sub>2</sub> has a drastic negative effect on the specific surface area of ZrO<sub>2</sub> materials (around 47% decrease). Fortunately for zirconia applications as a support, the temperature window of existence of the metastable  $t$ -ZrO<sub>2</sub> is expanded by 200 °C for aged samples in comparison to the non-aged ones.

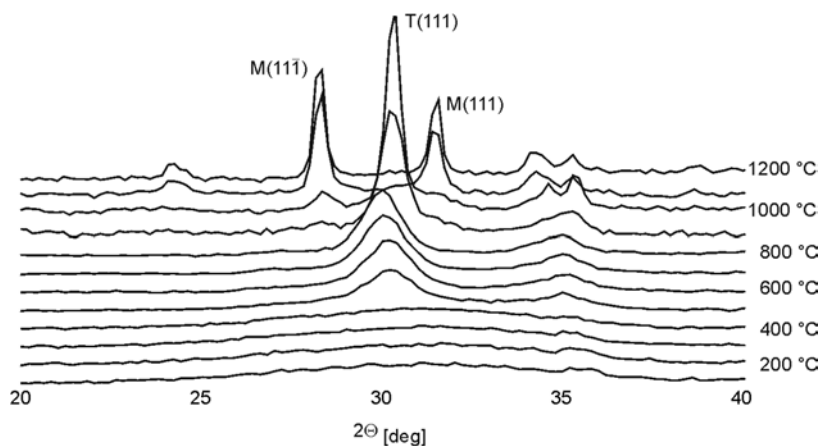


Fig. 1. Variable temperature XRD patterns (VT-XRD) for hydrous zirconia aged in the mother solution at 100 °C for 48 h

The observed differences in temperature of crystallization and in thermal decay of  $t$ -ZrO<sub>2</sub> clearly reflect differences in grain sizes and degrees of their agglomeration between non-aged and aged zirconia. It is noteworthy that the particle sizes of both polymorphs coexisting at 800 °C, evaluated based on Eq. (2), were always distinctly higher for the non-aged samples ( $D_t = 28.2$  nm,  $D_m = 56.3$  nm) in comparison to those obtained for aged preparations ( $D_t = 8.7$  nm,  $D_m = 39.2$  nm). Simultaneously, in both cases  $D_m$  was higher than the critical particle size for the tetragonal to monoclinic transformation, reported in the literature to be equal to 30 nm [7]. Simultaneously, as revealed by TEM images of the non-aged samples, the particles were strongly agglomerated forming a hard compact, whereas in the case of aged materials the particles were loosely arranged, preserving their distinct shape giving rise to microporosity development, observed in N<sub>2</sub>-sorption experiments.

Particle size and the nature of the grain boundaries are thus the primary factors controlling metastabilization of  $t$ -ZrO<sub>2</sub>. They can be modified by both ageing and the calcination temperature, allowing effective controlling of the  $t$ -ZrO<sub>2</sub>/ $m$ -ZrO<sub>2</sub> ratio. Figure 2 shows the dependences of the content of  $t$ -ZrO<sub>2</sub> phase on crystallite size eva-

luated from Eq. (2) for the aged (curve a) and non-aged (curve b) zirconia, heated in the temperature range 400–900 °C.

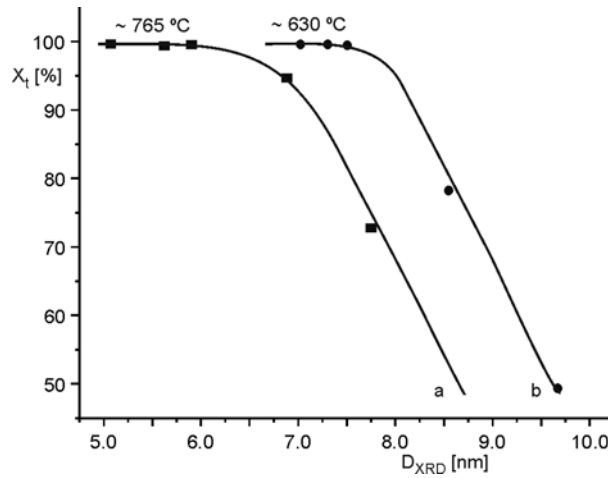


Fig. 2. Particle-size dependent changes in the  $t$ -ZrO<sub>2</sub> content in the aged (a) and non-aged (b) samples, calculated from XRD data recorded in the temperature range 400–900 °C

The content of  $t$ -ZrO<sub>2</sub> phase remained constant until  $d = 7.0$  nm and 8.5 nm for aged and non-aged samples, respectively, i.e. below the threshold particle size for metastabilization of the tetragonal ZrO<sub>2</sub> [7]. Then it severely decreased as the particle size increased due to rapid sintering caused by migration of grain boundaries. If the process of destabilization of the low-temperature  $t$ -ZrO<sub>2</sub> phase by its transformation into  $m$ -ZrO<sub>2</sub> is governed mainly by the thermodynamic properties, then neglecting the strain difference between  $t$ - and  $m$ -ZrO<sub>2</sub> crystals, the inequality should be fulfilled:

$$(G_m + \gamma_m S_m) - (G_t + \gamma_t S_t) < 0 \quad (3)$$

where  $G$  stands for the molar free enthalpy,  $\gamma$  for the surface energy and  $S$  for the surface area of the monoclinic and tetragonal phases [7]. The term  $(G_m - G_t)$  is negative at room temperature ( $-4.73$  kJ/mol [7]), thus to preserve the  $t$ -ZrO<sub>2</sub> polymorph, the term  $(\gamma_m S_m - \gamma_t S_t)$  should be positive and higher than the difference in the free enthalpies. Taking into account anomalous excess of the surface energy of the monoclinic phase ( $\gamma_m = 1.13$  J/m<sup>2</sup>) in comparison to the tetragonal one ( $\gamma_t = 0.77$  J/m<sup>2</sup>) [12], the sign of the term  $(\gamma_m S_m - \gamma_t S_t)$  depends on the surface area, which, within the spherical shape approximation, is closely related to the particle size following the equation:

$$S = \frac{6 \times 10^3}{D_{BET} \rho} \quad (4)$$

where  $\rho$  stands for the density of a given phase and  $D_{BET}$  is the particle size (in nm). The results of our porosimetric measurements, performed for non-aged and aged zir-

conia samples calcined at 600 °C for 6 h, revealed that the surface area in the case of aged zirconia,  $S = 77.05 \text{ m}^2/\text{g}$  is almost 3.5 times higher than that of the non-aged sample ( $23.28 \text{ m}^2/\text{g}$ ) [13]. Because the aged samples were purely tetragonal at 600 °C, the particle size determined from Eq. (4) using  $\rho_t = 6.10 \text{ g/cm}^3$  was equal to  $D_{BET} \approx 12.7 \text{ nm}$ , being in a nice agreement with  $D_{hkl} = 11.2 \text{ nm}$  obtained from the XRD data. This finding indicates that the entire surface is accessible for the adsorbate which is in line with the loose structure of the nanopowder observed in TEM. Thus the digestion of the hydrous zirconia in the mother liquid leads to a fine-grained  $\text{ZrO}_2$  of well developed porosity, which is more resistant to the sintering as the temperature increases and remains tetragonal over a wider temperature range. The non-aged, agglomerated zirconia is more susceptible to the transformation into monophase  $m\text{-ZrO}_2$ . The influence of ageing on the morphology and metastabilization of  $t\text{-ZrO}_2$  was discussed elsewhere [10].

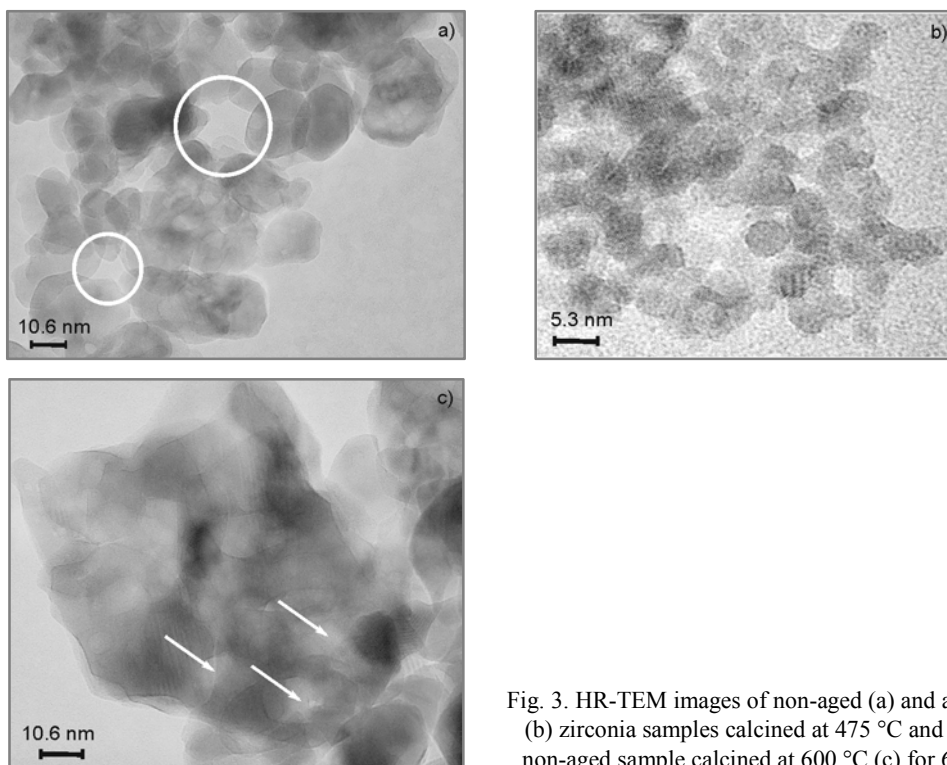


Fig. 3. HR-TEM images of non-aged (a) and aged (b) zirconia samples calcined at 475 °C and of non-aged sample calcined at 600 °C (c) for 6 h

As already mentioned, temperature increase results not only in changes in particle sizes but also in their shape. HR-TEM images taken for non-aged zirconia samples calcined at 475 °C for 24 h show numerous crystallites of a distinct size and shape variety, typical of  $t\text{-}$  and  $m\text{-ZrO}_2$  mixtures (Fig. 3a). Inspection of the corresponding XRD pattern confirmed the presence of both polymorphs. In majority, the crystallites are oval, elongated with one or two slightly marked facets. Smaller, isolated particles

of ca. 17–25 nm in diameter are accompanied by several more sintered larger grains of 34–40 nm. Very characteristic is a tendency of non-aged  $\text{ZrO}_2$  particles to agglomerate in crown-like structures which are marked with white circles in Fig. 3a. HR-TEM micrographs for aged zirconia samples calcined in the same conditions (Fig. 3b) revealed the presence of distinctly smaller non-agglomerated crystallites, typical of  $t\text{-ZrO}_2$ , generally not exceeding 6 nm. The crystallites are more oval, relatively well separated and loosely arranged. High-resolution images for samples calcined at 600 °C show distinct effects caused by temperature increase which are much more pronounced for non-aged zirconia. The arrangement of crystallites is distinctly denser in comparison to that observed after zirconia calcination at 475 °C, with very few partially or completely filled crown-like structures which appear in some favourable cases and are marked with arrows in Fig. 3c. Parallel XRD patterns indicate the presence of  $m\text{-ZrO}_2$  as a majority polymorph. Crystallites are large, of diameters often exceeding 80–100 nm and rectangular shapes. The grain boundaries are favoured over free surface, and the interparticle coordination number increases. Contrary to this, the crystallites of aged  $\text{ZrO}_2$  remain separated and do not exceed 7–17 nm in size (Fig. 4). The voids between the grains are well pronounced accounting for relatively well developed micro- and mesoporosity, characteristic of the  $t\text{-ZrO}_2$  samples [13, 14].

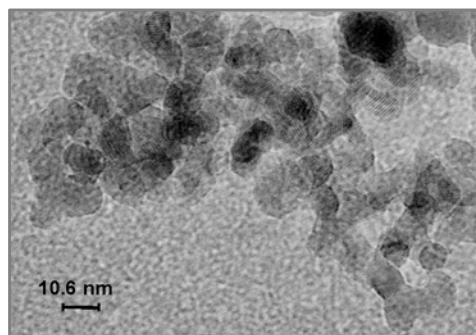


Fig. 4. HR-TEM image of aged zirconia sample calcined at 600 °C for 6 h

## 4. Conclusions

Ageing and thermal treatment are the most important synthetic steps of zirconia preparation, decisive for controlling the  $t\text{-ZrO}_2/m\text{-ZrO}_2$  ratio. Prolonged digestion of the zirconia precipitate in the mother liquor at 100 °C allows effective controlling of the zirconia grain size and grain boundaries, resulting in expansion of the thermal stability of the  $t\text{-ZrO}_2$  polymorph.

### Acknowledgements

This work was financially supported by The Polish State Committee for Scientific Research (KBN) within the project No. 3 T09 147 26.

## References

- [1] LEE J.-H., *J. Mater. Sci.*, 38 (2003), 4247.
- [2] RAINFORTH W.M., *J. Mater. Sci.*, 39 (2004), 6705.
- [3] YAMAGUCHI T., *Catal. Today*, 20 (1994), 199.
- [4] MERCERA P.D.L., VAN OMMEN J.G., DOESBURG E.B.M., BURGGRAAF A.J., ROSS J.R.H., *Appl. Catal.* 57 (1990), 127.
- [5] WELLS A.F., *Structural Inorganic Chemistry*, Polish Ed., WNiT, Warsaw, 1993.
- [6] JUNG K.T., BELL A.T., *J. Mol. Catal. A*, 163 (2000), 27.
- [7] GARVIE R.C., *J. Phys. Chem.*, 69 (1965), 1238.
- [8] CHEN S.-G., YIN Y.-S., WANG D.-P., *J. Mol. Struct.*, 690 (2004), 181.
- [9] TANI E., YOSHIMURA M., SÖMYIA S., *J. Am. Ceram. Soc.*, 66 (1983), 11.
- [10] ADAMSKI A., JAKUBUS P., SOJKA Z., *Nukleonika* 51 (Suppl. 1) (2006), S27.
- [11] PATTERSON A.L., *Phys. Rev.*, 56 (1939), 978.
- [12] CHRASKA T., KING A.H., BERNDT CH.C., *Mat. Sci. Eng. A*, 286 (2000), 169.
- [13] JAKUBUS P., ADAMSKI A., KURZAWA M., SOJKA Z., *J. Therm. Anal. Calorim.*, 72 (2003) 299.
- [14] ADAMSKI A., JAKUBUS P., SOJKA Z., *Solid State Phenom.*, 128 (2007), 89.

*Received 28 April 2007*  
*Revised 16 February 2008*

## Nickel-free nanocrystalline austenitic stainless steels

M. TULINSKI<sup>1\*</sup>, K. JURCZYK<sup>2</sup>, M. JURCZYK<sup>1</sup>

<sup>1</sup>Poznań University of Technology, Institute of Materials Science and Engineering,  
ul. M. Skłodowskiej-Curie 5, 60-965 Poznań, Poland

<sup>2</sup>Poznań University of Medical Sciences, Department of Conservative Dentistry and Periodontology,  
ul. Bukowska 70, 60-812 Poznań, Poland

Nanocrystalline Ni-free austenitic stainless steel powders have been synthesised by mechanical alloying followed by nitrogenation. Phase transformation from ferritic to austenitic phases was confirmed by the XRD analysis. After mechanical alloying microhardness reached the values almost twice higher than those of materials obtained by conventional methods. The effect is directly connected with the structure refinement. The results of the corrosion resistance showed that mechanical alloying process and nitrogen absorption treatment significantly lowered corrosion rates.

Key words: *Ni-free stainless steel; mechanical alloying; biomaterials*

### 1. Introduction

Microcrystalline materials such as metals and alloys are widely used today. Over the last decade, the use of nanostructured materials has already changed the approach to designing materials in many applications by seeking structural control at the atomic level and tailoring mechanical engineering properties [1].

Today, it is possible to prepare metal/alloy nanocrystals with nearly monodisperse size distribution. Nanostructures represent key building blocks for nanoscale science and technology. They are needed to implement the “bottom-up” approach to nanoscale fabrication, whereby well-defined nanostructures with unique properties are assembled into mechanical as well as functional properties [2].

One of the potential applications of nanostructured materials (made of elements of the size not exceeding 100 nm) is medicine. Presently, most biomedical implants, e.g. stents, contain stainless steel frameworks. However, widely used 316L steel is not fully biocompatible, and has induced high occurrences of restenosis and thrombosis.

---

\*Corresponding author, e-mail: maciej.tulinski@doctorate.put.poznan.pl

Moreover, nickel ions produced due to corrosion are reported to cause allergies and even cancer. Scientists have therefore been searching for more biocompatible options which include gold, titanium, cobalt-chromium alloys, tantalum alloys and various polymers.

Mechanical and corrosion resistance properties of typical metallic biomaterials used for implant devices are satisfactory but they may cause many problems within human body and therefore need improvement. The main disadvantage of the most popular austenitic stainless steel (316L) [3] is lack of biocompatibility, toxicity of corrosion products and fracture due to corrosion fatigue [4]. Austenite stabilizer – nickel – is reported to be a particularly toxic element causing allergies and even cancer [5]. World Health Organization (WHO) estimated that nickel content below 0.2% is congruous with medical requirements [4]. Therefore, development of materials with either improved corrosion resistance and/or without nickel is absolutely imperative.

One of the most promising austenitizing elements to replace nickel is nitrogen [6]. Nitrogen increases austenite stability, corrosion resistance and prevents from the formation of sigma phase. Recently, a new manufacturing process of nickel-free austenitic stainless steels with nitrogen absorption treatment has been developed [7]. In this method, small devices can be precisely machined in a ferritic phase and then during nitrogenization of their surfaces under gaseous nitrogen at ca. 1200 °C they become nickel-free austenitic stainless steels with better mechanical and corrosion resistance properties.

In this work, a new manufacturing process of nickel-free austenitic stainless steels with nanostructure has been proposed. Details of the process and the enhancement of properties due to obtaining nanostructure in consolidated materials are presented.

## 2. Experimental

The experimental procedures are shown in Fig. 1. Mechanical alloying (MA) was developed in the 1970's at the International Nickel Co. as a technique for dispersing nanosized inclusions into nickel-based alloys [1]. During the last years, the MA process has been successfully used to fabricate a variety of alloy powders including powders containing supersaturated solid solutions, quasicrystals, amorphous phases and nano-intermetallic compounds. MA technique has been proved to be a novel and promising method for alloy formation.



Fig. 1. Flow chart of the experiment

Raw materials used for MA are commercially available as high purity powders that have sizes in the range of 1–100 µm. During the mechanical alloying process, the powder particles are periodically trapped between colliding balls and are plastically



deformed due to generation of a wide number of dislocations as well as other lattice defects. Furthermore, the ball collisions cause fracturing and cold welding of elementary particles, forming clean interfaces at the atomic scale. Further milling results in a decrease of sizes of elementary components from millimeter to submicrometer lengths, thus increasing the number of interfaces. Concurrently to this decrease of the elementary distribution, some nanocrystalline intermediate phases are produced inside the particles or at their surfaces. As the milling develops, the content fraction of such intermediate compounds increases leading to a final product whose properties depend on the milling conditions.

The FeCrMnMoN alloys were prepared by mechanical alloying of stoichiometric amounts of the constituent elements (99.9% or better purity). The mechanical alloying was carried out using a SPEX 8000 mixer mill fitted with a hardened steel vial and steel balls 10 mm in diameter. The vial of the SPEX mill was loaded with powder in a glove-box connected to a high purity argon supply. The elemental powders (Fe 10  $\mu\text{m}$ , Cr 5  $\mu\text{m}$ , Mn 44  $\mu\text{m}$ , Mo 10  $\mu\text{m}$ ) were mixed and poured into the vial (Fig. 2a). The mill was run up to 48 h for every powder preparation (Fig. 2b). The as-milled powders were heat treated at 750  $^{\circ}\text{C}$  for 0.5 h under high purity argon to form ordered phases (Fig. 2c). Nitrogenation of cold pressed samples was carried out at 1215  $^{\circ}\text{C}$  for 24 h at 120 kPa nitrogen pressure (Fig. 2e).

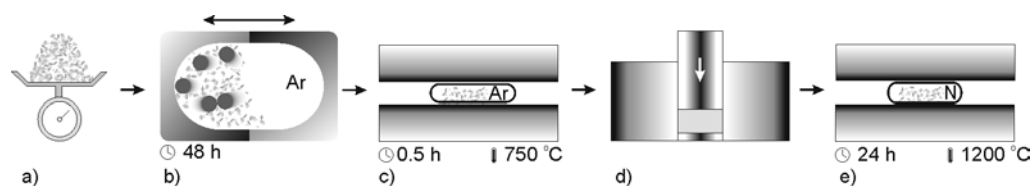


Fig. 2. Schematic presentation of manufacturing of nanocrystalline stainless steels: a) initial powders, b) mechanical alloying, c) heat treatment, d) cold pressing, e) nitrogen absorption

The powders were characterized by means of X-ray diffraction (XRD) and scanning electron microscopy (SEM) with an energy-dispersive X-ray microanalysis system (EDS). XRD was performed using an X-ray powder diffractometer with  $\text{CoK}\alpha$  radiation at various stages during milling, prior to annealing and after annealing as well as after nitrogenation. Microhardness measurements were carried out using the Vickers method with the load of 200 g. The micrographs were obtained using an optical microscope. The density of the sintered samples was determined by the Archimedes method. The analyses of the corrosion were conducted on a Solartron 1285 potentiostat in a Princeton Applied Research corrosion cell system interfaced to a personal computer. The experiments were controlled and the data were analyzed using a CorrWare analysis software. Counter electrodes were made of graphite, the reference electrode was a standard calomel electrode (SCE). The method of polarization resistance was employed to investigate changes in corrosion. The etching solution was 0.1 M  $\text{H}_2\text{SO}_4$ . Scanning range extended from  $-1$  V to 2.5 V with the rate of 0.5 mV/s. All

experiments were carried out at 25 °C. From the analyses, the corrosion currents,  $I_{\text{corr}}$ , were recorded. The corrosion rate (MPY) can be then calculated as follows:

$$MPY = \frac{0.00408 I_{\text{corr}} A}{nD} \quad (1)$$

where  $I_{\text{corr}}$  is the corrosion current ( $\text{A}/\text{cm}^2$ ),  $D$  is the density ( $7.8 \text{ g}/\text{cm}^3$  for stainless steel) and  $A/n$  is the effective weight ( $25.29 \text{ g}$ ).

The steel specimens were used in the form of rods 8 mm in diameter and 3 mm long. They were prepared and mounted as follows. A stainless steel rod 200 mm long and 3.5 mm diameter was used for establishing the electrical contact. The whole assembly was inserted in a glass tube. Silicon resin was used to ensure the exposure of a determined apparent surface area of  $0.5 \text{ cm}^2$ .

### 3. Results and discussion

X-Ray diffraction patterns in Fig. 3 are representative of a  $\text{Fe}_{74}\text{Cr}_{24}\text{Mo}_2$  alloy after MA, annealing and nitrogenation under various conditions. The first diffraction pattern

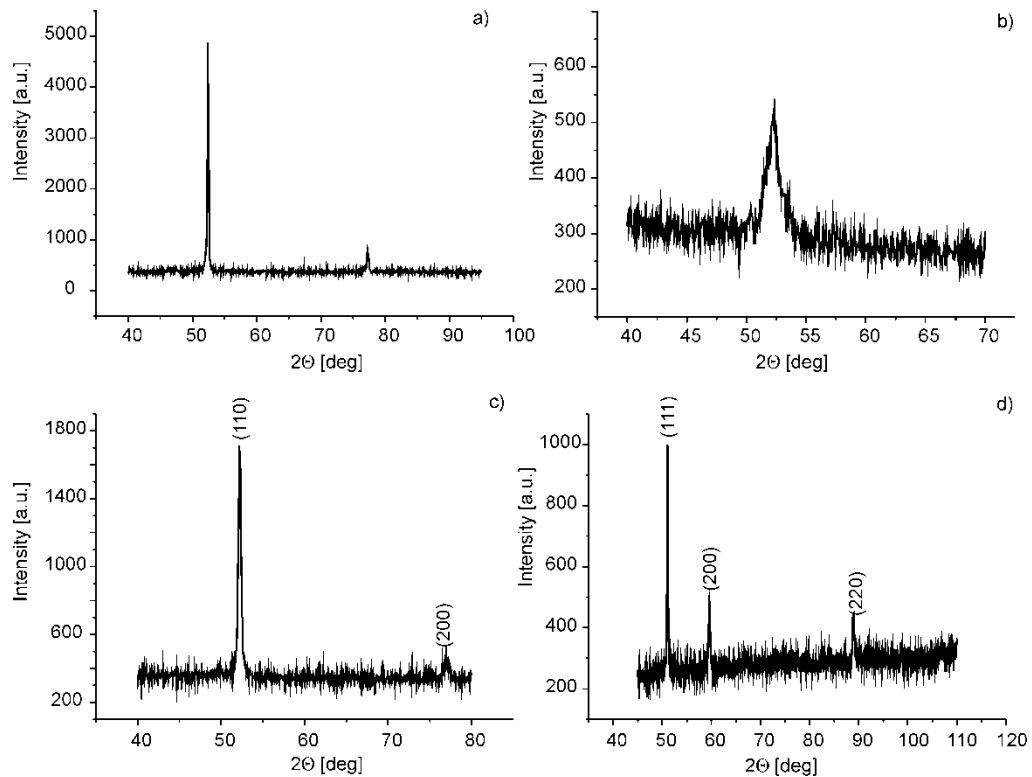


Fig. 3. X-ray diffraction spectra of  $\text{Fe}_{74}\text{Cr}_{24}\text{Mo}_2$  material: a) mixture of initial powders, b) after 48 h of mechanical alloying, c) after heat treatment at 750 °C for 0.5 h, d) after nitrogen absorption

shows a mixture of initial powders (Fig. 3a). After 48 h of MA the alloy decomposed into an amorphous phase and nanocrystalline  $\alpha$ -Fe (Fig. 3b). The heat treatment performed after MA resulted in crystallization into ferritic phase (Fig. 3c). Then the compacted material was nitrated at 1215 °C which resulted in phase transformation from ferritic phase to fully austenitic one (Fig. 3d). Crystallite size of the material, 27 nm, was estimated by Scherrer's method. Some small peaks might indicate a possibility of a presence of small amounts of nitrides or oxides as results from the chemical composition (Fig. 4).

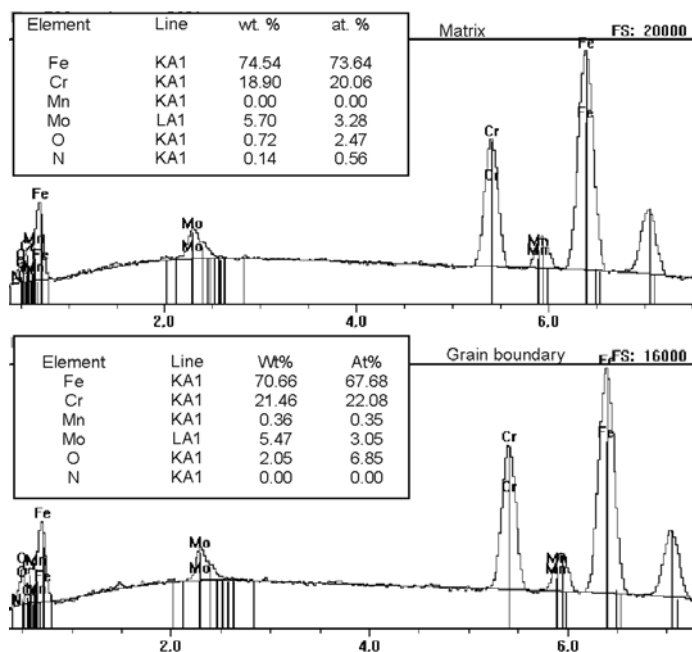


Fig. 4. EDX analysis of the matrix and at the grain boundary of  $\text{Fe}_{74}\text{Cr}_{24}\text{Mo}_2$  sample

EDX analysis (Fig. 4) of  $\text{Fe}_{74}\text{Cr}_{24}\text{Mo}_2$  alloy confirms that the material matrix contains 74% of iron, 20% of chromium and 3% of molybdenum, 0.56% of nitrogen and 2.47% of oxygen. Oxygen content in the synthesized materials was determined by the XPS method. At the grain boundaries one can observe a small amount of manganese and an increase of oxygen content up to 7%. Nitrogen content is dependent on the region, ranging from 0 to 2.16% due to diffusion effects.

Sizes and shapes of microcrystals of mechanically alloyed powder mixtures during MA have been determined by the SEM technique (Fig. 5). Starting materials forming the microstructure (Fig. 5a–5c) were mixed together (Fig. 5d). The lamellar structure is increasingly refined during further mechanical alloying (Fig. 5e) which leads to formation of solid solution (Fig. 5f). After alloying, the samples show cleavage fracture morphology and inhomogeneous size distribution (Fig. 5g).

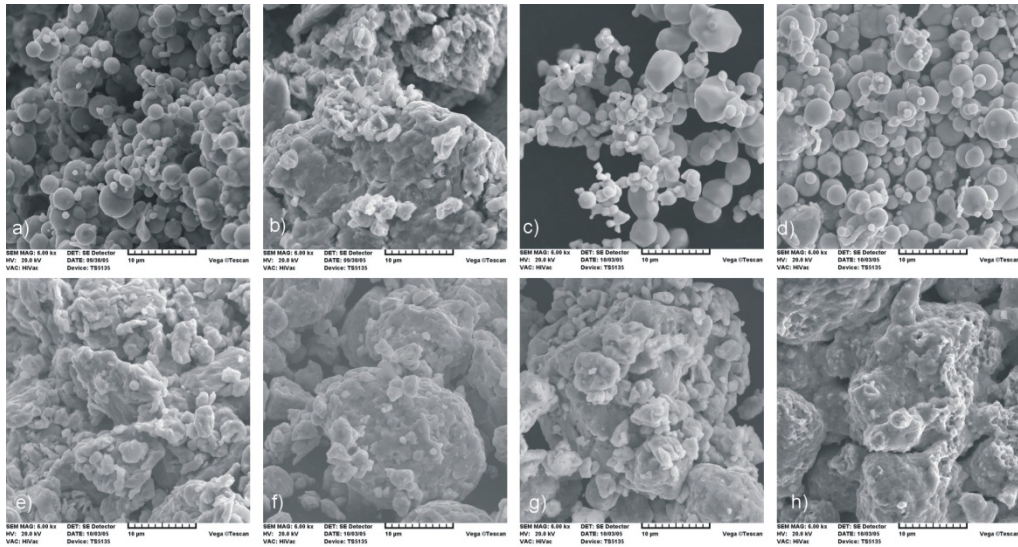


Fig. 5. SEM images: a) Fe, b) Cr, c) Mo, d) mixture of initial powders, e) after 1 h of MA, f) after 48 h of MA, g) after heat treatment, h) final bulk material  $\text{Fe}_{74}\text{Cr}_{24}\text{Mo}_2$  after nitrogen absorption

Many small powder particles tend to agglomerate. Bulk FeCrMo material with 98% theoretical density was prepared by sintering (750 °C for 0.5 h) and then nitrided at 1215 °C for 24 h (Fig. 5h).

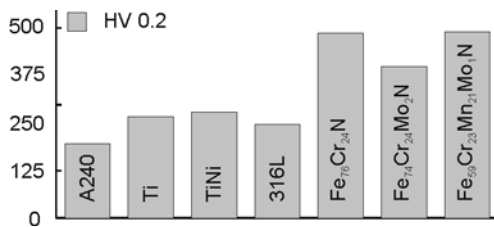


Fig. 6. Microhardness of FeCrMoN materials compared to A240 and 316L stainless steels, pure titanium and microcrystalline TiNi alloy

The microhardness of the final bulk material was studied using the Vickers method (Fig. 6). Compared with A240 commercial austenitic stainless steel (195 HV<sub>0.2</sub>), pure titanium (266 HV<sub>0.2</sub>), TiNi alloy (279 HV<sub>0.2</sub>) and widely used in medicine 316L stainless steel (248 HV<sub>0.2</sub>), microhardness of sintered nanocrystalline austenitic nickel-free nitrogen containing stainless steels obtained by mechanical alloying is significantly higher (378 to 487 HV<sub>0.2</sub>) being twice higher than microhardness of austenitic steel obtained by conventional methods. This effect is directly connected with structure refinement and obtained nanostructure, one should, however, consider also change in the phase composition since small peaks in the X-ray diffraction patterns might indicate a possibility of formation of oxides and nitride. Due to its small amount it is of lesser importance.

General shapes of the potentiodynamic curves are shown in Fig. 7. Results of the corrosion test are listed in Table 1. The linear parts of anodic and cathodic Tafel re-

gions extended over a wider current range in the case of  $\text{Fe}_{59}\text{Cr}_{23}\text{Mn}_{12}\text{Mo}_6$ . The calculated corrosion potential,  $E_{\text{corr}}$ , in the case of  $\text{Fe}_{59}\text{Cr}_{23}\text{Mn}_{12}\text{Mo}_6$  is  $-431$  mV with an associated corrosion current,  $I_{\text{corr}}$ , of  $1.3 \times 10^{-5}$  A/cm<sup>2</sup>. The corresponding values in  $\text{Fe}_{74}\text{Cr}_{24}\text{Mo}_2$  are  $-473$  mV and  $6.1 \times 10^{-3}$  A/cm<sup>2</sup>, respectively. Thus the addition of Mn and a decrease of the Fe content resulted in the shift of the corrosion potential to a more negative value and appreciable (two orders of magnitude) decrease in the corrosion current density. The values for  $\text{Fe}_{74}\text{Cr}_{24}\text{Mo}_2$  are similar as those for 316L stainless steel widely used in medicine while those for  $\text{Fe}_{59}\text{Cr}_{23}\text{Mn}_{12}\text{Mo}_6$  are considerably improved.

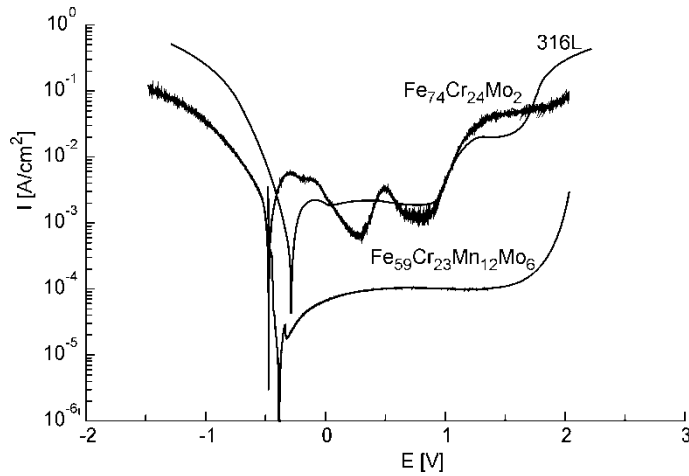


Fig. 7. Potentiodynamic curves for stainless steels in 0.1 M  $\text{H}_2\text{SO}_4$  at 25 °C

The potentiodynamic curve was characterized by the appearance of a well-defined anodic peak at  $-350$  mV, which corresponds to an anodic peak current of  $6.2 \times 10^{-4}$  A/cm<sup>2</sup> for  $\text{Fe}_{59}\text{Cr}_{23}\text{Mn}_{12}\text{Mo}_6$ . On the other hand, the corresponding values for  $\text{Fe}_{74}\text{Cr}_{24}\text{Mo}_2$  are  $-280$  mV and  $5.3 \times 10^{-2}$  A/cm<sup>2</sup>, respectively.

Table 1. Results of corrosion tests

Chemical composition	$I_{\text{corr}}$ [A/cm <sup>2</sup> ]	$E_{\text{corr}}$ [mV]	$R_p$ [ohm/cm <sup>2</sup> ]	Corrosion rate [MPY]
$\text{Fe}_{74}\text{Cr}_{24}\text{Mo}_2$	$6.1 \times 10^{-3}$	$-473$	22	47
$\text{Fe}_{59}\text{Cr}_{23}\text{Mn}_{12}\text{Mo}_6$	$1.3 \times 10^{-5}$	$-431$	1500	7.4
316L	$3.6 \times 10^{-3}$	$-349$	450	33

The polarization resistances  $R_p$  calculated from the potentiodynamic curves were  $1.467 \times 10^3$  and 22 Ohm/cm<sup>2</sup> for  $\text{Fe}_{59}\text{Cr}_{23}\text{Mn}_{12}\text{Mo}_6$  and  $\text{Fe}_{74}\text{Cr}_{24}\text{Mo}_2$ , respectively. The corresponding calculated corrosion rates are 7.4 and 47 MPY (milliinch per year),

respectively, resulting in lowering by ca. 85% of the rate of corrosion of the stainless steel in the 0.1 M H<sub>2</sub>SO<sub>4</sub> solution.

#### 4. Summary

Nanocrystalline austenitic nickel-free nitrogen containing stainless steel samples were produced by mechanical alloying process and nitrogen absorption. Microhardness test showed that the obtained material exhibits the Vickers microhardness as high as 487 HV<sub>0.2</sub> being about two times higher than that of conventional austenitic stainless steels, including widely used in medicine 316L stainless steel. This effect might be smaller when considering possibility of presence of nitride. This is due to the structure refinement and the transformation into nanostructured material. Mechanical alloying is also a very effective technology to improve the corrosion resistance of stainless steel. Decreasing the corrosion current density is a distinct advantage for prevention of ion release. According to existing concepts, decreasing size of material crystallites to a nanometric scale allows one to achieve much better mechanical properties (e.g. microhardness) compared to conventional materials.

Nitrogen absorption treatment contributes to a higher corrosion resistance, also in the presence of wear. With regard to austenitic stainless steels this may lead to obtaining biomedical implants (e.g., stents) with better mechanical properties, corrosion resistance and biocompatibility.

#### References

- [1] GLEITER H., *Prog. Mater. Sci.*, 33 (1989), 323.
- [2] JURCZYK M., *Bull. Pol. Ac. Tech.*, 52 (2004), 67.
- [3] LIM I.A.L., *MIT Undergraduate Res. J.*, 11 (2004), 3.
- [4] IARC Monographs on the Evaluation of Carcinogenic Risks to Humans: *Surgical Implants and Other Foreign Bodies*, Lyon, 74 (1999), 65.
- [5] UGGOWITZER J., MAGDOWSKI R., SPEIDEL M., *ISIJ Int.*, 36 (1996), 901.
- [6] ORNHAGEN C., NILSSON J.O., VANNEVIK H., *J. Biomed. Mater. Res.*, 31 (1996), 97.
- [7] SUMITA M., HANAWA T., TEOH S.H., *Mater. Sci. Eng. C*, 24 (2004), 753.

*Received 28 April 2007*  
*Revised 16 February 2008*

# Properties of films fabricated from ZnS/Mn<sup>2+</sup> nanoparticles

A. ZDYB\*, K. CIEŚLAK, J. M. OLCHOWIK

Institute of Physics, Technical University of Lublin, ul. Nadbystrzycka 38D, 20-618 Lublin, Poland

Nanoparticles of manganese doped zinc sulfide (ZnS/Mn<sup>2+</sup>) were obtained by wet chemical method. AFM images of the nanoparticles were analysed and their size distribution was estimated. The layer of ZnS/Mn<sup>2+</sup> nanoparticles reveals a semiconducting character. Conductivity increases with temperature and its value is of the order of 10<sup>-9</sup> Ω·cm<sup>-1</sup>.

Key words: *nanoparticles; ZnS*

## 1. Introduction

II–VI semiconductor nanoparticles attract much attention because of their size-dependent properties and promising applications in optoelectronics. ZnS is a II–VI material that can find future applications such as window layers of solar cells, data storage, data transfer and coatings sensitive to UV light. ZnS has also the advantage of being safer than commonly used CdS, considered to be very harmful. In a bulk state, ZnS has a direct large bandgap of 3.66 eV at 300 K. It exists both as cubic zinc blende and hexagonal wurtzite structures. ZnS and ZnS/Mn<sup>2+</sup> nanoparticles can be obtained in many ways, e.g., by a spray-based method [1], mechanochemical route [2], ultrasonic radiation method [3], synthesis by  $\gamma$ -irradiation of solution [4], and in chemical reactions [5–10]. ZnS nanoparticle films are very promising for large scale solar cell production with low material consumption. The bandgaps of sulfide nanoparticles can be adjusted by a change in their sizes. This allows use them as sensitizers in quantum dot sensitized solid-state solar cells [11–13].

In this work, a chemical technique is applied [14] to obtain ZnS/Mn<sup>2+</sup> nanoparticles. The AFM studies of nanoparticles size distribution have been performed, supplemented with temperature dependent conductivity measurements.

---

\*Corresponding author, e-mail: a.zdyb@pollub.pl

## 2. Experimental

To obtain ZnS/Mn<sup>2+</sup> nanoparticles the wet chemical synthesis method was used. Nanoparticles were fabricated by a co-precipitation reaction from homogenous solutions of zinc acetate and manganese acetate. Sodium sulfide was added resulting in formation of white precipitate of ZnS/Mn<sup>2+</sup> nanoparticles that were stabilized with equal amounts of sodium tripolyphosphate and sodium hexametaphosphate. All syntheses were carried out under ambient conditions. All chemicals used were of high purity purchased from Sigma-Aldrich.

Nanoparticles were washed several times with distilled water and their existence in the colloid suspension was proved by the atomic force microscopy (AFM) study. The samples for AFM analyses were fabricated at room temperature. Water suspension of nanoparticles was dropped on a clean GaAs substrate and allowed to dry in air. The samples were examined with a Nanosurf easyScan 2 AFM. In  $I-V$  measurements, two Au stripes, 15 mm distant, deposited on glass using a Cressington sputter coater played the role of electrodes. Ag colloidal paste was used to make electric contacts to the Au stripes. ZnS/Mn<sup>2+</sup> nanoparticle suspension was deposited onto the area between the electrodes and allowed to dry at room temperature. For heating the samples, ITO glass was used. The electric contacts were made of Ag colloidal paste at two ends of the ITO glass and applied voltage was tuned in order to obtain a proper temperature. A thermocouple was used to measure the temperature of ZnS/Mn<sup>2+</sup> sample placed on the ITO glass.

## 3. Results

AFM images of ZnS/Mn<sup>2+</sup> nanoparticles are shown in Fig. 1. The mean particle size is 19.4 nm and ranges from 11 nm to 34 nm as revealed from the AFM images. They are well immobilized on the GaAs substrate. Figure 2 presents the particle size distribution as determined from the AFM images.

Figure 3 presents the temperature dependence of current for voltages in the range from 20 V to 50 V applied to the sample. The current increases during heating and it has higher values for higher voltages. The curves shown in Fig. 3 reveal semiconductor like behaviour of ZnS/Mn<sup>2+</sup> nanoparticle films.

The temperature dependence of ZnS/Mn<sup>2+</sup> nanoparticle film conductivities is shown in Fig. 4. In order to determine the specific conductivities of a ZnS/Mn<sup>2+</sup> layer, its dimensions should be estimated. The ZnS/Mn<sup>2+</sup> film thickness was estimated by measuring the mass of the film and its surface area. First a glass slide with Au contacts was weighted without and with ZnS/Mn<sup>2+</sup> film deposited on it. Using macroscopic ZnS/Mn<sup>2+</sup> density of 4.06 g/cm<sup>3</sup>, the thickness value was calculated according to the formula:



$$d = \frac{m}{\rho A} \tag{1}$$

where  $m$  is mass,  $\rho$  – density,  $A$  – surface area. The calculated thickness equals to 14.3  $\mu\text{m}$ .

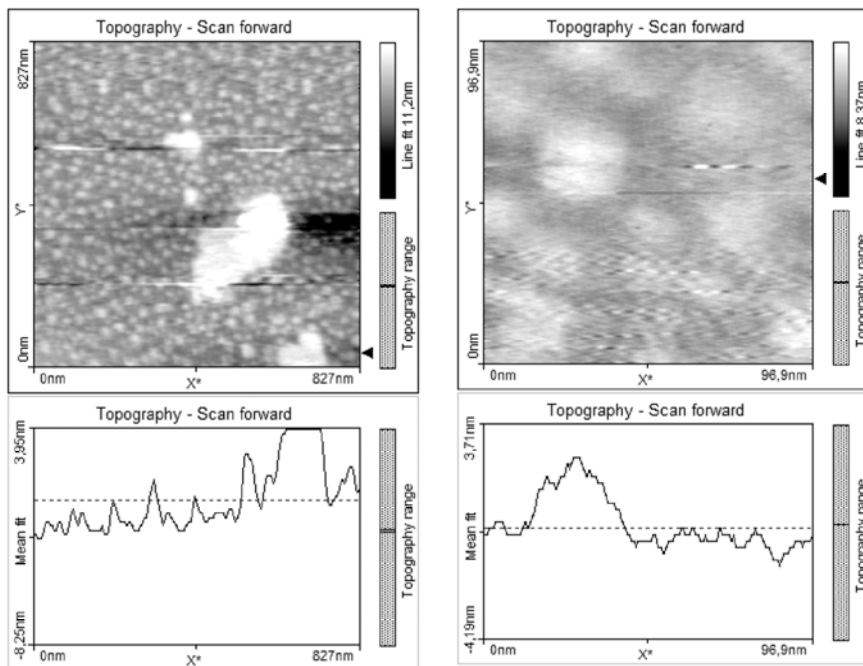


Fig. 1. AFM images of ZnS nanoparticles

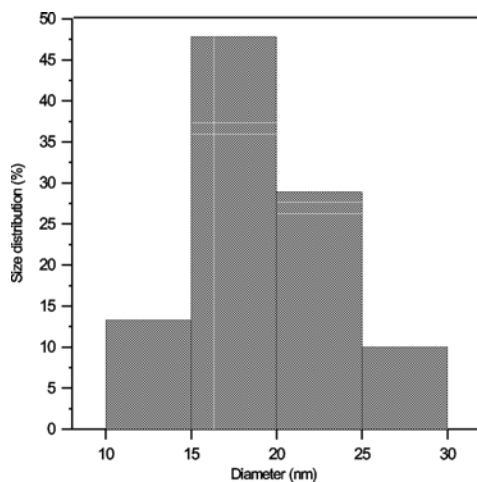


Fig. 2. Size distribution of ZnS nanoparticles.  
The average particle diameter is 19.4 nm

The film conductivity was calculated from the formula:

$$\sigma = \frac{Il}{SU} \quad (2)$$

where  $I$  is the current,  $l$  – the sample length,  $S$  – area of cross section,  $U$  – voltage.

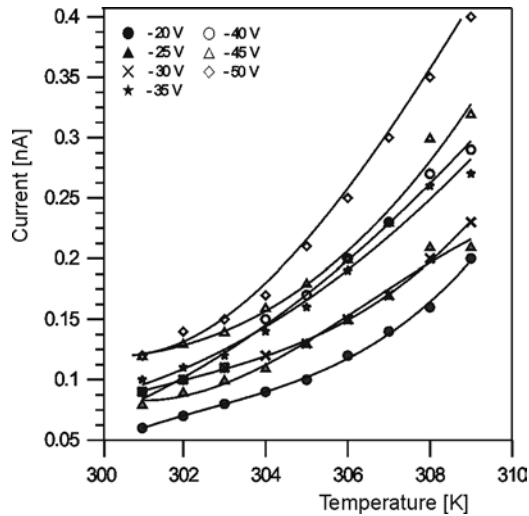


Fig. 3. Temperature dependence of current for the voltage 20–50 V applied to the sample

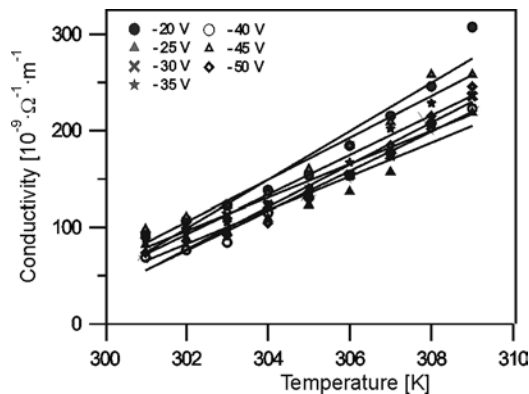


Fig. 4. Temperature dependence of ZnS nanoparticle film conductivity for voltage 20–50 V applied to the sample

The obtained values of conductivity are of the order of  $10^{-9} (\Omega \cdot \text{cm})^{-1}$  locating the investigated ZnS/Mn<sup>2+</sup> nanoparticle films in semiconductor materials. They are lower than the reported conductivity of ZnS film [15] which is  $10^{-4}$ – $10^{-5} (\Omega \cdot \text{cm})^{-1}$ . In the paper of Fathy and Ichimura [15], ZnS film is prepared by electrochemical deposition

from aqueous solutions and therefore it is certainly more homogenous than our nanoparticle layers. Low conductivity of our samples is caused by highly defected structure of the film which in turn comes from grains walls.

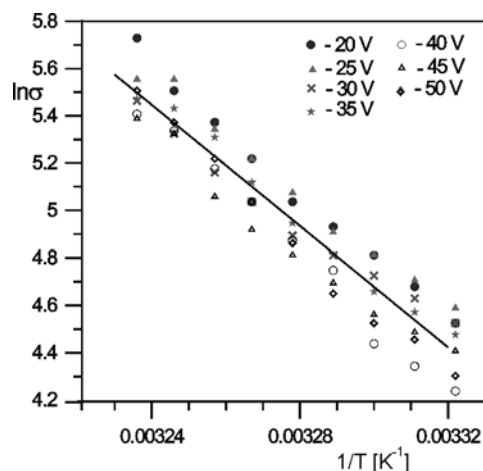


Fig. 5. Temperature dependence of conductivity; points – experimental data, line – a least square fit

Figure 5 shows the plots  $\ln\sigma f(1/T)$ . The particular sets of data measured at various voltages and marked by different symbols follow straight lines. The plotted line is a least square fit made using all experimental points. From the line slope, the energy of 2.22 eV was determined, corresponding to 559.6 nm. This value is close to the value of 590 nm reported in the luminescence experiment [16] for energy transfer between  ${}^4T_1-{}^6A_1$  Mn<sup>2+</sup> states. This suggests that manganese levels act as intermediate levels for electrons to be excited to the conductivity band.

#### 4. Summary

We have obtained ZnS/Mn<sup>2+</sup> nanoparticles by a co-precipitation reaction. Their size distribution was determined by the AFM with the mean size of 19.4 nm in diameter. Conductivity measurements were performed and from the temperature dependence the wavelength of 559.6 nm was calculated which might be associated with energy transfer between  ${}^4T_1-{}^6A_1$  Mn<sup>2+</sup> dopant states.

#### References

- [1] AMIRAV L., AMIRAV A., LIFSHITZ E., J. Phys. Chem. B, 109 (2005), 9857.
- [2] BALAZ P., BOLDIZAROVA E., GODOCKOVA E., BRIANCIN J., Mat. Lett., 57 (2003), 1585.
- [3] XU J.F., Ji W., LIN J.Y. TANG S.H., DU Y.W., Appl. Phys. A, 66 (1998), 639.

- [4] SOUICI A.H., KEGHOUCHE N., DELAIRE J.A., REMITA H., MOSTAFAVI M., *Chem. Phys. Lett.*, 422 (2006), 25.
- [5] YANG H., HOLLOWAY P., *J. Appl. Phys.*, 93 (2003), 586.
- [6] CHUNG J.H., AH C.S., JANG D.-J., *J. Phys. Chem. B*, 105 (2001), 4128.
- [7] YU I., TETSUHIKO I., SENNA M., *J. Phys. Chem. Solids*, 57 (1996), 373.
- [8] MANZOOR K., VADERA S.R., KUMAR N., KUTTY T.R.N., *Mat. Chem. Phys.*, 82 (2003), 718.
- [9] KARAR N., SUCHITRA R., SINGH F., *J. Cryst. Growth*, 268 (2004), 585.
- [10] KONISHI M., ISOBE T., SENNA M., *J. Luminescence*, 93 (2001), 1.
- [11] YANG S., HUANG C., ZHAI J., WANG Z., JIANG L., *J. Mater. Chem.*, 12 (2002), 1459.
- [12] PLASS R., PELET S., KRUEGER J., GRATZEL M., *J. Phys. Chem. B*, 106 (2002), 7578.
- [13] GRATZEL M., *J. Photochem. Photobiol. C*, 4 (2003), 145.
- [14] WARAD H.C., GHOSH S.C., HEMTANON B., THANACHAYANONT C., DUTTA J., *Sci. Techn. Adv. Mater.*, 6 (2005), 296.
- [15] FATHY N., ICHIMURA M., *Solar Energ. Mater. Solar Cells*, 87 (2005), 747.
- [16] SOOKLAL K., CULLUM B.S., ANGEL S.M., MURPHY C.J., *J. Phys. Chem.*, 100 (1996), 4551.

*Received 28 April 2007*  
*Revised 16 February 2008*

# Consolidation and sintering of nanometric ceramic powders

Ł. ZYCH\*

AGH University of Science and Technology, Faculty of Materials Science and Ceramics,  
al. Mickiewicza 30, 30-059 Cracow, Poland

Two powders containing 97 mol %  $ZrO_2$  and 3 mol %  $Y_2O_3$  with different crystallite sizes have been prepared by the hydrothermal method and calcination of co-precipitated gel. The hydrothermal powder was filter pressed under 5 MPa and dry pressed under 20 to 200 MPa. Filter pressed samples showed a more uniform particle arrangement than dry pressed samples which resulted in a better densification of the samples during sintering. Milling in water, and subsequent sedimentation of the calcinated powder allowed selecting fine particles for the filter pressing process.

Key words: *zirconia nanopowder; suspension; pressure filtration; sintering*

## 1. Introduction

Today many ceramic materials can be produced in a form of nanopowders with particle sizes below 100 nm. As a result of their activity related to a high surface area, they have recently been applied in many fields of technology such as cosmetic industry, catalysis, polymer processing etc. Sintering of ceramic nanopowders may lead to dense, nanocrystalline materials attractive due to their mechanical and electrical properties such as superelasticity at low temperatures, and high ionic conductivity. Nanopowders sinter at considerably lower temperatures than conventional powders, but their effective sintering, i.e. densification without extensive grain growth requires application of a consolidation technique which would lead to a uniform nanoparticle packing in a green body. Nanopowders tend to form agglomerates whose presence in the green body results in a wide pore size distribution. Based on the Kingery and Francois concept of the critical pore size [1], it is clear that small intra-agglomerate pores disappear during sintering process, while relatively large inter-agglomerate pores remain in a sintered body and hinder its densification.

---

\*E-mail: lzych@agh.edu.pl

Uniform arrangement of particles during uniaxial pressing of nanopowders requires high pressures, often in the range of GPa [2, 3], which are necessary to crush agglomerates and overcome friction forces acting between nanoparticles. In the case of isostatic pressing, the applied pressures are lower, but still they are relatively high for this technique [4]. High compacting pressures cause many technological problems and generate internal stresses in a green sample, which may lead to sample cracking [2]. It seems that uniform particle arrangement in green samples can be achieved by means of one of the colloidal shaping techniques, e.g. centrifugal casting [5] or filter pressing [6]. A liquid wetting nanoparticles acts as a “lubricant”, and allows them to move more easily and to arrange in a more uniform manner. Moreover, wet shaping techniques provide a better control of the shaping process than dry pressing [7].

The aim of this work was application of the filter pressing technique to consolidation of two zirconia nanopowders with different crystallite sizes, and investigation of their sintering process. Results of the filter pressing of the hydrothermal powder were compared with those of its dry uniaxial pressing.

## 2. Experimental

Two 3 mol % yttria-doped zirconia powders with different crystallite sizes were prepared by the co-precipitation method followed by hydrothermal treatment or calcination of X-ray amorphous gel. The common solution of  $ZrOCl_3$  and  $YCl_3$  was introduced into aqueous solution of ammonia. The co-precipitated gel was washed with distilled water in order to remove  $NH_4Cl$ . A part of the gel was hydrothermally treated at 250 °C for 4 h under an autogenous water vapour pressure [8], and the other part was calcinated at 850 °C for 1 h followed by attrition milling of the synthesised powder in ethanol for 5 h. The specific surface areas of the powders were measured by the BET method (Nova 1200e, Quantochrome Ins.). The crystallite size was determined by the X-ray diffraction method ( $CuK_{\alpha}$ , X'Pert Pro, Philips) using the Scherrer formula, and the powders were observed under a TEM microscope (AEM CM 20, Philips). The average crystallite size of the hydrothermal powder was about 8 nm. The powder was kept in water suspension of the concentration of ca. 9 vol. %. Part of the suspension was dried at 120 °C, and the resulting powder was ground below 5  $\mu m$  and then uniaxially dry pressed under 20–200 MPa. The dry pressed samples were sintered at 1150 °C for 2 h [9].

The original suspension of the hydrothermal powder was electrostatically dispersed by adjusting pH to 3 with  $HNO_3$ , and after 1 min of ultrasonification it was filter pressed in the apparatus shown in Fig. 1 [10]. The suspension was pressed with a steel piston (30 mm diameter) against a ceramic filter covered with a few layers of filter paper, and cellulose films. Pressure was increased up to 5 MPa, and kept constant until no water leakage was observed. Green samples were carefully dried up to

the constant weight at ambient temperature in a desiccator over silica gel. The green density of the samples was measured based on their weight and dimensions.

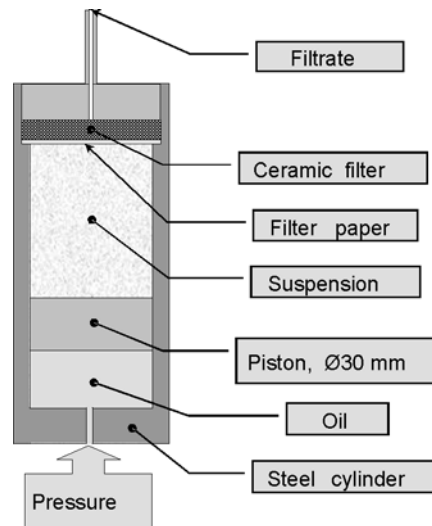


Fig. 1. Filter pressing apparatus

The average particle size of the calcinated powder was about 18 nm. The powder was milled for 24 h in water at pH 3, and after that it was left to sediment for 24 h, then the stable suspension collected from the sediment was filter pressed under 5 MPa. Particle sizes in both suspensions, as well as in the dried powders were determined using the DLS technique (Zetasizer Nano-ZS, Malvern Inc.). Before measurement, the dried powders were dispersed in water at pH 3, and all suspensions were ultrasonicated for 1 min.

The filter pressed samples were heat-treated at temperatures ranging from 600 °C to 1400 °C in air. Temperature was increased at the rate of 6 °C/min to a predetermined level, and kept constant for 30 min, then the samples were cooled with a furnace. The apparent density of the sintered sample was measured by the Archimedes method, the pore size distribution was evaluated using mercury porosimetry (Poremaster 60, Quantachrome Ins.), and the microstructure was observed using a SEM microscope (Leo 1530). The theoretical density (TD) of 3 mol % Y-TZP used in calculations was 6.08 g/cm<sup>3</sup>.

### 3. Results and discussion

#### 3.1. Characteristics of powders

TEM microphotographs of the zirconia nanopowders are shown in Fig. 2, and their particle sizes determined by three different methods are given in Table 1. Particle sizes of the hydrothermal powder determined from TEM micrographs and calculated from X-ray diffraction line broadening are very close to that calculated from the pow-

der specific surface area, which indicates that no broad contacts between particles were formed. The value of the particle size of the calcinated powder calculated from the specific surface area was significantly higher than the other two values suggesting formation of phase contacts between particles during the calcination process.

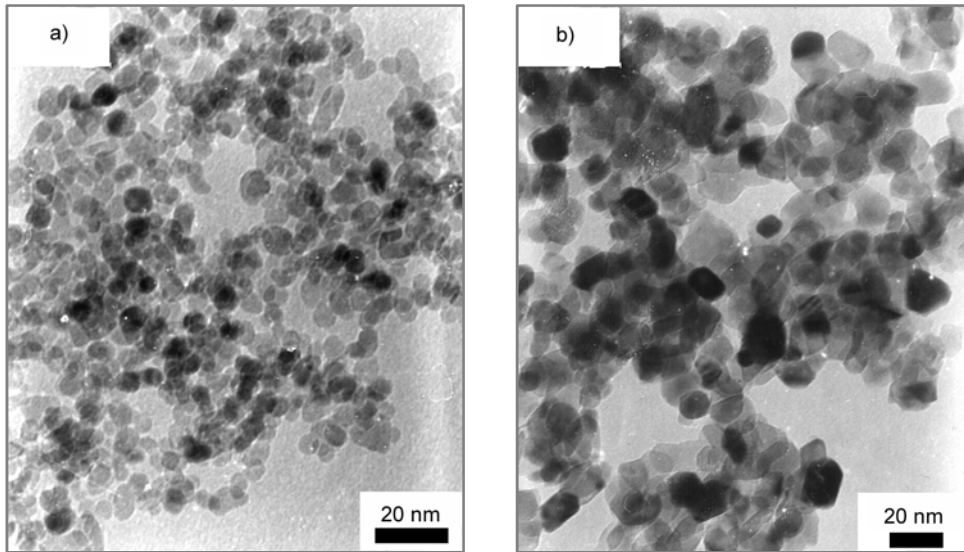


Fig. 2. TEM microphotographs of zirconia nanopowders: a) hydrothermal, b) calcinated

Table 1. Particle sizes of the zirconia nanopowders

Material	$D_{\text{BET}}$ [nm]	$D_{\text{TEM}}$ [nm]	$D_{\text{hkl}}$ [nm]
Hydrothermal powder	$8.1 \pm 0.4$	$7.5 \pm 0.2$	$8.6 \pm 0.2$
Calcinated powder	$26.8 \pm 1.3$	$17.9 \pm 0.7$	$18.9 \pm 0.2$

Particle size distribution provides more useful information on the characteristics of powders than the calculated mean particle size (Fig. 3). The particle size distribution of the hydrothermal powder in the original suspension was relatively narrow with the modal value of about 47 nm, which means that no single crystallites were present in the suspension. Dried hydrothermal powder consisted of much larger particles, even of micrometric size. The original calcinated powder consisted mainly of submicron particles (modal values 177 nm and 530 nm). Milling of the calcinated powder for 24 h with a subsequent sedimentation shifted the particle size distribution towards smaller values (modal size 56 nm) but still some much larger particles remained in the powder.



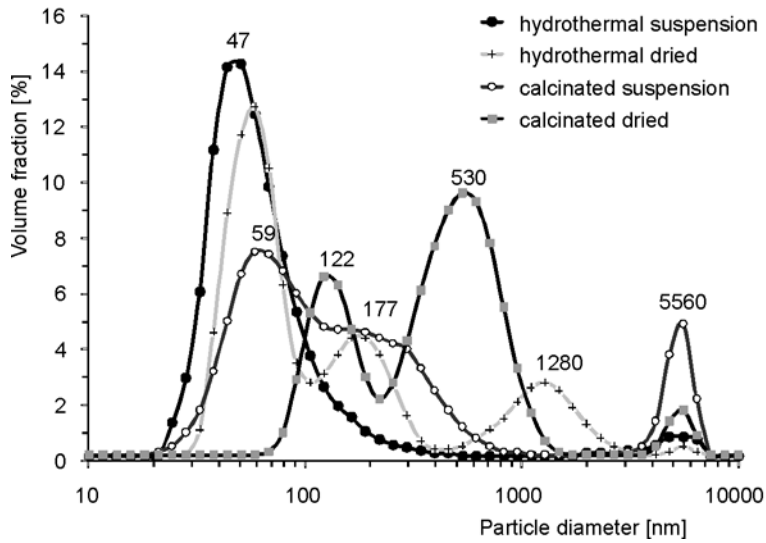


Fig. 3. Particle size distribution of hydrothermal and calcinated powder

### 3.2. Consolidation of the hydrothermal powder

The hydrothermal powder was consolidated by dry uniaxial pressing, and filter pressing of its water suspension (Fig. 4). The green density of dried, filter pressed samples did not depend on the applied filtration pressure. On the other hand, pressures higher than 5 MPa lead to cracking of samples during drying, thus this value was used in the powder consolidation. The relative density of the green filter pressed samples was about 40%, which is comparable with the density of samples dry pressed under 200 MPa (Fig. 4).

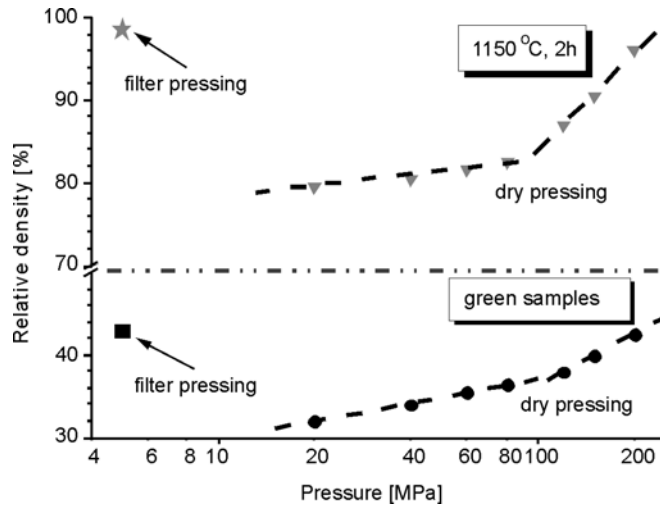


Fig. 4. Relative density of the samples prepared from the hydrothermal powder in function of compaction pressure

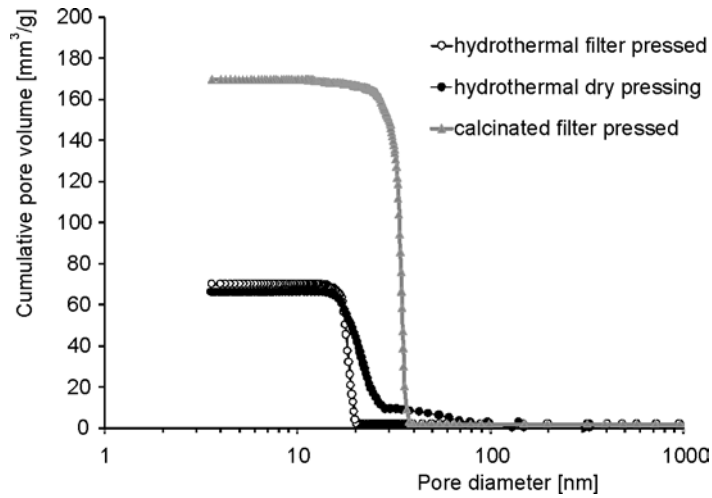


Fig. 5. Pore size distribution in dry pressed, and filter pressed samples sintered at 1000 °C, 1h

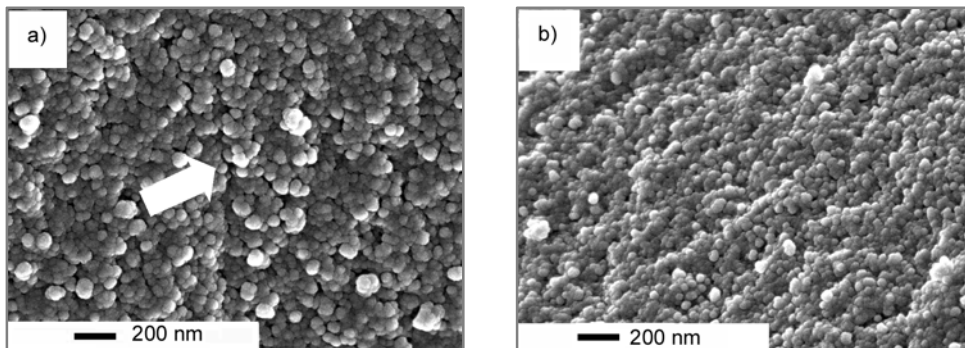


Fig. 6. SEM micrographs of green samples prepared by:  
a) dry pressing, b) filter pressing of the hydrothermal powder

After sintering at 1150 °C for 2h, the filter pressed sample densified to 98.5% TD, while the sample dry pressed under 200 MPa reached 96.0% TD. The differences in the sintering behaviour between the two samples can be related to non-uniform arrangement of the particles in the dry pressed sample resulting in a wide pore size distribution (Fig. 5). Larger pores are created between agglomerates which survived the compaction process (Fig. 6a). Such pores are detrimental to the sintering process, and cannot be removed under usual sintering conditions. Contrary to that, the pore size distribution of the filter pressed samples is extremely narrow, which means a uniform arrangement of the particles (Fig. 6b) and is beneficial for the sintering process. The filter pressed samples reached 99.99% TD after sintering at 1200 °C for 30 min (Fig. 7), and grain size was in the range 100–200 nm (Fig. 8).

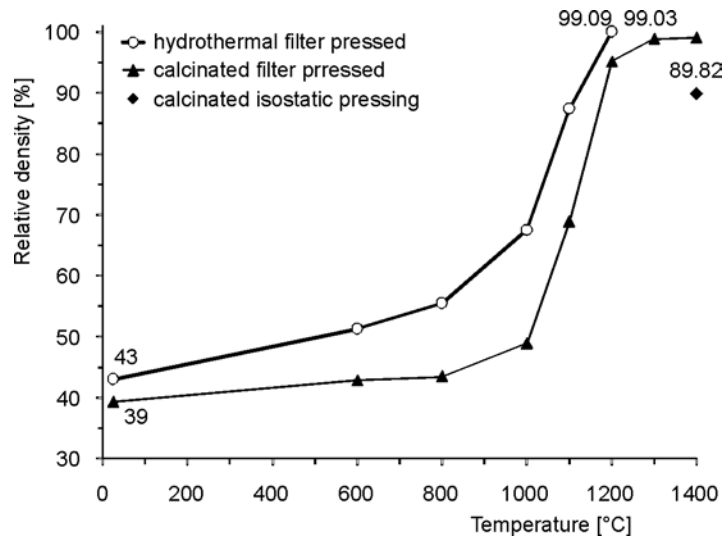


Fig. 7. Relative density of samples vs. sintering temperature (0.5 h, 6 °C/min)

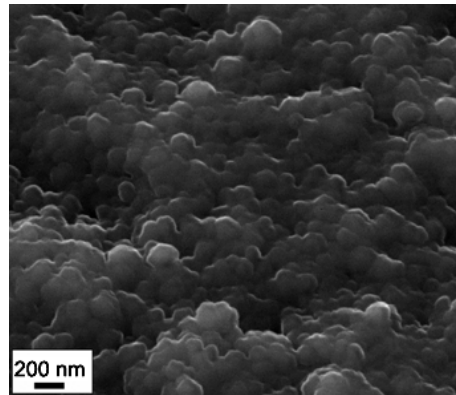


Fig. 8. SEM microphotograph of a fracture surface of the filter pressed sample sintered at 1200 °C, 0.5 h

### 3.3. Consolidation of the calcinated powder

The main goal of the calcinated powder ball milling in a dispersing medium (water, pH 3) with subsequent sedimentation was to select possibly finest particles for the consolidation process (Fig. 3) which would lead to sample densification at a temperature lower than in the case of the original powder. Filter pressing of the milled powder lead to a green body of about 40% TD and a very narrow pore size distribution, similar to that of the hydrothermal powder but with a larger modal pore size (Fig. 5). The filter pressed samples reached 99.03% TD after sintering at 1400 °C for 30 min, while samples consolidated by isostatic pressing of the original powder under 250 MPa achieved 89.82% TD (Fig. 7). This clearly results from the presence of large agglome-

ates (Fig. 3) in the original powder and a wide pore size distribution in the dry pressed samples (Fig. 5).

#### 4. Summary

Filter pressing of zirconia nanopowder under 5 MPa led to a sample of about 40% theoretical density being similar to the density of a sample uniaxially pressed under 200 MPa. Filter pressed samples had very uniform particle arrangement which resulted in a better sintering behaviour. Samples prepared from the hydrothermal powder sintered at 1200 °C for 0.5 h reached almost full density with the grain size of about 150–200 nm. Filter pressed samples of the calcinated powder reached 99.03% TD after sintering at 1400 °C for 0.5 h.

The filter pressing method can be used for successful shaping of ceramic nanometric powders, although further studies are necessary to make use of its potential.

#### Acknowledgements

The work was financially supported by the Polish State Committee for Scientific Research under grant no 3 T08D 028 30.

#### References

- [1] KINGERY W.D., FRANCOIS B., *The Sintering of Crystalline Oxides. I. Interactions between Grain Boundaries and Pores*, [in:] *Sintering and Related Phenomena*, G.C. Kuczynski, N.A. Hooton, C.F. Gibbon (Eds.), Gordon and Breach, New York, 1967, p. 471.
- [2] MAYO M.J., CHEN D.-J., HAGUE D.C., *Consolidation of Nanocrystalline Materials by Compaction and Sintering*, [in:] *Nanomaterials. Synthesis, Properties and Applications*, A.S. Edelstein, R.C. Cammerata (Eds.), Institute of Physics Publ., Philadelphia, 1997, p. 165.
- [3] GAO L., LI W., WANG H.Z., ZHOU J.X., CHAO Z.J. AND ZAI Q.Z., *J. Eur. Ceram. Soc.*, 21 (2001), 135.
- [4] DURÁN P., VILLEGAS M., CAPEL F., RECIO P., MOURE C., *J. Eur. Ceram. Soc.*, 16 (1996), 945.
- [5] RHODES W.H., *J. Am. Ceram. Soc.*, 64 (1981), 19.
- [6] UCHIKOSHI T., SAKKA Y., OZAWA K., HIRAGA K., *J. Eur. Ceram. Soc.*, 18 (1998), 669.
- [7] LANGE F.F., *J. Am. Ceram. Soc.*, 72 (1989), 3.
- [8] BUČKO M.M., HABERKO K., FARYNA M., *J. Am. Ceram. Soc.*, 78 (1995), 3397.
- [9] ZYCH L., HABERKO K., *Solid State Phenom.*, 94 (2003), 157.
- [10] ZYCH L., HABERKO K., *Key Eng. Mater.*, 264–268 (2004), 2323.

Received 28 April 2007  
Revised 16 February 2008

# Nano-ceramic aspect of preparation and processing of zirconia nanopowders

W. PYDA\*

AGH University of Science and Technology, Faculty of Materials Science and Ceramics,  
al. Mickiewicza, 30-059 Cracow, Poland

The hydrothermal method of preparation of zirconia nanopowders was reviewed with respect to the influence of solution pH, mineralizer and  $\text{TiO}_2$  concentration on the composition and morphology of zirconia crystallite phase. The pH dependence of both the ratio of the needle-shaped monoclinic to oval tetragonal zirconia nano-crystallites and CaO concentration in the zirconia solution has been described. Compressibility improvement and sinterability deterioration of zirconia nanopowders due to the presence of needle-shaped crystallites have been shown. Hydrothermal crystallisation of zirconia nanopowders with a mineralizer-dependent amount of the tetragonal and monoclinic zirconia polymorphs composed of oval and elongated crystallites with various ratios or plate-shaped crystallites has been discussed. The effect of  $\text{TiO}_2$  on hindered hydrothermal crystallisation of zirconia solid solutions was shown. A potential of the *in-situ* method for shaping the nano-structure of the  $\text{TiC}/\text{ZrO}_2$  composites has been presented. A slight effect of the carbon precursor and a significant one of the carbon incorporation way on the morphology of  $\text{TiC}$  in-situ inclusions have been documented.

Key words: *zirconia; nanopowder; nanocomposite; TiC; hydrothermal crystallisation*

## 1. Introduction

Zirconia ceramics, a truly remarkable group of materials, range from electrically insulating, mechanically weak pure monoclinic zirconia through the fast ion conducting stabilised cubic and tetragonal forms to the TZP and Mg-PSZ ceramics characterised by superb mechanical properties. The latter materials utilize benefits of the transformation toughening associated with the tetragonal (t) to monoclinic (m) phase transformation. Furthermore, zirconia brings a potential for nanotechnology development. The last 35 years of extensive studies of the zirconia systems have delivered a wealth of exciting results [1–3], also those usable in the nanotechnology. Developed methods of fabrication of zirconia micropowders with controlled chemical and phase compositions and morphology can be

---

\*E-mail: pyda@uci.agh.edu.pl

easily adopted to produce zirconia nanopowders [4–6]. Reactivity of zirconia-based ceramics has been studied contributing to development of new methods of production of the zirconia matrix composites and nanocomposites [7–9].

This paper is devoted to a nano-technological aspect of the methods of fabrication of zirconia nanopowders. Selected factors influencing the chemical composition, morphology and structure of hydrothermally crystallised zirconia nanopowders have been described. The potential of the *in-situ* method for shaping the nano-structure of the TiC/ZrO<sub>2</sub> and TiB<sub>2</sub>/TiC/ZrO<sub>2</sub> composites is shown.

## 2. Zirconia nanopowders crystallised under hydrothermal conditions

### 2.1. Effect of pH

The effect of pH of the mineralizer solution on chemical and phase compositions, morphology, compaction and sintering behaviour of zirconia nanopowders was studied using zirconia solid solutions doped with 6 mol % CaO. The nanopowders were fabricated by the co-precipitation method followed by hydrothermal crystallisation described in detail elsewhere [10]. Calcia-zirconia hydrogels were precipitated from aqueous solutions of zirconyl and calcium chlorides with a solution of NaOH free of Na<sub>2</sub>CO<sub>3</sub>, hydrothermally crystallised for 4 h under autogeneous water vapour pressure at 240±5 °C and at pH ranging from 8.2 to 12.4.

Two populations of zirconia nano-crystallites differing in shape are observed as revealed by TEM (Fig. 1). The population content depends on the solution pH. Oval and nearly isometric particles belong to the first population. The second one is composed of needle-shaped particles. It was arbitrarily assumed that an aspect ratio of the needle-shape crystallites exceeds a value of 1.6.

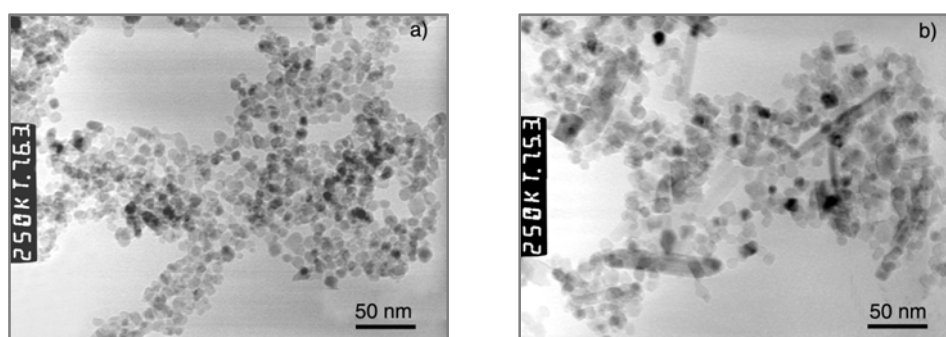


Fig. 1. SEM microphotographs of the 6 mol % CaO–ZrO<sub>2</sub> nanopowders crystallised at solution pH of: a) 8.2, b) 12.1

Oval crystallites prevail over the needle-shaped ones at any pH. Their sizes change slightly upon pH changes (Fig. 2). An increase of the average values from 9.3 nm to 14.0 nm has been found within the studied pH range. An aspect ratio of the

oval crystallites remains nearly constant in this pH range (Fig. 3) keeping an average value of  $1.32 \pm 0.03$ . The needle-shaped crystallites triple their width from  $7.3 \pm 0.8$  nm to  $20.5 \pm 7.8$  nm (Fig. 2). Simultaneously, their length increases more than seven times reaching  $102 \pm 39$  nm. As a result, the aspect ratio increases to the value of  $5.2 \pm 1.9$ .

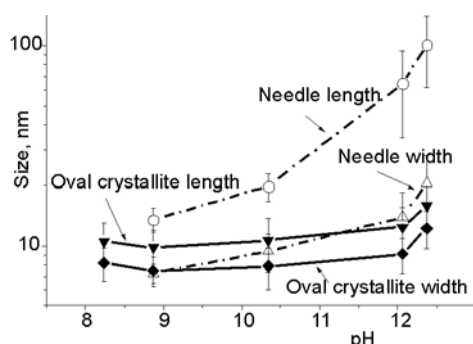


Fig. 2. Size of oval and needle-shaped crystallites in function of pH

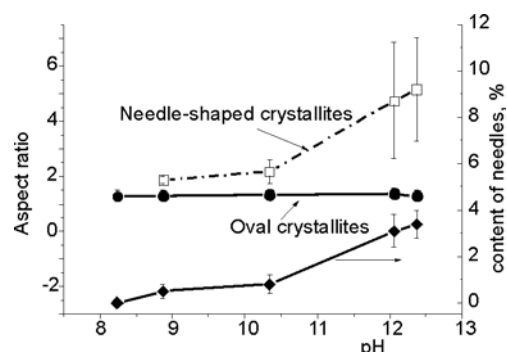


Fig. 3. Aspect ratio of oval and needle-shaped crystallites and number content of needle-shaped crystallites in function of pH

The crystallites which look like plates have been sporadically found in the zirconia nanopowders crystallised at pH 8.2 and 12.0. In this case, the average crystallite sizes are equal to  $13.7 \pm 1.9$  nm and  $18.1 \pm 6.4$  nm and aspect ratios to  $1.37 \pm 0.12$  and  $1.30 \pm 0.22$ , respectively. The amount of CaO introduced into the zirconia solid solution during the hydrothermal treatment depends on the solution pH as is shown in Fig. 4. Only pH values higher than  $\sim 10.3$  are suitable to retain CaO quantitatively in the zirconia nanopowder. The tetragonal and monoclinic zirconia polymorphs are present in the zirconia nanopowders (Fig. 4). The X-ray diffraction measurements reveal the tetragonal and monoclinic symmetries for the oval and needle-shaped crystallites, respectively. This is consistent with the finding that both the monoclinic phase content and number of the needle-shaped crystallites (Fig. 3) increase with pH.

The presented data indicate an in-situ transformation as the most probable crystallisation mechanism of tetragonal zirconia nanocrystallites suggested first by Adair et al. [11] for pure zirconia crystallising under hydrothermal conditions. This mechanism assumes a spontaneous transformation of amorphous zirconia hydrogel particles into a crystalline form with no dissolution-precipitation. A continuous and great increase of the needle-shaped particle aspect ratio with pH suggests a dissolution-precipitation mechanism for growth of monoclinic zirconia crystallites. Its contribution to development of the calcia-zirconia powder morphology increases with pH as a result of an increased zirconia solubility in the mineralizer solution. Tani et al. [12] and Bućko et al. [13] also reported this mechanism for hydrothermally grown pure zirconia crystallites.

The needle-shaped crystallites affect densification of zirconia nanopowders during compaction and sintering. The green density increases with pH reaching the value of

49.5 % of theoretical density for pH = 12.4 (Fig. 5). This is consistent with a general knowledge on densification of polymodal systems with controlled grain size distributions during compaction. An opposite dependence is observed for the density of a sintered body (Fig. 5). Therefore, the presence of needle-shaped nanocrystallites improves compressibility of the nanopowders but deteriorates their sinterability. The latter property is most probably related to the effects of both differential sintering and back stresses which can be generated by relatively large needles.

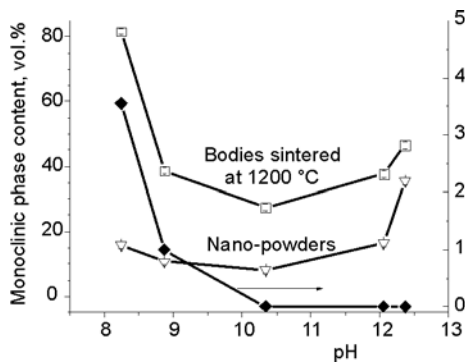


Fig. 4. Monoclinic phase content in 6 mol % CaO-ZrO<sub>2</sub> nanopowders and the bodies sintered at 1200 °C, and loss of CaO during zirconia hydrogel processing in function of pH

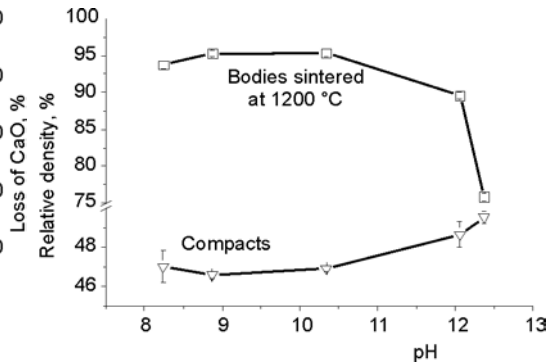


Fig. 5. Relative density of green compacts and bodies sintered at 1200 °C in function of pH

The phase composition of the sintered materials is shown in Fig. 4. Zirconia phases of the monoclinic and tetragonal symmetry are detected. A minimum exists in the dependence of monoclinic zirconia content on pH. An increase of the monoclinic zirconia content observed at pH lower than 10.3 is attributed to destabilisation of the zirconia solid solution due to the loss of CaO. An increase of the monoclinic zirconia content observed at pH above 10.3 is attributed to needle-shape crystallites which reduce sinterability of the zirconia nanopowder. This finding is crucial for fabrication of TZP materials stabilised with CaO indicating that zirconia nanopowders with the monoclinic phase content limited to minimum and containing nanocrystallites of slightly diverse shapes and sizes are only suitable for the production of tetragonal calcium-zirconia based materials and nanomaterials.

## 2.2 Effect of mineralizer on the zirconia nanopowder morphology

Zirconia nanopowders with no stabilizer were crystallised under hydrothermal conditions. Water, 1 M water solutions of NaCl, Na<sub>2</sub>SO<sub>4</sub>, NaNO<sub>3</sub> or Na<sub>2</sub>CO<sub>3</sub> and saturated water solutions of Na<sub>2</sub>B<sub>4</sub>O<sub>7</sub> or NaF were used as mineralizers. Zirconia hydrogels were precipitated with ammonia, washed with water, mixed with the mineralizer and hydrothermally treated for 4 h at 250 °C under a saturated water vapour pressure at pH < 9.1.



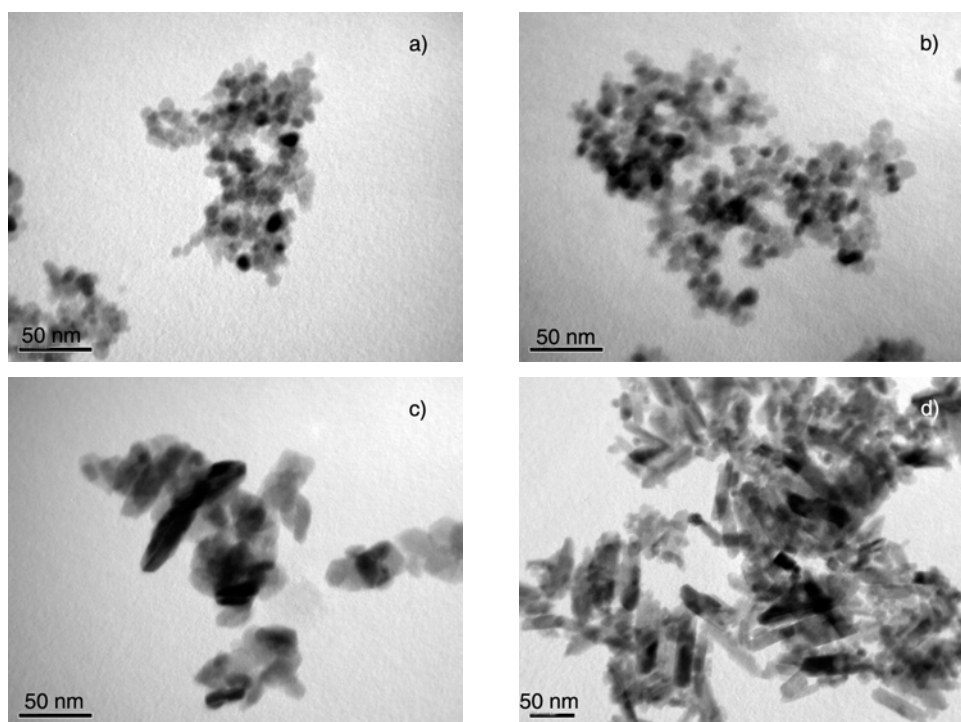


Fig. 6. Morphology of zirconia nanopowders depending on a mineralizer: a)  $\text{H}_2\text{O}$ , b)  $\text{Na}_2\text{SO}_4$ , c)  $\text{NaF}$ , d)  $\text{Na}_2\text{CO}_3$

A strong dependence has been found of the morphology of zirconia nanopowder on the mineralizer applied. Nanopowders with a mineralizer dependent amount of the tetragonal and monoclinic zirconia polymorph composed of oval, elongated, a mixture of oval and elongated or plate-shaped crystallites were produced. The zirconia nanopowders derived from  $\text{H}_2\text{O}$  (Fig. 6a),  $\text{NaCl}$  (Fig. 6b),  $\text{Na}_2\text{SO}_4$  and  $\text{NaNO}_3$  crystallization environments are similar to one another having an oval crystallite shapes, a projection size of  $10.3 \pm 0.4$  nm, a specific surface area of  $97 \pm 2$   $\text{m}^2/\text{g}$ , and tetragonal and monoclinic phase contents of  $79 \pm 6\%$  and  $21 \pm 6\%$ , respectively.  $\text{NaF}$  crystallisation environment leads to increased crystallites of the size ranging from 10 nm to 47 nm, nearly plate-shaped morphology (Fig. 6c) and solely monoclinic symmetry. The zirconia nanopowders crystallised in the  $\text{Na}_2\text{B}_4\text{O}_7$  (Fig. 6d) and  $\text{Na}_2\text{CO}_3$  environments were composed of both oval and needle-shaped crystallites. Monoclinic phase contents of 75.3 % and 80.9 %, oval crystallite projection sizes of 2.6–10.2 nm and 5.6–26.6 nm, needle-shaped crystallite projection sizes of 6.0–27.4 nm and 10.5–75.1 nm, the aspect ratios of the needle-shaped crystallites of 4.5 and 4.3 were measured for the nanopowders crystallised in the  $\text{Na}_2\text{B}_4\text{O}_7$  and  $\text{Na}_2\text{CO}_3$  environments, respectively. The presented results indicate that the  $\text{B}_4\text{O}_7^{2-}$  ions inhibit growth of tetragonal crystallites and aid monoclinic but the  $\text{CO}_3^{2-}$  ions aid also some growth of the tetragonal crystallites.

The latter ions especially favour an increase of a monoclinic crystallite length. The value of 154 nm was measured being the largest for the studied nanopowders.

### 2.3 Effect of TiO<sub>2</sub> content on zirconia crystallisation

Hydrothermal crystallisation of zirconia solid solutions containing 3 mol % Y<sub>2</sub>O<sub>3</sub> and 20–50 mol % TiO<sub>2</sub> with the step of 10 mol % was studied. Zirconia hydrogels were co-precipitated from aqueous solutions of appropriate chlorides with ammonia at pH = 9, washed with water and hydrothermally treated for 4 h at 250 °C under a saturated water vapour pressure at pH = 7.5.

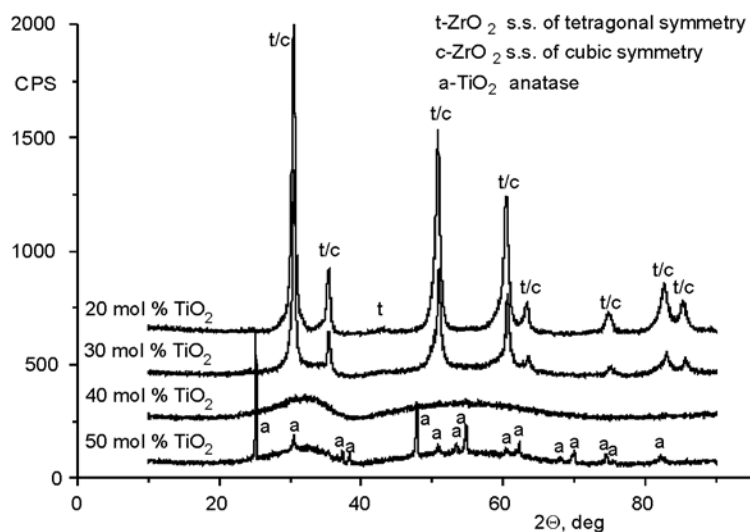


Fig. 7. X-ray diffraction patterns of the zirconia powders containing 3 mol % Y<sub>2</sub>O<sub>3</sub> and the indicated TiO<sub>2</sub> concentration after hydrothermal crystallisation for 4 h at 250 °C

The X-ray diffraction measurements revealed TiO<sub>2</sub> playing a very important role in hydrothermal crystallisation of the zirconia solid solutions as shown in Fig. 7. TiO<sub>2</sub> contents exceeding 30 mol % hindered crystallisation of tetragonal and cubic polymorphs of the zirconia solid solution and left the zirconia hydrogel in an amorphous state accompanied additionally by anatase in the case of the 40 mol % TiO<sub>2</sub> sample. The results suggest that nuclei formation and growth of the TiO<sub>2</sub> rich phases, e.g., ZrTiO<sub>4</sub> requires temperatures and/or pressures higher than the applied ones.

### 2.4. An in-situ synthesis of the TiC and TiB<sub>2</sub> inclusions in the zirconia matrix

Carburisation of the zirconia structure and chemical reaction occur when carbon encounters with zirconia. Carbon easily diffuses throughout the zirconia lattice occupying the octahedral interstitial sites as a neutral atom [15]. Diffusion kinetics depends

on time and temperature. The process commences when the temperature exceeds 700 °C. The carburisation prevents degradation of tetragonal zirconia polycrystals doped with 3 mol % of yttria (3Y-TZP) in water or steam at 200 °C [15]. Heat treating of sintered 3Y-TZP in a carbon atmosphere resulted in a surface layer formation stabilised by carbon ions but the bulk strength was slightly decreased.

Carbothermal reduction of zirconia is another result of the interaction of carbon with zirconia solid solutions. The value of the standard Gibbs free energy of ZrC formation indicates that the carbothermal reduction of zirconia can occur at about 1627 °C under CO partial pressure of 1 atm. Decreasing the CO partial pressure decreases the reaction temperature.

Titanium oxide forms a substitutive solid solution with zirconia which is well known and documented [16]. Titanium oxide segregation during the solution formation has been reported [17]. The segregation factor of 5 was determined within a layer extending up to 6 nm into the zirconia grain. The titanium segregation affects zirconia grain growth increasing the rate of growth. Finally, in some conditions titanium can reduce its valence and increase the oxygen vacancy concentration. This affects the phase composition of zirconia polycrystals increasing the amount of the cubic zirconia polymorphs which do not participate in transformation toughening. Titanium oxide dissolved in the zirconia structure is subject to carbothermal reduction at 1280 °C under CO partial pressure of 1 atm as indicated by the thermodynamic calculations [7, 8]. This temperature, being lower than that of zirconium carbide formation, provides opportunity to carbonise TiO<sub>2</sub> selectively while leaving ZrO<sub>2</sub> unchanged. Therefore, a new process aiming at preparing tetragonal zirconia powders containing titanium carbide was developed at the AGH University of Science and Technology in 1998 [7]. A year later, Liu et al. reported similar studies [18]. The process was further developed to produce titanium diboride inclusions in the zirconia matrix [19]. This new approach provides methods to control the morphology and size of the inclusions via a control of nucleation and nuclei growth opposite to the physical mixing method in which reduction of the reinforcement particle size proceeds. Therefore, it is attractive for production of the zirconia based transformation toughened composites and nano-composites reinforced with hard and stiff inclusions.

The preparation route of the zirconia matrix composites with in-situ TiC and/or TiB<sub>2</sub> inclusions utilises benefits of the TiO<sub>2</sub> doped zirconia nanopowders produced by the co-precipitation method followed by calcination or hydrothermal treatment. The original zirconia nanopowder is homogenised with a carbon precursor, e.g., phenol-formaldehyde resin [7, 9], sucrose [18] or carbon nanotubes and a boron precursor in the case of the TiB<sub>2</sub>/TiC/ZrO<sub>2</sub> composites [19]. The *in-situ* synthesis is performed at temperatures ranging from 1000 °C to 1650 °C in argon or under vacuum. The composite powder is always ground to receive an appropriate sinterability.

A method of surface carburisation of dense tetragonal zirconia polycrystals combined with carbothermal TiO<sub>2</sub> reduction has also been reported [8]. The presence of both TiC and TiB<sub>2</sub> *in-situ* inclusions affects sintering of titania–zirconia nanopowders.

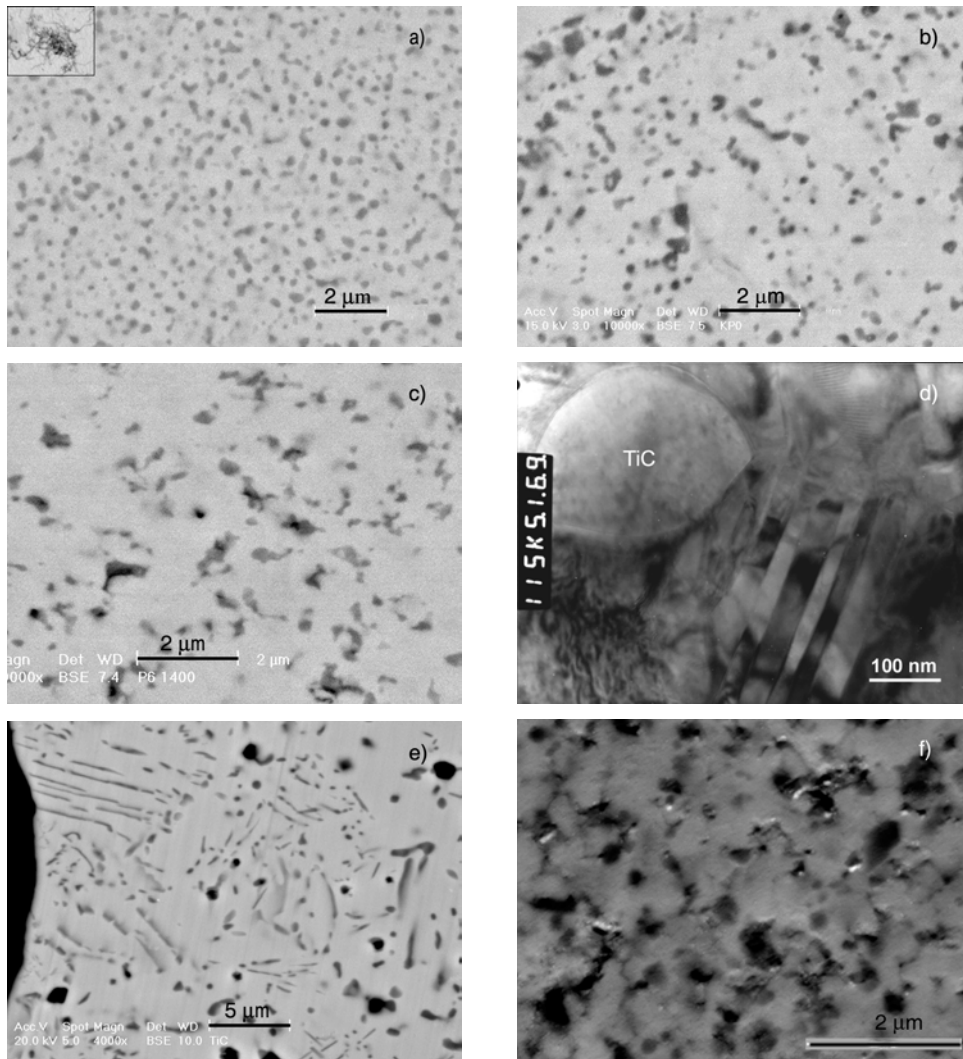


Fig. 8. Morphology of the in-situ inclusions depending on the carbon precursor (PF – phenol–formaldehyde resin, CNT – carbon nanotubes), processing (B – bulk synthesis, S – surface carburisation) and sintering temperature: a) 10.2 wt. % TiC–ZrO<sub>2</sub>, B, 1500 °C, b) 10.7 wt. % TiC–ZrO<sub>2</sub> – PF, B, 1500 °C; c) and d) TiC–ZrO<sub>2</sub>–PF, B, 1400 °C, e) ~10 wt. % TiC–ZrO<sub>2</sub>–PF, S, 1650 °C, f) 12.9 vol. % TiB<sub>2</sub>, 8.9 vol.% TiC–ZrO<sub>2</sub>–PF, H<sub>3</sub>BO<sub>3</sub>, B, 1500 °C

The inclusions inhibit grain growth by a pinning effect leading to a decreased densification. The composites derived from the nanopowders with unreacted carbon exhibit increased porosity due to CO which evolves when the additional amount occurs of the carbothermal TiO<sub>2</sub> reduction.

Hardness improvement ( $18.3 \pm 1.0$  GPa) of the surface carburised TZP has been reported [8]. Promising fracture toughness ( $K_{Ic} = 8.8 \pm 0.5$  MPa·m<sup>0.5</sup>) and bending strength

( $\sigma = 912 \pm 72$  MPa) were obtained for not optimised composites with *in-situ* TiC and TiB<sub>2</sub> inclusions [19].

Morphological diversities of the *in-situ* inclusions depending on the carbon precursor and processing conditions are shown in Fig. 8. A comparison of Figs. 8a and 8b indicates a slight effect of the carbon precursor morphology on the morphology of the TiC *in-situ* inclusions. However, the way of introducing carbon, i.e., surface or bulk carburisation, was found to be a significant factor influencing the TiC inclusion shape (Fig. 8e).

### 3. Concluding remarks

The results presented show that the hydrothermal method of fabrication of zirconia nanopowders is a real example of the ceramic nanotechnology. pH of the solution, type of mineralizer and TiO<sub>2</sub> concentration belong to factors influencing composition and morphology of the zirconia crystallite phase. However, processing the zirconia nanopowders to nanoceramics is not an easy task. Even very sophisticated methods of nanocomponent homogenisation do not lead to fully nanostructural materials if high temperature treatment is applied. This is proved by the results of the *in-situ* synthesis of TiC inclusions by using carbon nanotubes or carbon delivered by phenol-formaldehyde resin. A TiC inclusion size touching the nanometric limit was only obtained. However, when benefits of the carbon diffusion through the zirconia lattice are fully utilized, the real nanometric *in-situ* TiC is produced as a surface carburisation method shows.

#### Acknowledgements

Financial support from the resources allocated for science in 2006–2008 under the grant No. N507 017 31/0527 has been provided for this research work.

#### References

- [1] *Science and Technology of Zirconia I*, Vol. 3, A.H. Heuer, L.W. Hobbs (Eds.), The American Ceramic Society, Columbus, OH, 1981.
- [2] *Science and Technology of Zirconia II*, Vol. 12, N. Claussen, M. Rühle, A.H. Heuer (Eds.), The American Ceramic Society, Columbus, OH, 1984.
- [3] *Science and Technology of Zirconia V*, S.P.S. Badwal, M.J. Bannister, R.H.J. Hannink (Eds.), Technomic Publ. Co., Lancaster, Basel, 1993.
- [4] BYRAPPA K., YOSHIMURA M., *Handbook of Hydrothermal Technology*, Noyes Publications, William Andrew Publ. LLC, USA, 2001, Chapter 1.2.
- [5] SOMIYA S., ROY R., Bull. Mater. Sci., 23 (2000), 453.
- [6] PYDA W., HABERKO K., BUĆKO M. M., J. Am. Ceram. Soc., 74 (1991), 2622.
- [7] PYDA W., [in:] Proc. II ICCST, S. Adali, E.V. Morozov, V.E. Verijenko (Eds.), 3–11 June 1998, Department of Mechanical Engineering, University of Natal, Durban, 1998, 195.
- [8] HABERKO K., PYDA W., PEĐZICH Z., BUĆKO M.M., J. Eur. Ceram. Soc., 20 (2000), 2649.

- [9] PYDA W., *Ceramics Int.*, 30 (2004), 333.
- [10] PYDA W., *Advances in Science and Technology*, Vol. 45, Trans Tech Publications, Switzerland, 2006, pp.194–199.
- [11] ADAIR J. H., DENKEWICZ R.P., ARRIAGADA F. J., OSSEO-ASARE K., [in:] *Ceramic Powder Science II*, G. L. Messing, E. R. Fuller, H. Hausner (Eds.), The American Ceramic Society, Inc. Westerville, OH, 1988, p. 135.
- [12] TANI E., YOSHIMURA M., SOMIYA S., *J. Am. Ceram. Soc.*, 66 (1983), 11.
- [13] BUČKO M. M., HABERKO K., FARYNA M., *J. Am. Ceram. Soc.*, 78 (1995), 3397.
- [14] NISHIZAWA H., YAMASAKI N., MATSUOKA K., MITSUSHIO H., *J. Am. Ceram. Soc.*, 65 (1982), 343.
- [15] ZHAO Z., LIU C., NORTHWOOD D.O., *J. Aust. Ceram. Soc.*, 36 (2000), 135.
- [16] BANNISTER M.J., BARNES M.J., *J. Am. Ceram. Soc.*, 69 (1986), C269.
- [17] ALLEMANN J.A., MICHEL B., MÄRKI H.-B., GAUCKLER L.J., MOSER E.M., *J. Eur. Ceram. Soc.*, 15 (1995), 951.
- [18] LIU J., LI J., WANG H., HUANG Y., *J. Am. Ceram. Soc.*, 82 (1999), 1611.
- [19] MOSKALA N., PYDA W., *Kompozyty (Composites)*, 5 (2005), 56.

*Received 28 April 2007*  
*Revised 16 February 2008*

# Iron filled carbon nanotubes for bio-applications

E. BOROWIAK-PALEN\*

Centre of Knowledge Based Nanomaterials and Technologies, Institute of Chemical and Environment Engineering, Szczecin University of Technology, al. Piastów 42, 71-065 Szczecin, Poland

One of the most interesting bio-applications of nanoparticles refers to as “magnetic fluid hyperthermia” (MFH), i.e. a controlled heating of tumor tissue. In the MFH therapy, magnetic nanoparticles are infiltrated in deep tumor tissue and inductively heated by applying alternating current magnetic fields. The biggest challenge of MFH therapy is the temperature control for which fibre-optic thermometers should be inserted into a tumor. A potential way to overcome this problem seems to be application of carbon nanotubes filled with iron which could provide *in-situ* temperature controlling. Therefore, the synthesis routes of iron filled single-walled carbon nanotubes (Fe-SWCNT) and iron filled multi-walled carbon nanotubes (Fe-MWCNT) has been presented. These two types of nanostructures were prepared *via* wet chemistry technique and by *in situ* single step chemical vapour deposition for Fe-SWCNT and Fe-MWCNT, respectively. The samples were examined by means of transmission electron microscopy, in bright and dark field images modes, and X-ray diffraction.

Key words: *carbon nanotubes; filling of carbon nanotubes; transmission electron microscopy; X-ray diffraction*

## 1. Introduction

Carbon nanotubes (CNT) are carbon nanostructures of a small diameter on the nanometer scale with one or more walls, and a length large in comparison to the diameter. They have mechanically and chemically stable carbon shells which can be opened, filled and closed again without losing their stability. Experiments in filling CNT date back to their identification in 1991 [1, 2]. Extensive work has been performed to synthesize CNT and to endohedrally and exohedrally functionalize them [3–18]. CNTs may be filled with metals, biomolecules, salts, organic materials, etc. The filling procedure can be done during the synthesis process or through subsequent opening and filling of the CNT. In particular, the filling can consist of ferromagnets such as Fe, Ni, and Co [17, 18]. Due to a large form anisotropy of ferromagnetically filled CNT, an

---

\*E-mail: eborowiak@ps.pl

enormously large heating efficiency compared to other nanoparticles is realized when exposing them to AC magnetic fields.

An outstanding example for the use of ferromagnetic nanoparticles is magnetic fluid hyperthermia (MFH), i.e., controlled heating of a tumor tissue. In the MFH therapy, magnetic nanoparticles are infiltrated in deep tumor tissues and inductively heated by applying AC magnetic fields. One challenge of the MFH therapy, however, is the temperature control for which fibre optic thermometers must be inserted into the tumor. A potential way to overcome this problem seems to be the use of CNT which could provide *in-situ* temperature controlling [19, 20].

## 2. Experimental

Pristine SWCNTs, with a mean diameter of 1.50 nm and length up to several  $\mu\text{m}$ , were fabricated by using a standard laser ablation technique [21]. The ‘as produced’ material contains amorphous carbon and catalyst particles (Pt, Rh, Re). In order to purify and open the tubes, acid treatment was performed. The laser ablated soot was placed in a diluted aqua regia solution and refluxed for 24 h at ca. 400 K. Subsequent filtration and washing for several hours with distilled water opened and purified the nanotubes which were then transferred to a beaker containing an over-saturated solution of iron(III) chloride ( $\text{FeCl}_3$ ). The as-prepared solution was then stirred for 20 h at room temperature.

To yield pure Fe filled SWCNTs, washing out the  $\text{FeCl}_3$  which is not incorporated into the tubes but remains on the walls or in the space between the bundles, was very important. This was accomplished by quick washing with concentrated HCl (several seconds) and multiple centrifugations with distilled water at which the water was removed and replaced after each centrifugation cycle. As the last step, the sample was heated in air at 593 K for 1 h in order to decompose the  $\text{FeCl}_3$  to iron and chlorine.

The sample was synthesized by catalytic decomposition of ferrocene, under methane gas flow, in a quartz tube reactor inside a dual zone furnace. Ferrocene is the iron source, while methane acts as the carbon feedstock and the carrier gas. The main parameters are the sublimation temperature of ferrocene (applied in the first furnace stage),  $T = 174\text{ }^\circ\text{C}$ , the deposition temperature (in the second furnace stage),  $T = 950\text{ }^\circ\text{C}$ , and the methane flow rate of  $200\text{ cm}^3/\text{min}$ . The reaction time was 0.5 h and before the process took place, the system was evacuated to ca.  $10^{-3}$  mbar at room temperature.

The as-produced material was purified by annealing in air at  $350\text{ }^\circ\text{C}$  for 1 h, after which the acid treatment was performed. Afterwards, the product was filtrated and washed thoroughly with distilled water and acetone.

The chemical composition of iron filled single-walled carbon nanotubes (Fe-SWCNT) and iron filled multi-walled carbon nanotubes (Fe-MWCNT) was examined using X-ray diffraction (XRD) and the morphology of the sample was studied using high resolution transmission electron microscopy (HR-TEM).



### 3. Results and discussion

The high angle dark field images in scanning TEM (HAADF-STEM) show thin and long nanowires, as expected with the efficient filling of SWCNTs (Fig. 1a). A more systematic study of the nanowires indicates that most of them have lengths in the range 5–100 nm. Absolute identification of the iron filling using standard TEM was very challenging due to the diameter of the metal wires being so small that it was impossible to differentiate between individual single nanowires and nanotube walls in the bundle. Therefore, Fig. 1a presents an HAADF-STEM image of the pristine SWCNT. Here, one cannot notice any presence of lines indicating formation of iron nanowires in the cavity of the tubes.

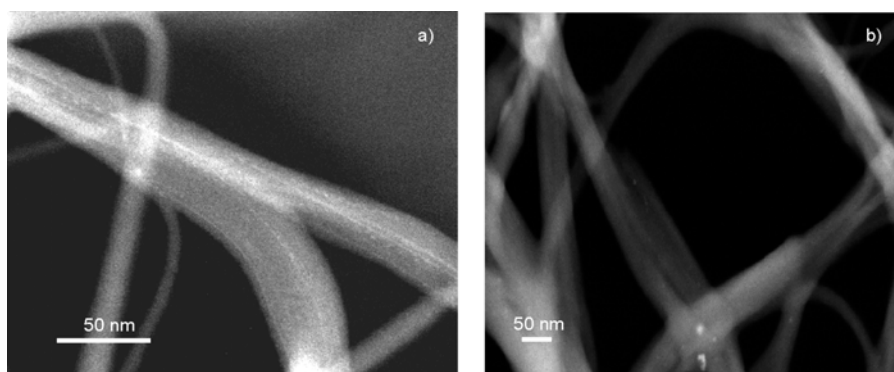


Fig. 1. HAADF-STEM images of Fe-SWCNT (a) and pristine SWCNT (b)

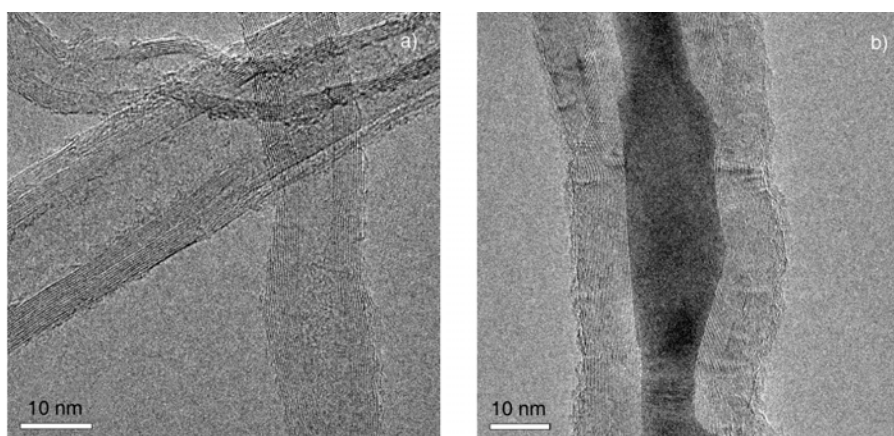


Fig. 2. TEM images of unfilled MWCNTs (a) and Fe-MWCNT (b)

The identification of multi-walled carbon nanotubes and their filled core is much easier due to much higher tube diameters. Bright field TEM was sufficient to observe the morphology of the sample. In Figure 2a, one can observe MWCNT with empty

core and parallel graphitic layers forming the multiwalled structure of the tubes. Figure 2a presents an individual MWCNT with a filled iron nanowire. The analysis of TEM images enabled estimation of the mean outer diameter of the tubes (40 nm) and of the filling iron nanowires (100 nm).

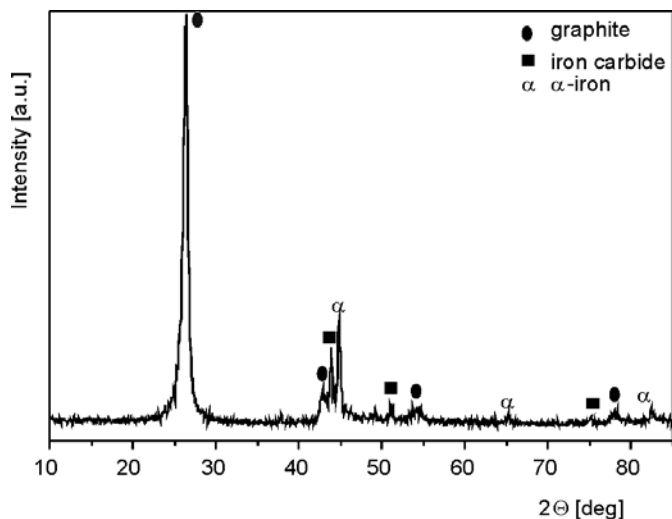


Fig. 3. XRD pattern of Fe-MWCNT

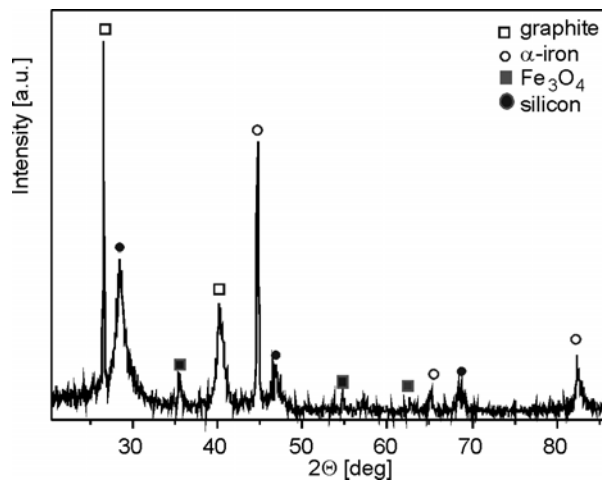


Fig. 4. XRD pattern of Fe-SWCNT

The XRD pattern presented in Fig. 3 shows only the peaks originating from carbon (MWCNT), iron carbide and  $\alpha$ -Fe, with a body centered cubic crystal structure. The presence of only one iron structure is very unusual as normally the composition of different iron phases is produced. Here, one can observe that MWCNT are filled only with the ferromagnetic phase of iron.

The crystallographic analysis of Fe-SWCNT clearly indicates the presence of graphite,  $\alpha$ -Fe and  $\text{Fe}_3\text{O}_4$  in the sample (Fig. 4). The peaks associated with silicon originate from the substrate used for XRD measurements.

The presence of  $\alpha$ -iron is not surprising as our previous investigations of the magnetic properties of Fe-SWCNT proved that SWCNTs are filled with ferromagnetic form of iron. The ferromagnetic behaviour was observed at room temperature and at liquid nitrogen temperature [18]. The  $\text{Fe}_3\text{O}_4$  signal comes probably from the oxidized reminiscence of iron which was not incorporated into the cavities of the tubes. The carbon layers protect against the oxidation only the iron incorporated into the interior of the singlewalled tubes [18].

## 4. Conclusions

We have presented a study on the synthesis and structural analysis of Fe-filled single- and multi-walled CNT bulk samples which can be suitable candidates for bio-applications. Due to the fact that iron filled carbon nanotubes contain a ferromagnetic form of iron, they can be investigated in the magnetic fluid hyperthermia. The insertion of iron filled tubes into the tumor could provide *in-situ* temperature controlling. Nevertheless, further medical investigations are required for a complete understanding of the interactions involved.

### Acknowledgement

The author is grateful to M.H. Rummeli and T. Gemming for help with TEM analysis. The work was funded by EU "CARBIO" project and Polish research grant No. 1 T09B-009-30.

### References

- [1] IJIMA S., ICHIHASHI T., *Nature*, 363 (1993), 603.
- [2] YAKOBSON B.I., SMALLEY R.E., *Am. Sci.*, 85 (1997), 324.
- [3] SHVARTZMAN-COHEN R., NATIV-ROTH E., YERUSHALMI-ROZEN R., BASKARAN E., SZLEIFER I., LEVI-KALISMAN Y., *J. Am. Chem. Soc.*, 126 (2004), 14850.
- [4] SINANI V.A., KOTOV N.A., YAROSLAVOV A.A., RAKHNYANSKAYA A.A., GHEITH M.K., WICKSTED J.P., SUN K., MAMEDOV A.A., *J. Am. Chem. Soc.*, 127 (2005), 3463.
- [5] NAKASHIMA N., OKUZONO S., MURAKAMI H., NAKAI T., YOSHIKAWA K., *Chem. Lett.*, 32 (2003), 456.
- [6] ZHENG M., JAGOTA A., SEMKE E.D., DINER B.A., MCLEAN R.S., LUSTIG S.R., RICHARDSON R.E., TASSI N.G., *Nature Mater.*, 2 (2003), 338.
- [7] TAGMATARCHIS N., PRATO M., *J. Mater. Chem.*, 14 (2004), 437.
- [8] HIRSCH A., *Angew. Chem. Int. Ed.*, 41 (2002), 1853.
- [9] DYKE C.A., TOUR J.M., *Chem. Eur. J.*, 10 (2004), 812.
- [10] STEVENS J.L., HUANG A.Y., PENG H., CHIANG I.W., KHABASHESKU V.N., MARGRAVE J.L., *Nano Lett.*, 3 (2003), 331.
- [11] HUDSON J.L., CASAVANT M.J., TOUR J.M., *J. Am. Chem. Soc.*, 126 (2004), 11158.
- [12] DUJARDIN E., EBBESEN T.W., HIURA H., TANIGAKI K., *Science*, 265 (1994), 1850.

- [13] CHU A., COOK J., HEESON R.J.R., HUTCHINSON J.L., GREEN M.L.H., SLOAN J., *Chem. Mater.*, 8 (1996), 2751
- [14] SLOAN J., HAMMER J., ZWIEFKA-SIBLEY M., GREEN M.L.H., *Chem. Commun.*, (1998), 347
- [15] ZHANG Z.L., LI B., SHI Z.J., GU Z.N., XUE Z.Q., PENG L-M., *J. Mater. Res.*, 15 (2000), 2658.
- [16] MATSUI K., PRADHAN B.K., KYOTANI T., TAMITA A., *J. Phys. Chem. B*, 105 (2001), 5682.
- [17] BOROWIAK-PALEN E., RUEMMELI M.H., GEMMING T., PICHLER T., KALENCZUK R.J., SILVA S.R.P., *Nanotechnology*, 17 (2006), 1.
- [18] BOROWIAK-PALEN E., MENDOZA E., BACHMATIUK A., RÜMMELI M.H., GEMMING T., NÓGUES J., SKUMRYEV V., KALENCZUK R.J., PICHLER T., SILVA S.R.P., *Chem. Phys. Lett.*, 421 (2006), 129.
- [19] PANKHURST Q.A., CONOLLY J., JONES S.K., DOBSON J., *J. Phys. D: Appl. Phys.*, 36 (2003), R167.
- [20] JORDAN A., SCHOLZ R., WUST P., FAHLING H., FELIX R., *J. Magn. Magn. Mater.*, 201 (1999), 413.
- [21] RUMMELI M.H., LOFFLER M., KRAMBERGER C., SIMON F., FULOP F., JOST O. SCHONFELDER R., GRUNEI A., GEMMING T., POMPE W., BUCHNER B., PICHLER T., *J. Phys. Chem. C*, 111 (2007), 4094.

*Received 28 April 2007*  
*Revised 16 February 2008*

# Synthesis of silver nanoparticles using microorganisms

Z. SADOWSKI\*, I. H. MALISZEWSKA,  
B. GROCHOWALSKA, I. POLOWCZYK, T. KOŹLECKI

Faculty of Chemistry, Wrocław University of Technology,  
Wybrzeże Wyspiańskiego 27, 50-370 Wrocław, Poland

Biosynthesis of silver nanoparticles using *Penicillium* fungi has been reported. The extracellular mechanism of silver nanoparticles creation was investigated by UV-Vis spectroscopy, electron microscopy and laser diffraction. The zeta potential of silver nanoparticles has also been determined.

Key words: *silver nanoparticles; Penicillium fungi; extracellular synthesis; zeta potential*

## 1. Introduction

The study of biosynthesis of nanomaterials offers a valuable contribution into materials chemistry. The ability of some microorganisms such as bacteria and fungi to control the synthesis of metallic nanoparticles should be employed in the search for new materials [1]. Biosynthetic methods have been investigated as an alternative to chemical and physical ones. These methods can be divided into two categories depending on the place where the nanoparticles or nanostructures are created as many microorganisms can provide inorganic materials either intra- or extracellularly [2]. For example, bacteria *Pseudomonas strutzeri* isolated from silver mine materials is able to reduce  $\text{Ag}^+$  ions and accumulates silver nanoparticles, the size of such nanoparticles being in the range 16–40 nm, with the average diameter of 27 nm [3]. The examples also include magnetotactic bacteria which produce magnetite ( $\text{Fe}_3\text{O}_4$ ) or greigite ( $\text{Fe}_3\text{S}_4$ ) and diatoms which produce siliceous material [4]. The intracellular methods need a special ion transportation system into the microbial cell. Formation of magnetite particles proceeds through a sequence of events: reduction of Fe(III) to Fe(II), precipitation of amorphous oxide and subsequent transformation to magnetite [4].

Gold nanoparticles have also been synthesized in human cells, both in cancer and non-cancer ones [5]; the scanning microscopic images confirmed that their morpholo-

---

\*Corresponding author, e-mail: zygmont.sadowski@pwr.wroc.pl

gies differed significantly. This behaviour can have an implication to cancer diagnostics. In contrast, extracellular synthesis of nanoparticles occurs in alkalothermophilic actinomycete, *Thermomonospora* sp., which reduces gold ions.

The metabolic activity of microorganisms can lead to precipitation of nanoparticles in external environment of a cell, the fungi being extremely good candidates for such processes. The extracellular synthesis of silver and gold nanoparticles by the fungus *Colletotrichum* sp. [1] or *Aspergillus fumigatus* has been reported [6]. A novel biological method for synthesis of silver nanoparticles using *Vericillum* was proposed by Mukherjee et al. [7, 8]; a two-step mechanism was suggested. The first step involves trapping of  $\text{Ag}^+$  ions at the surface of the fungal cells. In the second step, enzymes present in the cell reduce silver ions.

The extracellular production of metal nanoparticles by several strains of the fungus *Fusarium oxysporum* has been described by Duran et al. [9]. The presence of hydrogenase in the *F. oxysporium* broth was demonstrated. This extracellular enzyme shows excellent redox properties and it can act as an electron shuttle in metal reduction. It was evident that electron shuttles or other reducing agents (e.g., hydroquinones) released by microorganisms are capable of reducing ions to nanoparticles.

The Neem (*Azadirachta indica*) leaf broth and aqueous solution of silver nitrate or chloroauric acid were used for the extracellular synthesis of pure metallic silver and gold particles [10]. The time required for  $\text{Ag}^+$  and  $\text{Au}^{3+}$  ions to reduce was 4 h and 2 h, respectively, being extremely short compared to both bacteria and fungi (24 h and 120 h). Surface active constituents of the leaf broth stabilize nanoparticle suspensions – an aqueous suspension showed stability even after 4 weeks.

Our aim in the present contribution was to synthesize and characterize silver nanoparticles obtained by use of *Penicillium* fungi isolated from the soil. To our knowledge, extracellular synthesis of Ag particles by these fungi has not been reported so far.

## 2. Experimental

*Synthesis of silver nanoparticles.* *Penicillium* strain isolated from soil was studied. Inoculated fungi were prepared in Petri dishes at room temperature using 2% malt extract with 0.5% yeast extract. Fungal biomass used for biosynthetic experiments was grown aerobically in liquid medium containing [g/l]:  $\text{KH}_2\text{PO}_4$  7.0,  $\text{K}_2\text{HPO}_4$  2.0,  $\text{MgSO}_4 \times 7\text{H}_2\text{O}$  0.1,  $(\text{NH}_4)_2\text{SO}_4$  1.0, yeast extract 0.6, glucose 10.0. Erlenmeyer flasks were inoculated with spores and incubated at 25 °C with shaking (150 rpm) for 72 h. After the incubation, the biomass was filtered (Whatman filter paper No. 1) and then extensively washed with distilled water to remove any medium component. Fresh and clean biomass was taken into Erlenmeyer flasks containing 100 cm<sup>3</sup> of Milli-Q deionised water. The flasks were agitated at the same conditions as described above, then the biomass was filtered again (Whatman filter paper No. 1) and cell-free filtrate was used in experiments.  $\text{AgNO}_3$  (1 mM of final concentration) was mixed with cell-free

filtrate in an Erlenmeyer flask and agitated at 25°C in dark. Control (without silver ions) was also run along with the experimental flasks. Samples of 1 cm<sup>3</sup> were withdrawn at various times and the absorbance was measured at the resolution of 1 nm using a UV-visible spectrophotometer (HELIOS  $\lambda$ , ThermoElectron Corp.).

*Particle sizing measurements.* Particle sizing experiments were carried out by means of laser diffractometry, using an Mastersizer 2000 instrument (Malvern), equipped with HydroMu dispersing unit (Malvern). Measurements were taken in the range between 0.1 and 1000  $\mu\text{m}$ , under the following conditions: particle refractive index 0.54, particle absorption coefficient 4, water refractive index 1.33, and general calculation model for irregular particles. Ten measurement cycles of 10 s each were taken, and the data obtained were averaged by a software (Mastersizer 2000, ver. 5.20 from Malvern).

*Electron microscopy.* Scanning electron micrographs were taken using a DSM 982 GEMINI instrument (Zeiss, Germany). Samples were filtered and dried before measurements.

*The zeta potential measurement.* Measurements were carried out using a Zetasizer Nano ZS (Malvern) and a titrator MPT-2. An aqueous suspension of silver nanoparticles was filtered through a 0.45  $\mu\text{m}$  PTFE membrane before measurement. The zeta potential was calculated using Henry's equation.

### 3. Results and discussion

Upon addition of Ag<sup>+</sup> ions into the filtered cell-free culture in the dark, samples changed in colour from almost colourless to brown, with intensity increasing during the period of incubation. Control (without silver ions) showed no change in colour of the cell filtrates when incubated in the same conditions (data not shown). Formation of colloidal silver particles can be easily followed by changes of UV-Vis absorption (Fig. 1). Shankar et al. suggested that the shoulder at 370 nm corresponded to the transverse plasmon vibration in silver nanoparticles, whereas the peak at 440 nm due to excitation of longitudinal plasmon vibrations [11]. After 72 h the process was stopped and the particles were further analyzed by laser diffraction, scanning electron microscopy and zeta potential measurements.

Laser diffraction revealed that particles obtained are polydisperse mixture (uniformity 6.97), with the size ranging between hundreds on nanometers and micrometers (Fig. 2). The values of D10, D50 and D90 are 0.69, 4.87 and 13.31  $\mu\text{m}$ , respectively. There is still work to do on the control of particle sizes and uniformity. Probably changes in medium composition and *Penicillium* strain can substantially improve these parameters.

Scanning electron micrograph (Fig. 3) confirms data obtained from the laser diffraction, albeit preparation of samples (including drying) can affect their size and shape. It was observed that the nanoparticles are partially aggregated due to the drying process.

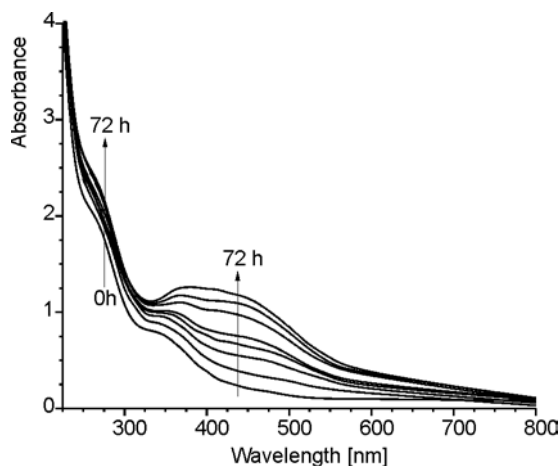


Fig. 1. Temporal evolution of UV-Vis absorption spectra during the formation of silver nanoparticles

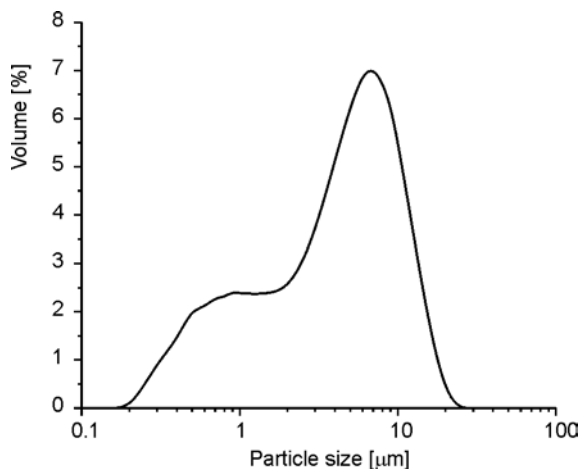


Fig. 2. Particle size distribution for silver nanoparticles

The effect of pH on the zeta potential of silver nanoparticles was also investigated (Fig. 4). At natural conditions (pH close to 8), the zeta potential was equal to  $-26.3 \pm 0.2$  mV. We can conclude that the silver nanoparticles got a negative zeta potential and the isoelectric point is below pH = 2; at pH > 8, particles are fairly stable due to the electrostatic repulsion. On the other hand, in acidic solutions low negative values of  $\zeta$ -potential clearly indicate instability of the aggregates.



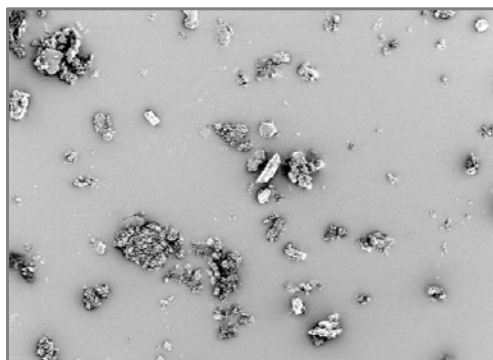


Fig. 3. Scanning electron micrograph of silver nanoparticles. Magnification 5000×

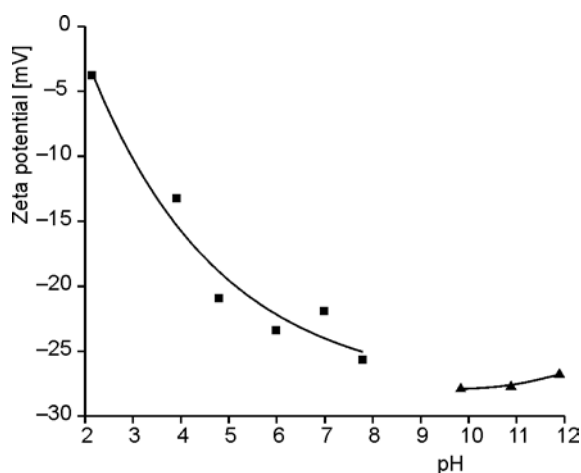


Fig. 4. Zeta potential of silver nanoparticles in function of pH

Fungi of *Penicillium* genus seem to be extremely good candidates for the synthesis of silver nanoparticles. Their formation proceeds via an extracellular mechanism but there are still some question regarding the details of the process. Nanoparticles obtained possess negative zeta potential and are fairly stable at pH value above 8 due to the electrostatic repulsion. The most important feature of *Penicillium* fungi is the fact they are widespread present in the waste biomass from pharmaceutical industry. Such cheap source of material gives an opportunity to cost-effective preparation of various silver-based nanostructures. Further research on the antimicrobial activity of produced nanoparticles will be carried out in this laboratory.

## References

- [1] MANDAL D., BOLANDER M.E., MUKHOPADHYAY D., SARKAR G., MUKHERJEE P., Appl. Microbiol. Biotechnol. 69 (2006), 485.
- [2] *Biomimetic Materials Chemistry*, S. Mann (Ed.), VCH, New York, 1996.
- [3] KLAUS-JOERGER T., JOERGER R., OLSSON E., GRANQVIST C.G., Trends Biotechnol., 19 (2001), 15.

- [4] MANN S., *Biomaterialization, Principles and Concepts in Bioinorganic Materials Chemistry*, Oxford University Press, 2001.
- [5] SAI VANKATARAMAN J.A., SUBRAMANIAM C., KUMAR R.R., PRIYA S., SANTHOSH R.T., OMKUMAR V.R., JOHN A., PRADEEO T., *Langmuir*, 21 (2005), 11562.
- [6] BHANSKA K.C., D'SOUZA S.F., *Coll. Surf. B*, 47 (2006), 160.
- [7] MUKHERJEE P., AHMED A., MANDAL D., SENAPATI S., SAIKAR S.E., KHAN I.M., RAMANI R., PARISHCHA R., AJAYAKUMAR P.V., ALAM M., SASTRY M., KUMAR R., *Angew. Chem. Int. Ed.*, 40 (2001), 3585.
- [8] MUKHERJEE P., AHMAD A., MANDAL D., SENAPATI S., SAIKAR S.R., KHAN I.M., PARISHCHA R., AJAYAKUMAR P.V., ALAM M., KUMAR R., SASTRY M., *Nano Lett.*, 1 (2001), 515.
- [9] DURAN N., MARCATO D.P., ALVES L.O., DE SOUZA I.H.G., ESPOSITO E., *J. Nanobiotechnol.*, 3 (2005), 8.
- [10] SHANKAR S., RAI A., AHMAD A., SASTRY M., *J. Colloid Inter. Sci.*, 275 (2004), 496.
- [11] SHANKAR S., AHMAD A., SASTRY M., *Biotechnol. Prog.*, 19 (2003), 1627.

*Received 28 April 2007*  
*Revised 16 February 2008*

# Nanosorbents for selective removal of odours

M. ZIOLEK\*, I. SOBCZAK, A. DUDZIK, Ł. KONWICKI, J. KUJAWA

Adam Mickiewicz University, Faculty of Chemistry, ul. Grunwaldzka 6, 60-780 Poznań, Poland

Y type zeolites modified with Cu, Ni, Mn as well as mesoporous hexagonally ordered silicates and niobosilicates of MCM-41 type with gold dispersed as an active component were studied in odour adsorption. Dibutyl sulfide and butyl amine were used as odour components and they were adsorbed separately and in the presence of high moisture content. The attractiveness of Au/MCM-41 samples for the selective adsorption of both odour compounds (much higher for the sulfide) and their possible further oxidation during the recovery of sorbents has been proved. The highest resistance for moisture adsorption was found for Au/NbMCM-41.

Key words: *Zeolites containing Cu, Ni, Mn; Au/MCM-41, Au/NbMCM-41; dibutyl sulfide; butyl amine*

## 1. Introduction

Recently, regulations concerning environmental protection have been concentrated on odour emissions. However, these regulations and guidelines to avoid odour annoyance presently differ from country to country [1]. It is because the so called “odour problems” are very complex issues. One point is a large variety of odour emission sources which can be divided into odours due to fermentation (i) and odours from processing plants (ii) [2]. Each of these categories includes a lot of sources which have not been systematically recorded, characterised, and evaluated so far. Talking about odour treatment technologies, one should define the source, taking into account whether the removal unit can be maintained on the way of odour emission (e.g., in power station or viscose industry) or it should be located in the area where odours are concentrated (e.g., agricultural origin, composting plants, food industry). Depending on that, various units and various technologies can be applied.

Another important task is chemical composition of odours and physical conditions for which a suitable treatment system should be selected. In order to do so, a detailed knowledge is needed about advantages and disadvantages of various technologies available for off-gas treatment. An overview of such technologies is presented in [1].

---

\*Corresponding author, e-mail: ziolek@amu.edu.pl

Long term exposed odours are often removed by biological units. However, they are not sufficient for the reduction of malodours below the odour threshold. To reduce concentrations below odour threshold, selective adsorption processes with on-site regeneration of the adsorbents are very promising [3]. Looking for selective adsorbents, one should take into account the nature of odour compounds (most of them are organic compounds containing nitrogen and/or sulphur) and the nature of elements (located on the surface of sorbents) which are active for the selective adsorption. Our former study [4] indicated that nickel located on the surface of mesoporous molecular sieves of MCM-41 type is an attractive component for selective adsorption of sulfides and their further oxidation with hydrogen peroxide. In the patent literature [5], one can find the description of gold grafted on silica-alumina system used for the removal of malodour.

In this contribution high pore volume nanomaterials (zeolites and mesoporous MCM-41 materials) modified with active components (Ni, Cu, Mn, Au) have been fabricated to obtain sorbents able to concentrate a maximum amount of pollutants in a minimum volume of adsorbent. A choice of active components was determined by the expected selectivity to sulfides and/or amines and a possible further recovery of sorbent via the catalytic oxidation of odours at room temperature. Butyl amine ( $\text{BuNH}_2$ ) and dibutyl sulfide ( $\text{Bu}_2\text{S}$ ) were adsorbed on the prepared materials in the presence and in the absence of water vapour.

## 2. Experimental

*Preparation and modification of mesoporous catalysts.* Mesoporous molecular sieves of MCM-41 type have been synthesized by the hydrothermal method [6] and modified in the preparation of NbMCM-41 according to [7]. Au/MCM-41 and Au/NbMCM-41 catalysts were prepared by incipient wetness impregnation of the MCM-41 support with  $\text{HAuCl}_4$  (Johnson Matthey) with loading of gold of 1 wt. %. The amount of solution used was chosen in such a way that the liquid filled up only the pores of the mesoporous support. Following the impregnation, the catalysts were dried at 373 K for 5 h and calcined at 773 K for 3 h in the air. After calcination, Au-modified MCM-41 materials were reduced in  $\text{H}_2$  (5 vol. %  $\text{H}_2/\text{N}_2$ ) at 773 K for 3 h.

*Modification of zeolite catalysts.* Cu-NaY, Mn-NaY and Ni-NaY catalysts were prepared from NaY zeolite ( $\text{Si}/\text{Al} = 2.6$ , Katalistiks) with copper(II) acetate (POCH, Poland), manganese(II) acetate (Aldrich) and nickel(II) nitrate (Aldrich) water solutions, respectively, by ion exchange at 323 K. The obtained samples, after filtration and washing, were calcined at 673 K for 4 h.

*XRD patterns.* The XRD patterns have been obtained on a TUR-62 diffractometer using  $\text{CuK}_\alpha$  radiation ( $\lambda = 0.154 \text{ nm}$ ), with a step size of  $0.02^\circ$  and  $0.05^\circ$  in the small-angle and high-angle ranges, respectively.

*$\text{N}_2$  adsorption/desorption.* The surface area and pore volume of the samples were measured by nitrogen adsorption at 77 K, using the conventional procedure, with

a Micromeritics 2010 apparatus. Prior to the adsorption measurements, the samples were degassed in vacuum at 573 K for 2 h.

*Adsorption of odours.* Adsorption of odours – dibutyl sulfide ( $\text{Bu}_2\text{S}$ ) and butyl amine ( $\text{BuNH}_2$ ) in the presence and absence of water vapour as well as adsorption of water were performed in two manners, both at room temperature. In the former method, the outgassed sorbents were weighed into vessels and put into the desiccator at the place with the highest odour concentration and kept for 7 days. After a certain storage time, the treatment efficiency of the considering medium was analysed by weight and chemical analysis. In another method, the outgassed sorbent was put on the balance scale in a glass box purged with nitrogen flow. In this box, an appropriate odour was evaporated and the amount of adsorbed compounds was continuously weighed, the course of the weight change was recorded by a computer program and adsorption isotherms were plotted.

### 3. Results and discussion

Among commonly used adsorbents, zeolites, exhibiting the crystalline structure and uniform, well defined pores, seemed to be attractive for the study. We have used an Y type zeolite of high sorption capacity (ca. 25 vol. %) modified with transition metals (Ni, Mn, Cu) to obtain high selectivity in the chemisorption of odours.

Another, relatively new, nanosorbents applied in this work, were mesostructured materials of MCM-41 type modified with niobium and gold. They are attractive because of very high surface areas (often exceeding  $1000 \text{ m}^2/\text{g}$ ) and pore volumes ca.  $0.7 \text{ cm}^3/\text{g}$ . Moreover, the uniform hexagonally ordered mesopored tubes make the diffusion of sorbats in pores easy. The silicate and niobosilicate materials were modified with gold to obtain high selectivity in sulfide and amine sorption. The texture/structure parameters of these sorbents are given in Table 1. One can notice very high surface areas (ca.  $1000 \text{ m}^2/\text{g}$ ) and pore volumes (ca.  $1 \text{ cm}^3/\text{g}$ ).

Table 1. Characteristic of the mesoporous catalysts

Catalyst	Surface area [ $\text{m}^2\cdot\text{g}^{-1}$ ]	Pore volume [ $\text{cm}^3\cdot\text{g}^{-1}$ ]	Pore diameter [nm]
SiMCM-41	1075	1.25	3.90
NbMCM-41	955	1.12	3.84
Au/MCM-41	1056	1.12	3.82
Au/NbMCM-41	901	0.99	3.62

The nitrogen adsorption/desorption isotherms (Fig. 1) of both gold catalysts are typical of nanostructured materials (type IV according to the IUPAC classification) with the inflection point at  $p/p_0$  between 0.2 and 0.4, depending on the sample. Not only  $\text{N}_2$  sorption isotherms but also small-angle X-ray diffraction (XRD) patterns

(Fig. 2a) indicate the hexagonally ordered mesopores. The Au-metal crystallites were found for both Au-containing catalysts. The characteristic reflections of metallic gold at  $2\theta = 38.2^\circ$  and  $44.8^\circ$  [8] are shown in the large-angle range of XRD patterns (Fig. 2b). The presence of metallic gold is confirmed by UV-Vis absorption band at ca 500 nm (not shown here).

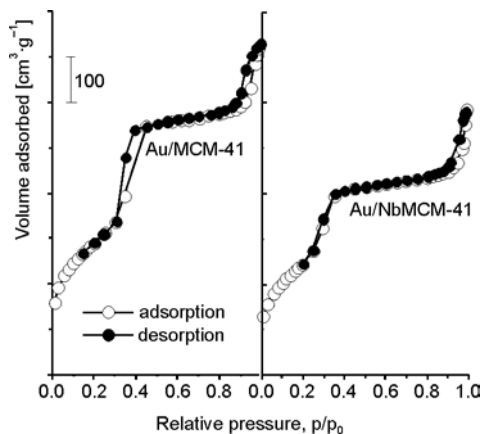


Fig. 1. N<sub>2</sub> adsorption/desorption isotherms of Au-containing MCM-41 materials

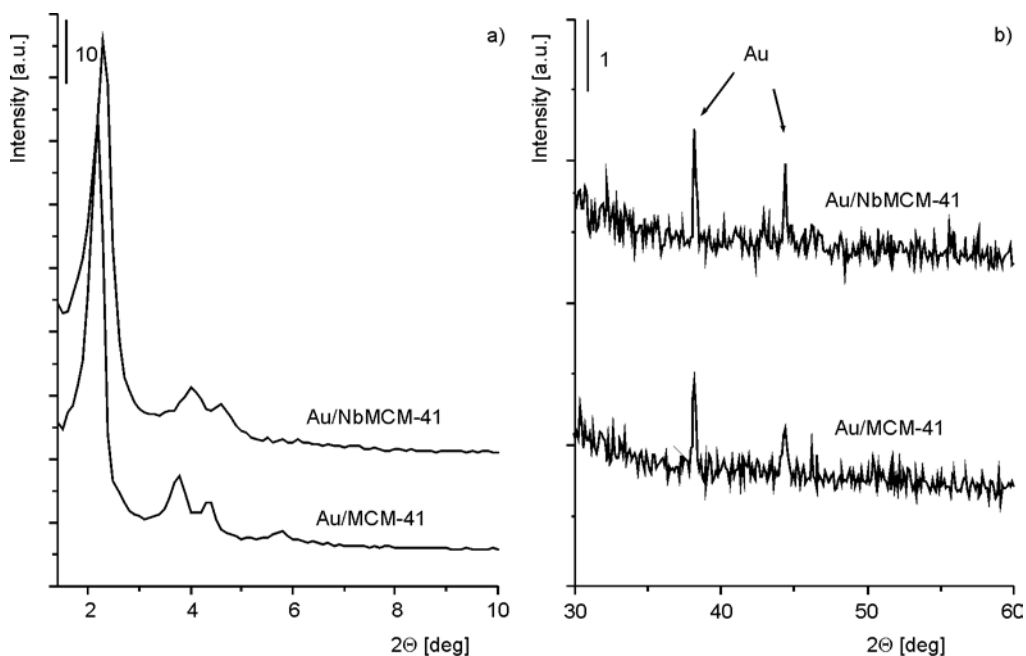
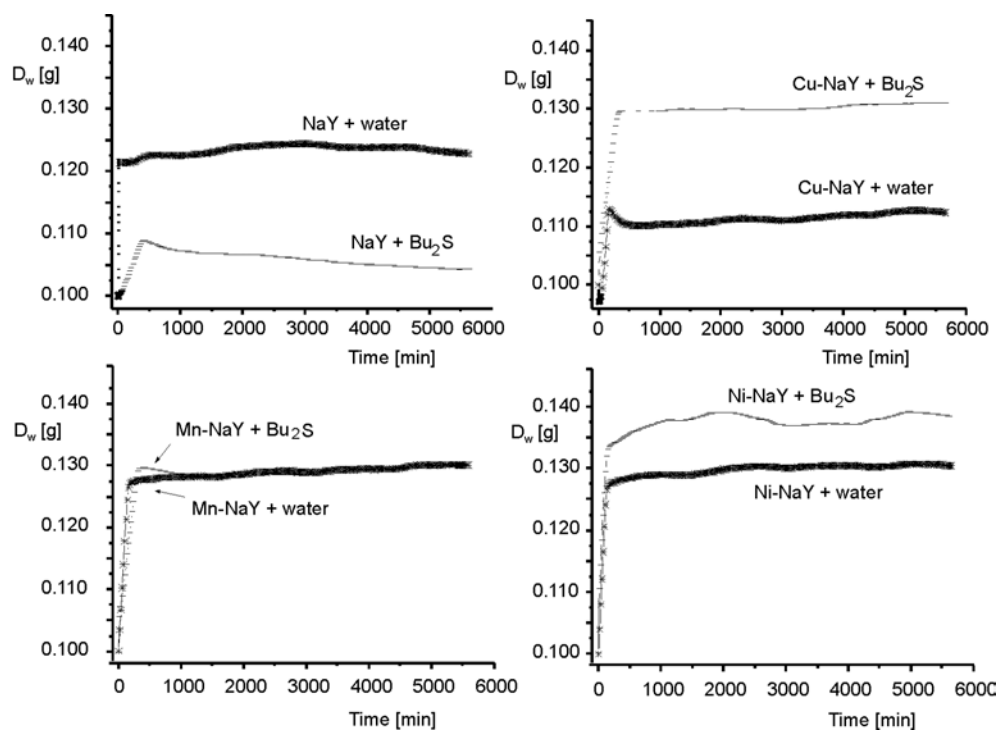


Fig. 2. XRD patterns of Au-containing MCM-41: small-angle (a) and large-angle (b) XRD range

UV-VIS spectroscopy appeared to be a useful tool for the determination of two cationic forms of copper in Cu-NaY zeolite (recorded at ca. 230 and 300 nm). Ni-NaY and Mn-NaY did not display cationic forms of metals detected by UV spectroscopy.

Fig. 3. Curves of water and Bu<sub>2</sub>S adsorption at room temperatureTable 2. The amount of Bu<sub>2</sub>S adsorbed on zeolites and MCM-41 materials

Adsorbent	Adsorbate	Wt. % of all adsorbates	Wt. % of Bu <sub>2</sub> S
NaY	Bu <sub>2</sub> S	22	0
Mn-NaY		15	1.5
Ni-NaY		25	0.8
Cu-NaY		25	6
Au/NbMCM-41		74	36
Au/MCM-41		70	37
MCM-41		56	9
NbMCM-41		52	17
NaY	Bu <sub>2</sub> S + H <sub>2</sub> O	29	0
Mn-NaY		30	0
Ni-NaY		29	0
Cu-NaY		29	0.2
Au/NbMCM-41		88	10
Au/MCM-41		87	6

The results of odour adsorption are presented as Bu<sub>2</sub>S adsorption curves (Fig. 3) and as the amount of adsorbed compound after 7 days of adsorption in a desiccator (Tables 2, 3).

Table 3. The amount of BuNH<sub>2</sub> adsorbed on zeolites and MCM-41 materials

Adsorbent	Adsorbate	Wt. % of all adsorbates	Wt. % of Bu <sub>2</sub> S
NaY	BuNH <sub>2</sub>	30	4
Mn-NaY		30	10
Ni-NaY		34	14
Cu-NaY		40	15
Au/NbMCM-41		67	22
Au/MCM-41		71	24
NaY	BuNH <sub>2</sub> + H <sub>2</sub> O	29	0.6
Mn-NaY		28	10.5
Ni-NaY		28	12
Cu-NaY		31	12
Au/NbMCM-41		81	18
Au/MCM-41		90	17

Zeolite sorption capacity ranges between 20 and 40 wt. %, depending on the nature of metal located in the structure, as indicated in Fig. 3. In the figure, the adsorption capacities have been compared for dibutyl sulfide and water. A high moisture content often has a negative effect on the adsorption process. It is especially the case of hydrophilic sorbents like NaY zeolite which preferentially adsorbs water not dibutyl sulfide. The same adsorption capacity for H<sub>2</sub>O and Bu<sub>2</sub>S was noted on Mn-NaY, whereas on Ni-NaY and especially on Cu-NaY, the amount of adsorbed sulfide was much higher than that of water. It is important that contrary to e.g., Mn-NaY, in Cu-NaY copper atoms occupy mainly cationic positions which strongly interact with dibutyl sulfide. When dibutyl sulfide was evaporated in a desiccator, in which the concentration of moisture increased by the location of the source of water vapour, the selectivity of sulfide adsorption decreased significantly (Table 2). Thus there is a high competition between adsorption of water and dibutyl sulfide. Contrary to these results, the adsorption of amine is not reduced by an increase of water vapour concentration (Table 3). It is clearly seen that the nature of transition metal is not a key point in the adsorption of butyl amine and that the selectivities of all transition metal-containing zeolites studied in this work towards amine sorption are much higher than that towards sulfide.

On the contrary, the sorbents based on mesoporous molecular sieves of MCM-41 type exhibit very high selectivity in sulfide adsorption. The role of gold in this behaviour is evident. The matrices without gold modification adsorb much less sulfide. The adsorption capacity towards sulfide does not depend on the nature of matrix (silicate MCM-41 or niobosilicate NbMCM-41) so long as the higher moisture content is not applied. In the latter case, the gold material based on NbMCM-41 support is more selective towards sulfide than Au/MCM-41. It is due to the lower hydrophilicity of NbMCM-41. The important advantage of mesoporous materials applied in this work is their extremely high total sorption capacity (> 70 wt. %) and sulfide sorption capacity



(ca. 35 wt. %), giving a possibility of concentration of high amount of odours in a small amount of sorbent. The other advantage is an easy recovery of sorbents via oxidation of odours catalysed by gold dispersed on the mesoporous support [9, 10].

Adsorption of dibutyl amine (Table 3) on mesoporous sorbents is less selective (22–24 wt. %) than that of dibutyl sulfide but significantly higher than the sorption selectivity on zeolites.

## 4. Conclusions

Zeolites containing transition metal ions exhibit a higher selectivity in sorption of amines than in sorption of sulfides. Among zeolites, the highest amounts of odours are adsorbed on Cu-NaY. Zeolites are not selective towards dibutyl sulfide in a high moisture content. However, the most attractive sorbents are gold modified MCM-41 materials which not only adsorb the highest amounts of both odours but also are highly selective. Niobium located in NbMCM-41 matrix enhances the hydrophobicity of the material and increases the adsorption of odour in a high concentration of water vapour. Gold containing sorbents are easily regenerated via catalytic oxidation of sorbats.

### Acknowledgement

Polish Ministry of Science and Higher Education (grant PBZ-KBN-116/TO9/2004; 2005-2008) is to be acknowledged for a support of this work. Acknowledge is made also to Johnson Matthey (UK-USA) for supplying HAuCl<sub>4</sub> and CBMM (Brasil) for Nb-oxalate.

### References

- [1] SCHLEGELMILCH M., STREESE J., STEGMANN R., *Waste Manag.*, 25 (2005), 829.
- [2] MARTIN G., LAFFORT P., BERSILLON K.M., *Odors and Deodorisation in the Environment*, VCH Publ., New York, 1994.
- [3] CALLTERIERI A., THIESEN P.H., NIEMEYER B., *Waste Manag.*, 25 (2005), 985.
- [4] ZIOLEK M., NOWAK I., POLTORAK H., LEWANDOWSKA A., SOB CZAK I., [in:] *Porous Materials in Environmentally Friendly Processes*, I. Kiricsi, G. Pal-Borbely, J.B. Nagy, H.G. Karge (Eds.), *Stud. Surf. Sci. Catal.*, 125 (1999), 691.
- [5] MATSUMOTO TOMOHIDE, Japan Patent 131139 (1993).
- [6] BECK J.S., VARTULI J.C., ROTH W.J., LEONOWICZ M.E., KRESGE D.T., SCHMITT K.D., CHU C.T.W., OLSON D.H., SHEPPARD E.W., MCCULLEN S.B., HIGGINS J.B., SCHLENKER J.L., *J. Am. Chem. Soc.*, 114 (1992), 10834.
- [7] ZIOLEK M., NOWAK I., *Zeolites*, 18 (1997), 356.
- [8] OKUMURA M., TSUBOTA S., HARUTA M., *J. Mol. Catal. A: Chem.*, 199 (2003), 73.
- [9] SOB CZAK I., KUSIOR A., GRAMS J., ZIOLEK M., [in:] *From Zeolites to Porous MOF Materials*, R. Xu, Z. Gao, J. Chen, W. Yan (Eds.), *Stud. Surf. Sci. Catal.*, (2007), in print.
- [10] ARAKI H., FUKUOKA A., SAKAMOTO Y., INAGAKI S., SUGIMOTO N., FUKUSHIMA Y., ICHIKAWA M., *J. Mol. Catal. A: Chem.*, 199 (2003), 95.

Received 28 April 2007  
Revised 16 February 2008

## Characterization of carbon nanotubes by Raman spectroscopy

S. COSTA, E. BOROWIAK-PALEN<sup>\*</sup>, M. KRUSZYŃSKA,  
A. BACHMATIUK, R. J. KALEŃCZUK

Centre of Knowledge Based Nanomaterials and Technologies, Institute of Chemical and Environment  
Engineering, Szczecin University of Technology, ul. Pułaskiego 10, 70-310 Szczecin, Poland

Application of Raman spectroscopy to analyse carbon nanotubes has been presented. Having a mixture of various carbon nanotube samples, one can easily distinguish, in a quick experiment, presence of singlewalled, doublewalled and multiwalled carbon nanotubes (SWCNT, DWCNT, MWCNT, respectively). The so-called G-line is a characteristic feature of the graphitic layers and corresponds to the tangential vibration of carbon atoms. Another characteristic mode is a typical sign of defective graphitic structures (D-line). A comparison of the intensity ratios of these two peaks gives a measure of the quality of the bulk samples. In addition, there is a third mode, named the radial breathing mode (RBM) which is very sensitive to the diameter of SWCNT and DWCNT. Additional option is application of Raman microscopy for mapping analysis and depth profiling to view the changes of intensity in various directions in the sample.

Key words: *Raman spectra; Raman mapping; carbon nanotubes*

### 1. Introduction

Carbon nanotubes (CNT) since their discovery became an important scientific objects of extensive research due to their interesting physical properties and technological applications. CNT have proven to be a unique system to study Raman spectra in one-dimensional (1D) systems [1, 2], and at the same time Raman spectroscopy has provided an exceedingly powerful tool to study vibrational properties and electronic structures of CNT [3, 4], particularly for characterization of CNT's diameters, and quality of the samples [5, 6]. Various carbon materials can be analysed by the Raman spectroscopy including singlewalled (SWCNT), doublewalled (DWCNT) and multi-

---

<sup>\*</sup>Corresponding author: email: eborowiak@ps.pl

walled (MWCNT) carbon nanotubes but, unfortunately, quantitative determination of each type is impossible at present [7].

### 1.1. Features of Raman spectroscopy. SWCNT and DWCNT

The Raman spectra present different features being all sensitive to chiral indices  $(n,m)$  specifying the perimeter vector (chiral vector), such as the radial breathing mode (RBM) where all the carbon atoms are moving in-phase in the radial direction, the G-band where neighbouring atoms are moving in opposite directions along the surface of the tube as in 2D graphite, the dispersive disorder induced D-band and its second-order related harmonic G'-band. From these four features, the RBM is the one which appears more sensitive to the nanotube diameter ( $d_i$ ) [8], according to the expression

$$\omega_{RBM} = \frac{A}{d_i} + B \quad (1)$$

where  $\omega$  is the vibration frequency, and  $A$  and  $B$  are constants and vary between individual tubes and bundle tubes [1, 9]. Some authors consider only the constant  $A$  in determination of the diameter [6, 10, 11].

A DWCNT can be considered to be a kind of MWCNT for which the interlayer interaction is generally considered to be turbostratic between the inner and outer nanotubes. For armchair–armchair DWCNT, some commensurate structure can be expected and the splitting of the G'-band which is observed in 3D graphite could be seen. Another novel direction for future exploration is a small RBM linewidth (down to  $0.25 \text{ cm}^{-1}$ ) occurring for the inner wall tube within an isolated DWCNT [1].

By measuring RBM for many laser energies, the diameter distribution of the nanotubes in a particular SWCNT bundle can be found [11]. The G-band is thus an intrinsic feature of a carbon nanotube closely related to vibrations in all  $\text{sp}^2$  carbon materials. The most important aspect of the G-band is the characteristic Raman lineshape which depends on whether the nanotube is semiconducting or metallic, allowing readily distinguishing between both types. This band shows two components, the lower frequency component associated with vibrations along the circumferential direction, ( $G^-$ ), and the higher frequency component, ( $G^+$ ), attributed to vibrations along  $G$  direction of the nanotube axis. Previous studies show that the former component is dependent on the diameter of a nanotube while the latter does not exhibit this dependence in both, metallic and semiconducting nanotubes [10]. The D-band and G'-band features are both observed in the Raman spectra of semiconducting and metallic SWCNT at a single nanotube level. The D-band in graphite involves scattering from a defect which breaks the basic symmetry of the graphene sheet. It is observed in  $\text{sp}^2$  carbons containing porous, impurities or other symmetry-breaking defects. On the other hand, the second-order G'-band does not require an elastic defect-related scattering process, and

is observable for defect-free  $sp^2$  carbons. These bands show a dependence on the chirality and diameter of nanotubes [1] and on laser excitation energy [12].

The analysis of all resonance Raman effects has been greatly facilitated by introduction of the Kataura plot of the interband transitions,  $E_{ii}$  as a function of  $d_t$  for all values of  $(n,m)$  showing that each pair of indices in a nanotube has a unique set of  $E_{ii}$  transition energies, which is physically due to the trigonal warping effect of the constant energy contours for a graphite sheet [11].

## 1.2. Multiwalled carbon nanotubes

Multiwalled carbon nanotubes are made of concentric graphene sheets rolled in a cylindrical form with diameters of tens of nanometers [13]. Due to a large diameter of the outer tubes for typical MWCNT and because they contain an ensemble of carbon nanotubes with diameters ranging from small to very large, most of the characteristic differences that distinguish the Raman spectra in SWCNT from the spectra for graphite are not so evident in MWCNT. For example, the RBM Raman feature associated with a small diameter inner tube (less than 2 nm) can sometimes be observed when a good resonance condition is established, but this is not the usual result, since the RBM signal from large diameter tubes is usually too weak to be observable and the ensemble average of inner tube diameter broadens the signal [1].

Whereas the  $G^+-G^-$  splitting is large for small diameter SWCNT tubes, the corresponding splitting of the  $G$  band in MWCNT is both small in intensity and smeared out due to the effect of the diameter distribution within the individual MWCNT, and because of the variation between different tubes in an ensemble of MWCNT in typical experimental samples. Therefore the  $G$ -band feature predominantly exhibits a weakly asymmetric characteristic lineshape, with a peak appearing close to the graphite frequency. The most effective influence of radiation is expected in the case of the electron irradiation of MWCNT. The feature is explained by a possible appearance of radiation defects whose presence contributes to the degradation of the nanotubes but seems to be also due to broken bonds appearing during creation of vacancies [14].

In the paper, we present a simple way of evaluation of various physical properties of SWCNT from Raman spectroscopy data.

## 2. Experimental

The synthesis of SWCNT was described elsewhere [15]. The Raman spectra were collected using a micro-Raman Renishaw spectrometer equipped with a CCD detector. Two laser lines were used to excite the samples, 514 nm (green laser) and 785 nm (red laser). Depth profiles and mapping of selected areas were also obtained with the Raman spectrometer. All the measurements were performed at room temperature.

### 3. Results and discussion

#### 3.1. Comparison between green and red lasers

The responses for excitation with different lasers revealed very rich spectra, strongly differing for each sample [16–18]. Figure 1a presents two examples, one for excitation with the green laser (514 nm) and the other for excitation with the red laser (785 nm). The resonance scattering caused by different lasers gives us information about different excitation levels as shown in the Kataura plot (Fig. 2).

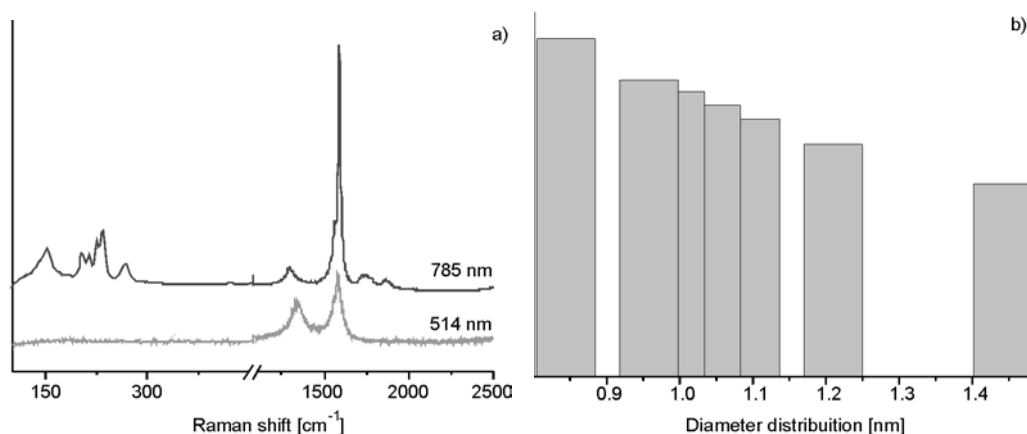
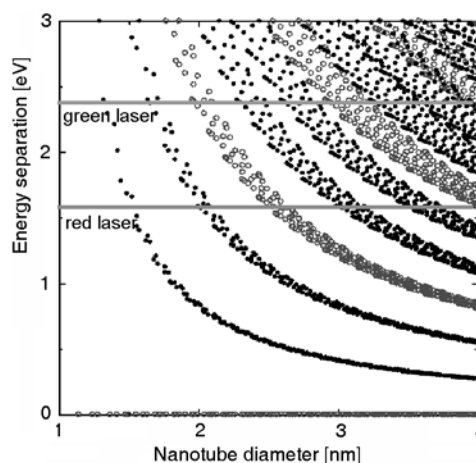


Fig. 1. Raman spectra of SWCNT excited with red (785 nm) and green (514 nm) laser radiations (a), and their diameter distribution (b)

Fig. 2. Kataura plot showing various resonance excitations as functions of various laser energies and nanotube diameters: full circles – semiconducting tubes, open circles – metallic tubes ( $\gamma = 2.9$  eV,  $a_{cc} = 0.144$  nm)



In the same figure, the radiation energies of the lasers used in our measurements are marked. In order to gain more information about the type of excited nanotubes, it is necessary to calculate the diameter distribution, using data from the red laser, since

the RBM with green laser is not clear. Also the intensity of *G* band increases when we use the 785 nm laser.

### 3.2. Determination of diameter distribution

Four characteristic features of a SWCNT sample may be found in Raman spectra presented in Fig. 1a. An RBM band is visible in the red laser spectra. For typical SWCNT bundles of the diameter  $d_t = 1.5 \pm 0.2$  nm,  $A = 234 \text{ cm}^{-1} \cdot \text{nm}$  and  $B = 10 \text{ cm}^{-1}$  have been calculated [1];  $B$  is an upshift in  $\omega_{\text{RBM}}$  due to tube–tube interactions. The calculated diameter distribution was obtained using Eq. (1) (Table 1, Fig. 1b). The range of diameters varies between 0.8 nm and 1.5 nm. According to the Kataura plot, with the red laser we only obtain signals from semiconducting tubes but the green laser shows that we also have metallic tubes. These facts indicate how the analysis with lasers of various energies is important, because each experiment can give different data on optical and physical properties. The analysis of RBM band also allows one to distinguish between SWCNT, DWCNT and MWCNT. Figure 3a shows different RBM bands in different nanotubes. DWCNT spectrum presents a double RBM due to the diameters of the inner and outer tubes. According to Eq. (1), the band of higher Raman shift corresponds to the inner diameter and the one with lower Raman shift to the outer diameter.

Table 1. Diameter distribution calculated from the RBM feature using Eq. (1)

Raman shift [ $\text{cm}^{-1}$ ]	Diameter [nm]
152.275	1.441997
183.419	1.209809
203.352	1.096779
214.397	1.042795
225.421	0.993964
234.225	0.958133
267.121	0.844396

### 3.3. D band–G band relation

The ratio of the intensities of D and G bands is a good indicator of the quality of bulk samples. Similar intensities of these bands indicate a high quantity of structural defects. Figure 3b presents these bands in various kinds of nanotubes. MWCNT spectrum is the one which shows the lowest ratio, consequently higher quantity of structural defects due to its multiple graphite layers. Both SWCNT and DWCNT show higher differences in intensities of D and G bands.

The ratio between D and G band and the RBM and its relation to the diameter distribution are very important factors allowing one to distinguish between three types of nanotubes with a single analysis.

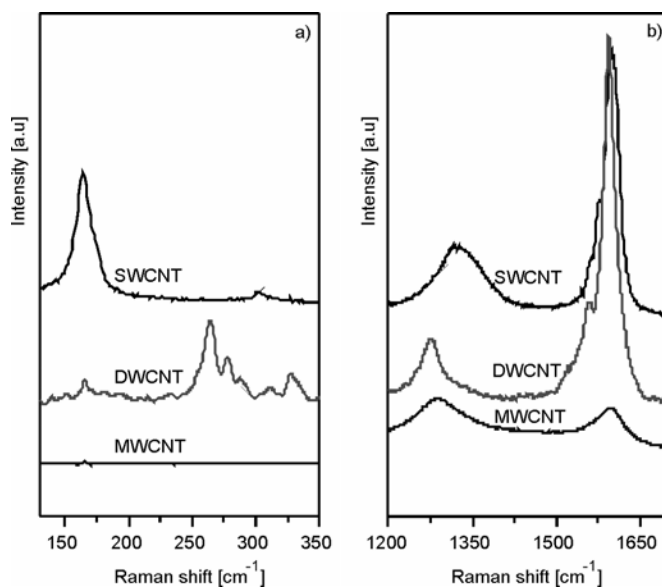


Fig. 3. Raman spectra of SWCNT, DWCNT and MWCNT:  
a) RBM, b) D and G bands (laser excitation 785 nm)

### 3.4. Mapping

The energy of the first electron transition between semiconducting SWNTs is usually too small to be observed with standard Raman spectroscopy setups. However

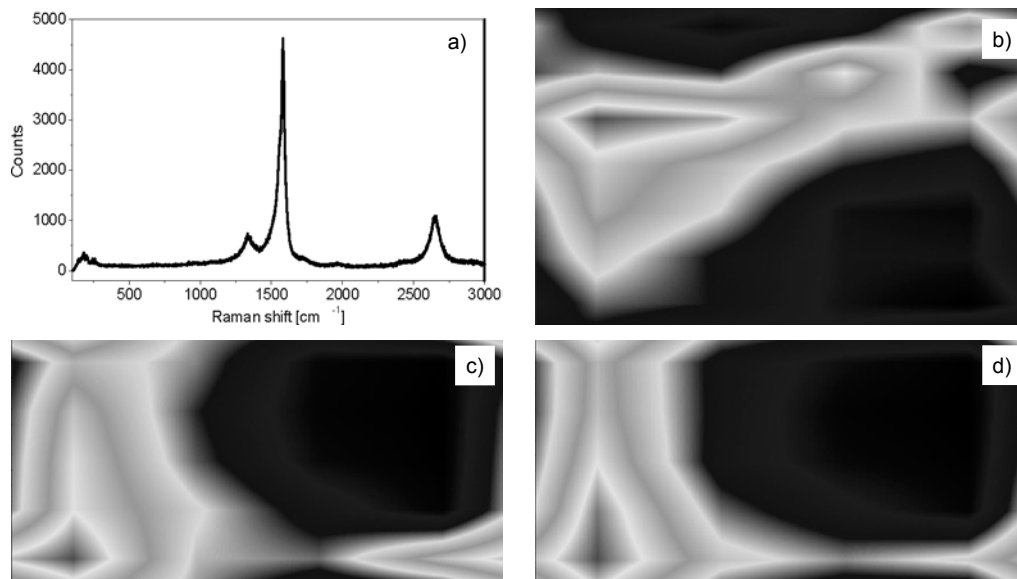


Fig. 4. Raman spectra of a CNT sample (a), and Raman two dimensional map images of RBM (b), G (c), and D (d) bands. Laser excitation 785 nm



Fig. 5. Raman mapping of RBM band. Comparison between a top view (left panel) and a 3D view (right panel). The grayscale indicates the intensities of the band. Laser excitation 785 nm

it is possible to observe it in a convenient range in a multidimensional map [1]. A map of each feature can be obtained with this technique. The mapping allows one to observe the homogeneity of the sample by screening a larger area as in the case of a standard Raman microscope measurement [19]. Figure 4 presents a mapping image of three most important features in Raman spectrum, and its distribution in the area of the analyzed sample. The mapping spectra can be visualized in two or three dimensions with similar results such as the images presented in Fig. 5.

### 3.5. Depth profile

With the technique described in the paper it is also possible to analyse the Raman response as a function of the depth of the sample. The depth profile of *G*-band of SWCNT is shown in Fig. 6 and it allows choosing the area of the sample which would give the highest intensity of the Raman signal. In the present case, one can conclude that the best signal is obtained at 1  $\mu\text{m}$  depth in the sample. The depth profile can also be visualized in two or three dimensions.

## 4. Conclusions

Raman spectroscopy is a powerful technique with various options such as area mapping, depth profile for beyond the standard spectra analysis. The energy of laser excitation is also very important due to the results obtained, as shown in the Kataura plot. One can also easily determine the presence of different types of carbon nanotubes in the analyzed sample including determination of the diameter in the case of SWCNT and MWCNT. The *G/D* ratio is a direct measure of the quality of a sample.



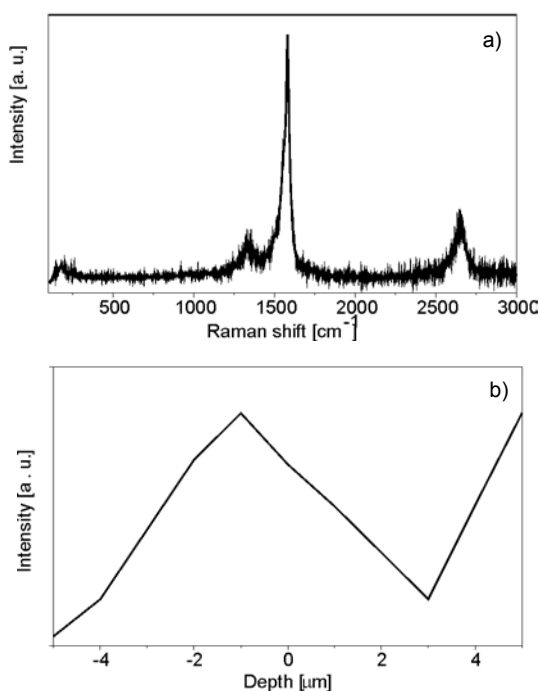


Fig. 6. Raman spectrum of SWCNT (a), and the depth profile of the G band in two dimensions

Mapping analysis is important to see the homogeneity of the sample and compare the different Raman features in the select area. The depth profile is useful beyond the standard spectra, to select how the Raman signal changes in respect to the depth of the sample.

## References

- [1] DRESSELHAUS M.S., DRESSELHAUS G., SAITO R., JORIO A., *Phys. Rep.*, 409 (2005), 47.
- [2] JORIO A., PIMENTA M.A., FANTINI C., SOUZA M., SOUZA FILHO A.G., SAMSONIDZE GE.G., DRESSELHAUS G., DRESSELHAUS M.S., SAITO R., *Carbon*, 42 (2004), 1067.
- [3] KAVAN L., RAPTA P., DUNSCH L., BRONIKOWSKI M.J., WILLIS P., SMALLEY R.E., *J. Phys. Chem. B*, 105 (2001), 10764.
- [4] ALVAREZ L., RIGHI A., GUILLARD T., ROLS S., ANGLARET E., LAPLAZE D., SAUVAJOL J.-L., *Chem. Phys. Lett.*, 316 (2000), 186.
- [5] ASTAKHOVA T.YU., VINOGRADOV G.A., MENON M., *Russian Chem. Bull., Int. Ed.*, 52 (2003), 823.
- [6] DRESSELHAUS M.S., DRESSELHAUS G., JORIO A., SOUZA FILHO A.G., PIMENTA M.A., SAITO D.R., *Acc. Chem. Res.*, 35 (2002), 1070.
- [7] QIAN W., LIU T., WEI F., YUAN H., *Carbon*, 41 (2003), 1851.
- [8] TAKEDA N., MURAKOSHI K., *Anal Bioanal Chem.*, 388 (2007), 103.
- [9] DOORN S.K., HELLER D.A., BARONE P.W., USREY M.L., STRANO M.S., *Appl. Phys. A*, 78 (2004), 1147.

- [10] DRESSELHAUS M.S., DRESSELHAUS G., JORIO A., SOUZA FILHO A.G., SAITO R., *Carbon*, 40 (2002), 2043.
- [11] DRESSELHAUS M.S., JORIO A., SOUZA FILHO A.G., DRESSELHAUS G., SAITO R., *Physica B*, 323 (2002), 15.
- [12] ZHANG H.B., LIN G.D., ZHOU Z.H., DONG X., CHEN T., *Carbon*, 40 (2002), 2429.
- [13] ANTUNES E.F., LOBO A.O., CORAT E.J., TRAVA-AIROLDI V.J., MARTIN A.A., VERISSIMO C., *Carbon*, 44 (2006), 2202.
- [14] RITTER U., SCHARFF P., SIEGMUND C., DMYTRENKO O.P., KULISH N.P., PRYLUTSKYY YU.I., BELYI N.M., GUBANOV V.A., KOMAROVA L.I., LIZUNOVA S.V., POROSHIN V.G., SHLAPATSKAYA V.V., BERNAS H., *Carbon*, 44 (2006), 2694.
- [15] GRIMM D., GRÜNEIS A., KRAMBERGER C., RÜMMELI M., GEMMING T., BÜCHNER B., BARREIRO A., KUZMANY H., PFEIFFER R., PICHLER T., *Chem. Phys. Lett.*, 428 (2006), 416.
- [16] DOORN S.K., O'CONNELL M.J., ZHENG L., ZHU Y.T., HUANG S., LIU J., *Phys. Rev. Lett.*, 16802 (2005), 1.
- [17] KUZMANY H., BURGER B., THESS A., SMALLEY R.E., *Carbon*, 36 (1998), 709.
- [18] KÜRTI J., KUZMANY H., BURGER B., HULMAN M., WINTER J., KRESSE G., *Synth. Metals*, 103 (1999), 2508.
- [19] KUZMANY H., PLANK W., HULMAN M., KRAMBERGER C., GRÜNEIS A., PICHLER T., PETERLIK H., KATAURA H., ACHIBA Y., *Eur. Phys. J. B*, 22 (2001), 307.

*Received 28 April 2007*  
*Revised 16 February 2008*

## Studies on biocompatible nanocapsules formed in microemulsion templated processes

K. ZIELIŃSKA<sup>1</sup>, K. A. WILK<sup>1\*</sup>, E. SEWERYN<sup>2</sup>, J. PIETKIEWICZ<sup>2</sup>, J. SACZKO<sup>2</sup>

<sup>1</sup>Faculty of Chemistry, Wrocław University of Technology,  
Wybrzeże Wyspiańskiego 27, 50-370 Wrocław, Poland

<sup>2</sup>Department of Medical Biochemistry, Wrocław Medical University,  
ul. Chałubińskiego 10, 50-368 Wrocław, Poland

Phase diagrams of the pseudoternary system: *N*-alkyl-*N*-methylgluconamines/isobutanol/isooctane/water have been determined. Size and morphology of organic/water microemulsion droplets (optically isotropic, low viscosity one-phase systems) have been characterized by dynamic light scattering (DLS) to select systems suitable to prepare by interfacial polymerization poly(ethyl-2-cyanoacrylate) nanocapsules, the latter analyzed by scanning electron microscopy (SEM). The diameter of the nanocapsules (ranging from 300 to 1550 nm) was found to be dependent on the monomer mass used in the polymerization process. Investigation of those nanoparticles as a cyanine IR-768 carrier, for enhancing the photosensitizer selective delivery to tumor cells, has been performed. Incubation of MCF-7 Dox cells with cyanine dye IR-768 (Indoc5), free or encapsulated in nanoparticles, allowed the cellular accumulation of the photosensitizer. Our preliminary experiments indicate that higher doses of encapsulated cyanine improved the cytotoxic effect.

Key words: *nanocapsule; microemulsion; alkylcyanoacrylate; IR-768 perchlorate; MCF-7 Dox; cytotoxicity*

### 1. Introduction

Oil-cored biodegradable nanocapsules suitable for the hydrophobic drugs encapsulation can be prepared by interfacial polymerization of oil-in-water (o/w) emulsions or microemulsions [1–4]. The use of the latter as templates for the preparation of nanocapsules by interfacial polymerization offers advantages over the use of size-reduced kinetically stabilized emulsions. Furthermore, if biocompatible oils and surfactants are used for the formation of microemulsions, the necessity of isolating the nanocapsules from the reaction matrix following polymerization is omitted [5]. Nanocapsules can therefore be prepared in situ in a microemulsion matrix.

---

\*Corresponding author, e-mail: kazimiera.wilk@pwr.wroc.pl

The main purpose of the present study was to find and characterize a microemulsion single phase region in pseudoternary phase systems with a potential application in drug delivery, especially as templates for synthesis of drug loaded nanocapsules. The o/w microemulsion isotropic area was found in the ternary systems: *N*-alkyl-*N*-methylglucamine/isobutanol/isooctane/water, and utilized in the template-directed polymerization of reactive ethyl 2-cyanoacrylate (ECA) monomer, solubilized in the o/w droplet interfacial area. The findings described in the paper have not been reported so far.

In biological studies, we applied the particles to the delivery of some photosensitizers to tumor cells in photodynamic therapy (PDT) – an alternative modality of cancer treatment. It has to be emphasized that the photosensitizer which is absorbed by all cells and selectively retained by malignant tissue, after light exposure is promoted to an excited state and induces local release of cytotoxic reactive oxygen species (ROS). Depending on the experimental conditions and cell sensitivity, the cytotoxic molecular species resulting from PDT may trigger cell apoptosis or induce necrosis [6]. In clinical PDT, the same side effects were observed as a result of the dark toxicity of photosensitizers towards normal tissues. Low dark toxicity is one of the important criteria for assessing the usefulness of photosensitizers [7]. In our experiments, we used cyanine IR-768 perchlorate in a free form and encapsulated in nanoparticles to determine their incorporation to the breast cancer MCF-7 Dox cells. The near-IR spectral region is particularly suitable for the PDT as it penetrates deeply into tissues without causing significant heating. It is selectively concentrated and retained *in vitro* and *in vivo* to greater extent in the mitochondria of carcinoma and melanoma cells than in normal cells [8].

## 2. Experimental

**Materials.** *N*-decanoyl and *N*-octanoyl-*N*-methylglucamine, isobutanol, ethyl 2-cyanoacrylate (ECA), chloroform, ethanol and the photosensitizer (Fig. 1): 2-[2-[3-[(1,3-dihydro-3,3-dimethyl-1-propyl-2H-indol-2-ylidene) – ethylidene]-2-phenoxy-1-cyclohexen-1-yl]ethenyl]-3,3-dimethyl-1-propylindolium perchlorate (IR-768) were purchased from Sigma Aldrich. Isooctane was obtained from Carl Roth KG Chemicals. Distilled water buffered to pH 7.4 with phosphate buffer was used in the experiments with ECA. Water used for all experiments was doubly distilled and purified in a Millipore (Bedford, MA) Milli-Q purification system.

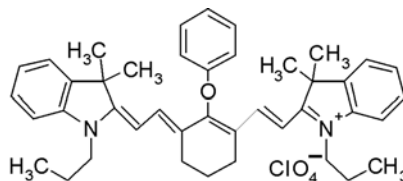


Fig. 1. Structure of the IR-768 photosensitizer

*Phase diagrams.* The four component systems were described by pseudo-ternary phase diagrams at 25 °C. All samples were prepared at a 1:1 surfactant-to-cosurfactant weight ratio. Surfactant/sobutanol/isooctane mixtures were diluted with water, after each dilution the samples were vigorously shaken and left for 24 h to attain equilibrium. Visual observations and cross-polarizers were used to identify the systems.

*Preparation of nanocapsules* Ethyl-2-cyanoacrylate monomer (5, 10, 20, 30  $\mu$ l) dissolved in of chloroform (20–90  $\mu$ l) was slowly added to 2 ml of selected microemulsion template (or microemulsion containing IR-768). Polymerization was performed at 4 °C and the system was stirred for at least 4 h. Nanocapsules were collected by centrifugation for 15 min at 25°C (Unipan 310 rotor). A Metertech SP8001 spectrophotometer with 1 cm path length quartz thermostated cell was used to determine the amount of photosensitizer solubilized in microemulsions or nanocapsules. IR-768 was detected at 768 nm. The obtained nanospheres were dispersed in the PBS solution.

*Characterization of nanocapsules.* The particle size and distribution of the PECA nanocapsules was determined by the dynamic light scattering (DLS, Zetanosizer Nano series ZS, Malvern Instruments Ltd.). Residual oil and surfactant were removed by repeated washing in ethanol, centrifugation (15 min at 25 °C) and then the dry nanocapsules were dispersed in ethanol. The external structure of nanocapsules was visualized by SEM (Jeol, JSM-5800 LV). The nanocapsules were coated with carbon before microscopic observations and viewed at an accelerating voltage of 22 kV.

*Cell culture.* Human breast cancer MCF-7 Dox cells (doxorubicin resistant cell line) were grown at 37 °C in a humidified atmosphere (95% air and 5% CO<sub>2</sub>), DMEM (Dulbecco's Modified Eagle medium) supplemented with phenol red, 3% L-glutamine, penicillin (100 U/ml), gentamycin (100 $\mu$ g/ml) and 10% foetal calf serum. Fresh medium was supplied every 3 days.

*Photosensitizer and photosensitization.* The cyanine dye IR-768 (Indoc5) was prepared as 1.4 mM stock solution by dissolving 1 mg of green powder in 1 ml of 0.1% DMSO/PBS, pH 7.4. Photosensitization experiments were performed with MCF-7 cells ( $5 \times 10^4$  cells/well) incubated in a 96-well microplate (Nunc, Denmark). Cyanine was then added from the stock solution to attain final concentrations ranging from 7 to 56  $\mu$ M. Equivalent amounts of 0.1% DMSO were added to other wells with cells that served as control. After 24 h incubation, the cells were photoirradiated (except the dark controls). The light source was a lamp (OPTEL, Opole, Poland) with polarized light and yellow filter ( $\lambda = 620$  nm). The nominal output energy (continuous wave) was 0.13 mW/cm<sup>2</sup>. Then the cells were incubated at 37 °C, 5% CO<sub>2</sub> – air atmosphere during 24 h in a drug-free medium. Experiments with encapsulated cyanine were performed in the same manner.

*Cytotoxicity assay.* Cell viability after irradiation was determined by the (MTT) 3-(4,5-dimethylthiazol)-2,5-diphenyltetrazolium bromide assay [9]. The absorbance of degraded MTT at 570 nm was measured using an ELISA reader (Labsystems Multiscan MS, Finland). All experiments reported herein included several controls.

**Fluorescence microscopy.** Microcultures derived from the culture dishes were conducted on 8-well glass slides. Subsequently, the cells were incubated with 47  $\mu\text{M}$  IR-768 (encapsulated and free dye) for 24 h at 37 °C. After incubation, the cells were fixed in 4% buffered formalin, washed with PBS and examined under a fluorescence microscope (Olympus BX51) using a yellow filter Y3Y3 ( $\lambda_{\text{ex}}$  = 612 nm).

### 3. Results and discussion

Odourless, nontoxic, non-irritant to eyes and skin, biodegradable surfactants, *N*-alkyl-*N*-methylgluconamines, appeared to be good candidates for stabilizing both o/w and water-in-oil (w/o) microemulsions with potential applications in various fields, for example as templates for biodegradable nanocapsules or as original drug carrier systems for transdermal delivery.

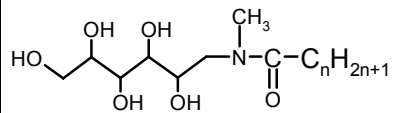
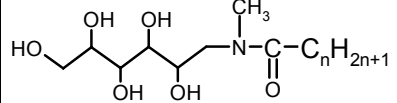
Surfactant	<i>n</i>	Abbreviation
	8	C <sub>8</sub> -MEGA
	10	C <sub>10</sub> -MEGA

Fig. 2. Structures of *N*-alkyl-*N*-methylgluconamines, C<sub>*n*</sub>-MEGA

The selected *N*-alkyl-*N*-methylgluconamines (Fig. 2) when added to a three-component system (cosurfactant/isooctane/water) make it possible to obtain either w/o or o/w and bicontinuous (bc) microemulsions. Figure 3 shows the pseudoternary phase triangles for the systems with *N*-alkyl-*N*-methylgluconamines of different chain lengths. The black areas represent microemulsion regions, the white ones representing anisotropic, two-phase regions. The length of the surfactant alkyl chain strongly influenced on the shape and extent of the microemulsion area; the largest microemulsion area was obtained for the system containing the surfactant with the decyl hydrophobic chain (C<sub>10</sub>-MEGA). For further studies some microemulsion systems based on the constructed pseudoternary phase diagrams have been selected and prepared.

The sizes and size distributions of droplets in microemulsions (at some compositions) and in nanocapsules were characterized by the DLS method. The corresponding diameters of microemulsion droplets (*D*) and polydispersity index *PdI* are given in Table 1. These systems were subject to interfacial polymerization and biological studies. The sizes of microemulsion droplets ranged from 6.4 to 8.1 nm and from 9.6 to 13.2 nm for C<sub>8</sub>-MEGA and C<sub>10</sub>-MEGA surfactants, respectively, making them good candidates for template-based reactions.

It can also be seen that the micelle size increases with the content of isooctane. In the case of formed nanocapsules, the size ranges from around 300 to 1550 nm. Probably a decrease in the mass of monomer available per interfacial area unit causes that

nanocapsules have thinner polymer walls and hence smaller sizes. Nanocapsules of the order of 1000 nm in diameter have not been applied to biological studies. An increase in the particle size occurs with increasing the monomer concentration used in the polymerization process (Table 2). Furthermore, the diameters of empty nanocapsules were slightly smaller than those loaded with the photosensitizer. All nanocapsules were spherical as observed by SEM (Fig. 4a, b).

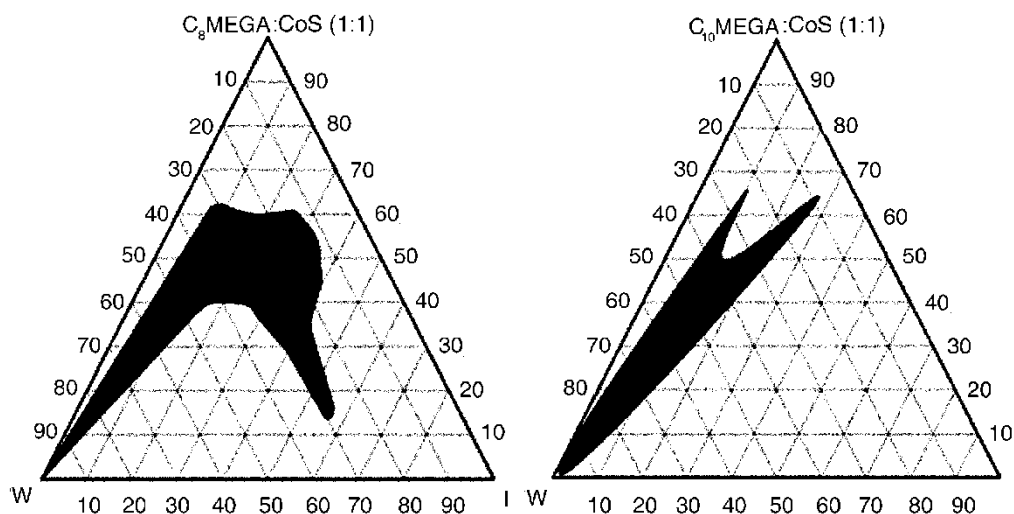


Fig. 3. Phase diagrams of the *N*-alkyl-*N*-methylgluconamine  $C_n$ -MEGA/isobutanol/isooctane/water ternary systems at 25 °C: a)  $C_8$ -MEGA, b)  $C_{10}$ -MEGA. Black areas represent the microemulsion monophasic regions, white – two phase regions; W – water, I – isooctane, Cos – isobutanol (cosurfactant)

Table 1. Diameter ( $D$ ) and polydispersity index (PDI) of the microemulsions droplets obtained by the DLS method for  $C_n$ -MEGA/cosurfactant/isooctane/water systems

Surfactant	Weight fraction [%]			$D$ [nm]	PDI
	Surfactant/isobutanol (1:1)	Oil	Water		
$C_8$ -MEGA	35	10	55	8.2	0.244
	25	5	70	7.4	0.489
	15	3	82	6.4	0.123
$C_{10}$ -MEGA	35	10	55	13.2	0.254
	25	5	70	12.0	0.325
	15	3	82	9.6	0.189

The efficiency of IR-768 entrapment within poly(ethyl-2-cyanoacrylate) o/w microemulsions-templated nanocapsules was influenced by the mass of monomer used in the polymerization (Table 2). The encapsulation of the examined photosensitizer with-

in PECA nanocapsules increased with increasing the monomer concentration from 32.9–39.0% for  $2.5 \times 10^{-3} \mu\text{l/ml}$  to 88.5–78.7% for  $12.5 \times 10^{-3} \mu\text{l/ml}$ .

Table 2. Characterization of empty and loaded nanocapsules

Surfactant	Concentration of monomer [ $10^{-3} \mu\text{l/ml}$ ]	Nanocapsules				Encapsulation [%]
		Without IR 768		With IR 768		
		D [nm]	PdI	D [nm]	PdI	
C <sub>8</sub> -MEGA	2.5	207	0.740	291	0.157	32.9
	5.0	390	0.475	468	0.491	59.9
	10.0	962	0.611	1200	0.568	75.4
	12.5	1368	0.754	1450	0.639	88.5
C <sub>10</sub> -MEGA	2.5	367	0.298	415	0.237	39.0
	5.0	647	0.708	728	0.195	47.0
	10.0	1310	0.454	1560	0.479	66.2
	12.5	2660	0.250	2855	0.490	78.7

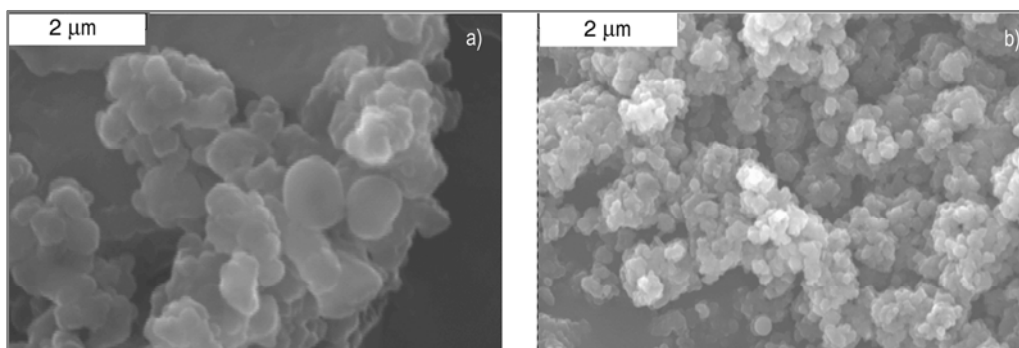


Fig. 4. Scanning electron micrographs of nanocapsules: a) in the o/w microemulsion template, b) from the sample pallet

MCF-7 cells are remarkably resistant to various treatments including chemotherapeutic cisplatin and some types of photosensitizers used in PDT [10]. Previous studies demonstrated the effect of indocyanine green ICG775 on the survival of MCF-7 cells [11]. In our experiments, we established whether cyanine IR-768 photosensitizer (Fig. 1) can be delivered to cancer cells in a free form or *via* nanoparticles. The concentration of IR-768 in nanocapsules chosen for cytotoxicity experiments was 0.517 mg/ml. In the fluorescence microscopy, the free IR-768 cyanine penetration in the cytoplasm of the MCF-7 Dox cell line after 24 h incubation was observed (Fig. 5a). The fluorescence of the dye molecules incorporated into nanocapsule particles was located in cytoplasm as well (Fig. 5b). A weak intensity of the fluorescence (Fig. 5b) was probably caused by the covering effect of the nanocapsule wall.



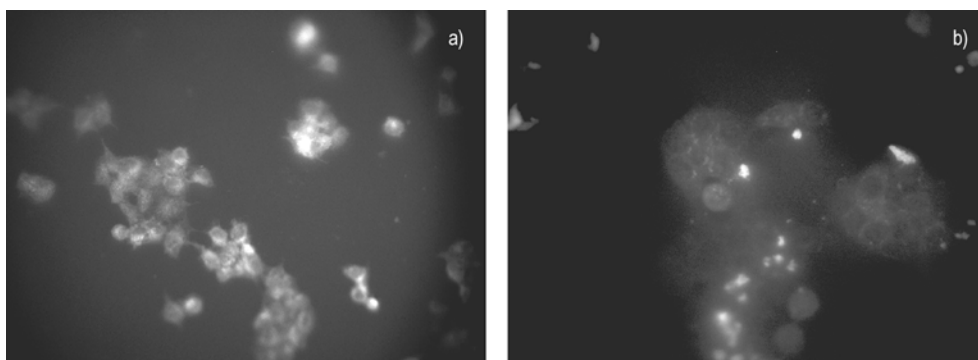


Fig. 5. Intracellular fluorescence the photosensitizer in MCF-7 Dox cells after 24 h incubation (a) free IR-768 and (b) nanocapsule with IR-768

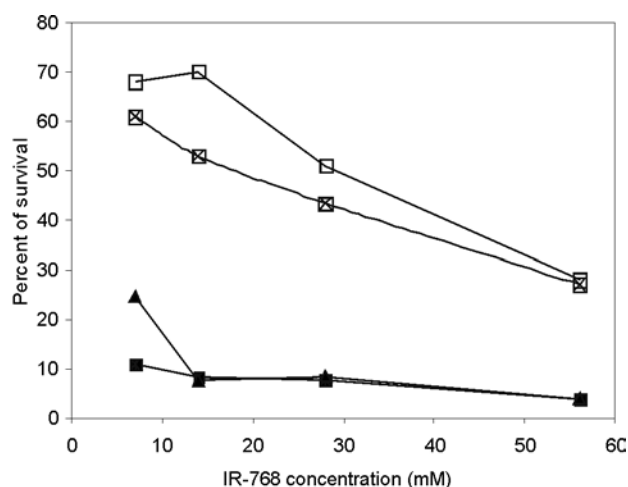


Fig. 6. Effect of IR-768 concentrations on MCF-7 Dox cells viability:  
 □ – nanoparticle/IR-768 nonirradiated, × – nanoparticle/IR-768 after 10 min irradiation, ■ – IR-768 nonirradiated; ▲ – IR-768 after 10 min irradiation

Determination of cell survival by MTT colorimetric assay reflect metabolic conditions in mitochondria compartment and concerns mitochondrial dehydrogenase activities [12]. The viability of MCF-7 Dox cells upon photoirradiation in the presence of free IR-768 or encapsulated IR-768 were evaluated by the MTT assay as a function of dye concentrations (Fig. 6). Encapsulated IR-768 showed significant lower cytotoxicity than free cyanine. Evidently, nanocapsule prevents cells from the contact with the dye particles, being itself less toxic for the cells. However, cytotoxic effect of IR-768 loaded nanoparticles was increased under irradiation. Microemulsions used for the delivery of IR-768 into MCF-7 Dox cells caused a strong cytotoxic effect in the dark conditions (data not shown). For these reasons they were not useful for further PDT studies.

Our preliminary *in vitro* studies in MCF-7 Dox cell lines showed that nanocapsule particles may be used as carriers of a photosensitizer. IR-768 in a nanocapsule may represent a useful formulation of the photosensitizer for practical PDT. Free IR-768 caused high cytotoxicity effect independently of light treatment. In spite of these effects, it cannot be used in a free form because IR-768 is poorly soluble in polar solvents. The problem of a weak solubility of IR-768 in polar environment could be solved by incorporating the dye into biocompatible nanocapsules. These carriers penetrate tumor cells but a higher concentration of IR-768 should be used to obtain more effective cytotoxicity. In future experiments, we will use nanoparticles with thin walls to obtain a better cytotoxic effect after irradiation of tumor cells. A very important problem is selective targeting of a drug carrier to subcellular mitochondrial compartment for induced apoptosis. Apoptosis has been shown to be a rapid and dominant form of cell death following photodynamic therapy. Tumor cell death by necrosis is an undesirable effect because of the inflammatory state generated in the process [13]. The construction of nanocapsules with specific tumor targets should improve the effective treatment and could be safer for normal cells. Future research will include analysis of metabolic state of cells exposed to photosensitization after using nanocapsule particles as carriers of cyanine dyes.

#### Acknowledgement

This work was financially supported by the Polish Ministry of Science and Higher Education (Grant No. NN205013854) and Wrocław medical University (Grant No. 1603).

#### References

- [1] HELLWEG T., *Curr. Opin. Colloid Interf. Sci.*, 7 (2002), 50.
- [2] TORCHILIN V.P., *J. Control Rel.*, 73 (2001), 137.
- [3] WATNASIRICHAIKUL S., DAVIES N.M., RADES T., TUCKER I.G., *Pharm. Res.*, 17 (2000), 684.
- [4] KONAN Y., GURNY R., ALLÉMANN E., *J. Photochem. Photobiol. B*, 66 (2002), 89.
- [5] VAUTHIER CH., DUBERNET C., FATTAL E., *Adv. Drug Del. Rev.*, 55 (2003), 519.
- [6] ALMEIDA R.D., MANADAS B.J., CARVALHO A.P., DUARTE C.B., *Biochim. Biophys. Acta*, 1704 (2004), 59.
- [7] ALLISON R.R., DOWNIE G.H., CUENCA R., HU X.H., CHILDS C.J.H., SIBATA C.H., *Photodiag. Photodyn. Ther.*, 1 (2004), 27.
- [8] DALEY E., VAN LAAR F., DE VOS D., KAMUHABWA A., JACOBS P., DE WITTE P., *J. Photochem. Photobiol.*, 55 (2000), 27.
- [9] HOSOKAWA K., DANTES A., TAJIMA K., KOTSUJI F., *Int. J. Oncol.* 17 (2000), 227.
- [10] JANICKE R.U., SPRENGARD M.L., WATI M.R., PORTER A.G., *J. Biol. Chem.*, 273 (1998), 9357.
- [11] CRESCENZI E., VARIALL L., IOVINO M., CHIAVIELLO A., VENEZIANI B.M., PALUMBO G., *Molec. Cancer Ther.*, 3 (2004), 537.
- [12] DONG Y., BERNES-PRICE S.J., THORBURN D.R., ANTALIS T., DICKINSON J., HURST T., QIU L., KHOO S.K., PARSONS P.G., *Biochem. Pharmacol.*, 53 (1997), 1673.
- [13] SHEU S.S., NAUDURI D., ANDERS M.W., *Biochim. Biophys. Acta*, 1762 (2006), 256.

*Received 28 April 2007*  
*Revised 16 February 2008*

## Detection of some chloroorganic compounds by a microbial sensor system

I. MALISZEWSKA\*, K. A. WILK

Faculty of Chemistry, Wrocław University of Technology,  
Wybrzeże Wyspiańskiego 27, 50-370 Wrocław, Poland

Cells of an isolated *Pseudomonas* sp. MB58 strain containing DL-2-haloacid dehalogenase were used as a biological component in microbial bioassay for the detection of 2,2-dichloropropionic and D-2-chloropropionic acids. The cells were entrapped in various matrices. The highest specific activity and stability have been obtained in calcium alginate. Temperature between 293 and 313 K did not affect the enzymatic activity of the cells, and pH between 6.0 and 8.0 had a little influence. Several organic substances did not influence the conversion, whereas some heavy metal ions inhibited the dehalogenase activity.

Key words: *detection; microorganism; whole cell biosensor; dehalogenation; chloroorganic compounds*

### 1. Introduction

Despite innumerable benefits, industrialization and new technologies create various environmental problems. Heavy metals originating from industrial production bioaccumulate in the aquatic food chain [1]. Organic compounds originating from widespread use of petroleum products are highly toxic and pose a threat for soil and drinking water quality [2].

Conventional chromatographic methods for evaluating contaminated sites are both expensive and technically complicated. In recent years, bacterial whole cell biosensors have been developed as tools to detect and quantify the toxicity of samples from various environments. Many studies used bacteria containing constitutively expressed *luxCDABE* operon from *Vibrio fischeri* to evaluate the presence of toxic compounds. The *lux* genes are usually highly expressed in cells that are not exposed to toxic effects in the medium. Measurements of the decrease in light production from these cells will therefore reflect an inhibitory effect of the compounds added to bacteria. This has led

---

\*Corresponding author, e-mail: irena.helena.maliszewska@pwr.wroc.pl

to a development of commercial toxicity tests such as Microtox [3], using the naturally luminescent *Vibrio fischeri*. As a consequence, similar constructs have been made in bacteria such as *Pseudomonas fluorescens* [4, 5] and *Rhizobium leguminosarum* [6]. Such measurements are nonspecific because many conditions decreasing the metabolic activity of a biosensor strain may reduce light production. Conditions such as pH, metals, xenobiotics and many other compounds are potential inhibitors of light production. These nonspecific sensors have been used to determine the toxicity level of such diverse substances as nitric oxide [7], xenobiotics [8–11], metals [5, 12, 13] and tetracyclines [14, 15]. Recently a novel type of bacterial biosensor has been developed using a recombinant DNA technology [16].

The application of biosensors for the specific estimation of various organic compounds has been investigated by several authors [17–21]. Rawson et al. [22] used the electron transfer chain of the photosynthetic microorganism *Synechococcus sp.* to detect chlorotoluron. A biosensor using *Escherichia coli* cells as a biological compound was introduced in the detection of pentachlorophenol tested on its effect on respiration [23]. A bioassay for the determination of halogenated hydrocarbons was described by Hutter et al. [24, 25]. It is based on the liberation of halogen ions by the action of the alkyl-halidohydrolase enzyme (EC 3.8.1.1) present in the cells of *Rhodococcus sp.*

The aim of the experiments described in this article was to establish a microbial system for the detection of 2-chloroalkanoic acid in water samples. Immobilized cells of *Pseudomonas sp.* MB58 and potentiometric ion selective electrodes (ISE) were used as sensing elements. The MB58 strain produces DL-2-haloacid dehalogenase (data not shown). This enzyme dehalogenates both D- and L-enantiomers of 2-haloalkanoic acids and the corresponding L- and D-2-hydroxyalkanoic acids are produced. The performance of the system and the influence of physical parameters and the number of heavy metals and salts on the system response were studied in detail.

## 2. Experimental

*Microorganism and growth.* *Pseudomonas sp.* strain MB58, grown on 2,2-dichloropropionate was isolated from soil in this laboratory, and was used for the immobilization and biodechlorination experiments. The MB58 strain was cultivated in a mineral medium containing per dm<sup>3</sup>: Na<sub>2</sub>HPO<sub>4</sub>×12H<sub>2</sub>O (5 g), NaH<sub>2</sub>PO<sub>4</sub> (2 g), (NH<sub>4</sub>)<sub>2</sub>SO<sub>4</sub> (0.5 g), MgSO<sub>4</sub>×12 H<sub>2</sub>O (0.1g), yeast extract (50 mg). Chloroorganic compound was filter-sterilized to prevent thermal dechlorination and added as the sole carbon and energy source. Bacteria were grown aerobically at room temperature under conditions of rotary shaking (120 rpm). After 72 h of incubation the cells were collected by centrifugation (3200 rpm, 15 min, 277 K). Then the packed cells were resuspended in a 10 mM phosphate buffer (pH = 7.6) and used for immobilization.

*Immobilization.* The immobilized cell preparations were carried out as described in [26] with the following modification: agarose/ carrageenan 2 ml cell suspension (0.5 g of wet cells) was mixed with 20 ml of 6% agarose (Sigma, type VI) or 4% carrageenan (Sigma, type 1) and poured onto Petri dishes on ice in order to form gel. The gels were cut into  $3 \times 3 \times 3$  mm<sup>3</sup> pieces. Alginate 2 ml cell suspension (0.5 g of wet cells) was mixed with 20 ml of 4% Na-alginate and the mixture was added dropwise to 0.02 M Ca(NO<sub>3</sub>)<sub>2</sub>, thus forming beads with the diameter of about 3 mm. After hardening for 1 h or 6 h in the solution, the beads were washed several times with water and used in the experiments. Instead of CaCl<sub>2</sub> a Ca(NO<sub>3</sub>)<sub>2</sub> was chosen to prevent the falsification of the measurement of the chloride concentrations.

*Determination of the dehalogenating activity of cells.* The activity of the immobilizate was assayed by the incubation (293 K, 120 min) of 2 g immobilizate (wet weight) in 20 ml phosphate buffer (10 mM, pH = 7.6) containing 20 mM of 2,2-dichloropropionate as a substrate. After removing the immobilizate by centrifugation (3200 rpm, 15 min, temp. 277 K), silver(I)-chromate (0.03 g) was added to 2 ml of the solution. The chloride content was determined as described by Isaacs [27]. One unit is defined as the activity catalyzing the formation of 1 μmol chloride/min under the conditions described above. The activity of resting cells was assayed in the same way using 20 mg cells (dry weight) and 20 mM substrate in 2 ml of phosphate buffer (10 mM, pH = 7.6).

*Measuring procedure.* The contents of organochlorides in aqueous solutions was determined as follows: 0.3 ml of NaNO<sub>3</sub> solution was added to 20 ml of the sample. The chloride selective electrode and an Ag/AgCl reference electrode were immersed into the solution. The electrodes were interfaced with a pH ionometer. The potential of the electrodes was allowed to stabilize for approximately 2 min, and 1 g of cell immobilizate was added to start the conversion. When monitoring the formation of chloride ions, 5 min proved to be a sufficiently long period to obtain a significant decrease in the electrode potential. The decrease in potential was recorded and used for the calculation of results. All experiments were carried out at room temperature.

*Effect of physical and chemical parameters.* The effect of several physical and chemical parameters on the dehalogenating activity of *Pseudomonas sp.* MB58 strain was investigated using 20 mM 2,2-dichloropropionate as a substrate with the incubation period of 30 min.

Cells of the tested strain were incubated at temperatures ranging between 293 K and 343 K at pH 8.0. The effect of pH on the dehalogenating cellular activity was determined in the range of pH between 2.0 and 10.0, at 293 K. The inhibition of the dehalogenating activity by several heavy metal ions and organic substances was studied at 293 K and pH = 8.0. For these experiments various salts (CuSO<sub>4</sub>, BaSO<sub>4</sub>, HgCl<sub>2</sub>, PbCl<sub>2</sub>) at the concentrations of 0.1 mM or 1mM were added at the beginning of incubation. Organic compounds such as glucose, urea, sodium citrate and sodium acetate at the concentration of 1 mM were used.

### 3. Results and discussion

Fresh cells of *Pseudomonas* sp. MB58 harvested from the cultivation broth by centrifugation showed the specific activity of 4.8 U/g dry biomass using 2,2-chloropropionate as a substrate. Catalytic active layers were formed by entrapment of bacterial cells in agarose, carrageenan and alginate. For estimating the efficiency in immobilization, specific activities of small pieces/beads which can be applied directly to the ion selective electrode were determined. A high specific activity of the immobilizate was achieved by using alginate as a matrix, resulting in the specific activity of 57 mU/g (100%) immobilizate using 2,2-chloropropionate as a substrate. Only a slightly reduced activity was found in cells immobilized in agarose (96%) and carrageenan (93%). Investigations into long-term stability were performed by storing pieces/beads at 277 K for six weeks in a solution of 2% sodium phosphate (agarose), ammonium sulphate (carrageenan) or calcium nitrate (alginate). The decrease of about 5% in the dehalogenating activity of cells immobilized in alginate beads was observed. The carrageenan and agarose immobilizate lost over 40% of the dehalogenating activity after six weeks at 277 K. Therefore, immobilized cells of *Pseudomonas* sp. MB58 in alginate were used as a component of a bioassay with chloride selective electrodes as sensors.

In our experiments, the response of this kind of biosensor was analysed by the addition of 2,2-dichloropropionate (final concentration 20 mM) to ionically stabilized water samples. Typical response curves from our experiments are shown in Fig. 1.

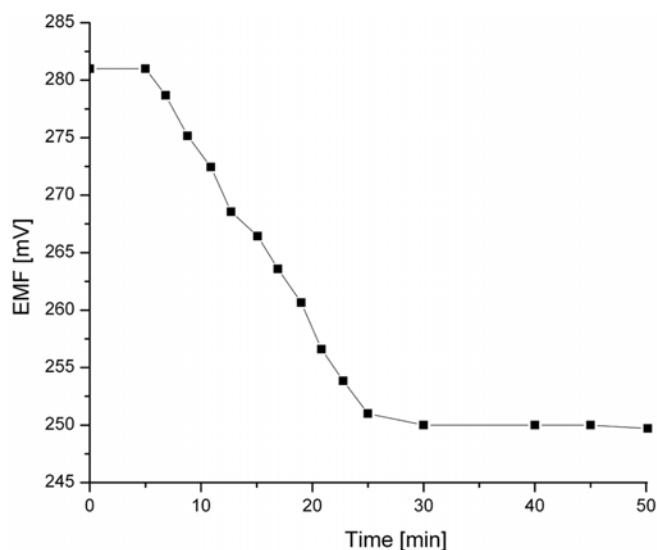


Fig. 1. Response of the microbial assay in a sample solution containing 2,2-dichloropropionate upon the addition of the chlorinated substrate at 0 min

After a dead time of 5 min, a first decrease in the electromotive force (EMF) was observed. A constant EMF was attained 30 min after sample application, thus repre-

senting the moment of attaining a steady state in the enzymatic conversion. In further experiments, the concentrations of 2,2-dichloropropionate and D-2-chloropropionate were varied with the aim to perform the calibration and to estimate the detection limit. The results are given in Fig. 2.

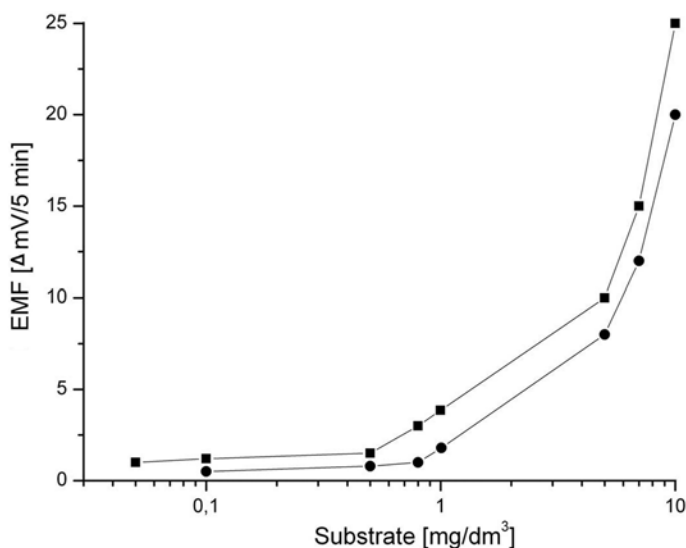


Fig. 2. Calibration graphs for the bioassay:  
 ■ 2,2-dichloropropionic acid, ● D-2-chloropropionic acid

Table 1. Relative degradation of chlorinated compounds by immobilized cells of *Pseudomonas* sp. MB58

Substrate	Relative activity [%]
2,2-dichloropropionate	100
D-2-chloropropionate	148
L-2-chloropropionate	136
2-chlorobutyrate	95
chloroacetate	15
dichloroacetate	10
trichloroacetate	8
1-chlorobutane	0
1-chlorohexane	0

Non-linear calibration plots were obtained due to the non-linearity of the potential of a chloride electrode in the range close to the detection limit. The detection limits for 2,2-dichloropropionate and D-2-chloropropionate were 0.1 mg/dm<sup>3</sup> and 0.05 mg/dm<sup>3</sup>, respectively. The relative standard deviation has been calculated at 6.8%.

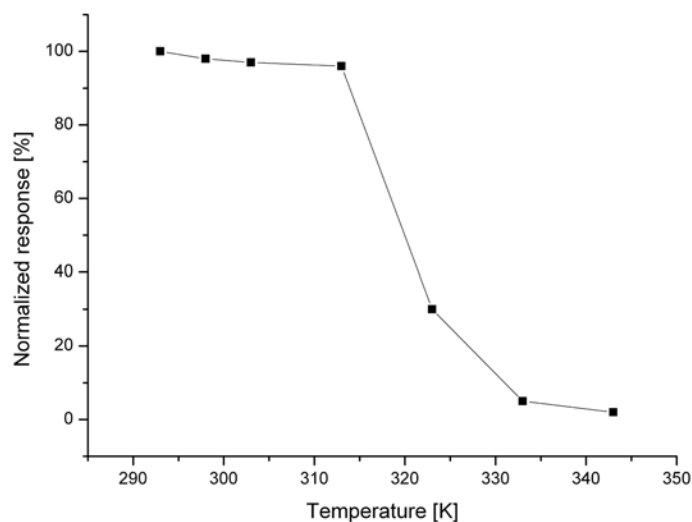


Fig. 3. Effect of temperature on dehalogenating cellular activity; the activities are expressed as percentages of the rate observed with 2,2-dichloropropionate at 293 K and pH = 8.0

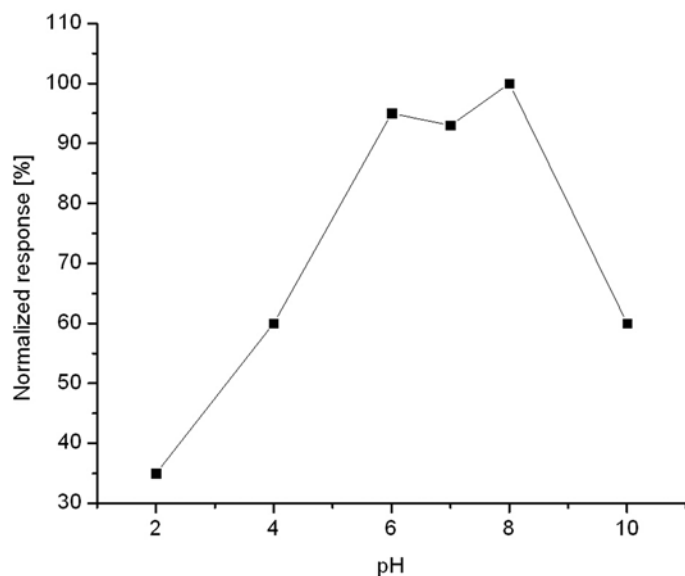


Fig. 4. Effect of pH on dehalogenating cellular activity; the activities are expressed as percentages of the rate observed with 2,2-dichloropropionate at pH = 8.0 and 293 K

The initial rates for the conversion of several chloroorganic compounds by immobilized cells were determined using 20 mM substrate. The measurements were carried out with alginate-immobilized cells. The results are given in Table 1, expressed relative to the conversion rate of 2,2-dichloropropionate. The data are averages of a triple



assay with the standard deviation of 3–5%. The activities are expressed as the percentage of the rate determined with 2,2-chloropropionic acid at 293K.

The studied enzyme acted towards both diastereoisomers D- and L-2-chloroalkanoic acids, however, an increased rate of dehalogenation of D-2-chloropropionic acid has been observed. Chloroacetate, di- and trichloroacetate were converted at a reduced rate. 1-chloroalkanes (1-chlorobutane and 1-chlorohexane) showed no detectable conversion. These results conform to data on substrate specificity obtained with the purified DL-2-halohydrolyase isolated from other bacterial strains [28].

The effect of several physical and chemical parameters on the dehalogenating activity of the studied MB58 strain was investigated using 20 mM 2,2-dichloropropionate as a substrate with the incubation period of 30 min. The results shown in Figs. 3 and 4 are mean values from a triple determination.

The temperature dependence of the dehalogenating activity of the studied MB58 strain has also been investigated in the temperature range 293–343 K (Fig. 3). There was no effect on dehalogenating activity at temperatures below 313 K, neither was there any significant deviation in the electric signal if measurements were performed within pH of 6.0–8.0 (Fig. 4). The influence of several heavy metals and organic compounds is summarized in Table 2.

Table 2. Inhibition of dehalogenating activity of *Pseudomonas* sp. MB58

Potential inhibitor	Concentration (mM)	Inhibition [%]
Glucose	1	0
Urea	1	4
Sodium citrate	1	0
Sodium acetate	1	5
Cu <sup>2+</sup>	1	20
Ba <sup>2+</sup>	1	45
Ba <sup>2+</sup>	0.1	11
Hg <sup>2+</sup>	1	89
Hg <sup>2+</sup>	0.1	65
Pb <sup>2+</sup>	1	74

Heavy metal ions inhibited the dehalogenating activity of the cells at concentrations of more than 0.1 mM. Several other substances like glucose, urea, citrate, acetate at the 1mM level caused only minor inhibition. These concentrations are far above the levels that can be expected to be present in water.

#### 4. Conclusion

2-chloroalkanoic acids can be detected by the application of whole cell biosensors in a sensitive and inexpensive way. Cells of *Pseudomonas* sp. MB58 producing DL-2-haloacid dehalogenase can be easily immobilized as a very active catalytic layer. The intracellular dehalogenase of tested microorganism enables the dehalogenation of several 2-

chloroalkanoic acids. Ion selective electrodes for chloride are applicable as specific transducer element, thus forming a very compact biosensor for some chlorinated acids in water samples e.g. 2,2-dichloropropionic acid known as the herbicide DALAPON.

#### Acknowledgement

This work was financially supported by the Faculty of Chemistry, Wrocław University of Technology.

#### References

- [1] HANSEN L.H., SORENSEN S.J., *Microb. Ecol.*, 42 (2001), 483.
- [2] APPLEAGE B.M., KEHRMEYER S.R., SAYLER G.H., *Appl. Environ. Microbiol.*, 64 (1998), 2730.
- [3] BULICH A.A., *Process Biochem.*, 17 (1982), 45.
- [4] PALMER G., MCFADZEAN R., KILLHAM K., SINCLAIR A., PATON G.I., *Chemosphere*, 36 (1998), 2683.
- [5] PATON G.I., CAMPBELL C.D., GLOVER L.A., KILLHAM K., *Lett. Appl. Microbiol.*, (20 (1995), 52.
- [6] PATON G.I., PALMER G., BURTON M., RATTRAY E.A.S., MCGRATH S.P., GLOVER L.A., KILLHAM K., *Lett. Appl. Microbiol.*, 24 (1997), 296.
- [7] VIRTA M., KARP M., VUORINEN P., *Antimicrob. Agents Chemother.*, 38 (1994), 2775.
- [8] BEATON Y., SHAW L.J., GLOVER L.A., MEHARG A.A., KILLHAM K., *Environ. Sci. Technol.*, 33 (1999), 4086.
- [9] BUNDY J.G., WARDELL J.L., CAMPBELL C.D., KILLHAM K., PATON G.I., *Lett. Appl. Microbiol.*, 25 (1997), 353.
- [10] SOUSA S., DUFFY C., WEITZ H., GLOVER L.A., BAER E., HENKLER R., KILLHAM K., *Environ. Toxicol. Chem.*, 17 (1998), 1039.
- [11] WISE A.A., KUSKE C.R., *Appl. Environ. Microbiol.*, 66 (2000), 163.
- [12] CHAUDRIA.M., KNIGHT B.P., BARBOSA-JEFFERSON V.L., PRESTON S., PATON G.I., KILLHAM K., COAD N., NICHOLSON F.A., CHAMBERS B.J. MCGRATH S.P., *Environ. Sci. Technol.*, 33 (1999), 1880.
- [13] RASMUSSEN L.D., SORENSEN S.J., TURNER R.R., BARKAY T., *Soil Biol. Chem.*, 32 (2000), 639.
- [14] D'HAESE E., NELIS H.J., REYBROECK W., *Appl. Environ. Microbiol.*, 63 (1997), 4116.
- [15] HANSEN L.H., FERRARI B., SORENSEN A.H., VEAL D., SORENSEN S.J. *Appl. Environ. Microbiol.*, 67 (2001), 239.
- [16] YAGI K., *Appl. Microbiol. Biotechnol.*, 73 (2007), 1251.
- [17] GUAN X., RAMANATHAN S., GARRIS J.P., SHETTY R.S., ENSOR M., BACHAS L.G., DUNERT S., *Anal. Chem.* 72 (2000), 2423.
- [18] SAYLER G.S., *Appl. Environ. Microbiol.*, 66 (2000), 4589.
- [19] GU M.B., CHANG S.T., *Biosens. Bioelectron.*, 16 (2001), 667.
- [20] MAEDA I., YAMASHIRO H., YOSHIOKA D., ONODERA M., UEDA S., MIYASAKA H., UMEDA F., KAWASE M., TAKAICHI S., YAGI K., *Curr. Microbiol.*, 51 (2005), 193.
- [21] RESHETILOV A.N., *Appl. Biochem. Microbiol.*, 41 (2005), 504.
- [22] RAWSON D.M., WILLMER A.J., CARDOIS M.F., *Toxic. Assess.*, 2 (1987), 325.
- [23] GAISFORD W.C., RICHARDSON N.J., HAGGETT B.G.D., RAWSON D.M., *Biochem Soc. Trans.*, 19 (1991), 15.
- [24] HUTTER W., PETER J., SWOBODA H., HAMPEL W., ROSENBERG E., KRAMER D., KELLNER R., *Anal. Chim. Acta*, 306 (1995), 237.
- [25] PETER J., HUTTER W., STOLLNBERGER F., KARNER F., HAMPEL W., *Anal. Chem.*, 69 (1997), 2077.
- [26] PETER J., BUCHINGER W., KARNER F., HAMPEL W., *Acta Biotechnol.*, 17 (1997), 123.
- [27] ISAACS M.L., *J. Biol. Chem.*, 53 (1922), 17.
- [28] SCHWARZE R., BROKAMP A., SCHMIDT R.J., *Curr. Microbiol.*, 34 (1997), 103.

*Received 28 April 2007  
Revised 16 February 2008*

# Ultrafiltration as a method of separation of natural organic matter from water

M. KABSCH-KORBUTOWICZ\*

Wrocław University of Technology, Institute of Environment Protection Engineering,  
Wybrzeże Wyspiańskiego 27, 50-370 Wrocław, Poland

The objective of the study was to investigate the influence of membrane material, membrane cut-off and water composition on transport and separation properties of ultrafiltration membranes. Nadir membranes made of regenerated cellulose and polyethersulfone, with the cut-off of 5–100 kDa, were used. Experiments were performed for model solutions and for water from Odra river. It was found that compact ultrafiltration membranes (of low cut-off) allow one to remove efficiently natural organic matter from water. Transport and separation properties of ultrafiltration membranes are strongly influenced by membrane cut-off and membrane material. Retention of natural organic matter particles decreases with the increase of membrane cut-off while the opposite trend is observed in the case of permeability. The study shows that the degree of ultrafiltration membrane blocking by organic particles is related to membrane material (hydrophilic/hydrophobic properties of polymer) and its cut-off. Strongly hydrophilic membranes made of regenerated cellulose of low cut-off display a low proneness to fouling.

Key words: *membrane; water treatment; separation; fouling*

## 1. Introduction

Shortage of drinking water around the world, and increasing requirements concerning its quality result in seeking for new effective processes of water treatment. Raw water being a source of water supply contains suspended solids, colloids, and organics including bacteria and viruses. Suspended particles are generally larger than 1  $\mu\text{m}$  and colloidal particles are in the range of 1–1000 nm. Those pollutants are of mineral and organic origin. Among organic substances the major fractions are natural organic matter substances.

Natural organic matter (NOM) is a mixture of organic compounds widespread in both surface and ground waters. Those substances range from macromolecules to low molecular weight compounds, such as simple organic acids and short-chained hydro-

---

\*E-mail: malgorzata.kabsch-korbutowicz@pwr.wroc.pl

carbons. Aquatic humic substances generally comprise from one-third to one-half of the dissolved carbon in water, thus are the dominant fraction of NOM in waters. Humic substances can be regarded as natural anionic polyelectrolytes of rather indeterminate structure. They have various functional groups, including carboxylic and phenolic ones, and a framework of randomly condensed aromatic rings. Because of ionization of carboxylic groups, humic substances will have negative charge at pH values above 4.5 [1] and are generally soluble under these conditions.

Due to unfavourable influence of NOM on water quality, this group of substances must be removed from potable waters. Among various physicochemical processes applied in water treatment, the most effective are coagulation, activated carbon adsorption and membrane separation. These water treatment processes can remove aquatic organic matter from water, with the efficiency depending on process operational conditions and the specific characteristics of the NOM such as molecular weight distribution, carboxylic acidity, and content of humic substances [2, 3].

Pressure driven membrane processes, i.e. reverse osmosis (RO), nanofiltration (NF), ultrafiltration (UF) and microfiltration (MF) are increasingly used in drinking water treatment. Depending on applied process they can remove a wide variety of substances from water. The basic parameters of pressure driven membrane processes are given in Table 1.

Table 1. Pressure driven membrane processes, their properties and applications [4, 5]

Process	Pore size [nm]	Pressure [MPa]	Separation capability
Microfiltration	50–5000	0–0.3	retention of bacteria, colloids, protozoa
Ultrafiltration	5–100	0.05–0.5	retention of viruses, bacteria and dissolved substances with MW 10–500 kDa
Nanofiltration	~ 1	0.5–2.5	separation of low MW substances (200–300 Da) and divalent salts
Reverse osmosis	< 1	1.5–10	retention of all dissolved ions

Microfiltration and ultrafiltration, due to relatively large membrane pores, have been employed primarily for removal of microorganisms and particles from waters. MF is effective in turbidity and particulate organic matter removal, as well as bacteria, protozoa and algae. UF can also remove viruses and some of the organic matter particles. Efficiency of NOM separation with use of the UF membranes is influenced by many factors, i.e. NOM character, molecular weight distribution, pH and ionic strength of water, and membrane cut-off. Generally, UF is effective in high-molecular weight fraction of the NOM removal.

A more widespread application of membrane processes is limited by the decrease in membrane performance occurring during potable water treatment as a result of fouling through the accumulation of particles and adsorption of the NOM [6, 7]. Extensive research has been carried out to understand factors influencing intensification of membrane fouling but these results are either inconclusive or sometimes even contra-

dictory. Generally, it may be said that the decrease in membrane permeability during water treatment depends on the type of the membrane used as well as on the amount and properties of the organic substances in the treated water.

The main objective of this investigation was to analyze the possibility of separation of natural organic matter from water by ultrafiltration. The influence of membrane properties such as their cut-off and membrane material on transport and separation properties was investigated. The molecular weight cut-off (MWCO) is the parameter used by manufacturers to characterize membrane separation properties. It indicates that at least 90% of dissolved macromolecules with molecular weight higher than the stated MWCO will be retained.

## 2. Experimental

*Characterisation of the membranes.* Nadir ultrafiltration membranes, made of regenerated cellulose and polyethersulfone, were used in the study. Their characterisation is given in Table 2. SEM picture of the investigated membranes is shown in Fig. 1.

Table 2. Principal parameters of the experimental membranes [8, 9]

Membrane	Membrane material	MWCO [kDa]	Mean pore radius [nm]	Contact angle [deg]	Polarity [%]
C5	regenerated cellulose	5	0.82	54.76	49.92
C10		10	5.01		
C30		30	12.55		
C100		100	no data		
PES5	polyethersulfone	5	0.62	50.01	44.27
PES10		10	2.04		
PES30		30	8.38		

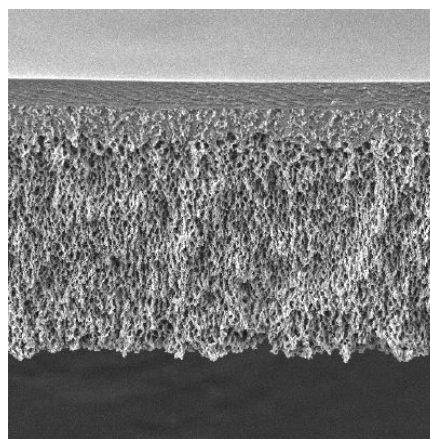


Fig. 1. SEM of the membrane cross-section [10]

*Solutions.* Water model solution and surface water from Odra river (Wroclaw, Poland) were used in this study. The model solution was prepared from natural water flowing out from The Great Batorow Peatbag (southwest Poland) dissolved in various proportions with dechlorinated tap water. Properties of feed waters are presented in Table 3.

Table 3. Properties of feed water

Parameter	Mean value				
	Model solutions				Odra river
	1	2	3	4	
Colour, g Pt/m <sup>3</sup>	33.0	64.3	93.3	120.6	25.3
Absorbance at 254 nm, cm <sup>-1</sup>	0.210	0.411	0.598	0.777	0.170

*Analytical methods.* The efficiency of examined processes was determined by measuring the amount of organic matter in samples before and after the process. NOM concentration was monitored by measurement of UV absorbance at 254 nm and colour intensity (Shimadzu QP2000 spectrophotometer). UV absorbance at 254 nm is a good measure of the presence of naturally occurring organic matter, such as humic substances, because they contain aromatic moieties and they are the dominant form of organic matter in natural waters. UV absorbance at 254 nm has been used in Europe for several years as a surrogate measure of TOC and THM precursors' concentration [11].

*Apparatus.* The experiments were carried out in a laboratory ultrafiltration cell (Fig. 2) at a pressure difference of 0.1 MPa. The main part of the system was an Amicon 8400 ultrafiltration cell with the total volume of 350 cm<sup>3</sup> and the diameter of 76 mm. The effective surface of the membrane amounted to 4.52 × 10<sup>-3</sup> m<sup>2</sup>.

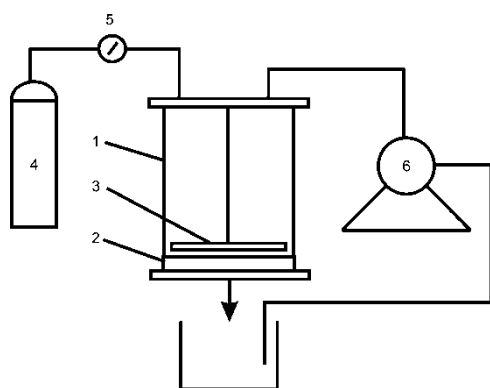


Fig. 2. Experimental set-up: 1– ultrafiltration cell (Amicon 8400), 2 – membrane, 3 – stirrer, 4 – gas cylinder, 5 – reducer, 6 – recirculation pump

*Assessment of separation and transport properties.* To estimate the separation and transport properties of the membranes under study, the volume flux of the permeate  $J$  and the retention factor  $R$  have been determined.

Volume flux of the permeate  $J$  describes the volume of liquid passing across a membrane surface unit per unit time:

$$J = \frac{V}{A t}, \quad \left[ \frac{\text{m}^3}{\text{m}^2 \cdot \text{d}} \right]$$

where  $V$  is the permeate volume,  $\text{m}^3$ ,  $A$  denotes an effective surface area of the membrane,  $\text{m}^2$ , and  $t$  stands for duration of measurement, d.

Retention factor  $R$  defines the efficiency of separation of a natural organic matter macromolecules from the feeding solution:

$$R = \frac{c_f - c_p}{c_f} \times 100\%$$

where  $c_f$ ,  $c_p$  denote the values of the measured parameter in the feed, and in the permeate, respectively.

### 3. Results and discussion

#### 3.1. Transport and separation properties of the membranes

The study aimed at the evaluation of the ultrafiltration membranes for separation of natural organic matter particles from aqueous solutions. The effect of membrane

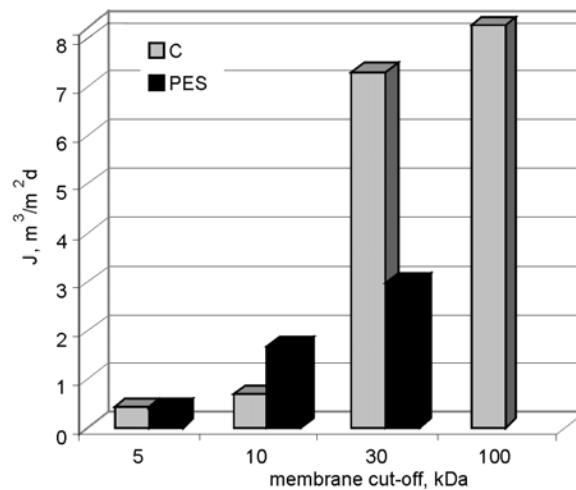


Fig. 3. Transport properties of ultrafiltration membranes (for distilled water)

cut-off on membrane permeability is shown in Fig. 3. The volume flux of distilled water varied from  $0.412 \text{ m}^3/(\text{m}^2 \cdot \text{d})$  for C5 membrane to  $8.258 \text{ m}^3/(\text{m}^2 \cdot \text{d})$  for C100

membrane, and from  $0.397 \text{ m}^3/(\text{m}^2 \cdot \text{d})$  to  $2.992 \text{ m}^3/(\text{m}^2 \cdot \text{d})$  for PES5 and PES30 membranes, respectively. The increase of membrane cut-off is connected with the increase of pore radius, resulting in a higher convective flux of the water. For membranes of cut-off 5 kDa, the hydrophilicity of membrane material did not affect transport properties of membranes but for membranes of cut-off 30 kDa a higher water flux was observed for a more hydrophilic C membrane.

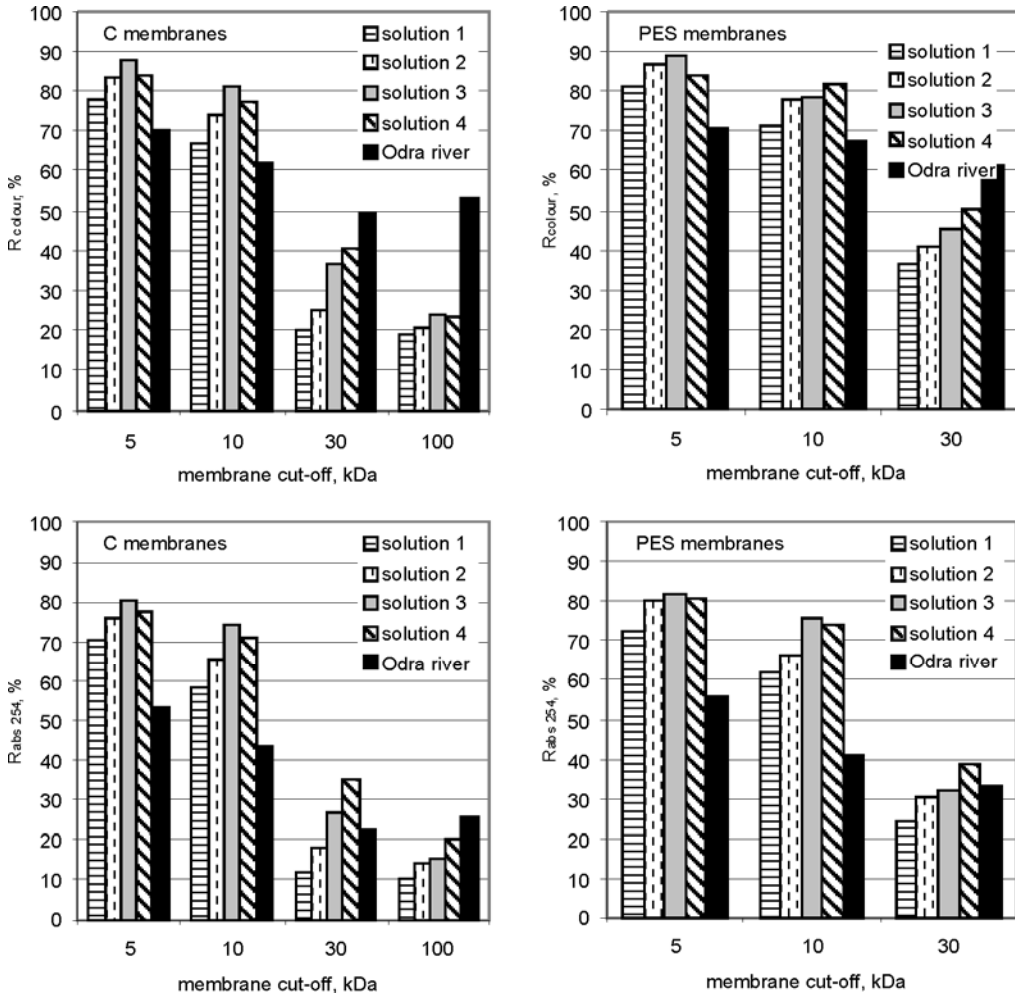


Fig. 4. Separation of natural organic matter by ultrafiltration membranes

The efficiency of separation of natural organic matter was found to be strongly influenced by membrane properties. Figure 4 shows the effect of membrane cut-off on the removal of colour and UV absorbance at 254 nm. The increase of membrane cut-off resulted in decrease of NOM removal efficiency. Slightly higher values of the retention factors obtained for PES membranes as compared to those for C membranes



result from higher hydrophobic sorption of macromolecules on strongly hydrophobic PES membranes (see Sect. 3.2.).

A preferential decrease of colour over the UV 254 nm absorption was observed. This is understandable, as the colour of water is related to the presence of NOM fractions. The UV absorption at 254 nm monitors the amount of the NOM fraction containing aromatic structures in their molecules. The smallest fractions may even contain compounds which exhibit no UV absorbance.

### 3.2. Membrane proneness to fouling

The flux decline of ultrafiltration membranes was studied in terms of the normalized flux  $J/J_0$  ( $J$  is the permeate flux and  $J_0$  is distilled water flux) – the highest the value  $J/J_0$ , the less capable of membrane fouling is a given membrane. Normalized flux values for various water compositions are presented in Fig. 5.

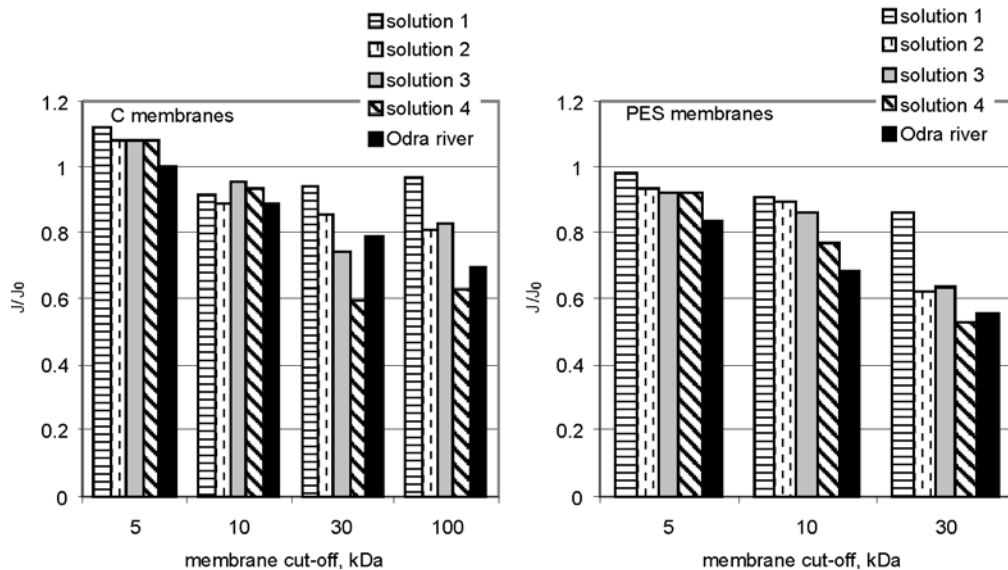


Fig. 5. The effect of the membrane type and properties of water on the normalized flux

The experimental results show that membrane fouling was strongly influenced by the membrane type and amount of organic particles in treated water. The decrease in permeate flux for a more hydrophilic C membrane was lower than that for a more hydrophobic PES membrane.  $J/J_0$  values decrease with increasing membrane cut-off. The obtained results suggest that decrease of membrane permeability results from adsorption of NOM particles on the membrane surface and in the pore interior. Hydrophobic organic particles adsorb strongly on more hydrophobic membranes. They can also penetrate into membrane pores (especially of higher radius) and block them.

This is in a good agreement with findings of Dal-Cin et al. [12] who stated that when the pore size is considerably smaller than the foulant size, the pore size of the membrane remains unchanged and the decrease of flux might be only due to surface adsorption of macromolecules. On the other hand, when the pore size is much larger than the foulant size, macromolecules enter the pores, adsorbing on the pore walls and reducing the effective pore sizes. In such a situation the flux decrease is due to the reduced flow area.

The results of the experiment also indicate that the increase of organic matter concentration in treated water strongly affected the decrease of permeate flux.

## 4. Conclusions

The suitability of membrane ultrafiltration process to the treatment of waters containing natural organic matter has been investigated. The results led to the following conclusions:

- Compact ultrafiltration membranes (of low cut-off) allow one to remove efficiently natural organic matter from water.
- Transport and separation properties of ultrafiltration membranes depend strongly on the membrane cut-off and membrane material; retention of NOM particles decreases with the increase of membrane cut-off; while an opposite trend is observed in the case of permeability.
- The degree of ultrafiltration membrane blocking by NOM particles is related to membrane material (hydrophilic/hydrophobic properties of polymer) and its cut-off. Strongly hydrophilic membranes made of regenerated cellulose of low cut-off display a low proneness to fouling.

### Acknowledgements

The work was partly supported by Polish Ministry of Science and Higher Education, Grant No. 3 T09D 014 29 (years 2005–2007).

## References

- [1] STEVENSON F.J., *Humus Chemistry*, Wiley, New York, 1982.
- [2] COLLINS M.R., AMY G.L., STEELINK C., *Environ. Sci. Technol.*, 20 (1986), 1028.
- [3] MATILAINEN A., LINDQVIST N., KORHONEN S., TUHKANEN T., *Environ. Int.*, 28 (2002), 457.
- [4] VAN RIJN C.J.M., *Nano and Micro Engineered Membrane Technology*, Elsevier, Amsterdam, 2004.
- [5] SINGH R., *Hybrid Membrane Systems for Water Purification*, Elsevier, Amsterdam, 2006.
- [6] KIMURA K., HANE Y., WATANABE Y., AMY G., OHKUMA N., *Water Res.*, 38 (2004), 3431.
- [7] LI C.-W., CHEN Y.-S., *Desalination* 170 (2004), 59.
- [8] MAJEWSKA-NOWAK K., KABSCH-KORBUTOWICZ M., BRYJAK M., WINNICKI T., *Separation of dyes by hydrophilic ultrafiltration membranes*, [in:] *Proc. of 7th World Filtration Congress*, Budapest, Hungary, 20–22.05.1996, Vol. 2, p. 885.

- [9] KOCHKODAN V., HILAL N., NIGMATULLIN R., GONCHARUK V., *Lipase-immobilized biocatalytic membranes in enzymatic esterification*, [in.] M. Bryjak, K. Majewska-Nowak, M. Kabsch-Korbutowicz (Eds.), *The Impact of Membrane Technology to Human Life*, e-book, Oficyna Wyd. PWr., Wrocław, 2006, p. 85.
- [10] <http://www.millipore.com>
- [11] EDZWALD J.K., BECKER W.C., WATTIER K.L., *J. AWWA* 77 (1985), 122.
- [12] DAL-CIN M.M., STRIEZ C.N., TWEDDLE T.A., CAPES C.E., MCLELLAN F., BUISSON H., *Desalination*, 101 (1995), 155.

*Received 28 April 2007*  
*Revised 16 February 2008*

## Contents

P. Mazur, S. Zuber, M. Grodzicki, A. Ciszewski, Effects of Ar <sup>+</sup> ion sputtering on morphology and electric conductance of 6H-SiC (0001) surface.....	265
K. Kolanek, T. Gotszalk, M. Zielony, P. Grabiec, Fabrication of micro- and nanostructures by scanning probe microscopy. Local anodic oxidation.....	271
Z. W. Kowalski, J. Wilk, Surface nanomodification induced by a neutralized ion beam .....	279
M. Krzywiecki, L. Grządziel, L. Ottaviano, P. Parisse, S. Santucci, J. Szuber, XPS study of air exposed copper phthalocyanine ultra-thin films deposited on Si(111) native substrates .....	287
A. Stupakiewicz, A. Fleurence, R. Gieniusz, A. Maziewski, T. Maroutian, P. Gogol, B. Bartenlian, R. Mégy, P. Beauvillain, Magnetic properties of ultrathin Co(0001) films on vicinal Si(111) substrate.....	295
A. Boczkowska, M. Marczewski, E. Ciecierska, B. Sienkiewicz, A. Pietrzykowski, Urea-urethane nanocomposites obtained from modified methylalumoxane oligomers.....	301
C. Czosnek, S. Kluska, J. F. Janik, Aerosol-assisted synthesis of SiC-based nanopowders from organosilicon precursor systems.....	309
M. Dudek, M. Mróz, Ł. Zych, E. Drożdż-Cieśla, Synthesis of ceria-based nanopowders suitable for manufacturing solid oxide electrolytes.....	319
N. Moskała, J. Morgiel, W. Pyda, Nanometric Y <sub>2</sub> O <sub>3</sub> -TiO <sub>2</sub> -ZrO <sub>2</sub> solid solution powders and their utilization in the synthesis of composite powders with TiB <sub>2</sub> and TiC inclusions .....	331
K. Niespodziana, K. Jurczyk, M. Jurczyk, Titanium-ceramic nanocomposites fabricated by the mechanical alloying process .....	341
R. Pelka, P. Glinka, W. Arabczyk, The influence of iron nanocrystallite size on a nitriding process rate.....	349
M. Podsiadły, U. Narkiewicz, W. Arabczyk, M. J. Woźniak, K. J. Kurzydłowski, Preparation of carbon encapsulated cobalt nanoparticles by catalytic ethane decomposition .....	357
J. Ryszkowska, M. Jurczyk, Structure and properties of polyurethane nanocomposites modified by dibutyl phosphate boehmite.....	365
A. Adamski, P. Jakubus, Z. Sojka, Structural and textural evolution of zirconia nanocrystals induced by thermal treatment .....	373
M. Tulinski, K. Jurczyk, M. Jurczyk, Nickel-free nanocrystalline austenitic stainless steels .....	381
A. Zdyb, K. Cieślak, J. M. Olchowik, Properties of films fabricated from ZnS/Mn <sup>2+</sup> nanoparticles .....	389
Ł. Zych, Consolidation and sintering of nanometric ceramic powders .....	395
W. Pyda, Nano-ceramic aspect of preparation and processing of zirconia nanopowders.....	403
E. Borowiak-Palen, Iron filled carbon nanotubes for bio-applications .....	413
Z. Sadowski, I. H. Maliszewska, B. Grochowalska, I. Polowczyk, T. Koźlecki, Synthesis of silver nanoparticles using microorganisms.....	419
M. Ziolk, I. Sobczak, A. Dudzik, Ł. Konwicky, J. Kujawa, Nanosorbents for selective removal of odours.....	425
S. Costa, E. Borowiak-Palen, M. Kruszyńska, A. Bachmatiuk, R. J. Kaleńczuk, Characterization of carbon nanotubes by Raman spectroscopy .....	433
K. Zielińska, K. A. Wilk, E. Seweryn, J. Pietkiewicz, J. Saczko, Studies on biocompatible nanocapsules formed in microemulsion templated processes.....	443
I. Maliszewska, K. A. Wilk, Detection of some chloroorganic compounds by a microbial sensor system.....	451
M. Kabsch-Korbutowicz, Ultrafiltration as a method of separation of natural organic matter from water.....	459

## GUIDELINES FOR AUTHORS

Manuscripts can be sent by conventional mail or by e-mail. Submission of a manuscript to *Materials Science-Poland* implies that it is not being considered for the publication elsewhere, and the authors have a necessary authorization to publish the material contained in the paper. **The manuscripts should conform to the formal standards of the Journal which may be found in the first issue of each volume and on the web page.**

Authors are encouraged to submit electronic versions of the manuscript by e-mail, to the address of the Journal. A single PDF file should be sent, containing text, references, figures, tables etc. Alternatively, the authors can submit the manuscript by conventional mail, sending a CD with the PDF file mentioned above, to the Editor-in-Chief at his address given below.

Each submitted manuscript will be reviewed, the final decision concerning its acceptance resting with the editors. Upon acceptance, the corresponding author will be requested to submit the following material (via e-mail or by conventional mail, on CD)

- A DOC or RTF file containing the final version of the text, references, tables and figure captions. The content of the file should be identical with that of the hard copy, and should exactly match the version seen and accepted by the referee(s).

- File(s) in appropriate formats containing figures. The required formats of the drawings (plots, schemes of technological processes) must be vector files such as XLS, OPJ, cdr (Excel, Origin, Corel-Draw) which may also be exported as EPS, EMF or WMF files. Drawings submitted in tiff or jpg formats (bitmaps, raster graphics), even if exported as EPS, EMF or WMF files, will not be accepted. **Bitmaps are acceptable only in the case of photographs.** The photographs (only in grayscale) should have the resolution not lower than 300 dpi (estimated for the size in which they are expected to be reproduced).

- A PDF file containing the complete manuscript (text, literature, tables, figures, etc). The file should be carefully checked as it will serve as a hard copy in case of doubts. **The contents of the PDF file should exactly match the material in other files.**

Irrespective of whether the final version is submitted by e-mail or by conventional mail, the authors should also send **via conventional mail** a signed copy of the Copyright Transfer Agreement (available on the web page of the Journal).

**For detailed information consult the first issue of each volume or the web page of the Journal.**

**The mail should be addressed to:**

Professor Juliusz Sworakowski  
Editor-in-Chief, Materials Science-Poland  
Politechnika Wroclawska, W-3  
Wybrzeże Wyspiańskiego 27  
50-370 Wrocław, Poland

**Electronic correspondence should be sent to:** [MatSci@pwr.wroc.pl](mailto:MatSci@pwr.wroc.pl)

**Web page of Materials Science-Poland:** [www.MaterialsScience.pwr.wroc.pl](http://www.MaterialsScience.pwr.wroc.pl)

The Publisher reserves the right to make necessary alterations to the text. Each corresponding author will be supplied with one free copy of the journal. Orders for additional offprints can be placed with the Publisher.

**Price 27 zł**  
**(0% VAT)**

Subscription of "Materials Science-Poland" can be ordered via "RUCH" S.A., O.K.D.P.  
Conditions and actual prices can be found at:  
<http://www.ruch.pol.pl>

Subscription orders together with the copy of payment confirmation should be addressed to:  
"RUCH" S.A., O.K.D.P.  
Subscription Department and Foreign Co-operation  
Jana Kazimierza 31/33  
PI 01-248 Warszawa

Single issues may be ordered at:  
Oficyna Wydawnicza Politechniki Wrocławskiej  
Wybrzeże Wyspiańskiego 27  
PI 50-370 Wrocław  
[oficwyd@pwr.wroc.pl](mailto:oficwyd@pwr.wroc.pl)

CHZ "Ars Polona" S.A.  
Obrońców 25  
PI 03-933 Warszawa  
[arspolona@arspolona.com.pl](mailto:arspolona@arspolona.com.pl)